Solar Wind-Magnetospheric Coupling and its Relationship with the Aurora in the Polar Regions of Jupiter

Hannah S. Joyce, MPhys (Hons)

Faculty of Science and Technology

Lancaster University

A thesis submitted for the degree of

Doctor of Philosophy

March, 2026

Solar Wind-Magnetospheric Coupling and its Relationship with the Aurora in the Polar Regions of Jupiter

Hannah S. Joyce, MPhys (Hons).

Space and Planetary Physics, Physics Department, Lancaster University

A thesis submitted for the degree of *Doctor of Philosophy*. March, 2026.

Abstract

The overarching aim of this research is to explore how solar wind–magnetosphere coupling influences Jupiter's polar aurora. In particular, the investigation focuses on whether magnetic reconnection, as a large-scale interaction, accounts for observed variations in auroral emissions at high latitudes. Additional consideration is given to energy transfer via vortices generated by the Kelvin-Helmholtz (K-H) instability, as well as the influence of solar wind dynamic pressure and interplanetary magnetic field (IMF) strength on auroral behaviour. The central question addressed in this thesis is whether emissions in the swirl, noon active and the dusk active regions are driven by solar wind interactions with the magnetosphere or result primarily from Jupiter's internal dynamics, as is the case for the main auroral emission.

To address this question, the study is structured around two complementary chapters. The first examines the statistical relationship between solar wind parameters and auroral brightness. The second evaluates reconnection voltage and energy transfer associated with the K-H instability. It is found that the swirl and noon active regions show no correlation with any solar wind parameters, while the dusk active region shows a moderate correlation with solar wind dynamic pressure, magnetic field strength and Kelvin-Helmholtz instabilities formed on the dawn flank.

The motivation for this research arises from the unresolved nature of Jupiter's

polar aurora. The driving mechanisms for the emissions in all three polar regions remain poorly understood. Although multiple theories propose different magnetic topologies and spectral characteristics, no consensus has been established. Assessing the influence of the solar wind contributes to the broader effort to characterise the processes responsible for Jupiter's polar auroral features.

Acknowledgements

'We are constantly searching, not just for answers to our questions, but for new questions. We are explorers. We explore our lives day by day, and we explore the galaxy, trying to expand the boundaries of our knowledge.'

- **Captain Benjamin Lafayette Sisko**, The Emissary, Part II.

Star Trek inspired me to begin this journey, and while I'm not sure rewatching it on loop is exactly useful, it makes me happy.

I thank everyone who helped me figure this out, including all the folks in the Space and Planetary Physics group who put up with my nonsense for multiple years. I'd also like to thank STFC for funding this project and making it possible for me to complete a PhD.

I'd like to specifically thank Ginger, Jasper, Schpeeb and Frosty the cats I have made friends with on the commute to the office. I know these are not your actual names (besides Jasper), but you seem to respond to them and come to say hi (or slap me, thanks Ginger). And of course, the softest cat in the world, Tribble, who lives with my parents. She only bites people she likes and I'm her favourite person.

I should also thank my partner Jay. He's nice and supportive of me even when my hyperfixations annoy him (unless its Animal Crossing). And my parents, they raised me pretty well, don't mine listening to me moan and provide the pretty solid advice of: 'yes well, sometimes you just gotta get on with it.'

One final thing - Dad, I love you and I although you're not going to be here to see me graduate, I know you're proud of me. I want you to know I made it, and that your support was invaluable.

Declaration

I declare that the work presented in this thesis is, to the best of my knowledge and belief, original and my own work. The material has not been submitted, either in whole or in part, for a degree at this, or any other university. This thesis does not exceed the maximum permitted word length of 80,000 words, excluding appendices and the bibliography. An estimate of the total word count is ∼41589 words.

Hannah S. Joyce

Contents

1 Space Plasmas **1**

1.1 Basic Principles 1

1.2 Single Particle Motion 3

1.2.1 Magnetic Mirroring and the Loss Cone 5

1.2.2 Particle Drift 7

1.3 Magnetohydrodynamics 9

1.3.1 Frozen-in Flux 11

1.3.2 Plasma Beta 13

1.4 Energy and Mass Transport in Plasmas 15

1.4.1 Magnetic Reconnection 15

1.4.2 Alfvén Waves 17

1.4.3 Kelvin-Helmholtz Instability 18

1.5 Summary 19

2 Jupiter and the Solar Wind **20**

2.1 The Solar Wind 20

2.1.1 The Interplanetary Magnetic Field 23

2.1.2 Magnetosphere-Solar Wind Interactions 24

2.2 Jupiter's Magnetosphere 27

2.2.1 Magnetospheric Structure 29

2.2.2 Magnetospheric Dynamics 31

2.2.2.1 The Io Torus and Plasma Source 31

2.2.2.2 Plasma Transport and the Interchange Instability . . 32

2.2.2.3 Magnetosphere-Ionosphere Coupling 35
2.2.2.4 The Vasyliunas Cycle 37
2.3 Jupiter's Aurora 40
2.3.1 Auroral Emission Wavelengths 40
2.3.1.1 Ultraviolet Emission 40
2.3.1.2 Other Wavelengths of Emission 43
2.3.2 The Main Emission 44
2.3.3 Low-Latitude Emissions 45
2.3.4 Polar Emissions 46
2.3.4.1 The Dark Polar Region 47
2.3.4.2 The Swirl Region 48
2.3.4.3 The Noon Active Region 54
2.3.4.4 The Dusk Active Region 55
2.4 Summary 57

3 Data Processing for Solar Wind and Auroral Studies 58
3.1 Instrumentation 58
3.1.1 Juno 59
3.1.1.1 Juno MAG 59
3.1.1.2 JADE 61
3.1.2 Hubble Space Telescope 62
3.2 Methodology 65
3.2.1 Processing and Organising the Solar Wind Data 65
3.2.1.1 Combining Solar Wind Datasets 65
3.2.2 Propagating the Solar Wind to Jupiter 65
3.2.2.1 Uncertainties in Solar Wind Propagation 70
3.2.2.2 Transforming Coordinate Systems 70
3.2.3 Visualisation of the Polar Regions 74
3.2.4 Conversion of Intensity to Power 78
3.2.4.1 Uncertainties in Auroral Power 80

3.2.5 Correcting for Viewing Geometry 82

4 Clock Angle Dependence on Jupiter's Polar Auroral Power 83

4.1 Introduction 83

4.2 Methodology 84

4.2.1 Clock Angle and Magnetic Field Strength 84

4.2.1.1 Calculation of Clock Angle 84

4.2.1.2 Calculation of Magnetic Field Strength 86

4.2.2 Comparing Datasets 87

4.2.2.1 Visual Comparison of Visits 89

4.2.2.2 Fitting the Data 92

4.2.2.3 Error Analysis of Fits 96

4.3 Results 98

4.3.1 Visual Identification of Features 98

4.3.1.1 Superimposed CML Images 98

4.3.1.2 Temporal Evolution of Auroral Power 100

4.3.2 Clock Angle Dependence on Polar Auroral Power 105

4.3.2.1 IMF Clock Angle Driving of the Swirl Region 113

4.3.2.2 IMF Clock Angle Driving of the Dusk Active Region 116

4.3.2.3 IMF Clock Angle Driving of the Noon Active Region 118

4.3.3 Other Solar Wind Parameter Relationships with Polar Auroral Power 119

4.3.3.1 Solar Wind Pressure Driving of the Polar Regions . . 119

4.3.3.2 Solar Wind Magnetic Field Driving of the Polar Regions 122

4.4 Conclusion 126

5 The Relationship between Energy Inputs from Solar Wind-Magnetosphere Coupling and Auroral Power at Jupiter 130

5.1 Introduction 130

5.2 Reconnection Voltages . . . 132
5.2.1 Calculation of Reconnection Voltages . . . 132
5.2.1.1 Calculation of Low-Latitude Reconnection Voltage . 132
5.2.1.2 Calculation of High-Latitude Reconnection Voltage . 133
5.2.1.3 Fitting and Error Analysis . . . 136
5.2.2 Reconnection Voltage and Auroral Power . . . 137
5.3 The Kelvin-Helmholtz Instability . . . 141
5.3.1 Calculation of the Kelvin-Helmholtz Power . . . 141
5.3.2 Kelvin-Helmholtz Instability and Auroral Power . . . 144
5.4 Conclusions . . . 154

6 Summary and Future Work **158**
6.1 Overview of Results . . . 159
6.2 Importance of Results to Research Field . . . 163
6.3 Further Questions and Potential Future Work . . . 165

Appendix A Linearisation of Equations **169**

Appendix B Additional Plots **172**
B.1 Auroral Keograms . . . 172
B.2 Clock Angle vs Auroral Power . . . 195
B.3 Other Solar Wind Variables . . . 202
B.3.1 Pressure . . . 202
B.3.2 Magnetic Field Strength . . . 202
B.4 Reconnection Voltages and Powers . . . 209
B.4.1 Low-Latitude Reconnection Voltage . . . 209
B.4.2 High-Latitude Reconnection Voltage . . . 209
B.4.3 Kelvin-Helmholtz Power . . . 216

List of Tables

4.1 Trigonometric functions and resulting values for the centre of each clock angle quadrant, used to determine appropriate coupling functions for magnetic reconnection at different locations along Jupiter's magnetopause. 93

4.2 Summary of the relationships between polar auroral power and potential solar wind driving parameters. HL = high-latitude; ML = multi-latitude; PC = post cusp. Here, crosses indicate no statistically significant relationship ($R^2 < 0.2$) and "tentative" denotes relationships that are present for nominal propagation times but do not persist across the whole ±20% propagation time window. . 126

5.1 Trigonometric functions and resulting values for each clock angle quadrant, used to determine appropriate functions for modulating the reconnection voltage at different locations along Jupiter's magnetopause. 133

5.2 Summary of the relationships between polar auroral power and reconnection rates due to the Kelvin-Helmholtz instability and large-scale reconnection at different magnetospheric latitudes. HL = high-latitude; LL = low-latitude; K-H = Kelvin-Helmholtz. Crosses indicate no statistically significant relationship ($R^2 < 0.2$). 155

List of Figures

1.1 Motion of a gyrating charged particle with velocity parallel to the magnetic field, showing the particle will move in a helical motion. Credit: Baumjohann and Treumann (1996). 5

1.2 Motion of a gyrating charged particle in a converging magnetic field with increasing magnetic gradient, showing the phenomena of magnetic mirroring. Credit: Baumjohann and Treumann (1996). . . 6

1.3 Motion of ions and electrons with an applied uniform magnetic field perpendicular to the electric field. Electrons and ions drift in the same direction. Credit: Baumjohann and Treumann (1996). 8

1.4 Motion of ions and electrons in a non-uniform magnetic field with a gradient strength. Electrons and ions move in opposite directions, generating a current. Credit: Baumjohann and Treumann (1996). . 9

1.5 Centrifugal force acting on a particle moving along a curved field line. Credit: Baumjohann and Treumann (1996). 10

1.6 Sketch of different regions during collisionless magnetic reconnection, where the X-point is represented by a black dot, magnetic field lines are solid black lines and the separatrix are green dashed lines. The pink area represents the electron diffusion region and the blue the ion diffusion region. Credit: Lee and Lee (2020). 16

2.1 Structure of the solar wind, viewed from above the Sun. Regions of both slow and fast wind are illustrated, as well as the eruption of a coronal mass ejection (CME) and corotating interaction region (CIR). The CIR is not explicitly labelled but represents the compression region between the slow and fast solar wind and is followed by a reverse shock and rarefaction region. Dashed lines indicate the shape of the Parker spiral, resulting from the combination of radial plasma flow and solar rotation. Credit: Prölss (2004). 21

2.2 Illustration of the noon-midnight meridian of Jupiter's magnetosphere. Credit: Fran Bagenal and Steve Bartlett. 25

2.3 Magnetic field topology in Jupiter's magnetosphere. The two panels show the magnetic field configuration (left) in the noon-midnight meridian plane and (right) the equatorial plane. The distortion of the field lines, caused by the magnetic filed being frozen into the rapidly rotating plasma, is distinctly visible. Credit: Krishan Khurana. 33

2.4 Diagram of the corotation enforcement currents. The dashed cyan lines represent the magnetic field, the solid red lines the electric currents and the green lines are the electric fields associated with accelerating electrons into the ionosphere to generate auroral emissions. Credit: Bonfond et al. (2020). 36

2.5 Diagram illustrating the flow of plasma in Jupiter's magnetosphere. Within $\sim 60\,R_J$, the plasma is within the Alfv́en radius and is thus corotational. Beyond this point, plasma moves outward while gradually falling out of corotation, resulting in a spiral flow pattern. Eventually, at distances of $\sim 80\,R_J$ to potentially as far as $200\,R_J$, blobs of plasma detach along the X-line and are shed down the magnetotail. The 'x' symbols in the figure represent the position of the X-line. Credit: Delamere and Bagenal (2010). 39

2.6 HST images taken on the 14th December 2000, illustrating the different auroral regions of Jupiter: the main emission (oval), dark (polar region), swirl region, active region (representing the noon and dusk active region) and the Io footprint (representing low-latitude emissions). The variability between the two images is typical of a 90 minute time period. Credit: Grodent et al. (2003b). 42

2.7 Maps of northern auroral images taken by Juno's UVS instrument. Two images correspond to each of the four labelled perijove passes: the left image shows the auroral morphology and brightness, while the right image shows the colour ratios associated with the observed emission. Credit: Greathouse et al. (2021). 49

2.8 Polar view of flux mapping results for the northern hemisphere under expanded magnetospheric conditions where the dayside magnetopause standoff distance is ~ 90 R_J. The outer dashed black line is the 15 R_J reference contour, which matches the Ganymede footprint, and the inner dashed black line is the bottom left panel is the location of the swirl region taken from Stallard et al., 2003. The black stars indicate the location of the magnetic pole. Colours indicate the equatorial local time mapping along the contour, where the small circles indicate the point closest to: local midnight (red/black), dawn (dark blue), noon (blue/green) and dusk (light green/yellow). Contours are also labelled with the distance they map out to in R_J, with each line representing increments of 10 R_J. The swirl region is shown to map to an area of open flux, while the dusk active regions map to the outer magnetosphere in their respective local time sector. Credit: Vogt et al. (2011). 51

2.9 Sketch of the proposed three components of flow in the Jovian system: the sub-corotating region, Vasyliunas flows and Dungey cycle flows. Here the 'O' and 'P' markings represent plasma streamlines and plasmoids, respectively. This Dungey cycle flow is initiated by magnetic reconnection with the interplanetary magnetic field and is suggested to be responsible for auroral emission in the swirl region. Credit: Cowley et al. (2003). 52

2.10 The two-day average topology of simulated Jovian magnetic field lines traced from four different sets of footprints at a low-latitude simulation boundary in the northern hemisphere: the green open field lines are connected to the interplanetary magnetic field and are mostly under solar wind control; the blue field lines map to the distant tail beyond 600 R_J; the the red closed field lines map outward to 35 - 40 R_J in the middle magnetosphere and return to the southern boundary; the black field lines emerging from Jupiter's polar region connect the two polar regions through the dawnside outer magnetosphere. Although only the black field lines are attributed to the polar region, the green and blue field lines map to areas associated with polar aurora. Credit: Zhang et al. (2021). 53

2.11 UV brightness maps for observations of 15.5 minutes by Juno's UVS instrument for perijoves 7 and 10. Concentric arcs on the dusk side of the polar collar are clearly displayed in both images, indicating that the arcs are a function of local time rather than System III longitude. Credit: Greathouse et al. (2021). 56

3.1 Diagram of the MAG instrumentation on the Juno spacecraft. Image credit: Connerney et al. (2017). 60

3.2 SPICE (Spacecraft, Planet, Instrument, C-matrix, Events) Toolkit coordinate frames. On the left (a) is JUNO_SUN_EQU_RTN, the coordinate frame of Juno's MAG data. In this frame, x is the Sun-spacecraft line, y is the cross product of x and the Sun's spin axis and z the cross product of x and y. On the right (b) is JUNO_JM, a coordinate frame designed for this study, where x is the Jupiter-Sun line, y is the cross product of x and Jupiter's magnetic axis and z is the cross product of x and y. 61

3.3 Diagram of the JADE instrumentation on the Juno spacecraft. Image credit: McComas et al. (2013). 62
3.4 Diagram of how the distance shift of the solar wind from Juno to the nose of the bow shock is determined. 66
3.5 Solar wind parameters from the JADE dataset shifted to represent the projected time the solar wind will reach the ionosphere. Top to bottom: pressure, velocity, mass density, magnetopause stand-off distance, and bow shock stand-off distance. The times of each HST visit are indicated by the labelled vertical dashed lines. 69
3.6 Projection of the $y-z$ plane representing the differences between the Sun's spin axis (S_S) Jupiter's spin axis (J_S) and Jupiter's magnetic axis (J_M). The two spin axes are separated by $\sim 6.3°$ during the HST visits, whilst the angle of the magnetic axis varies between the positions indicated by the two dashed lines. The maximum separation is 10.25°, which occurs twice a Jupiter day. The angles are not drawn to scale. 72
3.7 Polar projections of two different visits from the HST dataset, where the visit on the left (visit 19) represents a compression of the main auroral emission and the visit on the right (visit 12) represents an expanded main emission. The projections here show that latitudinal extent of the main emission influences the size of polar auroral region (located poleward of the main emission). A compressed main emission also distorts the shape of the main emission as the main auroral boundary is pushed further inward and distorted by the northern magnetic anomaly. 75

3.8 Polar projections of visits 12 (left) and 02 (right), representing the two different sets of regions selected for this study. Visit 12 is fitted with the 'high CML' regions and visit 02 is fitted with the 'standard CML' regions. The main difference between the two sets of regions is the dusk active region, which has a different shape between the two categories. For the 'high CML' regions, the dusk active region is curved around to follow the edge of the main emission, following the outward expansion of the main emission as local noon moves further away from the northern magnetic anomaly; for the 'standard CML' regions, the dusk active region is compressed inward due to local noon being close to the northern magnetic anomaly, but still follows the edge of the main emission. The 'standard CML' regions are also fit considering main emission compression, whereas the 'high CML' visits do not occur under main emission compression. The size in area of the regions is consistent between the two sets of regions. . . 77

3.9 The percentage of pixels seen for the swirl, noon active and dusk action region for the a) 'standard CML' visits and b) 'high CML' visits. For both categories, the noon active region is 100% visible and does not need to be scaled. For the 'standard CML' visits the swirl region and dusk active region require scaling, and for the 'high CML' visits only the dusk active region requires scaling as the swirl region is also 100% visible. 81

4.1 Clock angle (top) and magnetic field strength in the plane perpendicular to the Sun-Jupiter line, $B_\perp$ (bottom) for the whole Juno MAG dataset. The values are arranged by time estimated to reach the ionosphere, with the time of each HST visit indicated by a vertical dashed line. 84

4.2 The distribution of clock angles (a) within the whole solar wind dataset, (b) within all HST visits and (c) representing the median of each visit. The majority of the data falls within the $-B_y$ quadrant and $-B_z$ comprises the minority. Although IMF $-B_z$ is over represented and $+B_y$ under represented during HST visit times relative to the Juno dataset, the $+By$ quadrant is over-represented and $-B_z$ under-represented when the median average of each visit is taken. 85

4.3 The number of propagated Juno solar wind data points that coincide with each HST visit and their variation over the visit. Colours indicate the time resolution of the Juno dataset: 30 seconds (green), 60 seconds (orange) and 600 seconds (red). HST visit periods that occur near times of lower Juno resolution generally contain fewer propagated solar wind data points, with a few exceptions. 87

4.4 Clock angle data for each HST visit, highlighting the discrepancy in the number of data points across visits. The clock angle in visit 24 varies across the $\pm 180°$ boundary, creating visualisation artifacts despite minimal physical variability, as both extremes of the y-axis represent the same $-B_z$ orientation. 88

4.5 Superimposed images from the 9 visits that contain a CML of 177°. There are no features in the polar aurora associated with this CML configuration. 90

4.6 Examples of different levels of activity in the polar auroral region where panels show a) high pressure conditions and b) low pressure conditions. Although the regions are not indicated as to not disrupt the visibility of auroral features, the dusk active region clearly shows more auroral activity under higher pressure. 99

4.7 Solar wind dynamic pressure vs. magnetic field strength across all visits, demonstrating that higher pressures and higher field strengths typically co-occur, particularly during the most extreme observed conditions. 99
4.8 Comparison of auroral power distribution and solar wind conditions during Visit 18. The top three panels display keograms for the Swirl, Noon, and Dusk regions as a function of colatitude and Ionospheric Time. The bottom three panels show the corresponding IMF clock angle, solar wind dynamic pressure and IMF strength ($B_\perp$ in blue, B_{tot} in orange), respectively. 102
4.9 Comparison of auroral power distribution and solar wind conditions during Visit 25. The top three panels display keograms for the Swirl, Noon, and Dusk regions as a function of colatitude and Ionospheric Time. The bottom three panels show the corresponding IMF clock angle, solar wind dynamic pressure and IMF strength ($B_\perp$ in blue, B_{tot} in orange), respectively. 103
4.10 Comparison of auroral power distribution and solar wind conditions during Visit 03. The top three panels display keograms for the Swirl, Noon, and Dusk regions as a function of colatitude and Ionospheric Time. The bottom three panels show the corresponding IMF clock angle, solar wind dynamic pressure and IMF strength ($B_\perp$ in blue, B_{tot} in orange), respectively. 104
4.11 The relationship between median averaged clock angle per visit and median a) total polar power, b) swirl region power, c) dusk active region power and d) noon active region power. 106

4.12 The relationship between median averaged clock angle per visit and median a) total polar power, b) swirl region power, c) dusk active region power and d) noon active region power. The relationship is tested using the equation $(A_1 \times \cos^2(\frac{x}{2}) + (A_2 \times \sin^2(x)) + C$, representing multi-latitude reconnection, plotted as the black dashed line. 108

4.13 The same as figure 4.12 but with the addition of a ±20% propagation time uncertainty window applied to the solar wind travel time calculated from when Juno detected the solar wind to Jupiter's magnetosphere, thus shifting the clock angle data to the new data window for the time of the HST visit. 111

4.14 The relationship between median averaged solar wind dynamic pressure per visit and the median total power per visit for the dusk active region. Panel a) shows the fit for the nominal solar wind travel time and panel b) includes the fits for the ±20% solar wind travel time shifts. The relationship is plotted on a log_{10} pressure scale. All three fits exceed the $R^2 = 0.2$ threshold, indicating a correlation between pressure and auroral brightness in the dusk active region. 121

4.15 Relationship between median solar wind magnetic field magnitude and median auroral power for the dusk active region. Panels a) and b) show the fits for the perpendicular magnetic field magnitude at nominal and ±20% solar wind travel times, respectively. Panels c) and d) show the corresponding fits for the total magnetic field magnitude. While nominal correlations are moderate, the strength of the correlation varies significantly across the travel time uncertainty window, indicating this relationship is not robust. . . . 125

5.1 The distribution of reconnection sites under (a) $+B_y$ IMF and (b) $-B_y$ IMF conditions. Diagrams are orientated so the sun is out of the page along x, the dawn sector is on the left and the dusk sector is on the right, where the red crosses indicate the reconnection site. 135

5.2 The relationship between median auroral power in the dusk active region and median: (a) low-latitude reconnection voltage; (b) the same with the ±20% uncertainty window; c) high-latitude reconnection voltage favouring $+B_y$ IMF; (d) with the ±20% uncertainty window; (c) high-latitude reconnection voltage favouring $-B_y$ IMF; (d) with the ±20% uncertainty window 139

5.3 The relationship between median power generated by Kelvin-Helmholtz instabilities and median: (a) dusk active region auroral power under dusk flank conditions; (b) the same with the ±20% uncertainty window; (c) dusk active auroral power under dawn flank conditions; (d) with the ±20% uncertainty window 145

5.4 Contribution of velocity shear and mass density to the overall Kelvin-Helmholtz power, where panel a) represents the dawn flank and panel b) represents the dusk flank. The contribution of the velocity shear is effectively mirrored between the two flanks due to the oppositely directed internal flow of plasma in Jupiter's magnetosphere, suggesting that unless the solar wind velocity reaches a threshold value of over double the internal flow speed, higher solar wind velocities negatively impact the development of Kelvin-Helmholtz vortices. 148

6.1 Heat maps showing the adjusted R^2 values for correlations between solar wind derived parameters and auroral power, based on three different solar wind propagation time estimates between detection by Juno and the arrival at Jupiter's ionosphere: (top) nominal travel time, (middle) 20% longer travel time and (bottom) 20% shorter travel time. Colours represent the relative strength of the fitted R^2 values across all tested parameters, allowing for comparison of correlation strength under different solar wind arrival times. 160

A.0.1 Equation A.7 visualised with $\cos\theta$ representing x. 170

A.0.2 Equation A.7 plotted in linear predictor space with x as the linear predictor, to show equation 4.7 has been successfully linearised. In this form, the quality of the fit is easier visualised. 171

B.1.1 Comparison of auroral power distribution and solar wind conditions during visit 01. The top three panels display keograms for the Swirl, Noon, and Dusk regions as a function of colatitude and Ionospheric Time. The bottom three panels show the corresponding IMF clock angle, solar wind dynamic pressure and IMF strength ($B_\perp$ in blue, B_{tot} in orange), respectively. 174

B.1.2 Comparison of auroral power distribution and solar wind conditions during visit 02. The top three panels display keograms for the Swirl, Noon, and Dusk regions as a function of colatitude and Ionospheric Time. The bottom three panels show the corresponding IMF clock angle, solar wind dynamic pressure and IMF strength ($B_\perp$ in blue, B_{tot} in orange), respectively. 175

B.1.3 Comparison of auroral power distribution and solar wind conditions during visit 04. The top three panels display keograms for the Swirl, Noon, and Dusk regions as a function of colatitude and Ionospheric Time. The bottom three panels show the corresponding IMF clock angle, solar wind dynamic pressure and IMF strength ($B_\perp$ in blue, B_{tot} in orange), respectively. 176
B.1.4 Comparison of auroral power distribution and solar wind conditions during visit 05. The top three panels display keograms for the Swirl, Noon, and Dusk regions as a function of colatitude and Ionospheric Time. The bottom three panels show the corresponding IMF clock angle, solar wind dynamic pressure and IMF strength ($B_\perp$ in blue, B_{tot} in orange), respectively. 177
B.1.5 Comparison of auroral power distribution and solar wind conditions during visit 08. The top three panels display keograms for the Swirl, Noon, and Dusk regions as a function of colatitude and Ionospheric Time. The bottom three panels show the corresponding IMF clock angle, solar wind dynamic pressure and IMF strength ($B_\perp$ in blue, B_{tot} in orange), respectively. 178
B.1.6 Comparison of auroral power distribution and solar wind conditions during visit 09. The top three panels display keograms for the Swirl, Noon, and Dusk regions as a function of colatitude and Ionospheric Time. The bottom three panels show the corresponding IMF clock angle, solar wind dynamic pressure and IMF strength ($B_\perp$ in blue, B_{tot} in orange), respectively. 179

B.1.7 Comparison of auroral power distribution and solar wind conditions during visit 10. The top three panels display keograms for the Swirl, Noon, and Dusk regions as a function of colatitude and Ionospheric Time. The bottom three panels show the corresponding IMF clock angle, solar wind dynamic pressure and IMF strength ($B_\perp$ in blue, B_{tot} in orange), respectively. 180
B.1.8 Comparison of auroral power distribution and solar wind conditions during visit 11. The top three panels display keograms for the Swirl, Noon, and Dusk regions as a function of colatitude and Ionospheric Time. The bottom three panels show the corresponding IMF clock angle, solar wind dynamic pressure and IMF strength ($B_\perp$ in blue, B_{tot} in orange), respectively. 181
B.1.9 Comparison of auroral power distribution and solar wind conditions during visit 12. The top three panels display keograms for the Swirl, Noon, and Dusk regions as a function of colatitude and Ionospheric Time. The bottom three panels show the corresponding IMF clock angle, solar wind dynamic pressure and IMF strength ($B_\perp$ in blue, B_{tot} in orange), respectively. 182
B.1.10 Comparison of auroral power distribution and solar wind conditions during visit 15. The top three panels display keograms for the Swirl, Noon, and Dusk regions as a function of colatitude and Ionospheric Time. The bottom three panels show the corresponding IMF clock angle, solar wind dynamic pressure and IMF strength ($B_\perp$ in blue, B_{tot} in orange), respectively. 183

B.1.11 Comparison of auroral power distribution and solar wind conditions during visit 16. The top three panels display keograms for the Swirl, Noon, and Dusk regions as a function of colatitude and Ionospheric Time. The bottom three panels show the corresponding IMF clock angle, solar wind dynamic pressure and IMF strength ($B_\perp$ in blue, B_{tot} in orange), respectively. 184
B.1.12 Comparison of auroral power distribution and solar wind conditions during visit 17. The top three panels display keograms for the Swirl, Noon, and Dusk regions as a function of colatitude and Ionospheric Time. The bottom three panels show the corresponding IMF clock angle, solar wind dynamic pressure and IMF strength ($B_\perp$ in blue, B_{tot} in orange), respectively. 185
B.1.13 Comparison of auroral power distribution and solar wind conditions during visit 19. The top three panels display keograms for the Swirl, Noon, and Dusk regions as a function of colatitude and Ionospheric Time. The bottom three panels show the corresponding IMF clock angle, solar wind dynamic pressure and IMF strength ($B_\perp$ in blue, B_{tot} in orange), respectively. 186
B.1.14 Comparison of auroral power distribution and solar wind conditions during visit 20. The top three panels display keograms for the Swirl, Noon, and Dusk regions as a function of colatitude and Ionospheric Time. The bottom three panels show the corresponding IMF clock angle, solar wind dynamic pressure and IMF strength ($B_\perp$ in blue, B_{tot} in orange), respectively. 187

B.1.15 Comparison of auroral power distribution and solar wind conditions during visit 21. The top three panels display keograms for the Swirl, Noon, and Dusk regions as a function of colatitude and Ionospheric Time. The bottom three panels show the corresponding IMF clock angle, solar wind dynamic pressure and IMF strength ($B_\perp$ in blue, B_{tot} in orange), respectively. 188
B.1.16 Comparison of auroral power distribution and solar wind conditions during visit 24. The top three panels display keograms for the Swirl, Noon, and Dusk regions as a function of colatitude and Ionospheric Time. The bottom three panels show the corresponding IMF clock angle, solar wind dynamic pressure and IMF strength ($B_\perp$ in blue, B_{tot} in orange), respectively. 189
B.1.17 Comparison of auroral power distribution and solar wind conditions during visit 26. The top three panels display keograms for the Swirl, Noon, and Dusk regions as a function of colatitude and Ionospheric Time. The bottom three panels show the corresponding IMF clock angle, solar wind dynamic pressure and IMF strength ($B_\perp$ in blue, B_{tot} in orange), respectively. 190
B.1.18 Comparison of auroral power distribution and solar wind conditions during visit 27. The top three panels display keograms for the Swirl, Noon, and Dusk regions as a function of colatitude and Ionospheric Time. The bottom three panels show the corresponding IMF clock angle, solar wind dynamic pressure and IMF strength ($B_\perp$ in blue, B_{tot} in orange), respectively. 191

B.1.19 Comparison of auroral power distribution and solar wind conditions during visit 28. The top three panels display keograms for the Swirl, Noon, and Dusk regions as a function of colatitude and Ionospheric Time. The bottom three panels show the corresponding IMF clock angle, solar wind dynamic pressure and IMF strength ($B_\perp$ in blue, B_{tot} in orange), respectively. 192

B.1.20 Comparison of auroral power distribution and solar wind conditions during visit 34. The top three panels display keograms for the Swirl, Noon, and Dusk regions as a function of colatitude and Ionospheric Time. The bottom three panels show the corresponding IMF clock angle, solar wind dynamic pressure and IMF strength ($B_\perp$ in blue, B_{tot} in orange), respectively. 193

B.1.21 Comparison of auroral power distribution and solar wind conditions during visit 35. The top three panels display keograms for the Swirl, Noon, and Dusk regions as a function of colatitude and Ionospheric Time. The bottom three panels show the corresponding IMF clock angle, solar wind dynamic pressure and IMF strength ($B_\perp$ in blue, B_{tot} in orange), respectively. 194

B.2.1 Relationship between median averaged clock angle per visit and the median: (a) total polar power, (b) swirl region power, (c) dusk active region power and (d) noon active region power. The relationship is fitted with the equation $A \times cos^2(\frac{\theta}{2}) + b$, representing large-scale reconnection at low latitudes on the dayside where the use of cosine favours $+B_z$ reconnection due to Jupiter's $-B_z$ field orientation. 196

B.2.2 The same as figure B.2.1 but with the addition of a $\pm 20\%$ propagation time uncertainty window applied to the solar wind travel time from Juno to Jupiter's magnetosphere. 197

B.2.3 Relationship between median averaged clock angle per visit and the median: (a) total polar power, (b) swirl region power, (c) dusk active region power and (d) noon active region power. The relationship is fitted with the equation $A \times \sin^2(\theta) + B$, representing high latitude reconnection at the dawn and dusk sectors of the dayside magnetic field. 198

B.2.4 The same as figure B.2.3 but with the addition of a ±20% propagation time uncertainty window applied to the solar wind travel time from Juno to Jupiter's magnetosphere. 199

B.2.5 Relationship between median averaged clock angle per visit and the median: (a) total polar power, (b) swirl region power, (c) dusk active region power and (d) noon active region power. The relationship is fitted with the equation $A \times sin^2(\frac{\theta}{2}) + B$, representing reconnection with twisted open field lines emerging from the polar region and trailing behind the planet due to the flow of the solar wind. 200

B.2.6 The same as figure B.2.5 but with the addition of a ±20% propagation time error applied to the solar wind travel time from Juno to Jupiter's magnetosphere. 201

B.3.1 Relationship between median averaged pressure per visit and the median: (a) total polar power, (b) swirl region power, (c) dusk active region power, (d) noon active region power. Pressure is plotted on a log_{10} axis and the relationship is fit by taking a linear fit of $log_{10}(P)$ vs power. 203

B.3.2 The same as figure B.3.1 but with the addition of a 20% propagation time error applied to the solar wind travel time from Juno to Jupiter's magnetosphere. 204

B.3.3 Relationship between median averaged perpendicular magnetic field strength per visit and the median: (b) swirl region power, (c) dusk active region power, (d) noon active region power. Pressure is plotted on a log_{10} axis and the relationship is fit by taking a linear fit of $log_{10}(pressure)$ vs power. 205
B.3.4 The same as figure B.3.3 but with the addition of a 20% propagation time error applied to the solar wind travel time from Juno to Jupiter's magnetosphere. 206
B.3.5 Relationship between median averaged total magnetic field magnitude of the solar wind per visit and the median: (a) total polar power, (b) swirl region power, (c) dusk active region power, (d) noon active region power. The relationship is plotted as a linear line of best fit. 207
B.3.6 The same as figure B.3.5 but with the addition of a $\pm$20% propagation time error applied to the solar wind travel time from Juno to Jupiter's magnetosphere 208
B.4.1 The relationship between low-latitude reconnection voltage per visit, calculated from measured solar wind parameters using equation 5.2, and the median: (a) total polar power, (b) swirl region power, (c) dusk active region power and (d) noon active region power. The reconnection voltage is plotted on a log_{10} axis and the relationship is fit by taking a linear fit of $log_{10}(\phi_{LL})$ vs power. . . . 210
B.4.2 The same as B.4.1 but with the addition of a 20% propagation time error applied to the solar wind travel time from Juno to Jupiter's magnetosphere. 211

B.4.3 The relationship between high-latitude reconnection voltage per visit, calculated under conditions where reconnection with $+B_y$ orientated field is favoured using equation 5.3 , and the median: (a) total polar power, (b) swirl region power, (c) dusk active region power and (d) noon active region power. The reconnection voltage is plotted on a log_{10} axis and the relationship is fit by taking a linear fit of $log_{10}(\phi_{HL,-y})$ vs power. 212
B.4.4 The same as B.4.3 but with the addition of a 20% propagation time error applied to the solar wind travel time from Juno to Jupiter's magnetosphere. 213
B.4.5 The relationship between high-latitude reconnection voltage per visit, calculated under conditions where reconnection with $-B_y$ orientated field is favoured using equation 5.4 , and the median: (a) total polar power, (b) swirl region power, (c) dusk active region power and (d) noon active region power. The reconnection voltage is plotted on a log_{10} axis and the relationship is fit by taking a linear fit of $log_{10}(\phi_{HL,+y})$ vs power. 214
B.4.6 The same as B.4.5 but with the addition of a 20% propagation time error applied to the solar wind travel time from Juno to Jupiter's magnetosphere. 215
B.4.7 The relationship between Kelvin-Helmholtz generated power, calculated using equation 5.5, for the dawn flank of Jupiter's outer magnetosphere and median: (a) total polar power, (b) swirl region power, (c) dusk active region power and (d) noon active region power. The reconnection power is plotted on a log_{10} axis and the relationship is fit by taking a linear fit of $log_{10}(P_{K-H})$ vs power. . . 217
B.4.8 The same as B.4.7 but with the addition of a 20% propagation time error applied to the solar wind travel time from Juno to Jupiter's magnetosphere. 218

B.4.9 The relationship between Kelvin-Helmholtz generated power, calculated using equation 5.5, for the dusk flank of Jupiter's outer magnetosphere and median: (a) total polar power, (b) swirl region power, (c) dusk active region power and (d) noon active region power. The reconnection power is plotted on a log_{10} axis and the relationship is fit by taking a linear fit of $log_{10}(P_{K-H})$ vs power. . . 219

B.4.10 The same as B.4.9 but with the addition of a 20% propagation time error applied to the solar wind travel time from Juno to Jupiter's magnetosphere. 220

Chapter 1

Space Plasmas

In order to understand the complex nature of Jupiter's magnetosphere and its interactions with the solar wind, it is essential to first provide an overview of the fundamental physical concepts involved. This overview establishes the context necessary for understanding the background theory presented in Chapter 2. Throughout this chapter, Baumjohann and Treumann (1996) is the primary source for the fundamental plasma principles and magnetospheric phenomena discussed.

1.1 Basic Principles

Plasmas are the fourth state of matter, representing an ionised, electrically conducting gas. Plasmas contain a mixture of positive ions, negative ions and free electrons, and over large scales are known to be 'quasi-neutral' as there is no net charge present. There are multiple means in which a particle can become ionised, including: photoionisation, electron impact and charge exchange. Each of these processes involves particle interaction, determined by the electromagnetic forces acting between the particles.

The spatial scale in which an ion can influence another particle is limited by electrons collectively shielding its potential, given by the Debye length,

$$\lambda_D = \sqrt{\frac{\epsilon_0 k_B T_e}{n_e e^2}} \tag{1.1}$$

where the parameters of the equation are as follows: ϵ_0 is the permittivity of free space; k_B is Boltzmann's constant, which relates the average kinetic energy of particles to the temperature; T_e is the electron temperature; n_e is the electron density; e^2 is the electron charge.

The Debye length sets the characteristic scale over which electric potentials are 'screened' in a plasma, meaning that any local charge imbalance is neutralised within λ_D due to the collective response of the surrounding electrons. This screening leads to the plasma's ability to maintain quasi-neutrality, a state in which overall charge density is ∼zero on length scales larger than λ_D (i.e., $n_e \approx n_i$). Shielding occurs effectively only if the Debye length is sufficiently large compared to the inter-particle spacing, and smaller than the scale sizes within the system. This is quantified by the number of electrons within a a Debye sphere:

$$N_D = \frac{4\pi}{3} n_e \lambda_D^3 \gg 1 \tag{1.2}$$

A large N_D indicates that collective behaviour dominates over collisions, and that quasi-neutrality is maintained. As such, both the Debye length and Debye shielding are fundamental in identifying plasmas. This condition is easily satisfied in many space plasmas. For example, the solar wind near Earth has electron densities of $\sim 3 - 10$ cm^{-3} and temperatures of $\sim 10^5 - 10^6$ K, illustrating a low density, high temperature environment where $N_D \gg 1$. Another case is Jupiter's magnetosphere, which spans a wider range of conditions, with density ranging from 1000 cm^{-3} in the dense Io torus to ~ 0.01 cm^{-3} in the outer magnetosphere, and electron temperatures of $\sim 10^1 - 10^3$ eV, (Bagenal and Delamere, 2011). Under these conditions, the Debye length spans metres to kilometres, also giving $N_D \gg 1$.

The electromagnetic forces that govern plasma behaviour originate from the presence

of electric and magnetic fields. These fields are not static, and evolve due to the motion of charged particles and the resulting currents. Maxwell's equations describe how these fields behave and interact with plasma:

$$\nabla \cdot \vec{E} = \frac{\rho_q}{\epsilon_0} \tag{1.3}$$

$$\nabla \cdot \vec{B} = 0 \tag{1.4}$$

$$\nabla \times \vec{E} = -\frac{\partial \vec{B}}{\partial t} \tag{1.5}$$

$$\nabla \times \vec{B} = \mu_0 \left(\vec{j} + \epsilon_0 \frac{\partial \vec{E}}{\partial t} \right) \tag{1.6}$$

where $\vec{E}$ represents the electric field, ρ_q the charge density, $\vec{B}$ the magnetic field, μ_0 the permeability of free space and $\vec{j}$ the current density. The equations are described as follows: equation 1.3 is Gauss' law for electricity, showing that the electric field divergence is proportional to charge density; equation 1.4 is Gauss' law for magnetism, indicating magnetic field lines are continuous and have no divergence; equation 1.5 is Faraday's law of induction, which shows that a time-varying magnetic field induces a circulating electric field; finally, equation 1.6 is Ampère's law, showing that both electric currents and time-varying electric fields generate magnetic fields.

1.2 Single Particle Motion

A charged particle with charge q and velocity $\vec{v}$ in an electromagnetic field will experience the Lorentz force:

$$\vec{F} = m\frac{d\vec{v}}{dt} = q(\vec{E} + \vec{v} \times \vec{B}) \tag{1.7}$$

where m is the particle mass. The velocity $\vec{v}$ can be separated into two components relative to the magnetic field direction: a component perpendicular to the magnetic field, $v_\perp$, and a component parallel to the magnetic field, $v_\parallel$. These components govern the particle's motion around and along the magnetic field lines, respectively.

In the absence of an electric field, the Lorentz force simplifies to:

$$\vec{F} = q\vec{v} \times \vec{B}, \tag{1.8}$$

and acts as a centripetal force responsible for the gyration of the particle about the magnetic field lines.

In the presence of a uniform magnetic field but no electric field, the particle undergoes circular motion (gyration) around the magnetic field lines. This motion arises because the Lorentz force acts perpendicular to the velocity vector, continuously deflecting the particle without changing its speed.

The rate at which the particle orbits the field line is known as the gyrofrequency ω_g:

$$\omega_g = \frac{qB}{m} \tag{1.9}$$

The radius of the circular motion is known as the gyroradius r_g (or Larmor radius) and is given by:

$$r_g = \frac{mv_\perp}{qB} \tag{1.10}$$

As the Lorentz force is always perpendicular to the particle's velocity, the kinetic energy is conserved. This can be shown by considering the time derivative of the kinetic energy:

$$\frac{d}{dt}\left(\frac{1}{2}mv^2\right) = m\vec{v} \cdot \frac{d\vec{v}}{dt} = q\vec{v} \cdot (\vec{v} \times \vec{B}) = 0, \tag{1.11}$$

Thus, the magnitude of the velocity remains constant and only the direction changes, resulting in uniform circular motion.

As shown in figure 1.1, in the case that a particle has a velocity parallel to the magnetic field, the particle will move in a spiral 'helical' motion, gyrating around the field lines while simultaneously moving along them. The angle at which it moves with respect to the magnetic field is known as the pitch angle:

$$\alpha = \arctan\left(\frac{v_\perp}{v_\parallel}\right) \tag{1.12}$$

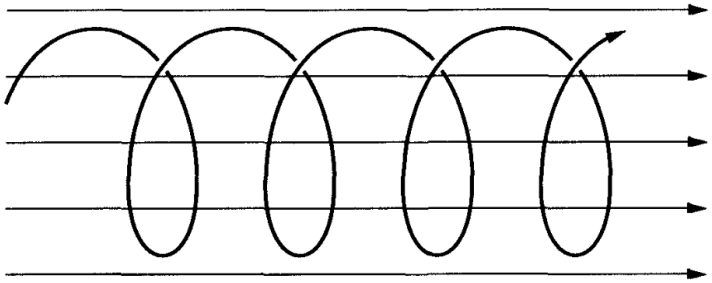

Figure 1.1: Motion of a gyrating charged particle with velocity parallel to the magnetic field, showing the particle will move in a helical motion. Credit: Baumjohann and Treumann (1996).

Pitch angle values of 0° and 180° represent parallel and anti-parallel motion to the background magnetic field, respectively. At 90° the only motion the particle experiences is gyration.

1.2.1 Magnetic Mirroring and the Loss Cone

If a particle has a small enough pitch angle, it is considered within the 'loss cone'. The loss cone refers to a range of pitch angles for which particles are not mirrored and can precipitate into the atmosphere. To define this, it is necessary to introduce the first adiabatic invariant, also known as the magnetic moment:

$$\mu = \frac{m v_\perp^2}{2B} \tag{1.13}$$

which is conserved provided the magnetic field strength and direction change slowly compared to the timescale of the particle's gyration.

As a charged particle moves from a region of weaker magnetic field to a region of stronger magnetic field, conservation of μ implies that its perpendicular velocity ($v_\perp$) must increase. As the particle's total energy must be conserved, this increase results in the parallel velocity ($v_\parallel$) being reduced and so the particle motion along the field slows down as the magnetic field becomes stronger. Eventually, $v_\parallel = 0$ and

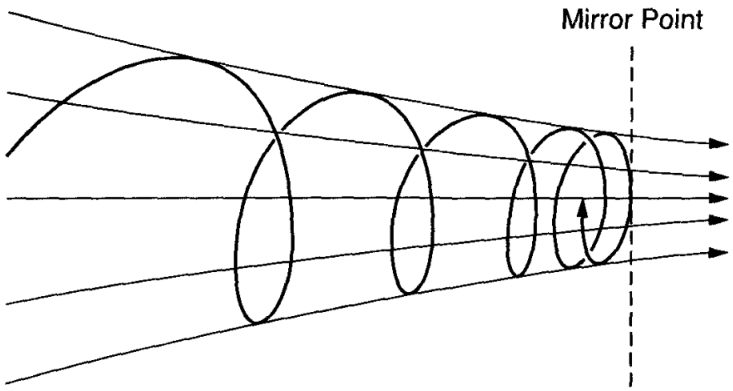

Figure 1.2: Motion of a gyrating charged particle in a converging magnetic field with increasing magnetic gradient, showing the phenomena of magnetic mirroring. Credit: Baumjohann and Treumann (1996).

the pitch angle becomes 90°. At this point, the particle is reflected or 'mirrored' back along the field line. If this mirroring occurs on both ends of the particle's trajectory, it becomes trapped, bouncing back and forth between two mirror points. A sketch of this phenomena can be seen in figure 1.2. In planetary magnetospheres, these mirror points are typically located near the magnetic poles. This phenomenon can lead to the formation of trapped particle populations in magnetospheres, such as high-energy radiation belts observed at Earth, Jupiter, and other planets.

By combining the pitch angle with equation 1.13, a relation between the pitch angle and the magnetic field strength can be derived:

$$\sin^2(\alpha) = \frac{B}{B_0}\sin^2(\alpha_0) \tag{1.14}$$

where B is the magnetic field at the current location of the particle, B_0 is the minimum magnetic field strength along the field line, and α and α_0 are the pitch angles at those respective locations. This relation also allows the boundary of the loss cone to be defined. The loss cone angle (α_{LC}) specifies the maximum equatorial pitch angle for which a particle will not be mirrored when it reaches a region of high

magnetic field strength. It is given by:

$$\sin^2(\alpha_{\mathrm{LC}}) = \frac{B_0}{B_{mirror}}, \tag{1.15}$$

where B_{mirror} is the field strength at the point mirroring will occur. Particles with pitch angles $\alpha_0 < \alpha_{LC}$ fall inside the loss cone and will precipitate into the atmosphere before reaching the mirror point. This precipitation can lead to auroral emission if the charged particles interact with neutral atoms or molecules - either through excitation followed by photon emission, or via charge exchange and transfer collisions.

1.2.2 Particle Drift

Introducing an electric field, or any other external force, adds an additional layer of complexity to single particle motion. The addition of force $\vec{F}$ causes the particle to undergo a drift motion perpendicular to both $\vec{B}$ and $\vec{F}$. This drift velocity is given by

$$\vec{v}_D = \frac{\vec{F} \times \vec{B}}{qB^2} \tag{1.16}$$

In the case of a uniform electric field $\vec{E}$ perpendicular to $\vec{B}$, the force experienced by a charged particle is

$$\vec{F}_E = q\vec{E} \tag{1.17}$$

Substituting into the drift equation gives the $\vec{E} \times \vec{B}$ drift:

$$\vec{v}_D = \frac{\vec{E} \times \vec{B}}{B^2} \tag{1.18}$$

This drift, visualised in figure 1.3, is independent of both the particle's charge and mass and so all charged particles will drift in the same direction with a same velocity. As a result, the $\vec{E} \times \vec{B}$ drift does not generate any net current.

In a non-uniform magnetic field, such as one where the magnetic flux density increases perpendicular to the magnetic field, a particle will move through regions

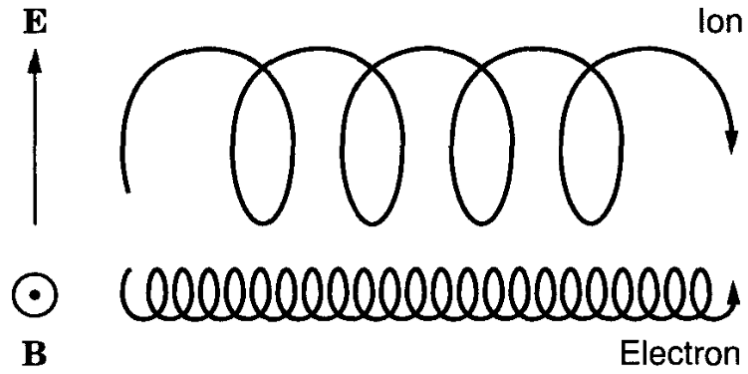

Figure 1.3: Motion of ions and electrons with an applied uniform magnetic field perpendicular to the electric field. Electrons and ions drift in the same direction. Credit: Baumjohann and Treumann (1996).

of different magnetic strength as it gyrates. This causes the particle's gyroradius to change as it moves - decreasing in areas of stronger magnetic field and increasing in weaker regions. The result is a net drift perpendicular to both $\vec{B}$ and the gradient of the magnetic field $\nabla\vec{B}$. This is called the gradient B drift and is given as

$$\vec{v}_{\nabla\vec{B}} = \frac{mv_{\perp}^2}{2qB^3}\left(\vec{B}\times\nabla B\right) \tag{1.19}$$

Unlike the $\vec{E}\times\vec{B}$ drift, the gradient B drift depends on the sign of the charge of the particle. As ions and electrons have different signs, they drift in opposite directions, leading to a separation of charge and the generation of current. This drift motion is shown in figure 1.4.

A similar effect occurs in curved magnetic fields, such as those found in planetary magnetospheres. Even if the magnetic field strength remains constant, the curvature of the field lines creates an effective centrifugal force as the particle follows the curved path.

$$\vec{F}_c = mv_{\parallel}\frac{\vec{R}_c}{R_c^2} \tag{1.20}$$

where $\vec{R}_c$ denotes the vector from the particle's position to the centre of curvature of the magnetic field line. A diagram of these forces is shown in figure 1.5

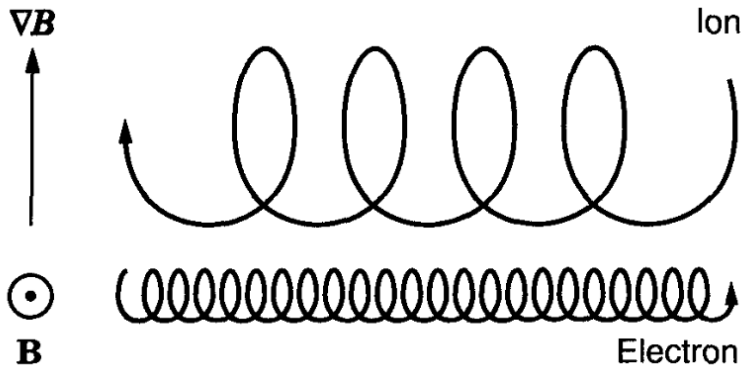

Figure 1.4: Motion of ions and electrons in a non-uniform magnetic field with a gradient strength. Electrons and ions move in opposite directions, generating a current. Credit: Baumjohann and Treumann (1996).

During each gyration, the particle experiences varying acceleration depending on its location along the curve. This results in a net drift known as the curvature drift:

$$\vec{v}_{curv} = \frac{mv_{\parallel}^2}{qB^2}\frac{\vec{R}_c \times \vec{B}}{R_c^2} \tag{1.21}$$

Like the gradient B drift, the direction of the curvature drift depends on the particle's charge and thus also leads to charge separation and a resulting current. The motion of the negative and positive charges are thus identical to those in figure1.4. These drifts are fundamental to understanding large-scale magnetospheric currents.

These principles of single-particle motion form the foundation for understanding how plasmas behave in large-scale environments, such as planetary magnetospheres and the solar wind.

1.3 Magnetohydrodynamics

The complex nature of plasma dynamics cannot be fully captured by a single-particle description. Since a plasma consists of many interacting charged particles and exhibits collective behaviour similar to that of a fluid, it is often more

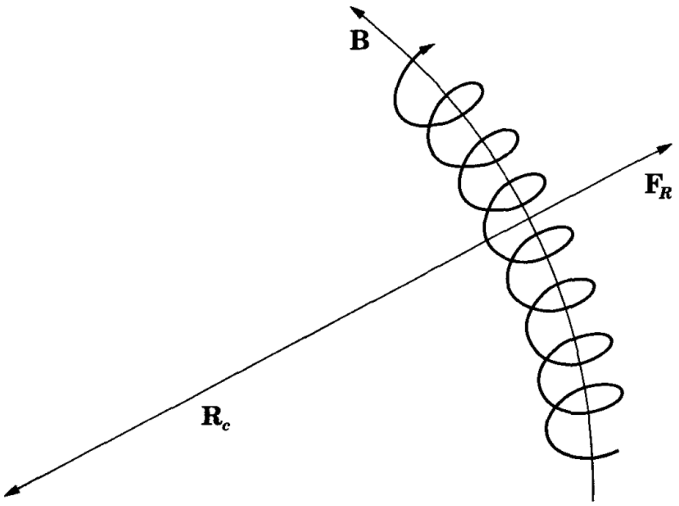

Figure 1.5: Centrifugal force acting on a particle moving along a curved field line. Credit: Baumjohann and Treumann (1996).

appropriate to describe it as a conductive fluid. This approach is the foundation of magnetohydrodynamics (MHD).

The MHD description is applicable under several conditions: the plasma must be quasi-neutral, the gyroradii of the particle population must be small compared to the spatial scales of the system, and the gyroperiod must be much shorter than the characteristic timescales of interest. When these conditions are met, the microscopic particle behaviour averages out, allowing the plasma to be described using macroscopic quantities.

In the single-fluid MHD framework, the plasma is treated as a single conductive fluid characterised by the mass density ρ, the bulk velocity $\vec{u}$, and the pressure P. The continuity equation, expressing conservation of mass, is given by:

$$\frac{\partial \rho}{\partial t} + \nabla \cdot (\rho \vec{u}) = S \tag{1.22}$$

where S is a source term representing mass input (e.g., ionisation or external injection).

The equation expressing the conservation of momentum for the plasma fluid, is:

$$\rho\left(\frac{\partial\vec{u}}{\partial t}+\vec{u}\cdot\nabla\vec{u}\right)=-\nabla P+\vec{j}\times\vec{B}+\rho\vec{g} \tag{1.23}$$

where $\vec{j}\times\vec{B}$ is the Lorentz force acting on the fluid, $\vec{j}$ is the current density and $\vec{g}$ the gravitational term. The gravitational term is not always included in the momentum equation, but it is necessary in high gravity environments, such as in planetary magnetospheres. In this form, pressure is assumed to be isotropic; if pressure anisotropies are significant, a full pressure tensor must be used.

Alternatively, in a two-fluid model, the plasma is described by separate fluid equations for each species s (ions or electrons). The momentum equation for each species becomes:

$$\frac{\partial(n_s\vec{v}_s)}{\partial t}+\nabla\cdot(n_s\vec{v}_s\vec{v}_s)=-\frac{1}{m_s}\nabla\cdot\vec{P}_s+\frac{n_s q_s}{m_s}\left(\vec{E}+\vec{v}_s\times\vec{B}\right) \tag{1.24}$$

where $\vec{P}_s$ is the pressure tensor and q_s is the particle charge for species s.

However, for many large-scale space plasmas, the single-fluid MHD model provides a sufficiently accurate approximation. It forms the theoretical foundation for understanding processes such as solar wind propagation, magnetospheric convection, and the formation of large-scale current systems.

1.3.1 Frozen-in Flux

One of the key results of ideal MHD is how the magnetic field evolves with the plasma. This behaviour is governed by the electric field and is captured through Ohm's law. In the general case, Ohm's law takes the form:

$$\vec{E}+\vec{u}\times\vec{B}=\eta\vec{j}+\frac{1}{ne}\vec{j}\times\vec{B}-\frac{1}{ne}\nabla p_e+\frac{m_e}{ne^2}\frac{\partial\vec{j}}{\partial t} \tag{1.25}$$

where η is the resistivity.

However, under conditions found in magnetospheric plasmas and the solar wind, several terms on the right-hand side can be neglected. In highly conductive plasmas,

the resistivity is very small ($\eta \ll 1$), making the resistive term $\eta\vec{j}$ negligible. Since characteristic spatial scales are much larger than the ion inertial length, the Hall term $\frac{1}{n_e}\vec{j} \times \vec{B}$ can likewise be omitted. Assuming the plasma is isothermal and relatively homogeneous, the electron pressure gradient term $-\frac{1}{n_e}\nabla p_e$ is typically small compared to the dominant electric and convective contributions. Lastly, the electron inertia term $\frac{m_e}{ne^2}\frac{\partial \vec{j}}{\partial t}$ is negligible due to the small electron mass and the slow temporal evolution of the current density.

Neglecting these terms reduces Ohm's law to its simplified form:

$$\vec{j} = \sigma(\vec{E} + \vec{u} \times \vec{B}) \tag{1.26}$$

where σ is the electrical conductivity. In the limit of perfect conductivity ($\sigma \to \infty$), the electric field in the plasma rest frame must vanish, leading to the ideal Ohm's law:

$$\vec{E} + \vec{u} \times \vec{B} = 0. \tag{1.27}$$

Substituting this condition into Faraday's law (Equation 1.5) leads to the ideal induction equation, which governs the evolution of the magnetic field:

$$\frac{\partial \vec{B}}{\partial t} = \nabla \times (\vec{u} \times \vec{B}). \tag{1.28}$$

If finite conductivity is retained, Ohm's law no longer reduces to the ideal form, and a resistive term appears. Using Ampère's law to eliminate $\vec{j}$, the induction equation becomes:

$$\frac{\partial \vec{B}}{\partial t} = \nabla \times (\vec{u} \times \vec{B}) + \frac{1}{\mu_0 \sigma}\nabla^2 \vec{B}. \tag{1.29}$$

The first term on the right-hand side represents the advection of the magnetic field with the plasma flow, showing that the field lines are 'carried' by the moving plasma. The second term represents the diffusion of the magnetic field through the plasma due to resistivity and gradients in the magnetic field. This diffusive term can be significant even if resistivity is low if the magnetic field has strong gradients, such as in current sheets. The presence or absence of the second term determines whether

the magnetic field is 'frozen-in' to the plasma. In regions where conductivity is high, the second term is negligible, and field lines are advected with the flow. However, when the plasma becomes resistive, when the magnetic field contains high gradients or when small-scale effects (e.g. turbulence or kinetic processes) become important, the frozen-in condition breaks down, allowing field lines to diffuse or reconnect.

The relative importance of the advective and diffusive terms in the induction equation is characterised by the magnetic Reynolds number, defined as

$$R_m = \frac{|\nabla \times (\vec{u} \times \vec{B})|}{|\nabla^2 \vec{B}/\mu_0 \sigma|} = \mu_0 \sigma U L = \frac{UL}{\eta}, \tag{1.30}$$

where U and L are characteristic velocity and length scales of the plasma, and $\eta = \frac{1}{\mu_0 \sigma}$ is the magnetic diffusivity. In typical collisionless plasmas with very high conductivity and large scale lengths, $R_m \gg 1$ and advection dominates. This means the magnetic field is effectively frozen into the plasma flow. As a result, the two are tightly coupled - the plasma cannot move freely across field lines and the magnetic field evolves with the plasma's motion.

Conversely, for $R_m \ll 1$, magnetic diffusion dominates, and the frozen-in condition breaks down. This criterion is critical for understanding the large-scale dynamics in plasma environments such as planetary magnetospheres, where localised deviations from ideal MHD enable processes such as magnetic reconnection and flux transport across boundaries. However, the bulk of magnetospheric dynamics occur within the $R_m > 1$ criterion.

1.3.2 Plasma Beta

The plasma beta (β) is defined as the ratio between the thermal and magnetic pressure:

$$\beta = \frac{P}{P_{mag}} = \frac{n k_B T}{B^2/2\mu_0} \tag{1.31}$$

where magnetic pressure (P_{mag}) is derived from the magnetic tension and pressure exerted on a conducting fluid by the magnetic field via the Lorentz force, whereas the thermal pressure (P) is derived from the statistical mechanics using the plasma temperature and density. The plasma β determines whether plasma motions are constrained by the magnetic field ($\beta \ll 1$) or the plasma pressure is sufficient to distort or control the magnetic field configuration ($\beta > 1$).

In the solar wind, plasma β varies with density and magnetic field strength. Fast solar wind (v $\sim$ 750 kms^{-1}) tends to have lower plasma β due to lower densities (n $\sim$ 3 cm^{-3}) and temperatures (T $\sim 5 \times 10^4$ K), while slow solar wind (v $\leq$ 400 kms^{-1}) is typically denser (n $\sim$ 7 cm^{-3}) and hotter (T $\sim 2 \times 10^5$ K), resulting in a moderate β. A value of $\beta \sim 1$ is typical at Earth's distance from the Sun. As the solar wind propagates outward, the plasma density decreases approximately as the inverse square of the heliocentric distance $\left(n \sim \frac{1}{r^2}\right)$, while the interplanetary magnetic field decreases roughly as the inverse of distance $\left(B \sim \frac{1}{r}\right)$. Consequently, the solar-wind plasma β is typically low by the time it reaches Jupiter's orbit. Jupiter's magnetosphere, on the other hand, is considered to be a high plasma β environment, as despite varying temperatures (T $\sim 10^1 - 10^3$ eV), densities (n $\sim$ 0.01 $-$ 1000 cm^{-3}) and magnetic field strength (B $\sim 1 - 2000$ nT) (Bagenal and Delamere, 2011; Gershman et al., 2017; Ness et al., 1979). In the outer magnetosphere, temperatures are high (T $\sim 10^3$ eV), but densities and magnetic field strength are low (n $\sim 0.01 - 0.1$, B $\leq$ 10 nT), giving a plasma β in the range of $\beta \sim 20 - 200$, which is much higher than the local solar wind. Details of the solar wind and Jovian system are discussed further in chapter 2.

1.4 Energy and Mass Transport in Plasmas

1.4.1 Magnetic Reconnection

Magnetic reconnection is the process in which magnetic fields in close proximity to each other undergo topological reconfiguration, occurring when a component of one field is oppositely directed to the other field. This process occurs due to the formation of a current sheet at the boundary between these components, which is subsequently thinned by the build up of thermal and magnetic pressure. This decreases the characteristic length scale and results in the diffusion term beginning to dominate, breaking down the frozen-in condition. The magnetic field can then diffuse into the current sheet, where the field lines break and reconnect in a new configuration. The centre of this diffusion region is free of magnetic fields and is known as the 'X-line' or 'X-point'. Following reconnection, the magnetic tension accelerates the newly connected field lines outward from the diffusion region. A diagram of the reconnection process can be seen in figure 1.6, illustrating the theoretical Sweet-Parker geometry of the process (Parker, 1957; Sweet, 1958), which has been shown to be the most consistent model in the context of MHD (Kulsrud, 2001).

Magnetic reconnection efficiently converts magnetic energy into thermal and kinetic energy, making it a key mechanism for transferring energy into a magnetosphere. At Earth, magnetic reconnection occurs on a large-scale as part of the Dungey Cycle. This involves reconnection along an X-line at the dayside magnetopause, typically at low-latitude and under mostly southward $-B_z$ directed IMF. These reconnected field lines are then carried anti-sunward by the flow of the solar wind, frozen into the plasma, and then undergo magnetic reconnection again in the equatorial region of the magnetotail (Dungey, 1961).

Magnetic reconnection can still occur between magnetic fields that are not anti-

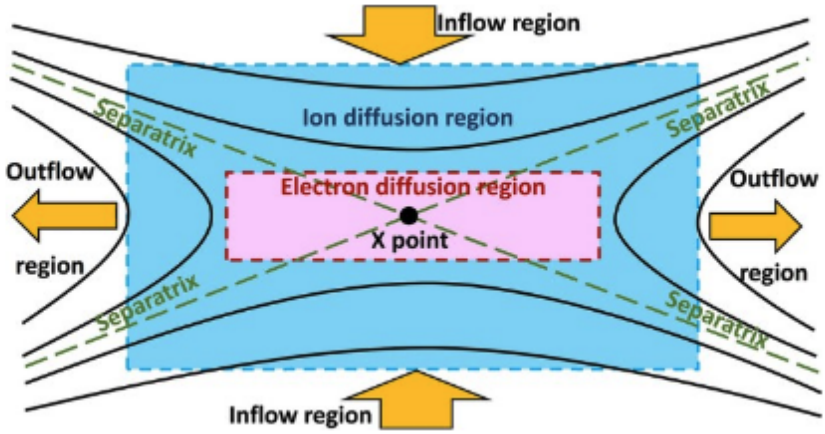

Figure 1.6: Sketch of different regions during collisionless magnetic reconnection, where the X-point is represented by a black dot, magnetic field lines are solid black lines and the separatrix are green dashed lines. The pink area represents the electron diffusion region and the blue the ion diffusion region. Credit: Lee and Lee (2020).

parallel, provided they contain significant anti-parallel components. This is known as component reconnection, and occurs where the magnetic fields meet at an angle. In this case, only the anti-parallel components reconnect, while the magnetic field component perpendicular to the reconnecting direction stays the same across the newly formed current sheet. This perpendicular component is known as the guide field. It prevents the magnetic field strength dropping to zero at the X-point, creating an asymmetric reconnection region that alters the shape and thickness of the current sheet and the orientation of the reconnected field lines. This can lead to asymmetric outflows and often a reduction in reconnection efficiency (Swisdak et al., 2005). Component reconnection is frequently observed at Earth's magnetopause under predominately IMF $\pm B_y$ conditions and typically occurs at higher latitudes.

In contrast, large-scale reconnection of either type is not generally expected at Jupiter, where magnetospheric conditions are considered less favourable for sustained reconnection events. The occurrence and limitations of magnetic reconnection at Jupiter's magnetosphere is discussed further in Section 2.2.1 of Chapter 2.

1.4.2 Alfvén Waves

Waves play an important role in the transfer of energy between different regions of plasma. A wide variety of wave modes, each with distinct properties, can occur in space plasmas - many of which lie beyond the scope of this thesis. In a warm plasma, three primary electromagnetic wave modes can be found: fast magnetosonic, slow magnetosonic and Alfvén mode waves. Of these, only the Alfvén mode wave is relevant to this discussion.

Alfvén waves represent a transverse shear mode that propagates parallel or obliquely to the background magnetic field. They travel at the Alfvén velocity:

$$v_A = \frac{B}{\sqrt{\mu_0 \rho}} \tag{1.32}$$

Magnetic field perturbations associated with Alfvén waves are oriented perpendicular to both the magnetic field and the wave vector ($\vec{k}$), with magnetic tension acting as the main restoring force. The wave vector represents the direction and wavelength, where the magnitude is related to the wavelength by $|\vec{k}| = \frac{2\pi}{\lambda}$ and the direction indicates the direction of wave propagation. For Alfvén waves, $\vec{k}$ typically lies along the the background magnetic field direction.

This wave mode is dispersionless in ideal MHD conditions, meaning its phase velocity is independent of wavelength. As such, Alfvén waves do not produce any changes in plasma density, pressure or magnetic field strength. However, they can contribute to the acceleration of auroral particles, making them significant in auroral dynamics.

In planetary magnetospheres, Alfvén waves play an important role in magnetosphere-ionosphere coupling as they enable the rapid transmission of momentum and energy along magnetic field lines. This rapid transmission can determine how energy inputs in different parts of the magnetosphere can influence ionospheric phenomena, such as the aurora. Thus, the propagation time of Alfvén waves between the magnetosphere and the ionosphere can provide valuable insights into the timings and dynamics of auroral responses (e.g. Lorch et al., 2022). It should be noted that while Alfvén

waves are a key mechanism for energy transfer, other processes such as particle precipitation and magnetospheric convection also play important roles in auroral dynamics.

The location at which radial outflow speeds exceed the local Alfvén speed is known as the Alfvén radius. This radius is important in space plasmas because beyond this point, Alfvén waves can no longer propagate effectively, preventing communication between different regions of plasma (e.g. Jenkins et al. (2024)). As a result, the coupling between these regions begins to break down, influencing processes such as angular momentum transfer and magnetic field topology.

1.4.3 Kelvin-Helmholtz Instability

The Kelvin-Helmholtz (K-H) instability is a fluid instability that arises when there is a velocity shear across a boundary between two fluids. This shear can generate surface waves at the boundary, which may grow and eventually 'roll up' into vortices (Chandrasekhar, 1961). While the K-H instability is commonly associated with cloud formations in planetary atmospheres, it can also occur in plasmas due to their fluid-like behaviour. In a magnetised plasma, this process can twist magnetic field lines and induce small-scale magnetic reconnection, facilitating plasma transport across the boundary.

The criterion for K-H is as follows:

$$\rho_1\rho_2(\Delta u)^2 > (\rho_1 + \rho_2)\frac{B_1^2 + B_2^2}{\mu_0} \tag{1.33}$$

where the subscript of '1' and '2' represents the two sides of the interface. Physically, the inequality states that the kinetic energy associated with the velocity shear overcomes the stabilising magnetic tension, meaning the interface is unstable and the K-H instability can develop.

The growth of the instability depends on multiple factors: the orientation and

strength of the magnetic field, flow velocity, and the difference in densities between the two plasmas. In particular, a strong magnetic field component perpendicular to the shear flow can suppress the instability due to the magnetic tension forces (e.g. Masters, 2017) Although individual K-H vortices are typically short-lived, frequent occurrence over significant lengths of a boundary can result in substantial mass and momentum transfer between adjacent plasma regions (e.g. Hasegawa et al., 2004).

In planetary magnetospheres, K-H waves have been observed at Earth's magnetosphere by the Magnetospheric Multiscale spacecraft (Eriksson et al., 2016) and is suggested to be an important energy transfer mechanism, that can result in the generation of auroral arcs, when solar wind conditions are unfavourable to large-scale reconnection (Kavosi et al., 2023). It is also suggested to be an important method of transporting energy from the solar wind into Jupiter's magnetopause (Delamere and Bagenal, 2010; Desroche et al., 2012; Masters, 2017)

1.5 Summary

This chapter introduces fundamental plasma principles essential for understanding the physics governing both the solar wind and Jupiter's magnetosphere, two distinct plasma environments. It begins with the basic motion of charged particles and progresses through to magnetohydrodynamics (MHD) and energy transfer in plasmas, outlining how these principles shape plasma interactions with magnetic and electric fields. These principles are crucial for understanding how the solar wind interacts with planetary magnetospheres, driving phenomena such as magnetic reconnection and auroral emission.

Chapter 2

Jupiter and the Solar Wind

Jupiter is the largest planet in the solar system, with the largest magnetosphere and most dynamic auroral emissions. Although significant progress has been made in understanding the Jupiter system, much remains unknown, such as the mechanisms behind the UV aurora in the polar regions of the planet. While this thesis aims to investigate the role of the solar wind in driving this emission, a background on both the system and the solar wind is necessary to provide context for the work.

2.1 The Solar Wind

The solar wind is a continuous stream of particles emitted from the solar corona, the Sun's outermost layer. The process begins deep in the solar core, where hydrogen fusion generates energy. This energy is transported outward through radiation and convection, ultimately heating the corona to temperatures exceeding 10^6 K. The resulting high thermal pressure overcomes the Sun's gravitational pull, continuously accelerating magnetised plasma into interplanetary space (Parker, 1958).

This plasma is the solar wind, and is primarily composed of protons and electrons,

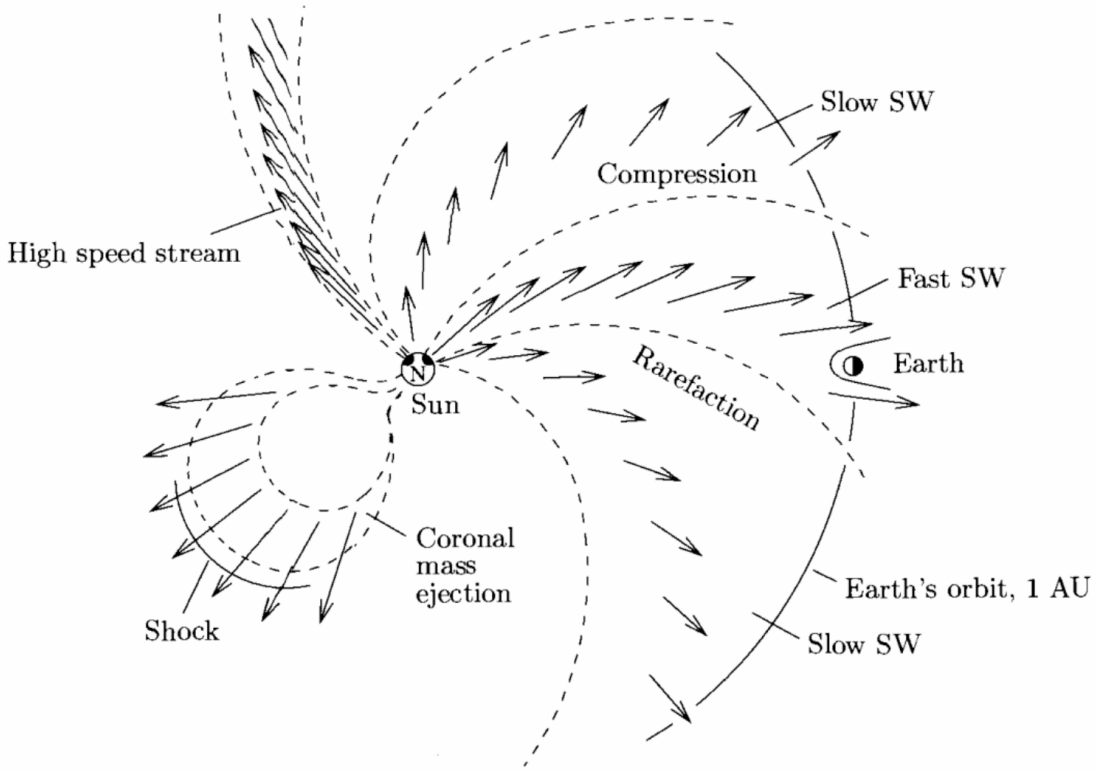

Figure 2.1: Structure of the solar wind, viewed from above the Sun. Regions of both slow and fast wind are illustrated, as well as the eruption of a coronal mass ejection (CME) and corotating interaction region (CIR). The CIR is not explicitly labelled but represents the compression region between the slow and fast solar wind and is followed by a reverse shock and rarefaction region. Dashed lines indicate the shape of the Parker spiral, resulting from the combination of radial plasma flow and solar rotation. Credit: Prölss (2004).

with a minor contribution ($\sim 5\%$) from alpha particles (He^{2+}). It flows outward through the solar system and interacts with the planets and other objects in its path (Baumjohann and Treumann, 1996). The solar wind continues to propagate until it reaches the termination shock, where it slows abruptly due to interaction with the interstellar medium. A shock is a narrow region in a plasma where physical conditions change rapidly and discontinuously, typically the result of the supersonic flow encountering an obstacle or a slower medium. In this case, the termination shock marks beginning of the heliosheath, where the solar wind becomes subsonic and turbulent. Beyond the heliosheath lies interstellar space, where the Sun's influence diminishes (see review by Jokipii (2013)).

The solar wind's properties, such as speed, density and temperature, vary with solar activity. The Sun has a roughly dipolar magnetic field, with the convection of plasma in the solar interior thought to act as a dynamo. The polarity of this field reverses every $\sim$ 11 years, with solar activity increasing and decreasing over this cycle. During periods of high activity, the solar wind is often more variable, with parcels of high density and velocity plasma known as coronal mass ejections (CMEs) ejected from the Sun more frequently. These typically originate from sunspots, which are dark spots on the Sun's surface that are cooler and feature intense magnetic field strengths. When there are little to no sunspots, solar activity is low.

Typical solar wind speeds range from $\sim 400 - 800$ kms^{-1}, and the solar wind is usually classified as slow or fast wind depending on where it falls within this range. However, this range is not typically continuous, as the solar wind exhibits a bimodal velocity distribution, with slow and fast wind originating from distinct solar sources. Slow solar wind is of the same composition as the corona and typically emerges from the equatorial region. Fast solar wind originates from higher polar latitudes, likely from coronal holes in the photosphere. If fast wind catches up to slow wind, it will form a large scale compression known as a corotating interaction regions (CIRs). CIRs are more common during periods of low solar activity. Alongside CMEs,

CIRs are associated with enhanced solar wind dynamic pressure, often preceded by a forward shock and followed by a rarefaction region. Such events can compress planetary magnetospheres and influence their internal dynamics. Both of these phenomena are illustrated in figure 2.1, where the CIR is the region of compression and subsequent rarefaction.

2.1.1 The Interplanetary Magnetic Field

Also contained within solar wind plasma is the Sun's magnetic field, which varies in strength and configuration throughout the solar cycle, alongside the solar wind speed, density and temperature. This magnetic field is more commonly known as the interplanetary magnetic field (IMF), and it is frozen into the plasma due to its high conductivity (see section 1.3.1 in Chapter 1). As the Sun rotates, with a period of ~ 25 days at the equator and ~ 36 days at the poles (Snodgrass et al., 1990), the IMF flows radially outwards by the solar wind. Beyond the Alfvén radius, where the plasma flow speed exceeds the Alfvén speed, the magnetic field lines decouple from the Sun (Cranmer et al., 2023) and are dragged into a spiral shape (see figure 2.1). This shape is known as the Parker spiral (Parker, 1958).

The angle between the tangential and radial components of the IMF, known as the Parker spiral angle, increases with distance from the Sun and can be approximated by:

$$\theta = \arctan\left(\frac{B_T}{B_R}\right) = \arctan\left(\frac{\omega r}{v_{sw}}\right) \tag{2.1}$$

where B_T and B_R are the tangential and radial components of the IMF, respectively, ω is the Sun's angular rotation rate, r is the distance from the Sun and v_{sw} is the solar wind speed. This angle is calculated as $\sim 79°$ for slow wind and $\sim 69°$ for fast wind at Jupiter's distance from the Sun. This simplification does not account for the complex structure of the Sun's magnetic field observed during solar maximum, however.

The IMF is typically decomposed into three orthogonal components aligned with a planet-centred coordinate system, such as the Geocentric Solar Magnetospheric (GSM) system used at Earth. These components, B_x, B_y and B_z describe the orientation of the magnetic field relative to the planet: B_x represents the planet-Sun line, B_y is calculated by taking the cross product of B_x and the Earth's dipole axis and B_z is defined as the cross product of B_x and B_y. The orientation of B_z is important for solar wind-magnetospheric coupling, especially at the Earth where a southward (negative) B_z component represents the ideal IMF orientation for efficient energy transfer via the Dungey cycle. Jupiter's magnetic field is oppositely directed, and so theoretically a northward (positive) B_z component would be more favourable for solar wind-magnetosphere coupling, though the nature and scale of any such interactions is likely to differ significantly from those at the Earth due to different conditions at the boundary between the solar wind and Jupiter's magnetopause (see section 2.1.2).

2.1.2 Magnetosphere-Solar Wind Interactions

A magnetosphere is the region surrounding a planet or other celestial body where the magnetic pressure exerted by the planetary magnetic field dominates over the dynamic pressure of the solar wind. It carves out a cavity in the solar wind, diverting its flow and creating a boundary between them known as the magnetopause. The magnetopause is sensitive to changes in the solar wind, with its size determined by changes in the pressure balance between the solar wind dynamic pressure and magnetic pressure of the planet and the combined internal pressure of the magnetosphere, including planetary magnetic pressure and plasma sources (e.g. Khurana et al., 2004). Before reaching the magnetopause, the solar wind first encounters the bow shock, a standing shock wave that decelerates, compresses and heats the supersonic solar wind plasma. Upstream of the bow shock is the foreshock region, where a portion of the incoming solar wind ions are reflected back along

magnetic field lines, generating plasma waves and turbulence.

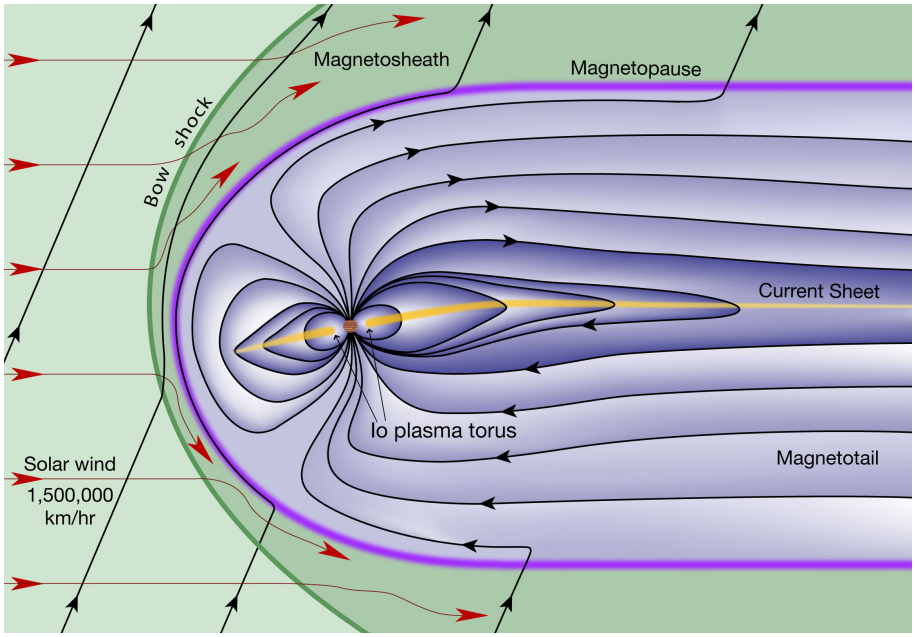

Figure 2.2: Illustration of the noon-midnight meridian of Jupiter's magnetosphere. Credit: Fran Bagenal and Steve Bartlett.

The region between the bow shock and magnetopause is the magnetosheath, containing slow, hot, dense and turbulent plasma transformed by the bow shock. The magnetosheath acts as a transitional zone, mediating the interaction between the solar wind and planetary magnetosphere. Its structure and thickness vary with solar wind conditions, particularly dynamic pressure and IMF orientation. High solar wind dynamic pressure compresses the bow shock and magnetopause, thinning the magnetosheath, while lower pressure allows it to expand. The IMF orientation influences sheath stability: when the IMF is anti-aligned with the planetary magnetic field, the magnetosheath tends to become more turbulent. This turbulence can lead to small-scale fluctuations in magnetic field orientation and variations in plasma properties across the magnetosheath, influencing the local conditions for solar wind-magnetosphere interactions at the magnetopause. Jupiter's magnetosheath is considered to be very dynamic, with plasma properties spanning multiple orders of magnitude (Ranquist et al., 2019).

The plasma environment inside a magnetosphere is shaped by both internal and external sources. Its properties vary by region, but are typically denser and colder near internal plasma sources, and hotter and more tenuous at higher latitudes and in the tail. Internal sources include ionisation of neutral material originating from the planet or its moons, while external sources involve the solar wind plasma entering the magnetosphere through various transport mechanisms. Several processes can facilitate solar wind entry into a magnetosphere. One direct pathway is via regions of open field lines, such as the polar caps in Earth's magnetosphere. Other methods require interactions between the magnetopause magnetic field and interplanetary magnetic field (IMF). These processes are more effective at transporting significant amounts of solar wind plasma into the magnetosphere. Two of these methods, magnetic reconnection and the Kelvin-Helmholtz instability, are discussed in sections 1.4.1 and 1.4.3. The efficiency of these processes depends on the solar wind conditions; in particular, the orientation of the IMF controls the reconnection rate for large-scale magnetic reconnection and the associated energy transfer. Outside the scope of this thesis, other methods which may contribute to plasma entry include diffusive transport across the magnetopause, wave-particle interactions and various plasma instabilities (Desroche et al., 2012).

Planetary magnetospheres can be broadly categorised based on whether their dynamics are primarily driven by the solar wind or by internal processes. Solar wind driven magnetospheres include the Earth and Mercury (Khurana et al., 2004), where external conditions control much of the dynamics. In contrast, Jupiter is an example of a planet dominated by its rapid rotation and internal plasma sources, most notably the volcanic moon Io. Although the solar wind is not considered to contribute largely as a plasma source, the solar wind still exerts considerable influence by modulating the overall size of the magnetosphere (Joy et al., 2002; Rutala et al., 2025) and brightness of ultraviolet auroral emissions through dynamic pressure changes (Giles et al., 2025; Nichols et al., 2009b; Yao et al., 2022).

The extent of solar wind-magnetosphere interactions at Jupiter's dayside magnetopause is uncertain, although some viscous-like processes are expected to occur along the flanks (Delamere and Bagenal, 2010). Large-scale magnetic reconnection is considered to be unlikely to occur due to two primary factors. The first is the substantial difference in the plasma β (see section 1.3.2 in Chapter 2) of the solar wind and Jupiter's magnetospheric plasma. A high $\Delta\beta$ suppresses reconnection by weakening the magnetic tension force and enhancing plasma pressure, which resists the reconfiguration of magnetic field lines. Secondly, the strong shear between the solar wind flow and Jupiter's rapidly corotating magnetospheric plasma drives turbulence along the magnetopause boundary, disrupting the formation of stable, large-scale, steady reconnection regions (Desroche et al., 2012). However, this turbulence can sometimes develop into Kelvin-Helmholtz instabilities, which can transfer energy into the magnetopause via boundary layer mixing, facilitating solar wind entry into the magnetosphere (e.g. Masters (2017)).

2.2 Jupiter's Magnetosphere

Jupiter has the largest and most powerful magnetosphere in the solar system. Its magnetic field is generated by dynamo action in convective metallic hydrogen and is offset by approximately 10.25° from its axis of rotation towards a System III longitude of 196.38°. It has a rotation period of 9 hours and 55 minutes, with an interior magnetic field of ~ 4 Gauss (Connerney et al., 2022).

System III longitude is a Jovian-specific coordinate system based on the internal rotation of the planet's magnetic field. Longitudes are measured relative to the System III prime meridian (0° longitude), which is defined by the intersection of the planet's central meridian plane with Jupiter's magnetic equator at a reference epoch defined by the 1965 reference epoch when 0° longitude was originally established from Jupiter's decametric radio emissions. Longitude increases eastward, following

a right-handed convention fixed in the planet's rotation frame (Dessler, 1983). This System III frame is widely used in studies of Jupiter's aurora and magnetosphere, although some older studies used a left-handed system in which longitude increases westward and thus opposite to planetary rotation. The central meridian longitude (CML) is the longitude line facing an observer on Earth at any given time (CML = 0°), and as the Earth is generally located near the sunward side of Jupiter, can be used as a proxy for local noon(Hill et al., 1983).

To fully understand Jupiter's magnetic environment, it is also important to consider its atmosphere and ionosphere. These regions form the interface between the planet and magnetosphere, where magnetospheric particles precipitate and deposit energy, resulting in auroral emissions. The ionosphere is the region of the upper atmosphere that contains a significant number of charged particles, allowing it to conduct electricity and interact with magnetic fields. It couples the magnetosphere to the atmosphere by facilitating the flow of electric currents that transfer energy and momentum between these two regions (see section 2.2.2.3).

Jupiter's ionosphere primarily consists of H^+ and H_3^+ ions, embedded within a neutral atmosphere dominated by molecular hydrogen (H_2) and helium (Strobel and Atreta, 1983; Yelle and Miller, 2004). Ionisation occurs through two primary processes: solar extreme ultraviolet (EUV) radiation, which penetrates relatively deeply and dominates at low latitudes, and energetic particle precipitation, which is concentrated at high-latitude auroral regions and deposits energy primarily at higher altitudes (Yelle and Miller, 2004). These ionisation processes not only shape ionospheric structure and composition but also heat the upper atmosphere, altering its temperature and density. This in turn influences ionospheric conductivity, especially the Pedersen conductivity, which is the component of ionospheric conductivity perpendicular to the magnetic field and parallel to the electric field. Pedersen conductivity varies with altitude and latitude and governs momentum transfer between the ionosphere and magnetosphere (Ray et al., 2010; Schunk and

Nagy, 2000). Together, these regions provide an environment for complex chemical interactions that drive auroral emissions (see section 2.3.1).

2.2.1 Magnetospheric Structure

The inner magnetosphere, extending to approximately 6 Jupiter radii ($6\,R_J$), is dominated by Jupiter's strong internal magnetic field and is largely dipolar in structure (Acũna et al., 1983). In this region, the influence of external forces such as the solar wind is negligible, and plasma motion is tightly controlled by the planet's magnetic field. The plasma environment is relatively stable and primarily corotates with the planet (Hill et al., 1983). The inner magnetosphere also contains the volcanic moon Io and its associated plasma torus. This dense torus, supplied continuously by volcanic outgassing from Io, plays a central role in mass-loading the magnetosphere and driving its overall plasma dynamics, as discussed further in section 2.2.2.1.

The middle magnetosphere spans roughly from $\sim 6\,R_J$ to between $30 - 50\,R_J$, with the outer boundary typically defined depending on what aspect of magnetospheric dynamics is being studied. This region is dominated by an azimuthal current sheet known as the magnetodisc, a disc-like structure formed by a dense, azimuthal current system and confined plasma (e.g. Khurana et al., 2004; Khurana and Schwarzl, 2005). While axisymmetric in the inner magnetosphere, the magnetodisc becomes increasingly warped and flared away from the equatorial plane as it extends to distances further from the planet, reflecting the influence of centrifugal forces, solar wind interaction and internal plasma dynamics (Khurana, 1992). The magnetodisc significantly distorts Jupiter's magnetic field, generating substantial magnetic stress and stretching it outward in the equatorial direction, altering the geometry beyond a dipolar configuration (Khurana and Schwarzl, 2005; McNutt et al., 1981). Plasma density is high within the magnetodisc, forming a relatively thin and dense layer of

confined plasma shaped by a balance of centrifugal, thermal and magnetic forces, while the regions above and below are relatively depleted (Huscher et al., 2021; McNutt et al., 1981). The middle magnetosphere is also where plasma corotation breaks down and interchange processes take place, which will be discussed in sections 2.2.2.2 and 2.2.2.3.

Embedded in this plasma sheet is a strong azimuthal current sheet, which is responsible for significant distortions of Jupiter's magnetic field beyond $\sim 20\,\mathrm{R_J}$ due to the ring current formed by the azimuthal currents (Connerney, 1981). The thickness and position of the plasma and current sheet vary with radial distance and local time, shaped by rotational stresses and the centrifugal interchange of magnetically confined plasma, which transports mass and introduces asymmetries in the magnetodisc (Kivelson and Southwood, 2005).

The outer magnetosphere extends out to the magnetopause distance and into the magnetotail on the nightside. This region is bounded by the magnetospheric cushion, or interaction region, which acts as a buffer sensitive to variations in external solar wind pressure (Acũna et al., 1983; Khurana et al., 2004; Went et al., 2011). This boundary region in the outer magnetosphere is known to be thicker on the dawnside than on the duskside (Delamere and Bagenal, 2010). The dayside outer magnetosphere is also highly compressible, moving significantly inward under periods of high solar wind dynamic pressure and altering the position of the magnetopause boundary (Joy et al., 2002). Juno measurements have placed the magnetopause at a distance of $\sim 74 - 114\,\mathrm{R_J}$ on the dawnside (Hospodarsky et al., 2017), although magnetopause locations at other local times remain uncertain, often relying on predictive models such as that of Joy et al. (2002).

The nightside outer magnetosphere, commonly referred to as the magnetotail region, extends several astronomical units (AU) downstream and does not have a well-defined length (Khurana et al., 2004), although it has been noted to occasionally stretch as far as Saturn (Kurth et al., 1982). The tail consists of stretched, anti-

parallel magnetic field lines embedded within a central plasma sheet, which forms the nightside continuation of the magnetodisc. However, the overall topology of the magnetotail remains an open question. While early interpretations described the tail as comprising a plasma sheet flanked by two open lobe regions, more recent analyses suggest that a significant portion of the tail flux may be closed.

Intermittent plasma blobs, or plasmoids, observed by the New Horizons and Juno spacecraft have been linked to magnetic reconnection processes occurring deep within the tail current sheet (McComas et al., 2007; Vogt et al., 2020). These structures are typically associated with closed magnetic field lines that have 'pinched off' to form detached loops of plasma, as described in the Vasyliunas cycle (see section 2.2.2.4) (Kronberg et al., 2007; Vasyliũnas, 1983; Vogt et al., 2020). This process is thought to play a role in periodic mass loss in the mangetosphere. MHD modelling has also indicated the presence of some open flux within the magnetotail, confined to a crescent-shaped region bounded by the magnetodisc and the high-latitude polar region (Delamere et al., 2024; Zhang et al., 2021). Juno observations show variations in the helium-to-proton ratio near boundaries within this region, consistent with some solar wind plasma entry along open field lines. However, the plasma composition in this region remains predominantly magnetospheric (Delamere et al., 2024).

2.2.2 Magnetospheric Dynamics

2.2.2.1 The Io Torus and Plasma Source

Io is the most significant source of plasma in the Jovian system. Orbiting at $\sim 5.9\,\mathrm{R_J}$ near the outer edge of the inner magnetosphere, Io is embedded within a dense plasma torus composed of ionised sulphur and oxygen atoms (e.g. O^+, S^+, S^{2+}). This torus extends roughly between $5.2\,R_J$ to $10\,R_J$ and is continuously replenished by material escaping from Io's atmosphere (Thomas et al., 2004).

Neutral particles escape Io's atmosphere through sputtering and thermal processes driven by interactions with Jupiter's corotating magnetospheric plasma. These escaping neutrals form a large neutral cloud around Io, primarily composed of oxygen and sulphur atoms, which in turn creates a neutral torus that continuously feeds the ionised plasma population (Thomas et al., 2004). Collisions of these neutrals with Io's atmosphere enhance the escape of additional neutrals. Once in the surrounding environment, a significant fraction of these neutrals are ionised and become 'pick-up ions', accelerated by Jupiter's rapidly rotating magnetic field. Electron impact is the primary ionisation mechanism, but photoionisation and charge exchange also occur in the torus (Delamere et al., 2007; Hill, 1979). These ions join the population of the torus and corotate with the planet. Charge exchange is the dominant process that occurs within the torus, exchanging ions for slower neutrals. Although it does not change the net ion density, it redistributes plasma momentum by altering particle velocities, slowing plasma corotation and replenishing the neutral population (Bagenal and Dols, 2020).

Over a period of 20−80 days, this plasma from the torus then moves outward via flux-tube interchange (see section 2.2.2.2 and fills the middle magnetosphere (Bagenal, 2007). Io's volcanic activity continuously resupplies the torus, keeping it an active plasma source for the system. However, the plasma source rate is not constant. Variations observed over time in the torus density and composition observed are considered to be the result of changes in the neutral source rate, widely attributed to fluctuations in volcanic activity (Delamere and Bagenal, 2003). This mass-loading process drives the magnetospheric dynamics and affects current systems, plasma transport and the transfer of angular momentum (Bagenal and Delamere, 2011).

2.2.2.2 Plasma Transport and the Interchange Instability

As plasma from the Io torus moves outward into the middle magnetosphere, it begins to lag behind corotation. This breakdown occurs gradually and becomes

increasingly significant beyond $\sim 10 - 20\,R_J$ (Bagenal and Delamere, 2011). As the plasma is frozen-in to the magnetic field (see section 1.3.1 in Chapter 1), it cannot easily move across field lines, and as a result the differential motion between Jupiter's rapidly rotating magnetic field and the lagging plasma causes the magnetic field lines to bend in the azimuthal direction (Khurana et al., 2004). This distortion of the magnetic field is shown in figure 2.3.

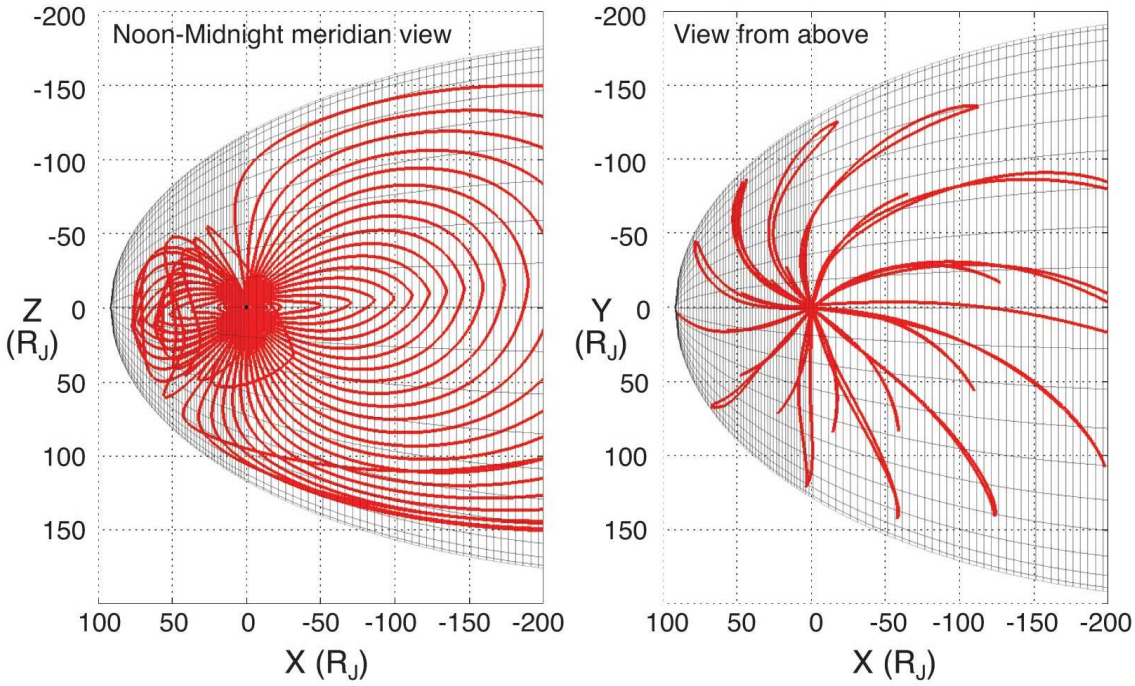

Figure 2.3: Magnetic field topology in Jupiter's magnetosphere. The two panels show the magnetic field configuration (left) in the noon-midnight meridian plane and (right) the equatorial plane. The distortion of the field lines, caused by the magnetic filed being frozen into the rapidly rotating plasma, is distinctly visible. Credit: Krishan Khurana.

With the plasma frozen into the field, outward plasma transport requires a breakdown of ideal MHD conditions. As the magnetic field lines bend due to the plasma lag, they develop magnetic tension, which acts as a restoring force resisting further distortion. This is known as the magnetic curvature force. This leads to an effective outward force as charged particles move along curved field lines, similar

to a centrifugal force (see section 1.2.2 in Chapter 1). When acting across entire flux tubes, this curvature-related force contributes to a force imbalance that can destabilise the configuration and drive the development of the interchange instability (Southwood and Kivelson, 1987, 1989). The interchange instability involves flux tubes containing dense, cold plasma from the Io torus moving outward by exchanging places with lighter, flux tubes containing hotter tenuous plasma from further out in the magnetosphere. The flux tubes exchange places to conserve magnetic flux at a boundary where a pressure gradient exists (Bagenal, 2007; Bagenal and Delamere, 2011). Here, a flux tube refers to a cylindrical region of space bounded by magnetic field lines, representing a volume of plasma attached to the magnetic field. This instability is analogous to the Rayleigh-Taylor instability, where a lighter fluid pushes into a heavier fluid. In this context, the 'swapping' of flux tubes is enabled by gradual shifts in the magnetic configuration, likely involving small-scale reconnection or other non-ideal processes, allowing radial plasma transport without requiring the plasma to cross field lines directly (Bagenal and Delamere, 2011; Khurana et al., 2004).

The interchange instability is theorised to occur on two different spatial scales: close to the Io torus, where it operates on smaller scales (Kivelson et al., 1997), and further out in the middle magnetosphere where large-scale instabilities are expected to be influenced by magnetic reconnection (Mauk et al., 2002). Theoretical timescales for this process range from hours to days depending on the region and scale of the instability (Bagenal and Delamere, 2011; Kivelson et al., 1997). However, recent Juno observations have provided new evidence suggesting that the instability near Jupiter occurs on much shorter timescales, potentially within minutes (Daly et al., 2024). While Juno has detected the instability close to Jupiter, no direct evidence of the instability has yet been found for it further out in the middle magnetosphere. However, plasma injections in this region have been shown to correlate with transient auroral features (Mauk et al., 2002), suggesting that plasma from the middle magnetosphere is being transported inward. This provides indirect support for the idea that the instability could be contributing to the radial plasma

transport, potentially influencing magnetospheric dynamics.

2.2.2.3 Magnetosphere-Ionosphere Coupling

As described in section 2.2.2.2, plasma begins to lag behind Jupiter's corotation as it moves out toward the middle magnetosphere, distorting the magnetospheric field lines that are frozen into the plasma. This lag creates a shear in the system, generates an electric field across the magnetosphere. Under the assumption of ideal MHD, this electric field satisfies the frozen-in condition $\vec{E} + \vec{u} \times \vec{B} = 0$, as derived in section 1.3.1 in Chapter 1. Because magnetic field lines act as equipotentials in this regime, the electric field generated by plasma flow in the magnetosphere maps along field lines down to the ionosphere (e.g. Ray et al., 2010).

The Pedersen conductivity facilitates the transfer of momentum from the magnetosphere to the ionosphere. The divergence of this current generates upward field-aligned currents (FACs) in the ionosphere, connecting the middle magnetosphere and ionosphere (Cowley and Bunce, 2001; Hill, 1979; Vasyliũnas, 2001). When FACs from opposite hemispheres meet, the FACs diverge into radially outward currents, applying a torque ($\vec{j} \times \vec{B}$ force) to the plasma. To balance this, the counterpart ionospheric currents then exert a torque on the ionosphere, enforcing partial corotation of the plasma as it transfers angular momentum from Jupiter's magnetic field to the magnetosphere (Hill, 1979). However, this system does not fully restore rigid corotation; at larger radial distances (e.g. $40\,\mathrm{R_J}$), the azimuthal velocity of the plasma can fall to less than half of the corotation value (Acũna et al., 1983; Delamere and Bagenal, 2010). This large-scale coupling system is closed by downward FACs, primarily located in the noon-to-dusk sector of the outer magnetosphere (Lorch et al., 2020). These FACs evolve with different magnetospheric conditions on timescales of minutes to hours, responding to variations in electric fields and plasma flow (Chané et al., 2013). The full current system is illustrated in 2.4.

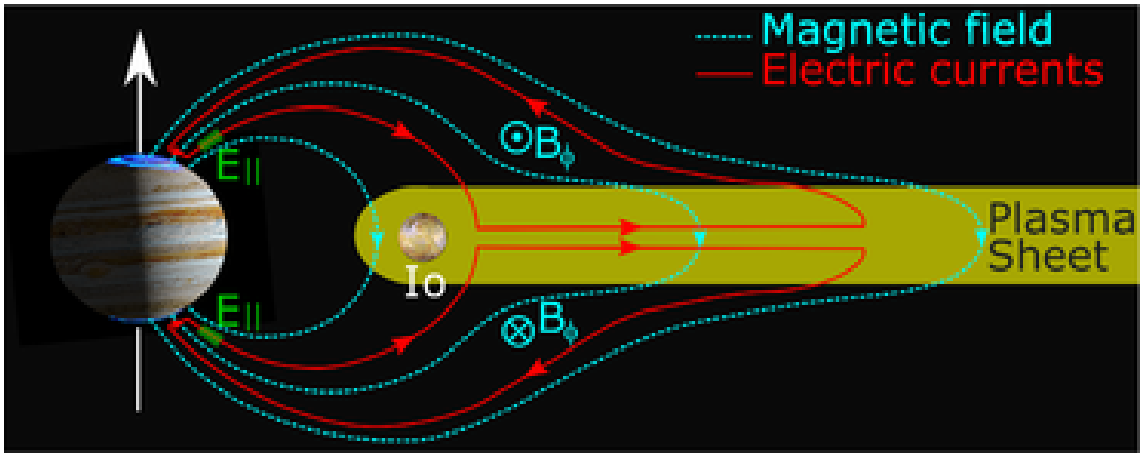

Figure 2.4: Diagram of the corotation enforcement currents. The dashed cyan lines represent the magnetic field, the solid red lines the electric currents and the green lines are the electric fields associated with accelerating electrons into the ionosphere to generate auroral emissions. Credit: Bonfond et al. (2020).

This breakdown in efficient coupling occurs at the Alfvén radius. As the plasma moves through the magnetosphere, Alfvén waves propagate between the ionosphere and magnetosphere, conveying information between the planet and the plasma. Beyond the Alfvén radius, Alfvén waves cannot travel faster than the plasma, leading to inefficient magnetosphere-ionosphere coupling. Consequently, angular momentum transfer from Jupiter to the plasma is limited outside this radius and thus the plasma begins to decouple from the magnetic field (Delamere and Bagenal, 2010). Modelling shows this radius is asymmetric: plasma decouples from the planet inside of $\sim 35\,\mathrm{R_J}$ on the nightside, as close as $\sim 30\,\mathrm{R_J}$ near local dawn and beyond $60\,\mathrm{R_J}$ from pre-noon to dusk. The exact distance, or whether the Alfvén radius even exists from pre-noon to dusk, is unknown as the model only goes out as far as $60\,\mathrm{R_J}$ (Jenkins et al., 2024). This asymmetry arises because the compressed dayside magnetic field is stronger, resulting in a higher Alfvén velocity.

Despite this decoupling, the magnetosphere-ionosphere coupling still plays an important role in Jupiter's magnetospheric dynamics. The corotation enforcement

current (CEC) theory is the most commonly accepted explanation of the main emission of Jupiter's aurora (Cowley and Bunce, 2001). Auroral emissions arise from the interaction of precipitating energetic particles with the upper atmosphere, where collisions excite and ionise atmospheric species. This leads to a complex network of chemical reactions involving ions, neutrals, and electrons, influencing the composition and energy balance of the ionosphere. The theory is that the main emission is driven by the precipitation of energetic electrons from the magnetosphere, which are guided into the ionosphere by downward FACs, as shown in figure 2.4 (Khurana et al., 2004; Ray et al., 2009). As the energetic particles collide with atmospheric species, they excite them, leading to the characteristic ultraviolet (UV) emission observed in Jupiter's aurora.

Certain features challenge the corotation enforcement model, suggesting that additional or more complex current systems may be involved in the driving of the main emission (Bonfond et al., 2015, 2020). An example of one of these features is dawn storms, which are transient brightening in the dawn sector of the main emission that sub-corotate with a lag of up to $\sim 50\%$ (Rutala et al., 2022). However, a complete alternative to the corotation enforcement model does not presently exist.

2.2.2.4 The Vasyliunas Cycle

Plasma originating from Io and transported through the magnetosphere eventually reaches the nightside outer magnetosphere. This outward flowing material stretches the field lines in the magnetotail, thinning the tail until the magnetic geometry collapses and magnetic reconnection occurs at the magnetic X-line, a non-physical boundary that spans the magnetosphere from the dawn to dusk sector (Vasyliũnas, 1983; Vogt et al., 2010). As shown in figure 2.5, the X-line's position is asymmetric, extending further tailward in the dusk sector. This asymmetry is consistent with the plasma sheet's thickness variations and flux tube depletion near dusk (Kivelson and Southwood, 2005), and the observed tailward extension of the X-line (Vogt et al.,

2010).

This tailward reconnection results in hot, tenuous plasma flows, which move back toward the middle magnetosphere via the interchange instability (see section 2.2.2.2). Plasmoids, self-contained bundles of Iogenic plasma and magnetic field lines, are also generated during this reconnection process and are lost down the tail (Vasyliũnas, 1983). The cycle, which involves mass loading from Io (described in section 2.2.2.1), plasma transport (described in section 2.2.2.2), tail reconnection, plasma loss down the tail and hot return flow is known as the Vasyliunas cycle (Vasyliũnas, 1983). This cycle helps redistribute plasma and magnetic field lines throughout the magnetosphere.

The return flow of hot, tenuous plasma can affect field-aligned currents (FACs) in the outer magnetosphere, impacting magnetosphere-ionosphere coupling and auroral emissions (see section 2.2.2.3). As such, variations in Io's mass loading rate, which directly influences the plasma distribution in the magnetosphere, can drive variability in auroral emissions. Solar wind-magnetospheric interactions may also influence the Vasyliunas cycle through modulation of internal plasma flow via enhanced dynamic pressure (Giles et al., 2025; Nichols et al., 2009b; Yao et al., 2022), or through direct plasma interactions within the magnetosphere, though the precise role of the solar wind at Jupiter remains unclear. While the link between the main emission and the Vasyilunas cycle is more established, other auroral components are suggested to be influenced by internal dynamics as well (see sections 2.3.3 and 2.3.4). Given the distinct morphologies and behaviours observed in different auroral regions, the Vasyliunas cycle alone is unlikely to account for all variations seen in Jupiter's aurora that are attributed to internal dynamics.

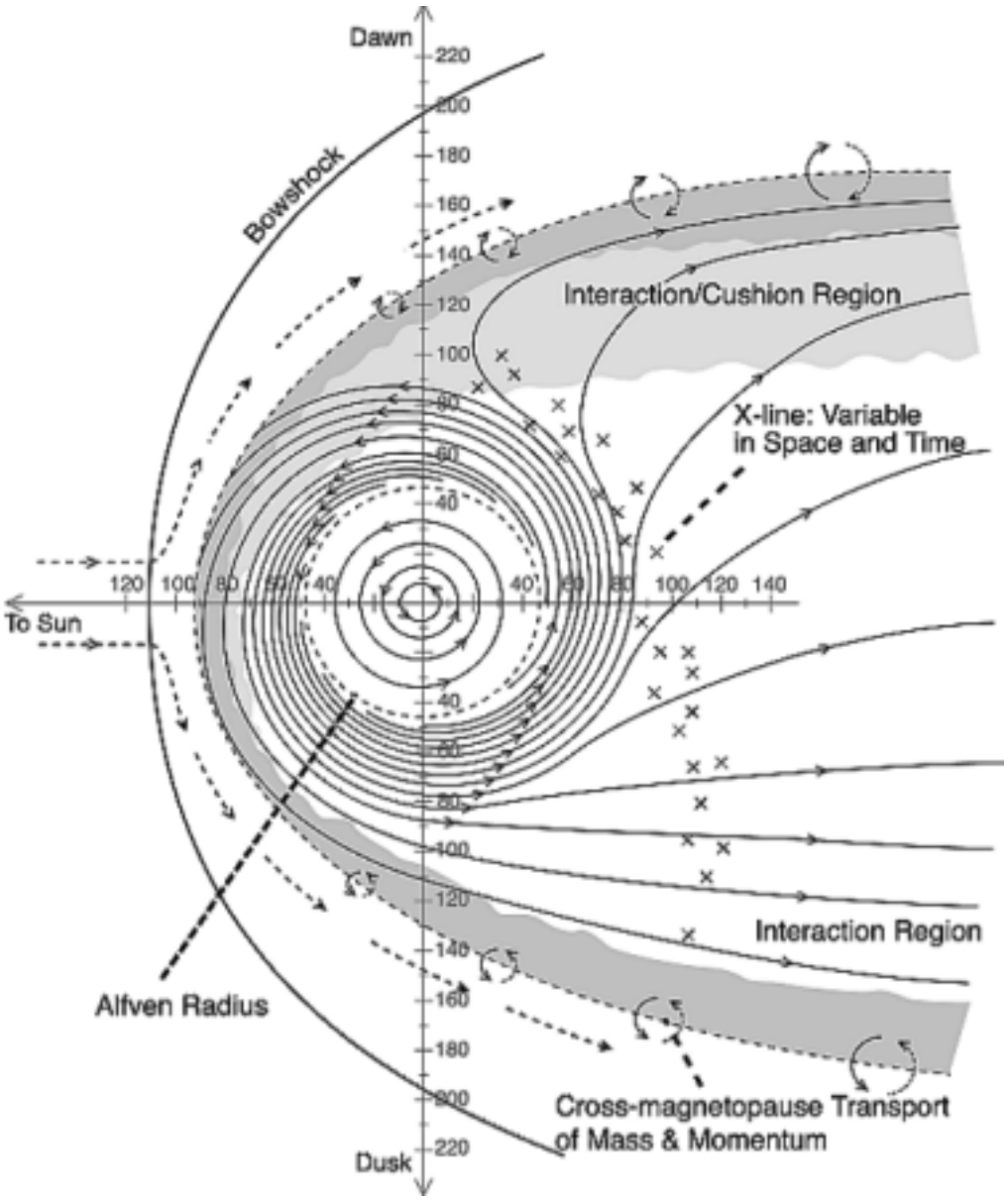

Figure 2.5: Diagram illustrating the flow of plasma in Jupiter's magnetosphere. Within $\sim 60\,\mathrm{R_J}$, the plasma is within the Alfv́en radius and is thus corotational. Beyond this point, plasma moves outward while gradually falling out of corotation, resulting in a spiral flow pattern. Eventually, at distances of $\sim 80\,\mathrm{R_J}$ to potentially as far as $200\,\mathrm{R_J}$, blobs of plasma detach along the X-line and are shed down the magnetotail. The 'x' symbols in the figure represent the position of the X-line. Credit: Delamere and Bagenal (2010).

2.3 Jupiter's Aurora

Jupiter exhibits the most powerful aurora in the solar system. Though typically outside the visible spectrum due to the atmospheric chemistry involved, the total emitted power of Jupiter's aurora is approximately 100 times greater than the Earth's, and its surface brightness can be up to 10 times higher (Clarke et al., 2004). This difference in scale arises from the spatial extent of the auroral region: power is defined as the total electromagnetic energy emitted per unit time, integrated over the entire emitting region and wavelength range of the aurora, whereas brightness refers to the local emission intensity per unit area and does not scale with the total size of the emitting region. The auroral power output is both extreme and highly variable, showing significant variability on timescales of seconds to hours driven by dynamic magnetospheric processes, where the total auroral power output can reach up to 10^{12} watts (Grodent, 2014).

Jupiter's aurora is generally divided into three categories of emission: the main emission, low-latitude emissions and the polar aurora (Clarke et al., 2004). Auroral emissions at Jupiter were first inferred in 1955 from radio observations at 13.6 metre wavelengths (Burke and Franklin, 1955; Franklin and Burke, 1956). Since then, emissions have been observed across a broad range of the electromagnetic spectrum - including emission from the ultraviolet (UV), with some X-ray, visible, and infrared (IR) parts of the spectrum (e.g. Clarke et al. (2004)).

2.3.1 Auroral Emission Wavelengths

2.3.1.1 Ultraviolet Emission

The ultraviolet aurora, which is the focus of this thesis, is well documented and has been observed by multiple spacecraft and telescopes. The majority of the UV emission corresponds to the main auroral emission, which is consistently active

compared to the high-latitude polar emissions, moon footprint emissions and other lower-latitude emissions. Figure 2.6 shows an example of the UV aurora in the northern hemisphere highlighting the variability in brightness between regions.

Jupiter's UV aurora is highly dynamic across all regions, with variations on timescales spanning from seconds to weeks. The auroral morphology is grouped into six families representing overall behaviour, defined as: quiet (Q), unsettled (U), narrow main emission (N), injection signatures with continuous main emission (i), strong injection signatures (I) and strong external perturbations (X). The overall emitted power is typically lower for the Q family and highest for the X family (Grodent et al., 2003a). These families are likely associated with specific magnetospheric responses to fluctuations in plasma density, plasma transport and magnetospheric dynamics. An example of this is plasma injections from the outer magnetosphere, which result in the breakdown of continuous emission across the main auroral region and observable enhancements in brightness in the low-latitude region (Grodent et al., 2018). Most of this variability is expected to be due to internal driving, such as changes in the mass loading from Io, although changes in solar wind dynamic pressure has been observed to affect the brightness and morphology of the main emission and dusk active polar region (Giles et al., 2025; Head et al., 2025; Nichols et al., 2009b; Yao et al., 2022). The full extent of the solar wind's role in generating and modulating UV emissions in Jupiter's aurora remains an open question.

Auroral chemistry plays a central role in generating UV auroral emissions. When energetic particles precipitate into Jupiter's upper atmosphere, they primarily interact with molecular Hydrogen (H_2), the dominant atmospheric molecule. These interactions include: raising electrons in H_2 molecules to higher energy states (excitation), the breaking of H_2 into atomic hydrogen (dissociation), and removing electrons to form ions (ionisation). The UV emissions arise primarily from the excited H_2 molecules returning to their ground state, observed in the H_2 Lyman and

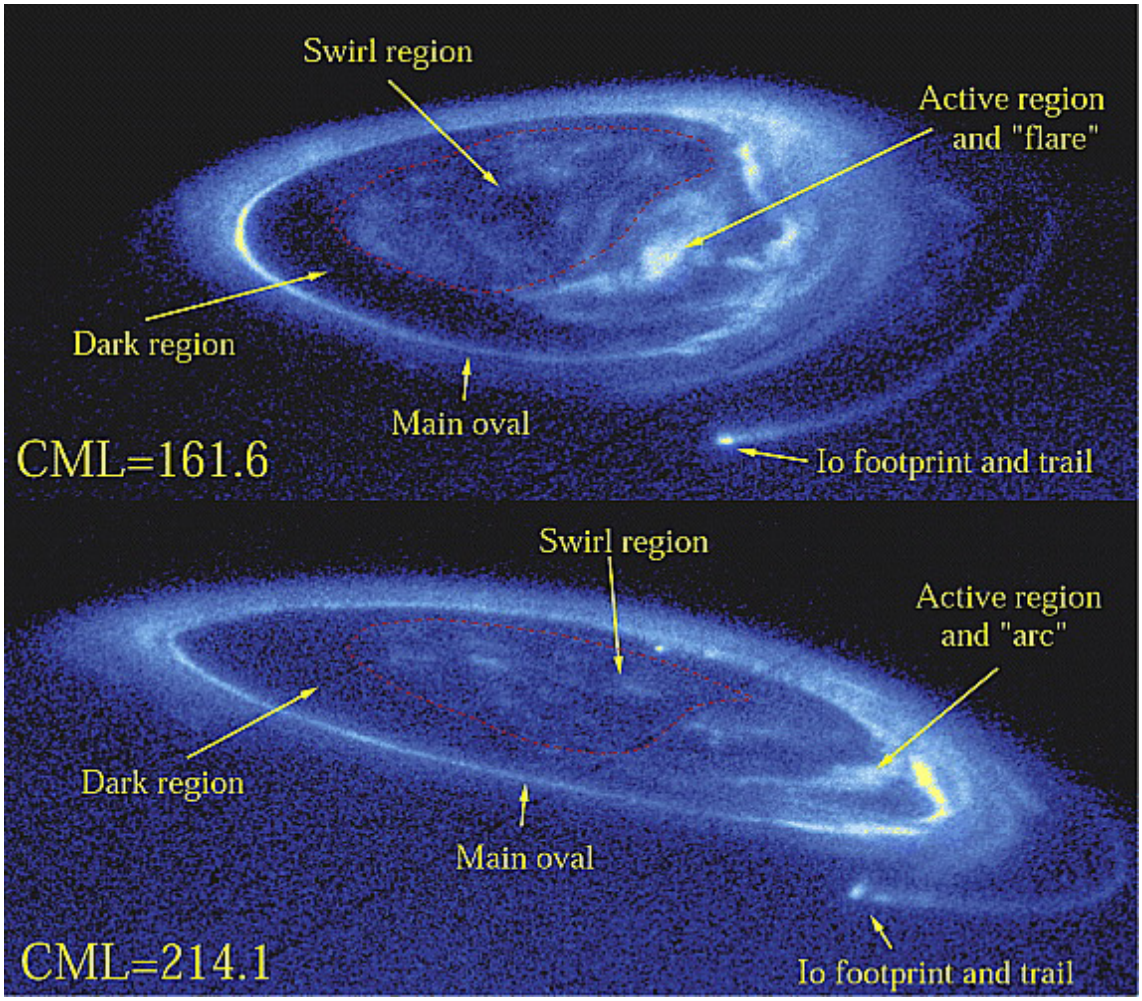

Figure 2.6: HST images taken on the 14th December 2000, illustrating the different auroral regions of Jupiter: the main emission (oval), dark (polar region), swirl region, active region (representing the noon and dusk active region) and the Io footprint (representing low-latitude emissions). The variability between the two images is typical of a 90 minute time period. Credit: Grodent et al. (2003b).

Werner bands. The excitation and emission occurs on nanosecond timescales, with the radiative lifetimes of excited H_2 molecules in the auroral atmosphere typically on the order of ~ 10 nanoseconds. Some dissociated H atoms can also emit in the Lyman α band as the return to ground state, with these emissions also occurring on nanosecond timescales, consistent with the radiative properties of atomic hydrogen (Clarke et al., 2004; Schunk and Nagy, 2000). The precipitating electrons range from 1-2 keV for Io's footprint aurora (Bonfond, 2010) to a few $150 - 600$s keV and $300 - 500$ keV for the main emission and polar regions, respectively (Benmahi et al., 2024).

Jupiter's ionosphere is composed primarily of H^+, He, H_2, and H_3^+. However, Helium plays a minimal role in the chemical processes involved in auroral emissions, as it is largely inert (Yelle and Miller, 2004). At lower altitudes, the main constituents of the Jovian atmosphere are H_2, He, and trace amounts of CH_4, NH_3, H, and other hydrocarbons (Strobel and Atreta, 1983). Hydrocarbons and H_2 significantly affect UV auroral emissions by absorbing UV photons. Hydrocarbons absorb UV below 130 nm, while H_2 absorbs below 120 nm. This absorption leads to an underestimation of the true emitted auroral power by instrumentation, and as such, observational data must be corrected for these absorption effects by accounting for absorption in the atmospheric layers above the emission regions in order to accurately estimate the actual auroral power (Gustin et al., 2012).

2.3.1.2 Other Wavelengths of Emission

X-ray emissions are observed in both the main auroral over and the polar regions and are linked to fluctuations in Jupiter's magnetic field (Yao et al., 2021). The northern polar region also hosts an X-ray hotspot, spatially coincident with UV emissions (Bunce et al., 2004; Gladstone et al., 2002). The X-rays associated with this hotspot are thought to be generated by electromagnetic ion cyclotron waves (EMICs) originating in the pre-dawn outer magnetosphere (Yao et al., 2021). This

will be discussed further in section 2.3.4.3.

Infrared auroral emissions arise from the H_3^+ ion in Jupiter's upper atmosphere. H_3^+ is produced through the ionisation of H_2 by either precipitating electrons and extreme ultraviolet (EUV) radiation, followed by a subsequent reaction with another H_2 molecule (Miller et al., 2000). As a strong radiator, H_3^+ acts as a heat sink, re-radiating thermal energy and serving as a key diagnostic for studying thermospheric cooling. Notably, the auroral regions are noted to also be asymmetric in their temperature distribution (Johnson et al., 2018).

Visible auroral emissions are substantially weaker than those in other spectral bands and occur due to the dissociative excitation of molecular hydrogen by energetic particles. These emissions were first imaged by the Galileo spacecraft in 1996, primarily in Jupiter's northern hemisphere (Ingersoll et al., 1998).

2.3.2 The Main Emission

The main emission at Jupiter represents half of the total power emitted by the aurora in the ultraviolet wavelengths with intensities of 500 – 3000 kiloRayleighs (kR) (Bonfond et al., 2015; Clarke et al., 2004). This emission is driven by the breakdown of plasma corotation in the middle magnetosphere, which generates upward field-aligned currents that are associated with accelerating electrons into the ionosphere. These electrons, typically with energies of several keV to tens of keV, collide with molecular hydrogen in the upper atmosphere, producing ultraviolet emission (Grodent, 2014). The resulting particle precipitation not only produces intense ultraviolet emissions but also heats and alters the upper atmosphere, driving thermospheric circulation and affecting ion chemistry such as the formation of H_3^+, which emits in the infrared (Miller et al., 2000).

While relatively stable in morphology, the main emission exhibits variability in intensity and fine structure, partly modulated by the solar wind dynamic pressure

(Giles et al., 2025; Nichols et al., 2009b; Yao et al., 2022). Despite being closely linked to the steady plasma supply from Io, it should be noted that the main emission is associated with electron precipitation only and not the heavy sulfur or oxygen (Clarke et al., 2004).

A distinct difference in auroral emissions exists between the northern and southern hemispheres. In the northern hemisphere, the main emission is distorted between $\sim 80^\circ$ and $\sim 150^\circ$ in System III longitude, an area called the northern magnetic anomaly (Grodent et al., 2008). At these longitudes, the main emission exhibits a distinct kidney bean shape, which appears more distinctly when the main emission is expanded rather than compressed. This expansion and compression is linked to both internal processes and the size of the magnetosphere, determined by the solar wind dynamic pressure (Head et al., 2024).

The main emission also contains multiple local time asymmetries, namely between the dawn and dusk sectors. Asymmetries in brightness and structure have been observed, with dusk often appearing broader and brighter, particularly in the southern hemisphere (Bonfond et al., 2015; Grodent et al., 2008). These differences may result from magnetic field geometry, varying field-aligned current densities, or localised enhancements, though the precise drivers remain uncertain (Lorch et al., 2020; Ray et al., 2014).

2.3.3 Low-Latitude Emissions

The low-latitude UV auroral emissions, also known as the equatorward emission, are among the least well-defined components of Jupiter's aurora. This category encompasses several distinct features, unified primarily by their location below the main auroral emission in latitude. Some of these features include: moon footprints, equatorial diffuse emission, the secondary oval and injection signatures.

The moon footprints are the most recognisable of the low-latitude emissions.

They appear as bright spots of emission equatorward of the main emission, often accompanied by a fainter trailing component. These footprints are associated with three Galilean moons: Io, Ganymede, and Europa, resulting from interactions between the moons and Jupiter's corotating plasma. These interactions generate Alfvén waves, which form structures called Alfvén wings that carry energy and currents between each moon and Jupiter's ionosphere (Bonfond et al., 2017). Io's footprint is brighter and more intense due to its dense plasma environment, which creates a stronger Alfvén wing (Gershman et al., 2019; Szalay et al., 2018). Callisto also produces a footprint emission but it overlaps with the main emission, making it difficult to distinguish (Bhattacharyya et al., 2018).

Other low-latitude emissions are even less well understood. The faint diffuse emissions appear across broad ranges of longitudes, most predominately in the dusk sector (Radioti et al., 2009). The secondary oval consists of arc fragments that appear parallel to the main emission, typically in the dawn and dusk sectors (Grodent et al., 2004). It has been observed to brighten as a result of large plasma injections and is not always present, with wave-particle interactions suggested as a generation mechanism (Gray et al., 2017). Finally, isolated compact auroral spots, often referred to as 'injection signatures' are believed to result from magnetospheric plasma injections (Mauk et al., 2002). Pitch-angle scattering has been suggested as a driving mechanism for these emissions (Dumont et al., 2018).

2.3.4 Polar Emissions

Jupiter's polar aurora remains one of the least understood components of the planet's overall auroral morphology. Located at the highest latitudes, this emission can be divided into four regions: the swirl region, noon active region, dusk active region and dark polar region. While the two active regions are often grouped together as a single 'active region' due to similarities in auroral behaviour, they differ subtly

in both morphology and dynamics (Greathouse et al., 2021; Nichols et al., 2017, 2009b). These regions are generally fixed in local time: the swirl region extends from dawn to midnight at the highest latitudes, while the the dark polar region, noon active region, and dusk active regions form a band of emission sometimes referred to as the 'polar collar', which sits poleward of the main auroral emission (Greathouse et al., 2021).

Despite ongoing observational efforts, the physical drivers and variability in auroral behaviour of Jupiter's polar regions remain open questions. Multiple studies have suggested that some of the auroral emission observed is related to solar wind interaction, specifically at the dayside boundary between open and closed field lines (Grodent et al., 2003b; Pallier and Prangé, 2001; Waite et al., 2001). However, there is no consensus on the magnetospheric mapping of each region, and the full extent of solar wind influence on the polar regions is still unclear. At present, only changes in solar wind dynamic pressure have been linked to variability in auroral emission brightness and morphology in the dusk active region (Head et al., 2025; Nichols et al., 2017).

2.3.4.1 The Dark Polar Region

Located in the high-latitude dawn sector, the dark polar region is the quietest polar region. It is almost devoid of UV aurora emissions and X-ray emission (Dunn et al., 2017). It is also shown to vary in both size and shape in response to solar wind dynamic pressure, extending duskward across the noon sector during periods of deep rarefaction and appearing larger in width near local noon under periods of compression (Swithenbank-Harris et al., 2019). The dark polar region has been suggested to map to mostly open flux due to the mostly absent auroral emission (Cowley et al., 2003; Delamere and Bagenal, 2010), and magnetic flux mapping proposes that the region maps to the magnetotail alongside the swirl region (Vogt et al., 2011). However, more recently work has shown that the dark polar region

cannot account for all open flux equated to the magnetotail, suggesting that Jupiter's magnetotail does not contain only open field lines (Swithenbank-Harris et al., 2019). Conversely, MHD modelling predicts that the dark polar region maps to mostly open field lines that are not part of the magnetotail, and that additional open flux exists in the polar regions outside of the dark polar region (Xu et al., 2024; Zhang et al., 2021). As such, the magnetic topology of the dark polar region remains an open question.

2.3.4.2 The Swirl Region

The swirl region is the region of the polar emissions situated at the highest latitudes and is characterised by faint, patchy, and short lived emission features. This emission is generally of the order ~ 10 kR, but can reach a few 100 kR in power (Nichols et al., 2009b). These features are turbulent, and occasionally form localised clockwise swirls (Grodent et al., 2003b). It is highly variable on short timescales (seconds) but stable over moderate timescales of $10 - 100$ minutes (Stallard et al., 2016). Past observations have also suggested the presence of arc-like features in this region (Nichols et al., 2009a; Pallier and Prangé, 2001), which contrasts with the otherwise transient nature of emission in the swirl region. The swirl region has also been observed to be brighter closer to the dayside (Greathouse et al., 2021).

Historically, the swirl region was associated with the dark polar region as both regions are much quieter in terms of UV emission than the active regions (Stallard et al., 2003), but recent studies have suggested that the two regions are distinct from one another (Grodent et al., 2003b). One of these distinctions is the colour ratio, which is often used as diagnostic of precipitating electron energies. The colour ratio is defined as the ratio of the radiance at 155–162 nm to the radiance at 125–130 nm, with higher values indicating higher energy electrons (e.g. Greathouse et al., 2021). The main emission, both active regions and the dark polar region all share similar colour ratios of ≤ 4 (commonly assumed as 2.5), but the swirl region has

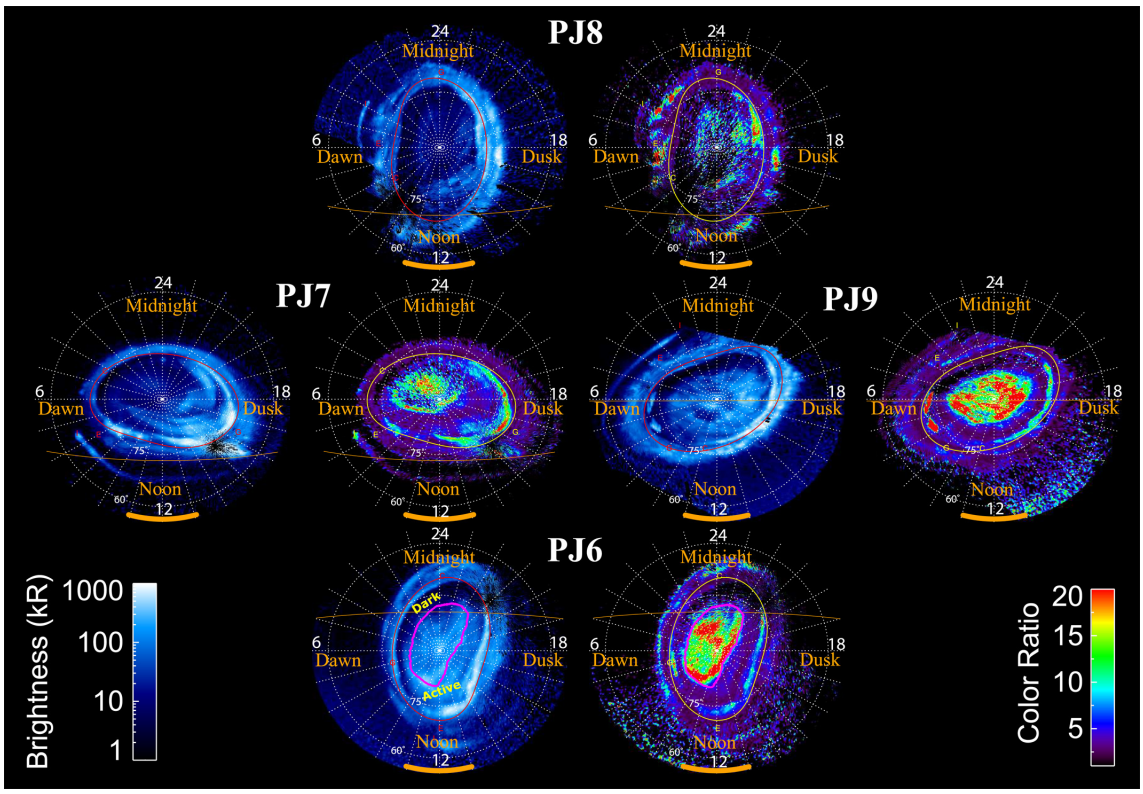

Figure 2.7: Maps of northern auroral images taken by Juno's UVS instrument. Two images correspond to each of the four labelled perijove passes: the left image shows the auroral morphology and brightness, while the right image shows the colour ratios associated with the observed emission. Credit: Greathouse et al. (2021).

a much higher colour ratio of $\geq$ 12. As shown in figure 2.7, this colour ratio is highly variable compared to the other areas of auroral emission, reaching up to 20. As such, the physical phenomena responsible for producing emissions in the swirl region must be different to the other regions. Higher energy electrons, which would travel deeper into Jupiter's atmosphere and excite H_2 at greater depths, are proposed to suggest this difference. However, Juno has only rarely observed high-energy downward propagating electrons over the swirl region. A different CH_4 vertical profile is also suggested, but has the same caveat. The final suggestion given is photoionisation of hydrocarbons (Greathouse et al., 2021).

The literature on the swirl region commonly indicates that the swirl region maps to open field lines. Magnetic flux mapping indicates the swirl region maps to an area of mostly open flux, as shown in figure 2.8, that form a nightside lobe and polar cap region (Vogt et al., 2011) - others argue that the existence of polar arcs and stagnant ionospheric flows (Pallier and Prangé, 2001; Stallard et al., 2001; Stallard et al., 2003) is evidence of the swirl region mapping to open flux. On this basis, the swirl region is often proposed as the polar region most likely to be directly influenced by the solar wind.

Cowley et al. (2003) argues that the open field lines associated with the swirl region are a result of a Dungey cycle process (see section 1.4.1 in Chapter 1) confined to the dawn side of the magnetosphere, displaced by the asymmetry imposed by the Vasyliunas cycle (see section 2.2.2.4). In this scenario, which is shown in figure 2.9, the swirl region emissions correspond to flux closure on the nightside. The opening of flux is suggested to occur on dayside boundary via magnetic reconnection along an X-line under northward directed IMF conditions. Due to the enormous size of Jupiter's magnetosphere, the timescales of any Dungey-like large-scale reconnection process would be on the order of days, as field lines opened on the dayside would need to be carried by the flow of the solar wind around to the tail region to close. The dawnside confinement and Jupiter's rapid rotation make the timescales even more

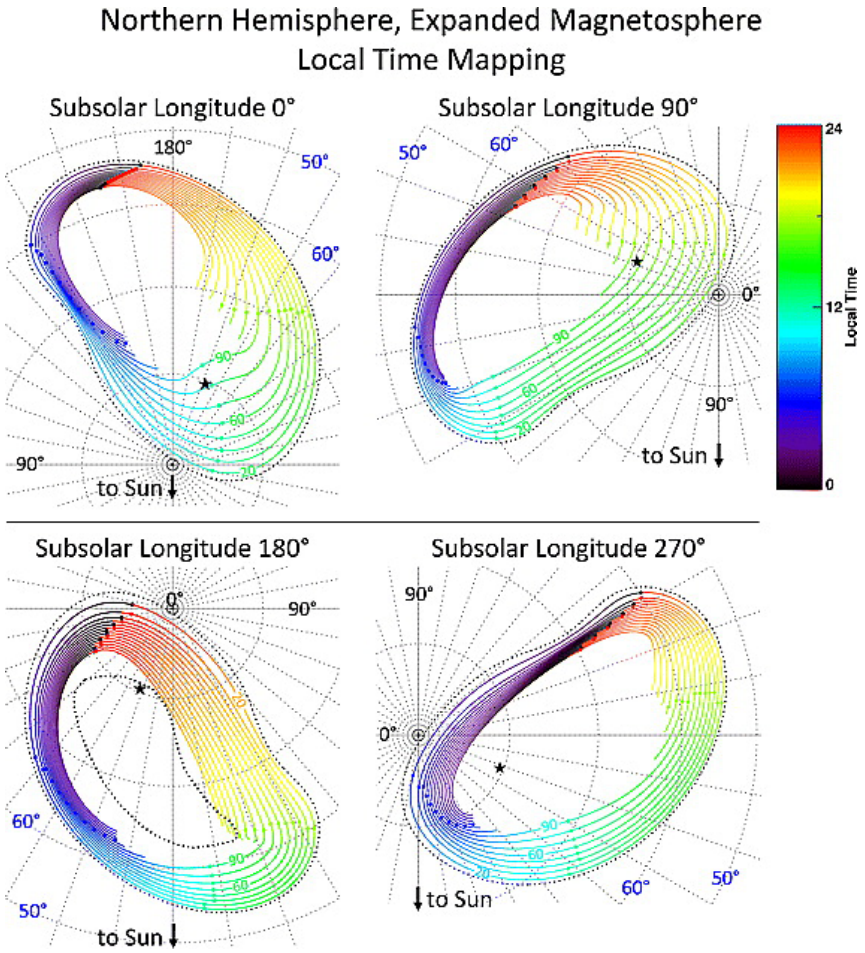

Figure 2.8: Polar view of flux mapping results for the northern hemisphere under expanded magnetospheric conditions where the dayside magnetopause standoff distance is ~ 90 R_J. The outer dashed black line is the 15 R_J reference contour, which matches the Ganymede footprint, and the inner dashed black line is the bottom left panel is the location of the swirl region taken from Stallard et al., 2003. The black stars indicate the location of the magnetic pole. Colours indicate the equatorial local time mapping along the contour, where the small circles indicate the point closest to: local midnight (red/black), dawn (dark blue), noon (blue/green) and dusk (light green/yellow). Contours are also labelled with the distance they map out to in R_J, with each line representing increments of 10 R_J. The swirl region is shown to map to an area of open flux, while the dusk active regions map to the outer magnetosphere in their respective local time sector. Credit: Vogt et al. (2011).

uncertain, as the field lines will likely be dragged through the dusk and midnight sectors before they can reconnect on the dawnside.

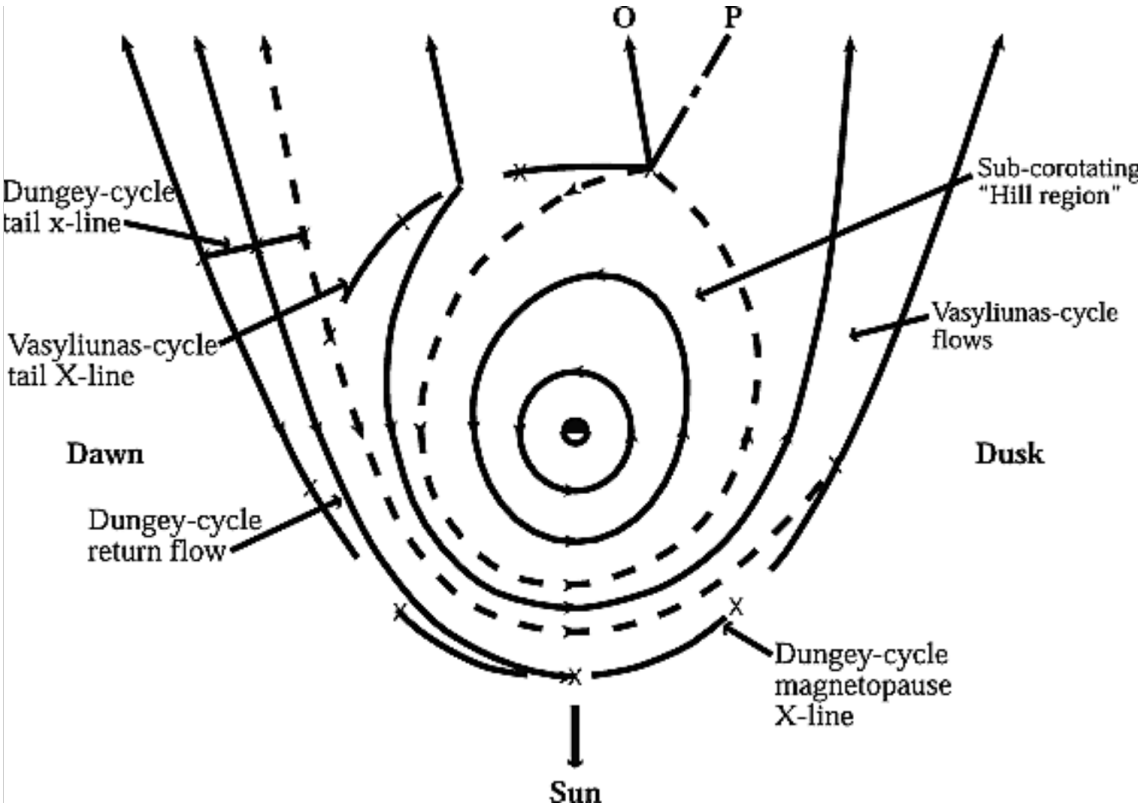

Figure 2.9: Sketch of the proposed three components of flow in the Jovian system: the sub-corotating region, Vasyliunas flows and Dungey cycle flows. Here the 'O' and 'P' markings represent plasma streamlines and plasmoids, respectively. This Dungey cycle flow is initiated by magnetic reconnection with the interplanetary magnetic field and is suggested to be responsible for auroral emission in the swirl region. Credit: Cowley et al. (2003).

Challenging these interpretations, MHD modelling suggests that the swirl region maps to a loop of mostly closed field lines extending outward on the dawn side of the planet (Zhang et al., 2021), as shown in figure 2.10. This model implies an internally driven source for swirl region emission. Supporting this, upward electron beams have been observed by Juno in regions of faint structured aurora, likely corresponding to the swirl region (Allegrini et al., 2017; Ebert et al., 2017). These observations are

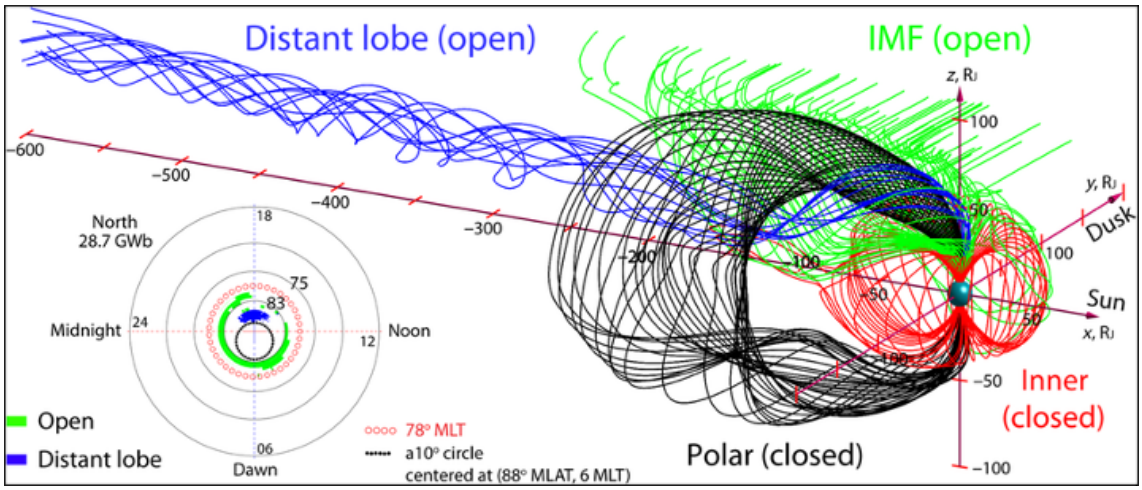

Figure 2.10: The two-day average topology of simulated Jovian magnetic field lines traced from four different sets of footprints at a low-latitude simulation boundary in the northern hemisphere: the green open field lines are connected to the interplanetary magnetic field and are mostly under solar wind control; the blue field lines map to the distant tail beyond 600 R_J; the the red closed field lines map outward to 35 - 40 R_J in the middle magnetosphere and return to the southern boundary; the black field lines emerging from Jupiter's polar region connect the two polar regions through the dawnside outer magnetosphere. Although only the black field lines are attributed to the polar region, the green and blue field lines map to areas associated with polar aurora. Credit: Zhang et al. (2021).

interpreted as signatures of downward field-aligned currents on closed or twisted field lines and implies that the swirl region maps, at least partially, to closed field lines. However, the energies associated with these downward currents appear to be weak, whereas the high colour ratio of the Swirl Region's emission implies a population of more energetic precipitating electrons (Greathouse et al., 2021). Considering all of this, the magnetic mapping and source of auroral emissions in the swirl region remains an active area of research.

2.3.4.3 The Noon Active Region

The noon active region is part of the polar collar, a ring of auroral emission between the swirl region and Jupiter's main auroral emission (Greathouse et al., 2021). It is named for the local time sector it occupies and is characterised by bright, transient flares of UV emission (Grodent et al., 2003b). These flares can increase rapidly in brightness from a few kR to over $\sim$ 10 MR within a few minutes (Waite et al., 2001). Although it is often grouped with the dusk active region under the broader category of the 'active region', the noon active region has been shown to display some distinct morphological and dynamic behaviour. In particular, the noon active region emission has been observed to be typically more patchy and less regularly pulsed than those observed in the dusk sector (Nichols et al., 2017).

Nichols et al. (2017) also observed that under high solar wind dynamic pressure, the noon active region can appear as a noonward extension of the dusk active region. However, this morphology is not consistently maintained over the full duration of such high-pressure intervals. Across both compressions and rarefactions of the magnetopause boundary location, the region generally exhibits unstructured morphology, consisting of multiple transient spots and occasional poleward arcs. Despite the apparent continuation of dusk-side morphology into the noon active region during intervals of high solar wind dynamic pressure, no associated increase in auroral power was observed.

The x-ray hotspot discussed in section 2.3 is located specifically within the noon active region. This feature is exclusive to the northern hemisphere (Gladstone et al., 2002) and is spatially coincident with UV auroral emission (Bunce et al., 2004). Although the noon active region is generally assumed to be internally driven, particle acceleration associated with field-aligned currents linked to the corotation enforcement current system cannot alone account for the high power observed in both UV and X-ray wavelengths (Bunce et al., 2004; Yao et al., 2021). Consequently, additional acceleration mechanisms have been proposed, with pulsed reconnection at the dayside magnetopause considered a likely driver (Bunce et al., 2004).

However, magnetic field mapping (see figure 2.8) predicts that the noon active region connects to field lines that extend outwards to the dayside outer magnetosphere near local noon (Vogt et al., 2011), a region where dayside reconnection is expected to be suppressed due to high shear flows and high plasma $\Delta\beta$ across the magnetopause boundary (Desroche et al., 2012). In contrast, figure 2.10 shows that MHD modelling suggests parts of the region may instead be associated with open magnetic flux broadly distributed across the nightside of the planet (Zhang et al., 2021). The majority of the noon active region is attributed to closed field lines mapping to the dawn - midnight equatorial magnetosphere, with auroral activity attributed to tail dynamics. Recent work to locate Jupiter's cusp has also suggested some open flux may be associated with the noon active region (Xu et al., 2024).

2.3.4.4 The Dusk Active Region

The distinction between the noon and dusk active regions is not clearly defined in the literature, but differences across local time within the active region have been observed. Although the dusk active region also exhibits transient flares of UV emission, it also tends to display more organised and structured auroral arcs than the noon active region (Greathouse et al., 2021), an example of which is shown in figure 2.11. A unique feature of the dusk active region is 'auroral bridges', which are

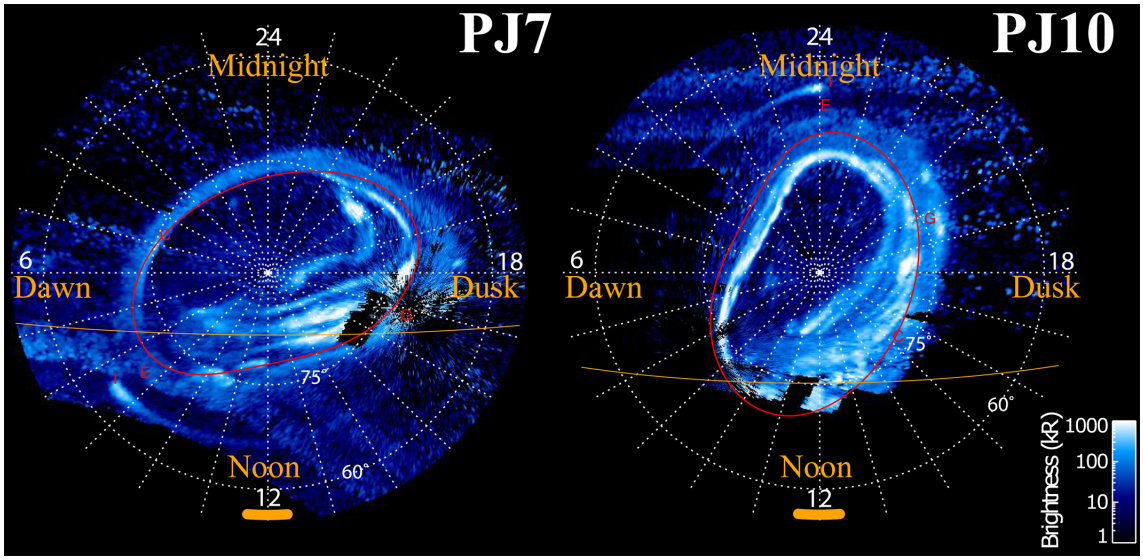

Figure 2.11: UV brightness maps for observations of 15.5 minutes by Juno's UVS instrument for perijoves 7 and 10. Concentric arcs on the dusk side of the polar collar are clearly displayed in both images, indicating that the arcs are a function of local time rather than System III longitude. Credit: Greathouse et al. (2021).

extended arcs of emissions appearing to connect the dusk active region to the main emission. These bridges are relatively common, forming on timescales of $\sim$ 2 hours and lasting potentially for a full planetary rotation, and are associated with solar wind compressions of the magnetosphere (Head et al., 2025). The flares and arcs in the dusk active region typically range from $\sim$ 10 to 100 kR in brightness, showing less extreme variability on short timescale than the noon active region (Greathouse et al., 2021).

In addition, Nichols et al. (2017) observed that the dusk active region shows an increase in auroral power in response to elevated solar wind dynamic pressure, suggesting some potential coupling with the solar wind. Bright strongly pulsed emissions, often in the form of arcs parallel to the main emission, are especially prominent during periods of high pressure, ranging from $\sim$ 3 - 11 minutes in duration. A positive correlation with solar wind magnetic field strength is also reported.

In terms of where the dusk active region is expected to map within Jupiter's magnetosphere, magnetic mapping has associated the region with the closed field lines in the outer dusk magnetosphere (Vogt et al., 2011), as indicated in figure 2.8. However, MHD modelling suggests the region may coincide with the crescent-shaped patch of open magnetic flux (Zhang et al., 2021) in figure 2.10. This patch is highly variable in terms of open flux content and is not always present, suggesting the dusk active region maps to a combination of open and closed field lines (Delamere et al., 2024).

2.4 Summary

The theory discussed in this chapter explores the interconnected processes governing Jupiter's magnetospheric dynamics and auroral activity, focusing on three key aspects: the solar wind, Jupiter's magnetosphere and Jupiter's auroral emissions. Although the full extent of the solar wind's influence on Jupiter is currently unclear, understanding the potential mechanisms through which the solar wind may interact with Jupiter's magnetosphere is crucial for further exploration.

The chapter begins by describing the solar wind and the associated interplanetary magnetic field, outlining the mechanisms by which they could interact with Jupiter's magnetosphere, such as through magnetic reconnection or viscous processes like the Kelvin-Helmholtz instability. The second section explores Jupiter's magnetosphere, detailing its structure and the complex internal plasma dynamics driven by Io and its plasma torus, and how this material is transported throughout the magnetosphere. These internal dynamics are associated with Jupiter's auroral emissions, and so the final section of the chapter examines the different auroral regions, highlighting their distinct morphologies and behaviours to demonstrate how current research cannot yet fully explain the driving processes behind the variability in these emissions.

Chapter 3

Data Processing for Solar Wind and Auroral Studies

This section details the instrumentation and methodology used to obtain the data and process it into an appropriate format for Chapters 4 and 5. Both studies involve comparing solar wind data to auroral power in the polar region of Jupiter's northern aurora and so it is appropriate to combine much of the methodology here to avoid repetition.

3.1 Instrumentation

This study utilises data from two primary sources, the Hubble Space Telescope (HST) and the Juno Spacecraft. All of this data is from the year 2016, during the final approach of Juno to Jupiter.

3.1.1 Juno

Juno is a NASA spacecraft, launched in August 2011, that has orbited Jupiter since July 2016. It is the second spacecraft to orbit Jupiter, with the first being the Galileo orbiter (1995 - 2003). Juno is designed to study Jupiter's atmosphere, moons, origin and evolution. Instrumentation aboard Juno includes a magnetometer (MAG), a UV imaging spectrograph (UVS), a microwave radiometer, an auroral mapper (JIRAM), a radio and plasma waves experiment (Waves), a gravity experiment, a visible light camera (JunoCam) and two particle detectors (JADE and JEDI); both particle detectors take in situ measurements of electrons and ions, but JEDI is designed for measuring higher energy particles and JADE for lower energy particles (McComas et al., 2013). The instruments of interest for this study are MAG and JADE.

Although the spacecraft arrived at Jupiter on 5th July 2016, JADE was turned on 7 weeks prior to measure upstream solar wind conditions (Wilson et al., 2018). This time period also coincides with multiple HST observations of Jupiter's aurora. The MAG instrument was turned on for the majority of the cruise phase and thus also has data available for this time (Connerney et al., 2017).

3.1.1.1 Juno MAG

The MAG instrument consists of two magnetometer suites, each consisting of a tri-axial fluxgate magnetometer (FGM) and a pair of co-located imaging sensors which form the advanced stellar compass (ASC), designed to provide accurate information on the spacecraft pointing direction. The fluxgate magnetometer contains an alloy core with high magnetic susceptibility and two coils: the drive winding coil and sense winding coil. The magnetometer operates by passing an alternating current through the drive coil, repeatedly magnetising and then demagnetising the core, inducing a current in the sense coil from which the 'interfering' magnetic field strength is derived. The magnetometers are capable of measuring up to 1.6×10^6

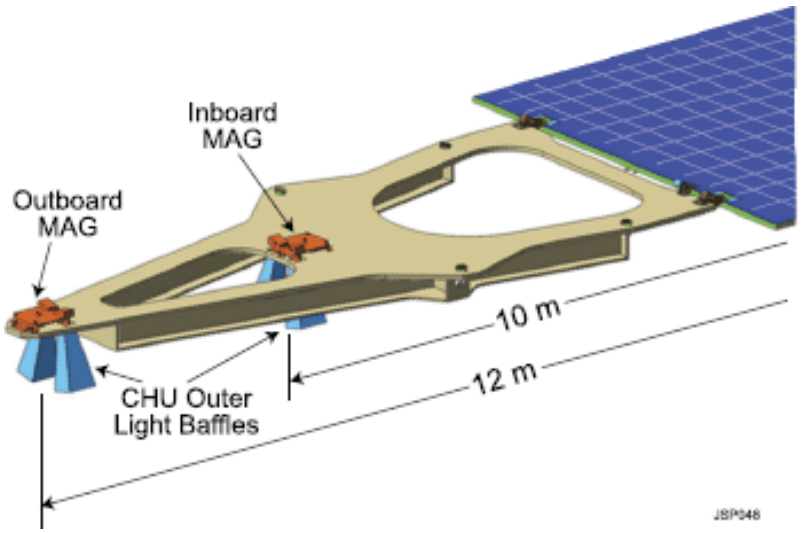

Figure 3.1: Diagram of the MAG instrumentation on the Juno spacecraft. Image credit: Connerney et al. (2017).

nT per magnetic field axis and have a resolution of $\sim$ 0.05 nT. Unlike the other instruments aboard Juno, the MAG instrument is not located on the main body of the spacecraft but is mounted along a dedicated boom attached to one of Juno's three large solar panels to remove the influence of spacecraft generated magnetic fields on the measurements (Connerney et al., 2017). A diagram of the instrument can be seen in figure 3.1.

MAG instrument data is taken from the Jupiter Data Archive on the Planetary Data System (PDS). The spacecraft-solar equator (SE) dataset chosen contains 60 second resolution data in radial tangential normal (RTN) coordinates (B_r, B_t and B_n), centred on the spacecraft. It is defined by the Sun-spacecraft vector: where R points away from sun, T is representative of the cross product Sun's spin vector and the R axis, and then N completes the system (see panel a of figure 3.2) (Bagenel and Wilson, 2016, Connerney et al., 2017).

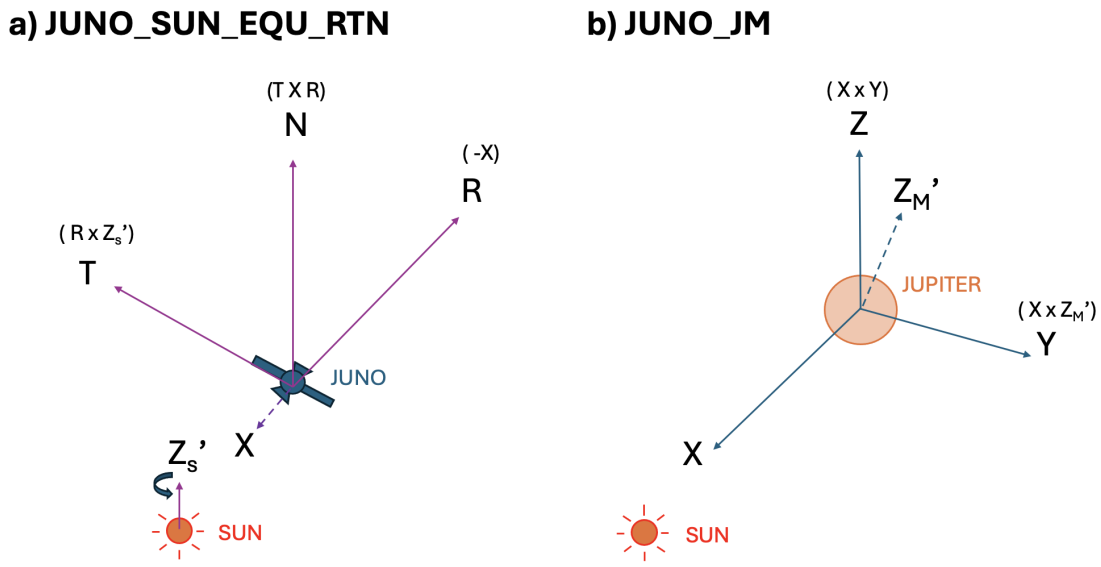

Figure 3.2: SPICE (Spacecraft, Planet, Instrument, C-matrix, Events) Toolkit coordinate frames. On the left (a) is JUNO_SUN_EQU_RTN, the coordinate frame of Juno's MAG data. In this frame, x is the Sun-spacecraft line, y is the cross product of x and the Sun's spin axis and z the cross product of x and y. On the right (b) is JUNO_JM, a coordinate frame designed for this study, where x is the Jupiter-Sun line, y is the cross product of x and Jupiter's magnetic axis and z is the cross product of x and y.

3.1.1.2 JADE

The Jovian Auroral Distributions Experiment (JADE) is designed for auroral measurements at Jupiter. JADE consists of three electron sensors (JADE-Es) and an ion composition sensor (JADE-I). The range of the ion sensor is 0.01-46.2 keV and 0.1-95 keV for the electron sensors. The three electron sensors are arranged 120° apart to provide detailed pitch-angle distributions independent of spacecraft spin phase. The ion sensor has an instantaneous field of view of $270° \times 90°$ and also provides ion composition measurements, with a range of 1 to 50 amu (atomic mass units) with an uncertainty of $\sim$ 2.5 amu. (McComas et al., 2013). It records 64 steps in energy by 78 look directions whilst in a low-rate mode, taking 30, 60, 300

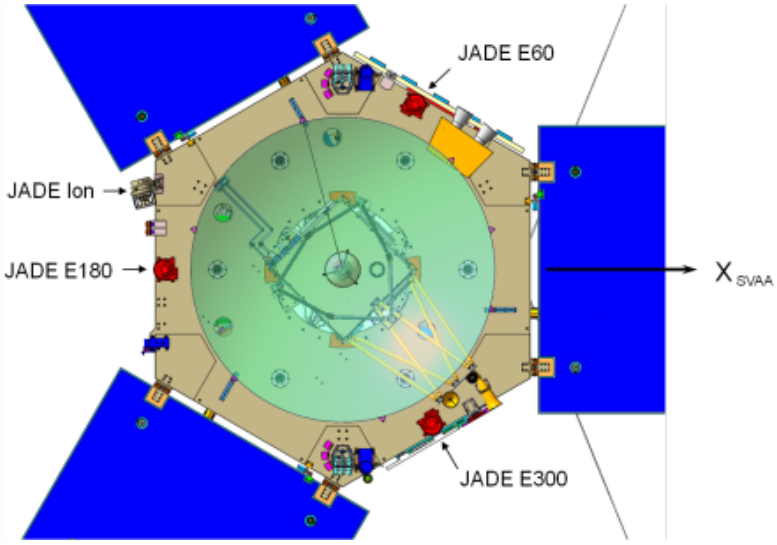

Figure 3.3: Diagram of the JADE instrumentation on the Juno spacecraft. Image credit: McComas et al. (2013).

or 600 seconds and 64 energy steps over 12 look directions in 2 seconds whilst in high-rate mode (Wilson et al., 2018). A diagram of JADE can be seen in figure 3.3.

JADE-I does not directly provide measurements of ion density, temperature or velocity. JADE-I is an electrostatic analyser (ESA), which measures the mass per charge and angular distribution of ions. It operates by varying the voltage between two metal plates, allowing only ions of specific mass per charge ratios to pass through and reach the detector, where they are registered as 'counts'. From these count rates, ion fluxes can be determined, which then can be processed to obtain various ion parameters such as velocity. The plasma data used in this study is a parameter set for the approach phase derived from counts by Wilson et al. (2018). The ion sensor data is in a low-rate mode and is 30 second averaged.

3.1.2 Hubble Space Telescope

The Hubble Space Telescope (HST) was launched in April 1990 into low Earth orbit for astronomers to observe space without the disruption of the Earth's atmosphere.

Designed to be a multi-purpose observatory, it has undergone 4 servicing missions in 1993 (1), 1997 (2), 1999 (3a) 2002 (3b) and 2009 (4) in which it has been upgraded and repaired. This includes the addition and/or replacement of instruments. The current instrumentation onboard HST is the Advanced Camera for Surveys (ACS), Cosmic Origins Spectrograph (COS), Space Telescope Imaging Spectrograph (STIS), Wide Field Camera 3 (WFC3), fine Guidance Sensor (FGS) and Near Infrared Camera and Multi-Object Spectrometer (NICMOS).

The instrument of interest for this work is STIS. STIS was installed in 1997 during servicing mission 2 and later repaired during servicing mission 4. It has three detectors, a Charged Coupled Device (CCD) for optical and near infra-red light and two Multi-Anode Microchannel Array (MAMA) photon counting detectors for near-ultraviolet and far-ultraviolet light (FUV), respectively. All three detectors are 1024 x 1024 pixels. The CCD has a 50 x 50 arcsecond field of view, whilst the MAMA detectors have a field of view of 25 x 25 arcseconds. The primary function of STIS is spectrography, but it is capable of imaging using its limited set of filters.

The HST observations used in this study are taken over the interval of May to July 2016 using the FUV MAMA detector. All observations use the F25SRF2 filter, which allows the detector to operate between $1250 - 1900$Å avoiding most of the H Lyman α emission while allowing the H_2 Lyman and Werner emission bands. The observations occur across three day of year (DOY) periods: 137-159, 174-182 and 193-200 (Nichols et al., 2017). The final group of observations is excluded as Juno is already within Jupiter's magnetosphere during that period. This results in 32 available observations. These observations henceforth will be known as 'visits'. Juno is also noted to encounter Jupiter's bow shock on 25th June 2016 (DOY 177), so visits on DOY 177 and beyond are dismissed. This reduces the appropriate visit count to 29 visits. Finally, the two remaining southern hemisphere visits are discarded as Jupiter's northern and southern polar emissions are asymmetric, and so the visits cannot be directly compared (Gérard et al., 2013, Grodent et al.,

2018). The two southern visits are not used as a second dataset as two visits is insufficient data to draw any conclusions. This reduced the available data to 27 northern hemisphere visits, which represent System III longitudes with a Central Meridian Longitude (CML) ranging from $\sim 90°$ to $\sim 250°$, almost half of the full planetary longitude. Each visit consists of 26 images with 100 second integration times, corresponding to $\sim$40 minutes of auroral observations.

The HST data is not in a raw image format, but in units of auroral brightness (kiloRayleighs, 1kR = 10^9 photons per second from 1 cm^2 column of atmosphere radiated into 4π steradians) with an total integration time of 100 seconds between images. These files are created using the Boston University pipeline (Clarke et al., 2009 (Appendix A), Nichols et al., 2009b). The pipeline takes the raw counts of photons hitting the detector and converts into values of auroral brightness whilst making a number of corrections to make sure the resulting intensity is appropriate. These corrections involve: dark count subtraction, flat field response correction, interpolation of values to correct for bad pixels on the detector, distortion correction and rotation to have the planetary northwards direction facing up. The planet centre in pixel space is also determined (Clarke et al., 2009). This process generates a fits file, where the auroral intensities from the brightness are stored within the file alongside several pieces of key information such as the CML, moon footprint locations, time of image, distance of observation from HST and declination angle. This is all done prior to when the dataset was obtained.

3.2 Methodology

3.2.1 Processing and Organising the Solar Wind Data

3.2.1.1 Combining Solar Wind Datasets

The JADE-I data contains solar wind data with an accumulation time of 30 seconds. The IMF data from the MAG instrument is interpolated to gain 30 second averaged data so that both datasets are of the same resolution. The dataframes are spliced together using the detection time of the instruments as a shared variable to avoid any mismatch in the data. A tolerance of 30 seconds is used to account for a slight offset in the timestamps, as the JADE-I and MAG instruments record measurements independently and therefore their timestamps do not perfectly align. This approach also accommodates two additional issues: the plasma data contains an extended section in which the data accumulation time increased from 30 seconds to 60 seconds and then to 600 seconds, and the MAG data has gaps in the data at random intervals. With this splicing method the majority of data is retained.

3.2.2 Propagating the Solar Wind to Jupiter

The next consideration is how to equate the solar wind data to the HST images of Jupiter's aurora. The solar wind MAG and plasma data needs to be propagated from Juno's position to Jupiter's ionosphere, where any interaction signatures may be visible as aurora. For this, the methodology of Nichols et al. (2007) is followed. This is divided into three sections: travel time to the bow shock, travel time through the magnetosheath and travel time from the magnetopause to ionosphere. In order to calculate the travel time to the bow shock, the distance from Juno to Jupiter is needed. The SPICE (Spacecraft, Planet, Instrument, C-matrix, Events) Toolkit (Acton, 1996, Acton et al., 2018) is used to determine Juno's location relative to

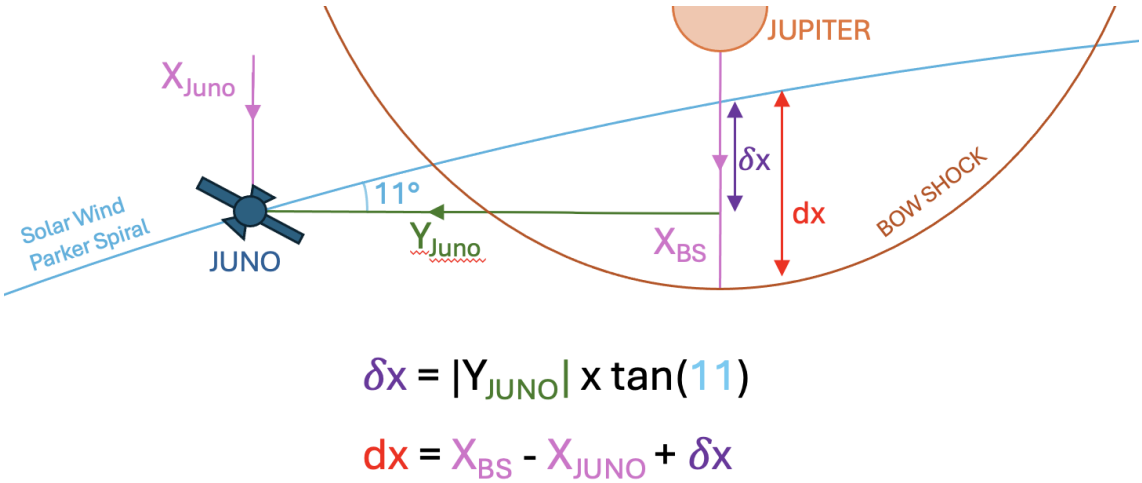

Figure 3.4: Diagram of how the distance shift of the solar wind from Juno to the nose of the bow shock is determined.

Jupiter through the SpiceyPy wrapper for python (Annex et al., 2020). SPICE contains multiple types of ancillary data files, known as kernels. Within these kernels is location, size and orientation information for various planetary bodies and spacecraft as well as defined coordinate systems. The SpiceyPy wrapper contains functions to access this information and perform calculations using this data, such as calculating a distance vector between two objects. Juno's location indicates that the spacecraft is approaching from the dawnside of Jupiter, where the first data point is located at approximately 40 R_J in x and -417 R_J in y away from Jupiter.

To follow the intended methodology, the solar wind needs to be shifted back to the nose of the bow shock. The Joy model (Joy et al., 2002) is used to predict the location of the bow shock and magnetopause using a pre-determined set of coefficients and the solar wind dynamic pressure, and the calculated stand-off distances for both of these boundaries can be seen in figure 3.5. Assuming a parcel of solar wind plasma is frozen into the IMF, which follows the Parker spiral, the distance shift the solar wind will undergo along the x axis before it reaches a point perpendicular to the nose of the bow shock and in-line with the spacecraft can be determined by:

$$\delta_x = |Y_{JUNO}| \times \tan(11^\circ) \tag{3.1}$$

where $|Y_{JUNO}|$ is the absolute value of the separation between Jupiter and Juno in the y-axis, and 11° is the mean Parker spiral angle measured from the y-axis (Nichols et al., 2007). Using this, the total distance shift in the x-axis between Juno and the nose of the bow shock can then be calculated:

$$d_x = X_{BS} - X_{JUNO} + \delta_x \tag{3.2}$$

where X_{BS} and X_{JUNO} are the distance of the bow shock and Juno from Jupiter in the x-direction (+ve pointing toward the Sun). This distance is then divided by the solar wind velocity to obtain the solar wind travel time to the bow shock, T_{shift}. A visualisation of this distance shift can be seen in figure 3.4.

Secondly, the solar wind is propagated from the bow shock to the magnetopause, where the bow shock rapidly decelerates the solar wind. If the magnetosonic Mach number of Jupiter's bow shock is taken as ~ 10 (Slavin et al., 1985), the velocity just downstream of the shock can be taken as $0.26v_{sw}$, where v_{sw} is the solar wind velocity detected by Juno. If a linear decrease is assumed between just downstream of the bow shock and the magnetopause boundary, the travel time to traverse the magnetosheath can be derived from the change in velocity over distance The resulting formulation is as follows (Khan and Cowley, 1999).

$$t = \frac{R_{bs} - R_{mp}}{v_{bs} - v_{mp}} \ln\left(\frac{v_{bs}}{v_{mp}}\right) \tag{3.3}$$

this gives the sheath transit time, T_{sheath}.

Finally, for the time taken to travel from the magnetopause to the ionosphere, the Cowley and Bunce (2003) estimate is used, which represents the one-way Alfvén travel time along the outer magnetospheric field lines ($\frac{1}{4}$ of an eigenmode period):

$$T_{iono} = 26 \times \left(\frac{R_{mp}}{20}\right)^{2.7} \tag{3.4}$$

where R_{mp} is the location of the magnetopause in Jupiter radii. It should be noted as this travel time is determined from the low-latitude magnetopause nose location; reconnection at higher latitudes will reduce or increase the travel time, depending on

if the reconnection occurs in the same hemisphere that the aurora is being observed in.

The overall travel time is then:

$$T_{propagation} = T_{sheath} + T_{iono} - T_{shift} \tag{3.5}$$

where T_{sheath}, T_{iono} and T_{shift} is the propagation time through the magnetosheath, time to reach the ionosphere and time shift to the bow shock nose, respectively. The time shift to the bow shock nose is negative as the solar wind is being shifted 'back' to Jupiter's bow shock. The travel times vary from Juno detecting the solar wind $\sim$ 2.7 hours before it reaches Jupiter's ionosphere (lagging) and $\sim$ 3.3 hours after it has reached the ionosphere (leading). Considering Juno's position, it is reasonable that Juno may detect solar wind data after it has interacted with Jupiter's magnetosphere. The propagated dataset can be seen in figure 3.5, which also shows the distribution of HST visits across the dataset.

The total travel times are then added to the Juno detection times to get 'ionospheric times', which represent the time the solar wind detected by Juno will impact the ionosphere. The solar wind dataframe now contains data for velocity, pressure, overall travel time, the time shift to the bow shock, travel time through the magnetosheath, travel time to the ionosphere, bow shock location, magnetopause location, Juno locations in x and y, B_r, B_t and B_n as well as a Juno detection time and an ionospheric time attached to every row. The dataframe is then rearranged by the ionospheric time so the data can be correlated with the timestamps of the HST images. As the solar wind plasma data can be highly variable over short time scales, the result is that the data is no longer evenly spaced and visits will likely have a non-uniform number of associated data points.

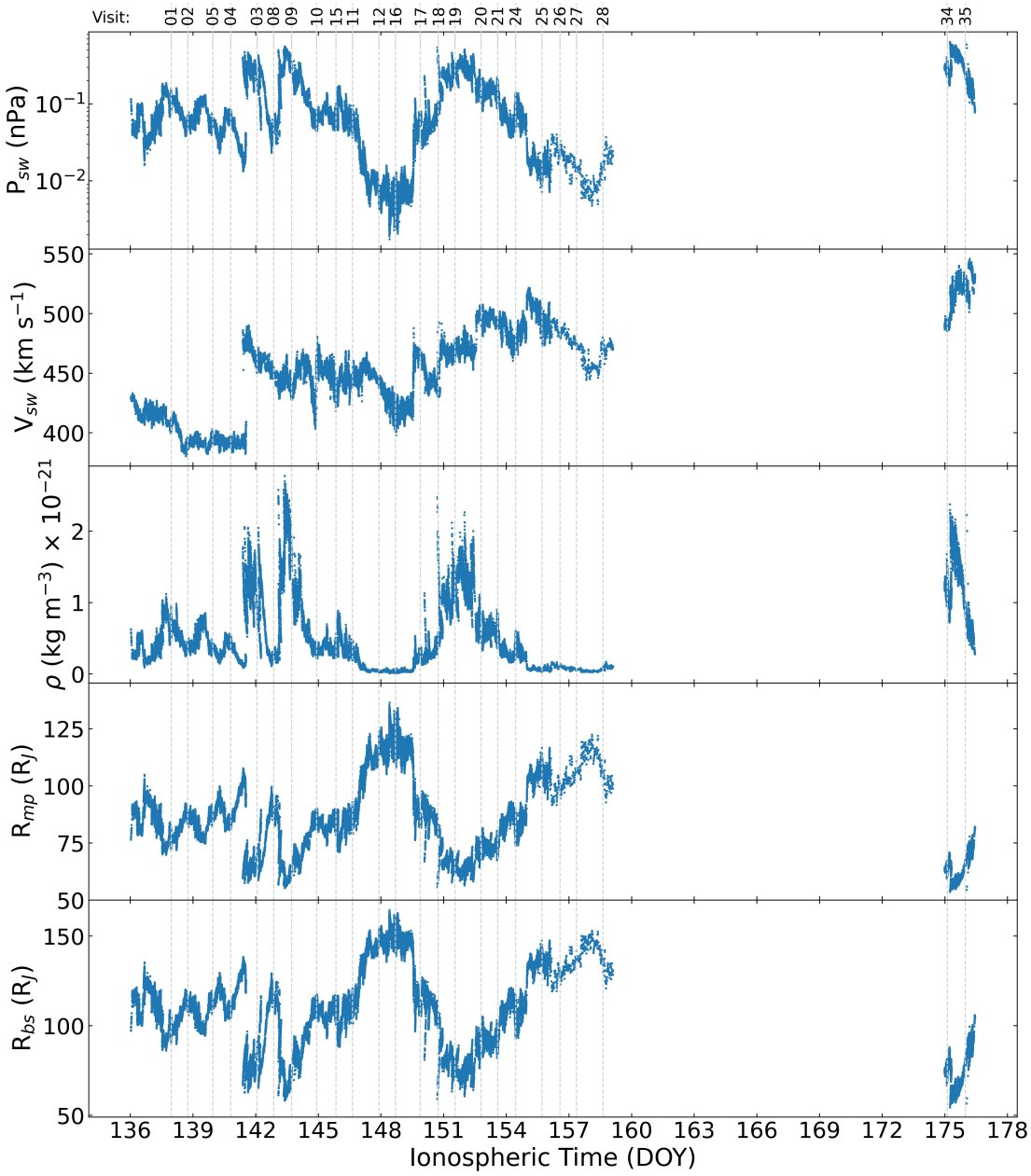

Figure 3.5: Solar wind parameters from the JADE dataset shifted to represent the projected time the solar wind will reach the ionosphere. Top to bottom: pressure, velocity, mass density, magnetopause stand-off distance, and bow shock stand-off distance. The times of each HST visit are indicated by the labelled vertical dashed lines.

3.2.2.1 Uncertainties in Solar Wind Propagation

In the calculation of propagation time, assumptions are made. Applying a broad error window to the propagation time is therefore appropriate as the assumptions make an exact uncertainty difficult to quantify. The assumptions are: 1. Variability of the solar wind; 2. Linear deceleration within the magnetosheath; 3. Location of the bow shock and magnetopause as a function of solar wind dynamic pressure; 4. Equation 3.4 as an estimate based on the calculated magnetopause location; 5. Assumption that the aurora reacts instantly when the solar wind is projected to impact the ionosphere.

The location of the bow shock and magnetopause is potentially the factor with the largest unknown - these boundaries do not instantaneously move in and out as the dynamic pressure changes, and the Joy model predicts the location based on individual pressure values without consideration of the overall trend of data. The primary source of uncertainty within this calculation is the time shift between Juno and the bow shock. For most of this dataset, this time shift represents the largest contribution to the total travel time and as a result changes in the bow shock location are expected to affect the time shift more strongly than any reduction in magnetosheath crossing time as the separation between Juno and the bow shock along the x-axis is typically much larger than that between the bow shock and the magnetopause. Due to these factors, an error window of $\pm 20\%$ is considered to be the most reasonable estimate for the propagation uncertainty.

3.2.2.2 Transforming Coordinate Systems

The magnetic field data is in RTN coordinates, which corresponds to the SPICE frame of JUNO_SUN_EQU_RTN (see panel a in figure 3.2). This frame is not appropriate for this work. The coordinate system needs to be defined with x positive in the direction pointing towards the Sun - RTN defines R pointing away from the

Sun. Whilst this in itself is not a significant issue, the direction of x determines the positive direction of the y axis. For the Juno centred RTN, T is positive on the left, making it a left-handed system. For studies at the Earth exploring the relationship of solar wind with auroral behaviour, y is traditionally defined positive to the right.

The best coordinate system available in SPICE is JUNO_JH, also known as Jupiter Heliospheric. This is a Jupiter-centric system defined with x pointing from Jupiter to the Sun, y as the cross product of the Sun's spin axis and x and then z completes the system. In this system, the Sun's spin axis lies in the $x - z$ frame, and z and y are positive in the directions required. The next stage is to test how reasonable this coordinate system is for the analysis.

A coordinate transform between a coordinate system centred on the Sun's spin axis (IAU_SUN) and a system centred on Jupiter's spin axis (IAU_JUPITER) establishes that the two are separated by $\sim 7.9°$ (Wilson, R., Private Communication, April 2025). Although the separation between Jupiter's and the Sun's spin axis varies very little over Jupiter's orbit, this is not the case in a $y-z$ projected plane. For exploring a relationship with the solar wind, the $y - z$ plane is significant as it is where the interaction with Jupiter's magnetosphere will mostly occur. If x is representative of the Jupiter-Sun line, Jupiter's spin pole points toward or away from the Sun during its solstices and points sideways during equinoxes. Using SPICE, it is shown that the difference between the two spin poles in the $y-z$ plane during the time period of interest is $\sim 6.3°$. As Jupiter is in equinox in 2015 and does not reach solstice until 2018, this value is consistent with expected results. Thus, any calculations using the Jupiter Heliospheric frame will be offset in the $y - z$ frame by $\sim 6.3°$. Additionally, the magnetic axis needs to be considered. Jupiter's magnetic pole is offset from its spin axis by $10.25°$ (Connerney et al., 2022). If projected into the $y - z$ plane, the projected angle between the poles varies over a ~ 10 hour period, representative of a Jupiter day. A diagram visualising the angles between all of these axes can be seen in figure 3.6.

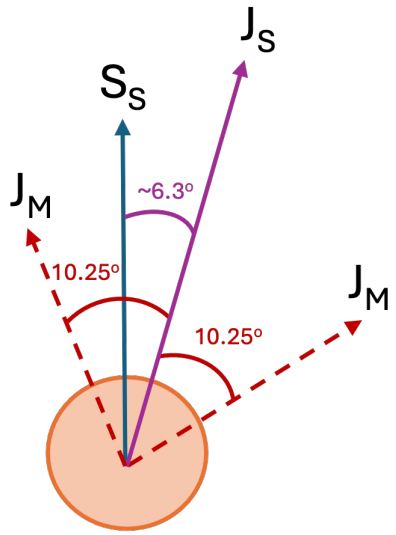

Figure 3.6: Projection of the $y - z$ plane representing the differences between the Sun's spin axis (S_S) Jupiter's spin axis (J_S) and Jupiter's magnetic axis (J_M). The two spin axes are separated by $\sim 6.3°$ during the HST visits, whilst the angle of the magnetic axis varies between the positions indicated by the two dashed lines. The maximum separation is 10.25°, which occurs twice a Jupiter day. The angles are not drawn to scale.

Previous studies have used coordinate systems dependent on the Sun's spin axis and then corrected for the separation between the two spin axes, giving the maximum angle of the magnetic axis as an uncertainty (Nichols et al., 2006, Nichols et al., 2017). This uncertainty is considered to be too large for this study. Though Jupiter's magnetic axis points toward the Sun at a longitude of 196.38° (Connerney et al., 2022), a longitude most of the HST visits pass though, the range of longitudes is wide enough ($\sim$ 90° - 250°) to warrant the definition of a new coordinate system for this work.

The new coordinate system is defined with x as the Jupiter-Sun line, y as the cross product between Jupiter's magnetic axis and x with z completing the system (see panel b in figure 3.2). Jupiter's magnetic axis will therefore lie in the $x - z$ plane. This mirrors the GSM (Geocentric Solar Magnetic) system for Earth,

a system defined specifically for studying solar wind interaction with the Earth's magnetosphere. GSM is defined as a frame with x as the Earth-Sun line, y as the cross product of x and the Earth's magnetic axis and with z completing the system. The SPICE coordinate frame of JUNO_MAG_VIP4 (Jupiter Magnetic) is used to determine the location of Jupiter's magnetic pole as the VIP4 frame defines z as the magnetic axis of Jupiter (with y aligned with the intersection of the magnetic and geographic equators, resulting in x being south of the geographic equator, which is why it is not suitable as a coordinate system for this study). The VIP4 frame uses the outdated VIP4 model (Connerney et al., 1998), where the separation between the spin and magnetic poles is 9.5° rather than the 10.25° defined in the updated JRM33 model (Connerney et al., 2022). This is, however, a difference of less than a degree and represents a much smaller uncertainty than using the spin axis as a basis for the coordinate system. This coordinate system is labelled as JUNO_JM and is designed with the assistance of Wilson, R. (Private Communications, April 2025). Once defined, SPICE is used to convert the magnetic field data from RTN into the JM coordinate system using the ionospheric time to determine the position of the magnetic pole.

It is important that the coordinate transform is performed at this time rather than the Juno detection time as Section 3.2.2 shows that the propagation times from Juno to the ionosphere can be on the scale of multiple hours, which could represent a significant portion of a Jupiter day. As the JM frame rotates with the planet, this could constitute a significant difference in the values of the different IMF components. The ionospheric time is used rather than creating a new timestamp for the time the solar wind will be projected to reach the magnetopause. This is considered to be acceptable as for the majority of the dataset, the travel time between the magnetopause and ionosphere is the shortest, typically on the timescale of minutes. The maximum time is $\sim$ 77 minutes, which when compared to the $\sim$ 10 hr period of Jupiter's rotation, is $\sim$ 13% of a Jupiter day. This is not insignificant, but it is less than the 20% uncertainty that has already been imposed

on the propagation time of the solar wind and thus is well represented within the propagation time uncertainty.

3.2.3 Visualisation of the Polar Regions

In order to obtain power values for the auroral polar regions, their location must be established. The best way to do this is to create visual images of the processed HST intensity data and then define the location for each region based on the behaviour of the emission. Before this can be done, the time associated with each visit needs to be corrected by accounting for light travel time between Jupiter to HST, an average time distance $\sim$ 40 minutes. Some limb trimming is also performed using the angle of the surface vector normal to the Sun to remove any excess data not caught by Boston University pipeline.

The intensities are plotted in System III longitude. Though the polar regions are fixed in local time, the main emission is distorted by the northern magnetic anomaly, which is fixed in System III longitude and thus distorts the shape of the aurora at different local times in different images. If fixed in local time, the polar regions will need to move with respect to the main emission and so will need to be redefined for every single image. Due to the viewing angle of HST, most of the visits have a similar range of CMLs, and so fitting based on longitude suffices.

The generated images are studied in reference with previous studies to pick out the regions (Nichols et al., 2017, Greathouse et al., 2021). Unfortunately, visits 07, 13 and 23 have poor viewing geometry for all of the polar regions and thus are dropped from the study, leaving 24 viable visits. This adjusts the CML range to a new range of $\sim 116^\circ$ - 135°.

There are several difficulties in defining appropriate regions: 1. The latitudinal location shifts between visits due to periods of compression and expansion; 2. As

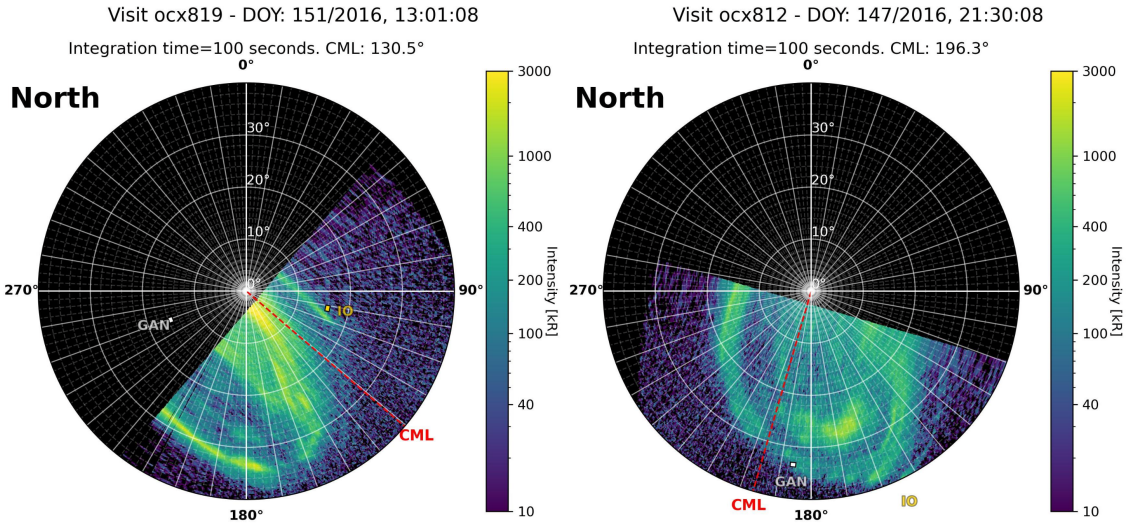

Figure 3.7: Polar projections of two different visits from the HST dataset, where the visit on the left (visit 19) represents a compression of the main auroral emission and the visit on the right (visit 12) represents an expanded main emission. The projections here show that latitudinal extent of the main emission influences the size of polar auroral region (located poleward of the main emission). A compressed main emission also distorts the shape of the main emission as the main auroral boundary is pushed further inward and distorted by the northern magnetic anomaly.

the polar regions are local time dependent and shift with CML, the regions are not at the same consistent location in all the images; 3. The northern magnetic anomaly, located between 80° and 150°, forces the polar regions to change shape as they move through it (Grodent et al., 2008). The 3rd issue is most egregious during a compressed main emission along the anomaly; the main emission often visually appears close to a straight line under these conditions, pushing the dusk active region inward and drastically compressing the swirl region. As local noon moves away from the anomaly, the main emission begins to move outwards at both higher and lower latitudes, forming the familiar 'kidney bean' shape. An example of this can be seen in figure 3.7). The location of the noon active region is also ambiguous in the left-hand side of this figure due to the combination of viewing

angle and compressed main emission. Though the location of active emission is very distinct, where the noon active region ends and the dusk active regions begins is difficult to discern.

Two sets of regions are defined in response to these issues, one set for 'standard CML' visits and another set for 'high CML' visits. Here 'standard CML' means the most common range of CMLs. The standard range contains CMLs of $\sim 116 - 205$ and the high range CMLs of $\sim 186 - 135$; the crossover between the two categories exists because all visits overlap across the CML range and each visit needs to maintain the same placement of regions throughout all 26 frames for consistency. Only 4 visits fit into the 'high CML' range category. These groupings attempt to just capture a 'sample' of each region. Due to the range of main emission latitudes within the two groups, it is impossible to capture the full area of emission for every visit without having inconsistent region sizes or regions containing some of the main emission; as the main emission is typically brighter, the presence of any of this emission could skew the results. As the polar regions move and change shape, it is more appropriate to measure a consistent area of emission for each region in order to capture any trends between the total auroral power and the various parameters of solar wind. As such, each region is set as the same size in both the 'standard CML' and 'high CML' groups.

The chosen regions can be seen in figure 3.8. The resulting regions are non-ideal, but this solution is assessed as better than attempting to fix the regions in a local time frame. For both groups, the noon active region is defined to follow the main emission in the average location of the CML. It is narrower in the 'high CML' visits due to the dusk active region being shifted to lower-latitudes. As a result, it stretches across a larger longitude range so that the size remains consistent. The dusk active region undergoes the most significant change; it should follow the shape of the main emission, like the noon active region. This works well for the 'high CML' visits, but many occur during periods of compressed main emission for the 'standard

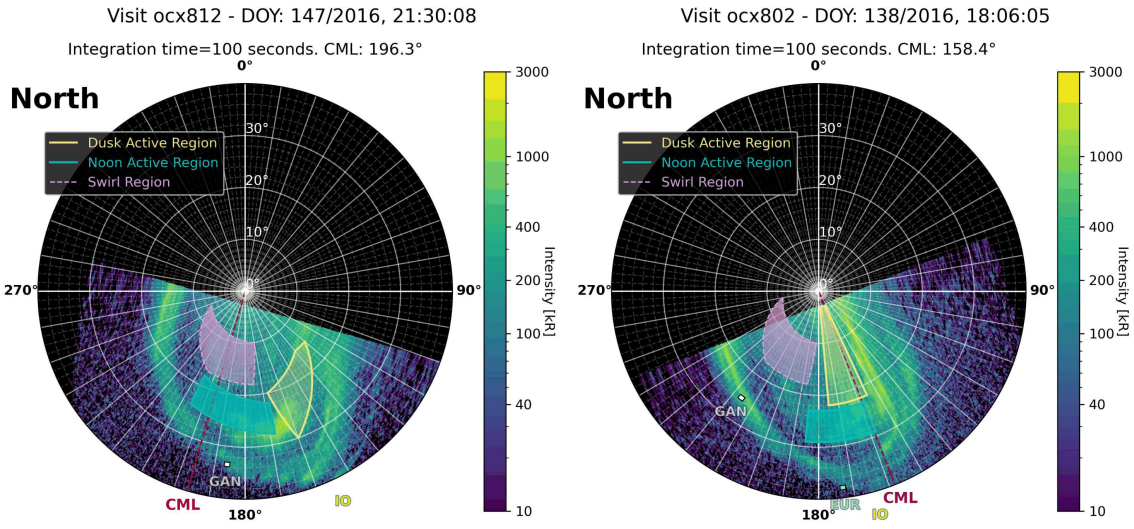

Figure 3.8: Polar projections of visits 12 (left) and 02 (right), representing the two different sets of regions selected for this study. Visit 12 is fitted with the 'high CML' regions and visit 02 is fitted with the 'standard CML' regions. The main difference between the two sets of regions is the dusk active region, which has a different shape between the two categories. For the 'high CML' regions, the dusk active region is curved around to follow the edge of the main emission, following the outward expansion of the main emission as local noon moves further away from the northern magnetic anomaly; for the 'standard CML' regions, the dusk active region is compressed inward due to local noon being close to the northern magnetic anomaly, but still follows the edge of the main emission. The 'standard CML' regions are also fit considering main emission compression, whereas the 'high CML' visits do not occur under main emission compression. The size in area of the regions is consistent between the two sets of regions.

CML' visits, further exaggerating the effect of the northern magnetic anomaly. This results in the region extending upward to higher latitudes, and so in this case it is defined as the the whole upper right of the polar emission. The swirl region is defined the same way for both groups, with the only difference between the 'high CML' and 'standard CML' visits being the location in longitude. The swirl region is defined based on lower activity and patchy emission on the left of the dusk active region and above the noon active region, allowing for a border between the swirl region and the main emission that represents the dark polar region.

3.2.4 Conversion of Intensity to Power

To analyse auroral power for each region, the intensities need to be converted from kiloRayleigh (kR, 1 kR = $\frac{10^9}{4\pi}$ photons cm^{-2} s^{-1} sr^{-1}) to power values (W). The approach of Bader (2020) (see their appendix A) is considered, however, this method does not correctly conserve photons between the projected intensities in the fits files and the derived auroral power. Reviewing work by Gustin et al. (2012), it became clear that a physically consistent conversion requires knowledge of the photo emission rate, which is most directly obtained from the photon counts in the raw detector data.

Due to the lack of access to the raw data, back-projecting the intensities onto the detector pixels is required to conserve the photo number. This is done geometrically by determining which detector pixels correspond to each latitude-longitude pixel in the projected intensity grid, using the angular size of the grid pixels, the detector pixel scale and the distance between HST and Jupiter. In this process, the intensity of each latitude-longitude pixel is redistributed over the corresponding detector pixels according to the angular area it subtends at its distance from HST, so that each back-projected pixel inherently accounts for the emitting surface area on the planet. For a square detector pixel of side length τ arcseconds at a distance r

metres from the planet, the emitting surface area covered (in m^2) is approximately $r^2 \times \tau^2$, where τ is expressed in radians (1 arcsecond = 4.84×10^{-6} radians). The resulting back-projected intensities, denoted B_{bp}, therefore represent photon-conserving detector-space intensities in kR for the selected auroral region.

The intensities of the pixels, representing the total unabsorbed H_2 emission across the $70-180$ nm range, are converted back to photon counts using a conversion factor dependent on the auroral colour ratio (CR) (Gustin et al., 2012). This conversion factor (HCF) also corrects for hydrocarbon absorption, which prevents HST seeing the full brightness of the emission. For the noon and dusk active regions, CR ~ 2.5 gives HCF = 4523. This CR is typical across the bulk of Jupiter's aurora. The swirl region has a much higher CR of ~ 12, giving HCF = 5120 (Greathouse et al., 2021; Gustin et al., 2012).

The resulting photon counts are then converted into auroral power by multiplying by the photon energy conversion factor (PEF), which incorporates the mean energy of an auroral photon in the $700 - 1800$Å wavelength range and the includes the integration over the full 4π steradians for a full-sphere emission. Therefore, multiplying by this factor directly yields the total auroral power emitted by the observed region. For a CR of 2.5 PEF = is 1.02×10^{-9} and for a CR of 12 PEF = 1.16×10^{-9} (Gustin et al., 2012). Finally, because the power observed at HST decreases with the square of the distance, the observed power for each region must be multiplied by the squared distance between Jupiter and HST to gain the total emitted auroral power.

The equation for auroral power is then:

$$PW = B_{bp} \times \frac{1}{HCF} \times r^2 \times PEF \tag{3.6}$$

where B_{bp} is the back-projected intensities for the selected region, r^2 is the squared distance between HST and Jupiter, HCF is the conversion factor including hydrocarbon absorption and PEF is the photon energy conversion factor. For each

region, all power values are summed to gain the total power per image. A median is then taken to obtain the average power for the visit. The median is used because it represents a physical value within the data, better captures the overall trend of a visit and does not directly incorporate extreme values as a mean does.

Pixels with an intensity of less than -100 kR are set as NaN values. Negative intensities are representative of pixels with a lower intensity than the subtracted background and should not be ignored as they can represent valid values, but a clear limit is set to remove any extreme variables as anything lower than -100 kR is likely to be an error in detection by the instrument. For example, the swirl region of visit 10 contains many non-physical values, resulting in an overall negative power when the power valued are summed. This is a non-physical result. Applying this limitation results in a positive total power for the region.

3.2.4.1 Uncertainties in Auroral Power

The standard error of the median is used to represent the uncertainties in the auroral power for each region. It is defined as:

$$error_M = 1.2533 \times \sigma_P \tag{3.7}$$

where σ_P is the standard deviation of the mean of the total power, calculated as follows:

$$\sigma_p = \sqrt{\frac{\Sigma(P - \mu_c)^2}{N}} \tag{3.8}$$

where P is the total power, μ_P is the mean of the total power. and N is the number of data points. As there is no quantifiable error associated with the methodology of obtaining power values, this standard error is used to represent the total uncertainty in the data.

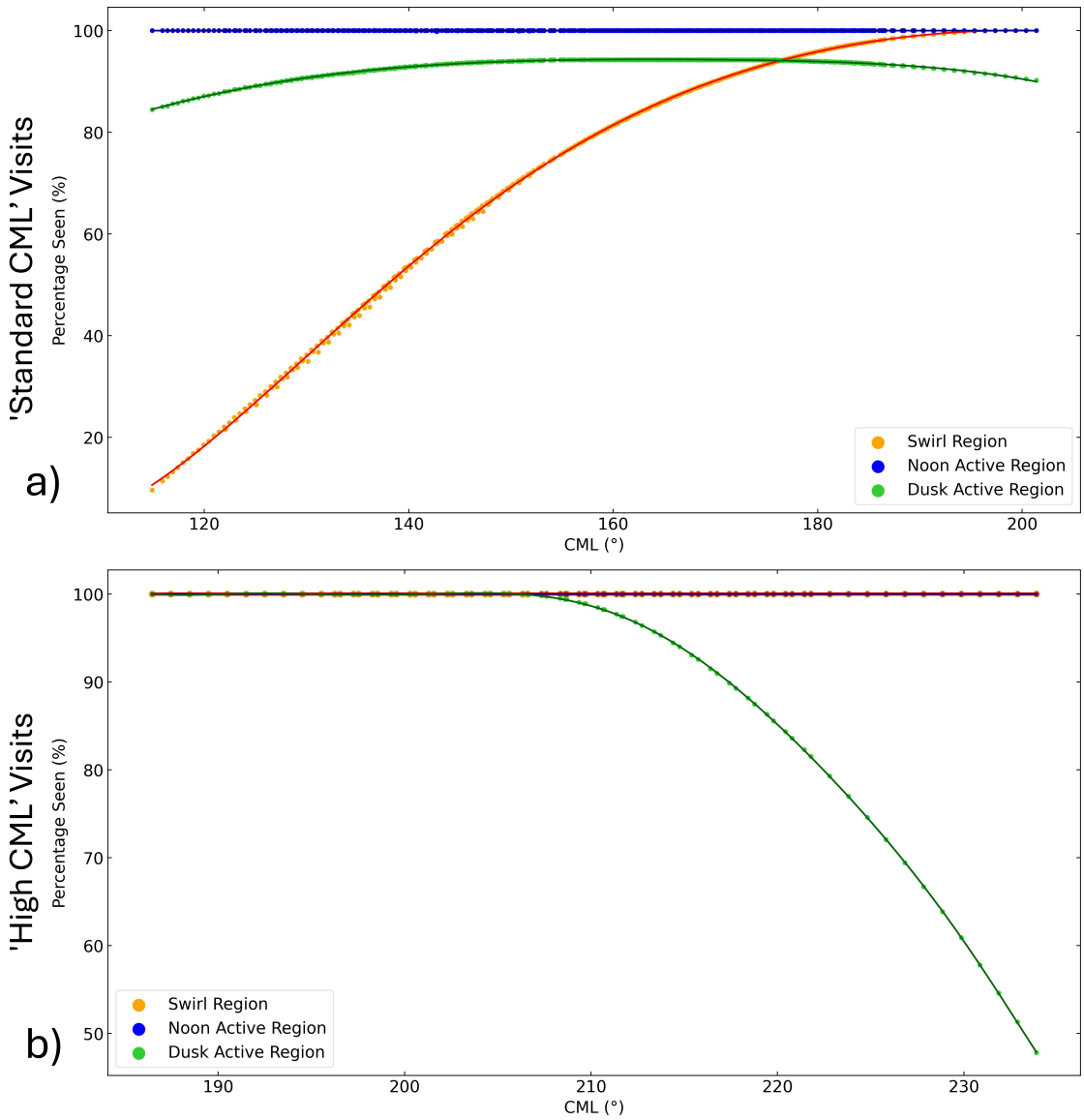

Figure 3.9: The percentage of pixels seen for the swirl, noon active and dusk action region for the a) 'standard CML' visits and b) 'high CML' visits. For both categories, the noon active region is 100% visible and does not need to be scaled. For the 'standard CML' visits the swirl region and dusk active region require scaling, and for the 'high CML' visits only the dusk active region requires scaling as the swirl region is also 100% visible.

3.2.5 Correcting for Viewing Geometry

Due to Jupiter's rotation, the defined regions are not always fully visible to HST and so the calculated powers are not a true representation of the region. To correct for this, the auroral powers are scaled by the fraction of pixels seen by HST for each region. By doing this for every image of each visit, a scaling function based on CML is created. Although one visit (visit 26) is omitted from defining this function due to an excess of NaN values that are not the result of the viewing geometry, the function is applied to all visits. As the reason for the excess of NaN values cannot be ascertained, the visit with an excess of NaN values is assumed to have the same visibility as other visits in the same CML range and so the function is applicable. Figure 3.9 shows these scaling curves for the 'standard' CML visits and 'high' CML visits, respectively.

It is clear from these functions that the scaling is of the least importance for the noon active region, which is 100% visible for all HST visits. For the 'high CML' visits, the swirl region is also 100% visible. Due to viewing geometry, scaling is the most important for the swirl region for 'standard CML' visits and for the dusk active region for 'high CML' visits. Though the dusk active region is not 100% visible for the 'standard' CML visits, its visibility is always above 80%; the issue is that a larger than expected number of the pixels are NaN values. The shape of the curve and the maximum visibility align with expectations based on the positioning of the region, and as the missing pixels appear consistently across all visits, this is potentially an issue with the detector or the image processing. The absence of this effect in the 'high CML' visits is likely due to the significant shift in location of the dusk active region.

With the total power for each of the polar auroral regions obtained and all solar parameters compiled into a single dataset, the data processing is complete and the data is ready for use in Chapters 4 and 5.

Chapter 4

Clock Angle Dependence on Jupiter's Polar Auroral Power

4.1 Introduction

The aim of this study is to investigate solar wind driving as a potential source for Jupiter's UV polar aurora. As discussed in Chapter 2, the polar region is divided into 4 different regions: the swirl region, dusk active region, noon active region and the dark polar region. Each region has unique properties; in particular, the swirl region exhibits higher colour ratios than the active regions (Greathouse et al., 2021). Previous studies also suggest that the active regions map to different local time sectors of the outer magnetosphere, indicating different conditions for solar wind driving (Vogt et al., 2011; Zhang et al., 2021). To explore this, the clock angle of the solar wind IMF is compared with the total power emitted from the swirl, noon active and dusk active region, as the dark polar region is judged as generally too quiet to obtain meaningful data. The solar wind pressure and the magnitude of the IMF are also examined.

4.2 Methodology

The data analysis procedures underpinning this study are described in Chapter 3. This section details the additional methods employed to compare the solar wind conditions with auroral power in the polar region.

4.2.1 Clock Angle and Magnetic Field Strength

4.2.1.1 Calculation of Clock Angle

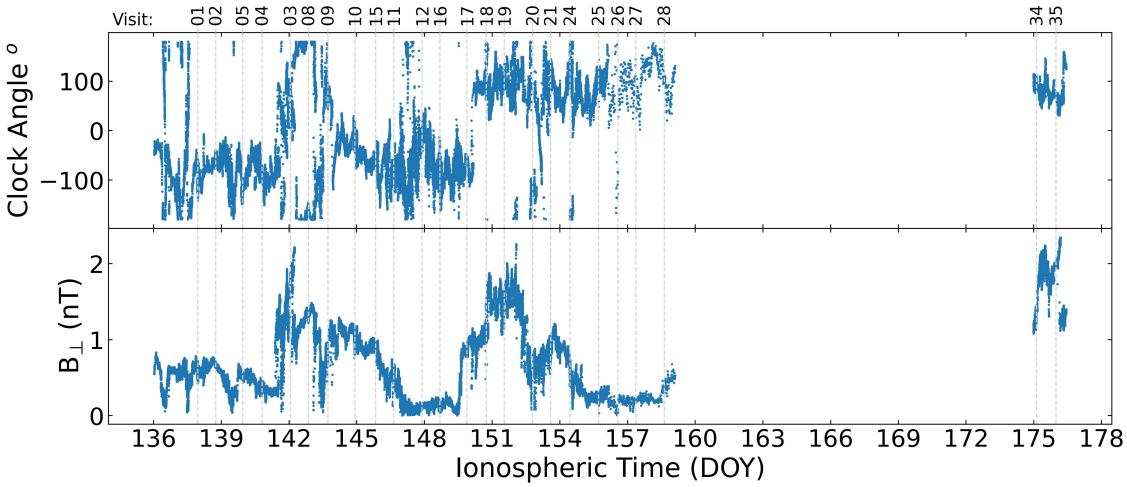

Figure 4.1: Clock angle (top) and magnetic field strength in the plane perpendicular to the Sun-Jupiter line, $B_\perp$ (bottom) for the whole Juno MAG dataset. The values are arranged by time estimated to reach the ionosphere, with the time of each HST visit indicated by a vertical dashed line.

The clock angle is the angle defined by the y and z components of the IMF projected into the plane perpendicular to the planet-Sun line, measured from the positive z-axis. It is in this 2D y-z plane that the solar wind predominately interacts with a planetary magnetopause. The relative orientation of the IMF y and z components and magnetopause fields indicates whether reconnection is possible. The formula

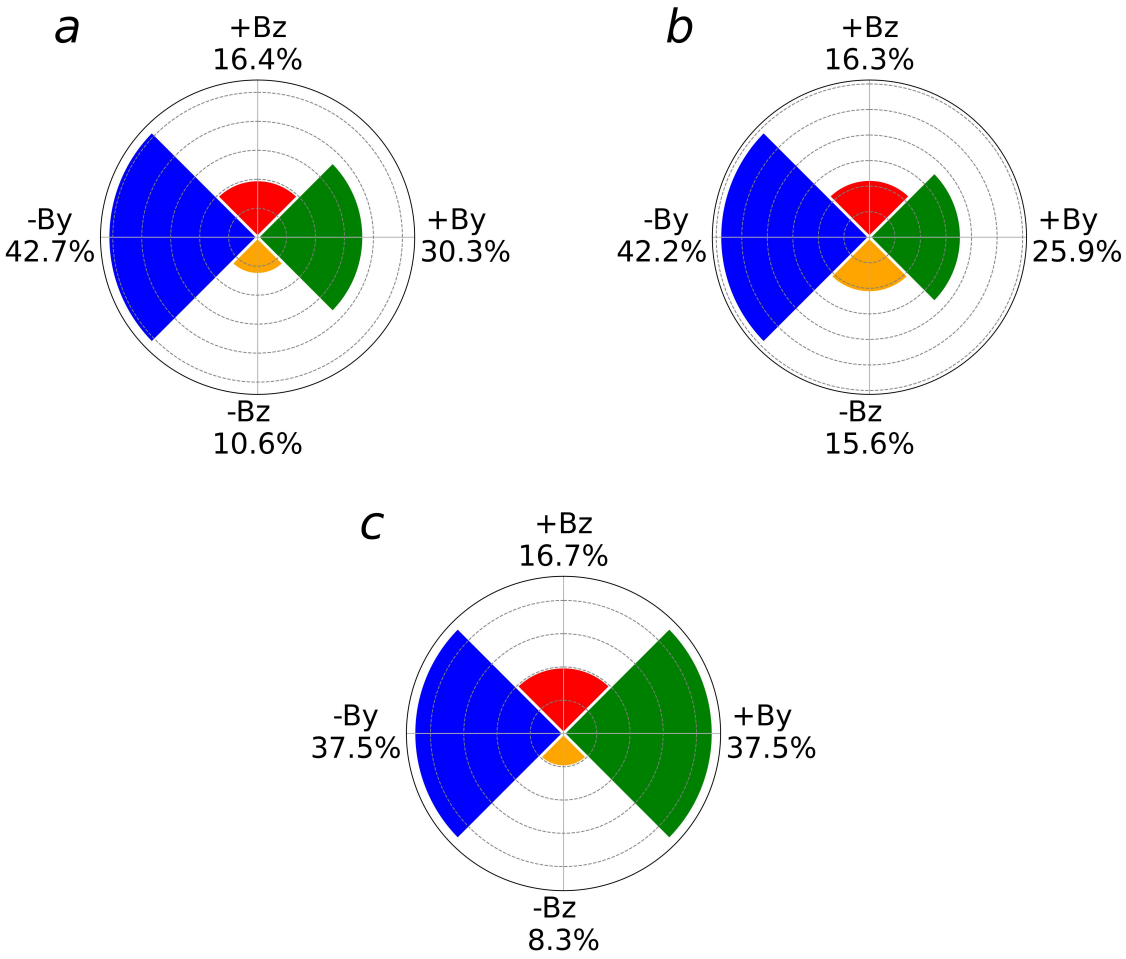

Figure 4.2: The distribution of clock angles (a) within the whole solar wind dataset, (b) within all HST visits and (c) representing the median of each visit. The majority of the data falls within the $-B_y$ quadrant and $-B_z$ comprises the minority. Although IMF $-B_z$ is over represented and $+B_y$ under represented during HST visit times relative to the Juno dataset, the $+By$ quadrant is over-represented and $-B_z$ under-represented when the median average of each visit is taken.

for clock angle is as follows:

$$\theta_c = \tan^{-1}\left(\frac{B_y}{B_z}\right) \tag{4.1}$$

where B_y is the y component and B_z is the z component of the IMF. However, this expression does not uniquely distinguish between the four possible IMF quadrants ($+B_z$, $+B_y$, $-B_z$ and $-B_y$), as different combinations of B_y and B_z can yield the same value of $\tan^{-1}\left(\frac{B_y}{B_z}\right)$.

To retain the correct sign and quadrant information, the four-quadrant arctangent formula is used instead:

$$\theta_c = \text{arctan2}(B_y, B_z) \tag{4.2}$$

This formulation maps all IMF orientations onto the full angular range $-180° \leq \theta_c \leq 180°$.

The resulting clock angles, calculated for all ionospheric times, are assigned to quadrants centred on: $+B_z$ (0°), $+B_y$ (90°), $-B_z$ ($\pm$180°) and $-B_y$ ($-$90°). The distribution of clock angles in the Juno dataset is shown in figure 4.2).

4.2.1.2 Calculation of Magnetic Field Strength

The magnitude of the IMF is important in modulating the strength of a reconnection event. It affects the energisation of current systems and particles, which can lead to auroral emissions. The formula for the magnitude of the magnetic field is as follows:

$$B_{total} = \sqrt{B_x^2 + B_y^2 + B_z^2} \tag{4.3}$$

The magnitude of the magnetic field perpendicular to the planet-Sun line can be calculated in the same way:

$$B_\perp = \sqrt{B_y^2 + B_z^2} \tag{4.4}$$

Both of these values are calculated for the whole solar wind dataset, but $B_\perp$ is considered to be more optimal for comparing with auroral power as it represents the magnitude of the magnetic field associated with the clock angle.

4.2.2 Comparing Datasets

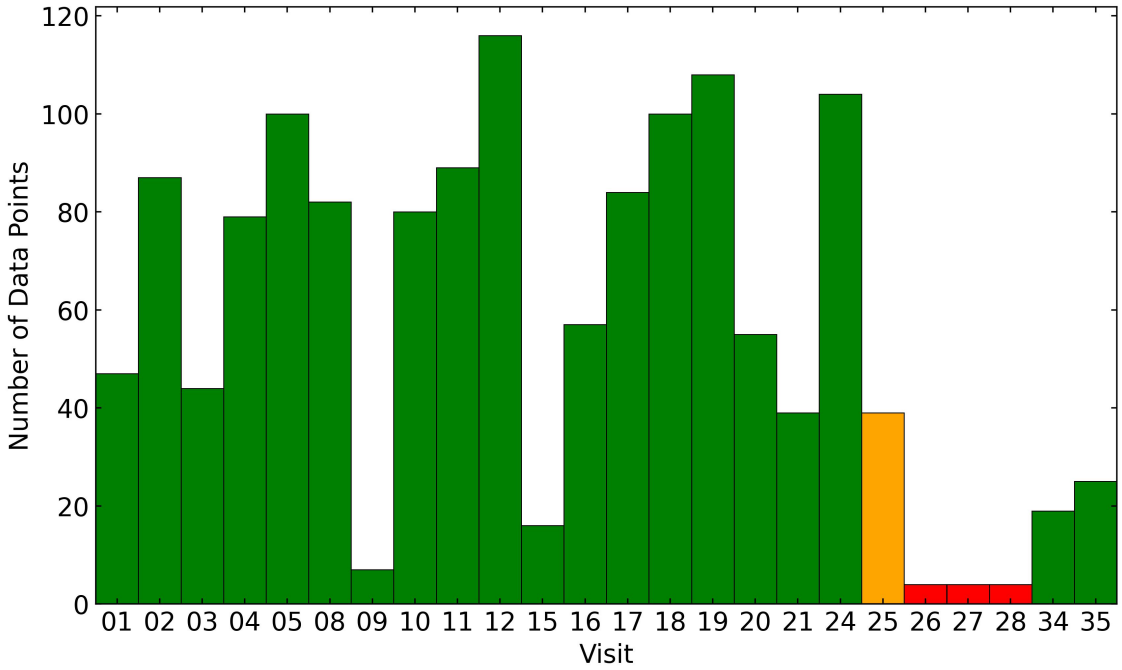

Figure 4.3: The number of propagated Juno solar wind data points that coincide with each HST visit and their variation over the visit. Colours indicate the time resolution of the Juno dataset: 30 seconds (green), 60 seconds (orange) and 600 seconds (red). HST visit periods that occur near times of lower Juno resolution generally contain fewer propagated solar wind data points, with a few exceptions.

The points appearing at opposite ends of the y-axis are a result of the clock angle crossing the $\pm 180°$ boundary. As both extremes of the axis represent the same orientation (the $-B_z$ axis), these jumps represent a visualisation artifact of the coordinate system rather than a physical shift in the IMF clock angle.

UV auroral power can be directly compared with solar wind data that has been time-shifted to the ionosphere, using HST visit timestamps as a reference. The variability in both solar wind conditions and instrument integration times results in a range of Juno data points associated with each HST visit, as shown in figure 4.3. Green bars indicate visits with a time resolution of 30 seconds, orange bars represent 60-

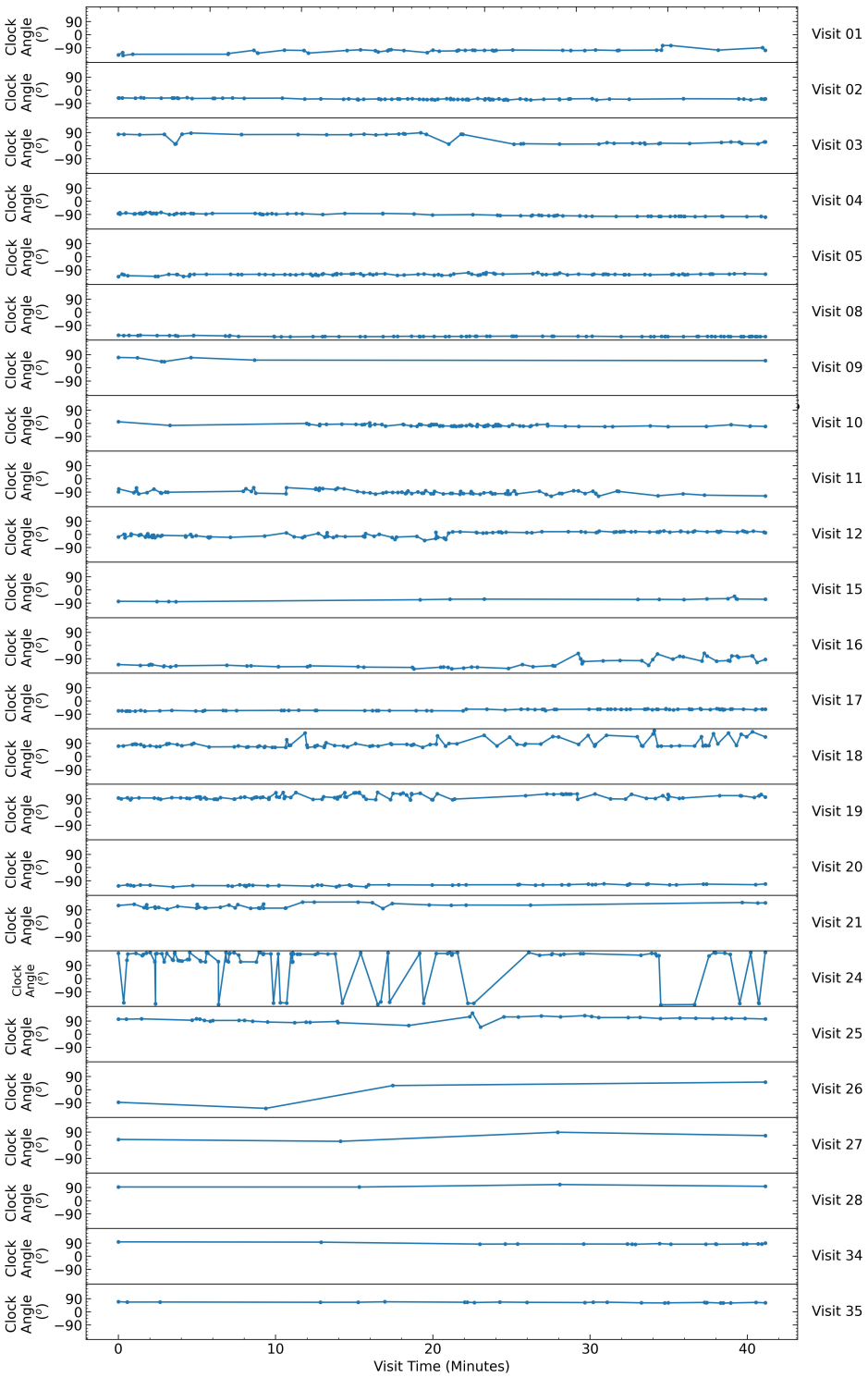

Figure 4.4: Clock angle data for each HST visit, highlighting the discrepancy in the number of data points across visits. The clock angle in visit 24 varies across the ±180° boundary, creating visualisation artifacts despite minimal physical variability, as both extremes of the y-axis represent the same $-B_z$ orientation.

second resolution, and red bars correspond to 600-second resolution. As expected, HST visits with the lowest time resolution are associated with fewer solar wind data points. However, visits 09, 15, 34, and 35 show an unusually low number of data points relative to their integration times. This is likely due to variations in solar wind velocity and dynamic pressure at the time of measurement associated with these visits, which affect the propagation time and result in fewer data points being shifted into the HST observation windows.

The median IMF clock angle, solar wind dynamic pressure and $B_\perp$ for each visit are compared with the median auroral power within each polar region. As the clock angle is defined on the interval $-180° \leq \theta_c \leq 180°$, linear medians are valid except where the clock angle distribution spans the $\pm 180°$ discontinuity. In those cases, negative angles are shifted by $+360°$ to preserve continuity prior to calculating the median. It is verified that none of the resulting distributions cross the new discontinuity at $0°/360°$, ensuring that the linear median correctly represents the circular nature of the clock angle. Any median that exceeds $180°$ after the shift is wrapped back into the original $-180° \leq \theta_c \leq 180°$ range (e.g. a median of $270°$ becomes $-90°$).

Using a median for these solar wind parameters avoids extreme values skewing the analysis. Variations in the data are represented by the standard error of the median, using equation 3.7. All relationships between solar wind parameters and auroral power are also evaluated considering the $\pm 20\%$ uncertainty window in solar wind propagation, discussed in Chapter 3, to ensure the robustness of results.

4.2.2.1 Visual Comparison of Visits

As the HST visits cover a similar range of CMLs and System III longitudes, the existence of any local time or System III longitude features is also investigated. If any prominent and/or persistent features independent of solar wind interaction are

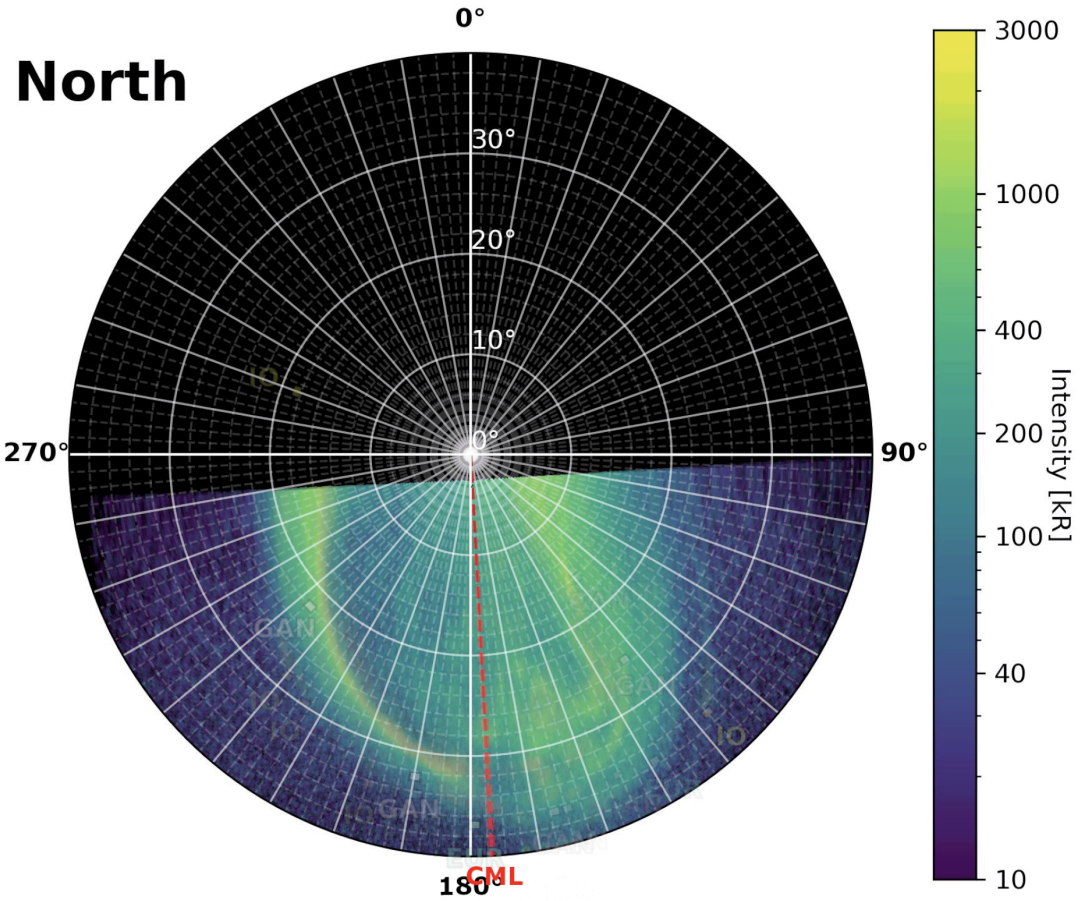

Figure 4.5: Superimposed images from the 9 visits that contain a CML of 177°. There are no features in the polar aurora associated with this CML configuration.

found, their effects can be separated from any relationship established between the polar auroral power and the solar wind. To investigate these potential features, two approaches are utilised.

For the first method, images with the same CML values (within ±0.5°) are superimposed to create an image for every 5° longitude of data. The layers, representing each visit with an appropriate CML, of this image are stacked with lowered opacity so that any persistent feature will appear bright and focused. An example of this can be seen in figure 4.5, which contains images from 9 different visits. Visits are also grouped by the quadrant of their median clock angle and

visually inspected to discern if any features or behaviour appear to be consistent with a trend. Pressure and solar wind magnetic field magnitude are also examined, using the parameters of Nichols et al. (2017); periods of high IMF strength ($\sim$1-3 nT) and pressures ($\sim$2-5$\times10^{-1}$ nPa) are classified as compressions whilst rarefactions are divided into shallow (IMF strengths of $\sim$0.5-0.7 nT and dynamic pressures $\sim10^{-2}$ nPa) and deep (IMF strengths of $\sim$0.1-0.2 nT and dynamic pressures $\sim10^{-3}$ nPa). The first of the compressions present in the data corresponds to a coronal mass ejection (CME), while the other two are identified as corotating interaction regions (CIRs) (McComas et al., 2017; Nichols et al., 2017). The dusk active region has a positive correlation between auroral power and pressure and is suggested to have a somewhat linear relationship with perpendicular magnetic field strength (Nichols et al., 2017), and so it is important to consider how this may influence the results and ensure that any pressure response is not mistakenly attributed to clock angle driving.

The second approach is to create keograms for each polar auroral region to observe how the power evolves over the duration of a visit. These are generated by taking slices of latitude and calculating the total power at all longitudes for each latitude for every image in a visit. This visualisation allows for the identification of transient features or any large spikes in auroral activity that would be obscured by a median-averaging approach. To assess whether the solar wind drives any of this intra-visit variability, these keograms are plotted against the corresponding Juno data (clock angle, dynamic pressure and magnetic field strength) for each visit. This multi-panel comparison provides a visual check for temporal correlation between solar wind fluctuations and changes in auroral power, despite the discrepancy in solar wind data points between visits.

4.2.2.2 Fitting the Data

To determine if any relationship exists between the IMF clock angle and polar aurora, a fit must be applied to the data. This fit should represent a possible coupling function based on the orientation of Jupiter's magnetic field. At low latitudes the field is directed in the $-z$ direction, regardless of local time. At higher latitudes the field is expected to align with $\pm y$ in the dusk and dawn sectors and $\pm x$ in the noon and midnight sectors, where dusk and dawn switch alignment in each hemisphere. However, Jupiter's magnetic field is more complicated than this; the magnetic field rapidly rotates with an internal source of driving, and because the field lines are frozen into the plasma, the expected magnetic field alignment for different local time sectors is distorted. Additionally, Jupiter's magnetosphere is flattened by its equatorial plasma disk, meaning that the magnetic field at higher latitudes is more closely aligned with the x-y plane (Ranquist et al., 2020). These factors complicate the relationship between clock angle and potential onset of reconnection.

Jupiter's field will be approximated as a dipole to derive appropriate coupling functions, despite these caveats. Each coupling function considers an offset of C, representing other unknown processes that could generate auroral emission. If the solar wind is the only driver of emission, quiet periods are expected when the IMF is aligned in an unfavourable orientation for reconnection. However, the polar region is rarely quiet, particularity in the active regions, making this offset appropriate. The coupling functions will also be tested without the offset, as additional driving sources are unknown and may not be quantifiable as a constant value.

Reconnection between the IMF and planetary magnetospheres is best understood at the Earth. At the Earth, large-scale reconnection typically originates at the equatorial dayside magnetopause. Reconnection occurs at higher latitudes as 'component reconnection' as it occurs on a smaller scale and in the presence of a strong guide field. Large-scale reconnection should be suppressed at low-latitudes

Function	$\theta = -90°$ (-B_y)	$\theta = 0°$ (+B_z)	$\theta = 90°$ (+B_y)	$\theta = 180°$ (-B_z)
$\cos^2(\theta)$	0	1	0	1
$\sin^2(\theta)$	1	0	1	0
$\sin^2(\frac{\theta}{2})$	$\frac{1}{2}$	0	$\frac{1}{2}$	1
$\cos^2(\frac{\theta}{2})$	$\frac{1}{2}$	1	$\frac{1}{2}$	0

Table 4.1: Trigonometric functions and resulting values for the centre of each clock angle quadrant, used to determine appropriate coupling functions for magnetic reconnection at different locations along Jupiter's magnetopause.

at Jupiter; in addition to the large shear flows (Desroche et al., 2012), the solar wind has a low plasma β and Jupiter's magnetosphere has a high plasma β (Barbosa et al., 1979; Mauk et al., 2004), meaning that the change in plasma β across the boundary is substantial. The possibility is still considered as a potential driver for auroral activity for this study, however, as modelling suggests the potential of low-latitude reconnection sites (Masters, 2017).

As Jupiter's magnetic field at low-latitudes is oriented in the $-B_z$ direction, the function needs to maximise at 0° (+B_z) and have a minimum value at 180° ($-B_z$):

$$A \times \cos^2\left(\frac{\theta_c}{2}\right) + C \tag{4.5}$$

where θ_c represents the clock angle of the IMF, A the amplitude of the fit and C the offset. This coupling function is referred to as *'dayside reconnection'* from this point forward.

Reconnection sites at high-latitudes are indicated to potentially exist in simulations (Masters, 2017). If reconnection at low-latitudes is fully suppressed, the reconnection at higher latitudes along the dawn and dusk flanks of the magnetosphere may be the only form of IMF clock angle driving. The plasma β will be lower at higher latitudes, meaning the change across the magnetopause boundary will be less significant. The flattened magnetosphere may also allow for the reconnection rate at higher latitudes to be more significant than at the Earth. As the IMF

is primarily B_y directed at Jupiter's distance from the Sun, this is a favourable alignment for reconnection to occur on frequent timescales, which could support the regular activity in the polar regions. To represent this reconnection, the coupling function needs to maximise at both $+90°$ ($+B_y$) and $-90°$ ($-B_y$), as the magnetic field at dawn and dusk is oppositely directed, with the assumption that reconnection in both hemispheres contributes to the northern polar aurora:

$$A \times \sin^2(\theta_c) + C \tag{4.6}$$

This coupling function will be referred to as *'high-latitude reconnection'*.

If low-latitude reconnection is not fully suppressed, high-latitude driving due to IMF B_y may still dominate. This is considered by combining equations 4.5 and 4.6:

$$A_1 \sin^2 \theta_c + A_2 \cos^2 \left(\frac{\theta_c}{2} \right) + C \tag{4.7}$$

This recognises the large-scale structure of the Jovian magnetosphere and allows for multiple processes to act at different regions of the magnetopause surface. In this case, an angle of $180°$ ($-B_z$) will represent the minima as the only location reconnection will not occur is at low-latitudes when the field is parallel to Jupiter's magnetopause. This coupling function will be referred to as *'multi-latitude reconnection'*.

The final coupling function is based on the model of Zhang et al. (2021), which predicts a 'distant lobe' of tangled open field lines trailing behind the planet in the midnight sector. Open field lines poleward of the cusp have also been suggested at Saturn, where the field lines are twisted due to their co-rotation with the rapidly rotating planet (Milan et al., 2005; Stallard et al., 2007). It stands to reason that if open field lines map to Jupiter's polar region that they will also be twisted due to Jupiter's rapid rotation. Whilst the reconnection of the IMF with these open field lines will not drive any large-scale dynamics, it could potentially energise and accelerate particles close to the reconnection site down into the polar region, resulting in particle precipitation and thus auroral emission. To explore this, a

coupling function that maximised at $-180°$ ($-Bz$) is required, which will represent a field antiparallel to the tangled flux:

$$A \times \sin^2\left(\frac{\theta_c}{2}\right) + C \tag{4.8}$$

This function also accounts for the possibility of smaller scale component reconnection with IMF B_y with sections of twisted flux that may be anti-parallel to the IMF. This coupling function will be referred to as *'post-cusp reconnection'*.

The other variables examined in this study, solar wind dynamic pressure and IMF strength, are plotted as best-fit regression lines. While IMF strength is analysed and plotted in linear space, the relationship for pressure is analysed in semi-log space (linear auroral power vs log pressure), representing a logarithmic relationship in linear space. This approach is necessary because the solar wind dynamic pressure in the dataset spans across multiple orders of magnitude; a standard linear fit would be disproportionally weighted towards the highest pressure values, whereas a log scale ensures any auroral response is evaluated across the full range of observed pressures. As the IMF strength exhibits significantly less variability across the dataset, a linear scale is appropriate.

Previous work has suggested a linear correlation between both of these parameters and the auroral power of the dusk active region (Nichols et al., 2017); given the exploratory nature of this study, it is reasonable to adopt this linear assumption for both pressure and magnetic field strength. Linear fits provide a simple and easily interpretable first-order approximation, allowing potential trends to be identified while minimising assumptions about the underlying physical relationships. Should these parameters demonstrate a correlation with auroral power, future studies may seek to characterise the precise nature of these relationships more thoroughly.

4.2.2.3 Error Analysis of Fits

To evaluate how well the clock angle coupling functions match the data, the coefficient of determination (R^2) will be used as a goodness-of-fit metric. R^2 represents the proportion of the variation in the dependent variable that can be explained by the independent variable. R^2 typically ranges between 0 and 1, where a value of 1 indicates 100% of the variance in the dependent variable (auroral power) is explained by the fit, and a value of 0 implies that the fit does not explain any of the variance. Negative values can occur when the model performs worse than a horizontal line plotted through the mean value, indicating a particularly poor fit.

The coefficient of determination is defined as:

$$R^2 = 1 - \frac{SS_{res}}{SS_{tot}} \tag{4.9}$$

where

$$SS_{res} = \sum (y_i - \hat{y}_i)^2 \tag{4.10}$$

and

$$SS_{tot} = \sum (y_i - \bar{y})^2 \tag{4.11}$$

in this function, y_i is the actual observed values. $\hat{y}_i$ is the predicted values from the model, and $\bar{y}$ is the mean of the observed values. SS_{tot} stands for the total sum of squares and SS_{res} stands for the residual sum of squares.

Whilst R^2 is widely used for evaluating the quality of model fits, it has several known biases and limitations. In small datasets, R^2 tends to overestimate the goodness of the fit. This occurs because the function is more likely to capture random noise rather than the potential underlying relationship in the data, thereby inflating the returned value. R^2 is also considered to be unstable with a limited dataset, as small changes in the dataset can lead to significant fluctuations in the returned value.

This instability is particularly relevant when assessing the robustness of the coupling functions in this study. For each coupling function, multiple fits will be utilised to

explore the same relationship, with the uncertainty of ±20% in the impact time of the solar wind on the ionosphere explicitly considered. As this study uses a small dataset, substantially different R^2 values may be returned; this would not necessarily be due to changes in fit quality, but variability in the clock angle between these propagation times.

To address these limitations, adjusted R^2 can be used instead. Unlike standard R^2 analysis, the adjusted version accounts for function complexity and provides a more conservative and robust estimate in the case of a small dataset. Though all coupling functions have the same number of predictors and so the complexity does not change, using adjusted R^2 makes the assessment of goodness-of-fit less sensitive to noise within the data.

Adjusted R^2 is calculated from R^2 as follows:

$$R^2_{adj} = 1 - \frac{(1 - R^2)(N - 1)}{N - p - 1} \tag{4.12}$$

where N is the size of the dataset and p is the number of predictors. Here, N = 24 corresponds to the number of visits, and p = 1 because the coupling functions should include only one predictor — the amplitude term, which depends on the input variable. The offset is a constant and does not contribute to p. From this point onward, any references to R^2 will refer to the adjusted R^2 value.

As R^2 analysis is based upon linear regression, the coupling functions must be of a linear form. However, as the coupling functions are sinusoidal, they are non-linear. To address this, the sine component in equations 4.6 (high-latitude reconnection) and 4.8 (post-cusp reconnection) and the cosine component in equation 4.5 (dayside reconnection) are each treated as independent variables (x). With this substitution, these three coupling functions can be interpreted as linear for the purpose of calculating R^2. Equation 4.7, (multi-latitude reconnection) is more complex and requires linearisation before it can be used for calculating R^2. This process is

described in Appendix A. Though the result is the polynomial function:

$$A_1^{'} \cos^2 \theta + A_2^{'} \cos \theta + C^{'} \tag{4.13}$$

which can also be interpreted as linear for the purpose of calculating R^2 if the $\cos \theta$ is taken assumed to be x.

Pressure and magnetic field strength, also examined in this study, are already tested using linear relationships and therefore do not require any transformation for adjusted R^2 to be applicable. Adjusted R^2 is also used to quantify the goodness-of-fit for these parameters to maintain consistency across all tested relationships in the analysis of results.

4.3 Results

4.3.1 Visual Identification of Features

4.3.1.1 Superimposed CML Images

No evidence of any trends or distinct features associated with CML or clock angle conditions is found in the HST data from superimposing visits with the same CML (within $\pm 0.5°$). A wide range of behaviour is seen within each clock angle quadrant, with the two $-B_z$ visits displaying explicitly different behaviour; visit 08 is very quiet, with a thin and bright dusk active region, where visit 24 is very dynamic in all regions. Whilst all four $+B_z$ visits appear quieter than average in the dusk active region, they all display variable emission with no behaviours or features that appear exclusive to that clock angle quadrant. Though there may be behaviours more likely to occur under different clock angle orientation than others, a simple visual analysis does not find any evidence of clock angle influence on the polar auroral regions.

In terms of other solar wind parameters, the dusk active region appears brighter

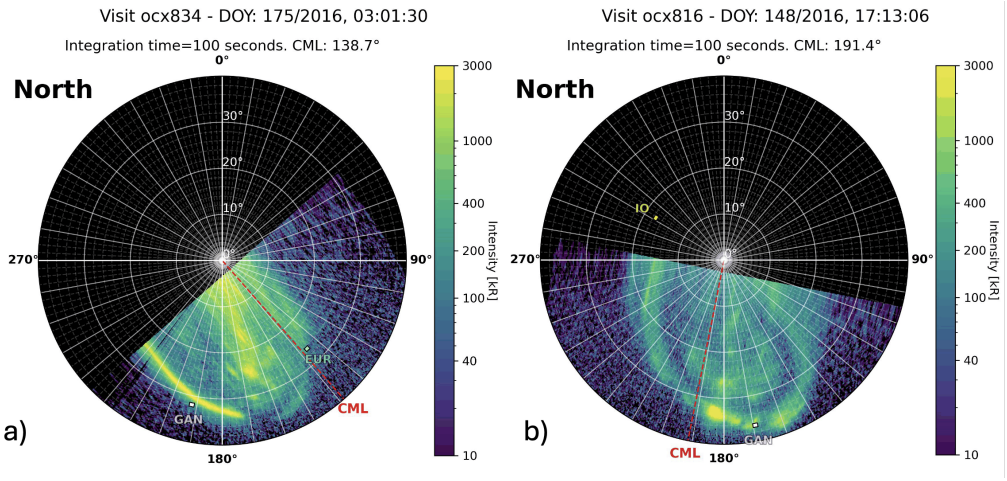

Figure 4.6: Examples of different levels of activity in the polar auroral region where panels show a) high pressure conditions and b) low pressure conditions. Although the regions are not indicated as to not disrupt the visibility of auroral features, the dusk active region clearly shows more auroral activity under higher pressure.

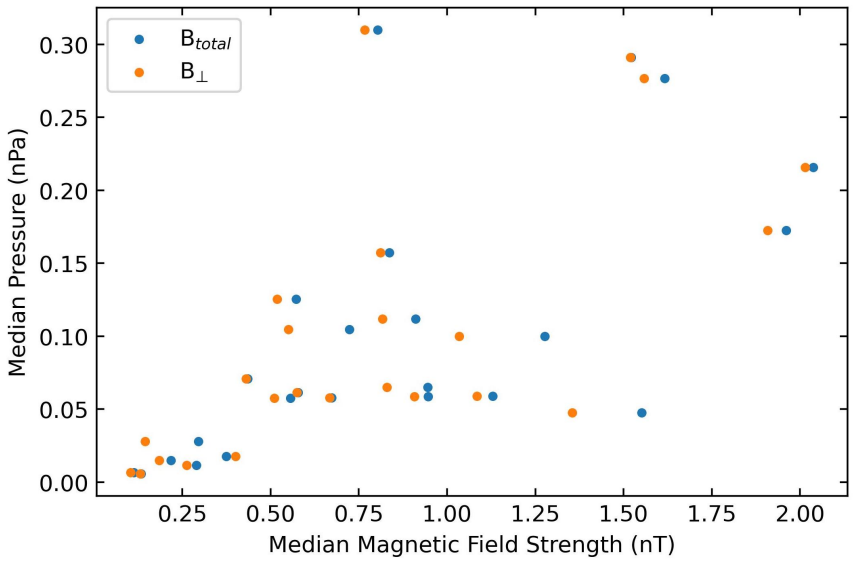

Figure 4.7: Solar wind dynamic pressure vs. magnetic field strength across all visits, demonstrating that higher pressures and higher field strengths typically co-occur, particularly during the most extreme observed conditions.

under high pressure conditions, consistent with previous results (Nichols et al., 2017). An example of this can be seen in figure 4.6. Visits with higher magnetic field strength also often appear visually brighter, but these visits typically occur during periods of high pressure. While the two solar wind parameters are not directly correlated, the periods of highest pressure are coincident with the periods of highest magnetic field strength, as shown in figure 4.7. This is as expected and follows the previous definition of compressions and rarefactions within the dataset. As such, the HST data indicates that the dusk active region is typically enhanced during compression events.

4.3.1.2 Temporal Evolution of Auroral Power

The comparison of auroral keograms for each polar region with IMF clock angle, solar wind dynamic pressure and IMF strength reveals no auroral features that can be confidently associated with changes in the solar wind during the timeframe of a visit. In general, the solar wind parameters remain relatively stable across most visits when compared with the variation that occurs over the whole dataset (see figures 3.5 and 4.1), with the majority of the variation in the solar wind parameters occurs on longer timescales between visits. While the keograms identify discrete auroral features, the majority of these do not correlate with, or follow, any notable change within the solar wind parameters.

There are few cases in which fluctuations in the solar wind could be potentially linked to auroral features. For example, in visit 18 (figure 4.8), the dusk active region displays periodic variations in auroral power across all latitudes. During this interval, the solar wind is in a state of flux; the clock angle varies between the $+B_y$ and $-B_z$ quadrants, and both the pressure and magnetic field strength are high and unstable. While this 'messy' auroral behaviour appears coincident with the varying solar wind, the activity persists throughout the entire visit. Consequently, a median of the total power remains an appropriate metric for the visit. Furthermore, no

individual auroral feature can be uniquely attributed to a specific rapid change in any single solar wind parameter, and other visits show periodic variations in auroral activity with no corresponding solar wind behaviour.

Another case is visit 25 (figure 4.9), representing an instance where features could potentially be attributed to the solar wind. Visit 25 shows an intense flare in the noon active region just before 17:35, with the top edge of this feature also visible at lower latitudes of the dusk active region. This event is preceded by a shift in clock angle and a minor spike in dynamic pressure approximately 5 minutes prior. However, the pressure change is negligible when considering the range of pressures observed across all visits, making it an unlikely driver. Regarding the clock angle, there is a rapid variation between $\sim 50°$ to $\sim 150°$, in which the clock angle flips between these positions twice before stabilising near $\sim 115°$. Although $\sim 115°$ is physically closer to the $+B_y$ axis (90°) than the $-B_z$ axis (180°), it still represents a significant shift from its initial $\sim 50°$ orientation. The failure of the aurora to persist or show a secondary response as the clock angle stabilises suggests that even if the $\sim 150°$ spike acted as a trigger, the subsequent evolution was not determined by the IMF clock angle.

A similar sequence of rapid fluctuations is observed in visit 03 (figure 4.10). Initially, the clock angle is at $\sim 80°$ before briefly dropping to $\sim 10°$ just before 01:40 and returning to $\sim 90°$. While a notable bright area appears in both the swirl and noon active regions, this brightening occurs prior to the change in IMF clock angle. Although this could be a result of imprecise solar wind propagation times between Juno and Jupiter, it makes a direct causal link difficult to verify. Later, at approximately 01:55, the clock angle drops again to $\sim 10°$, rapidly returns to $\sim 80°$ and then settles at $\sim 10°$ for the remainder of the visit. While an auroral response is observed in the noon active regions concurrent with this change, it represents a much less drastic auroral response than the flare in visit 25. There is also a feature in the dusk active region around this time, but it appears to present before the change

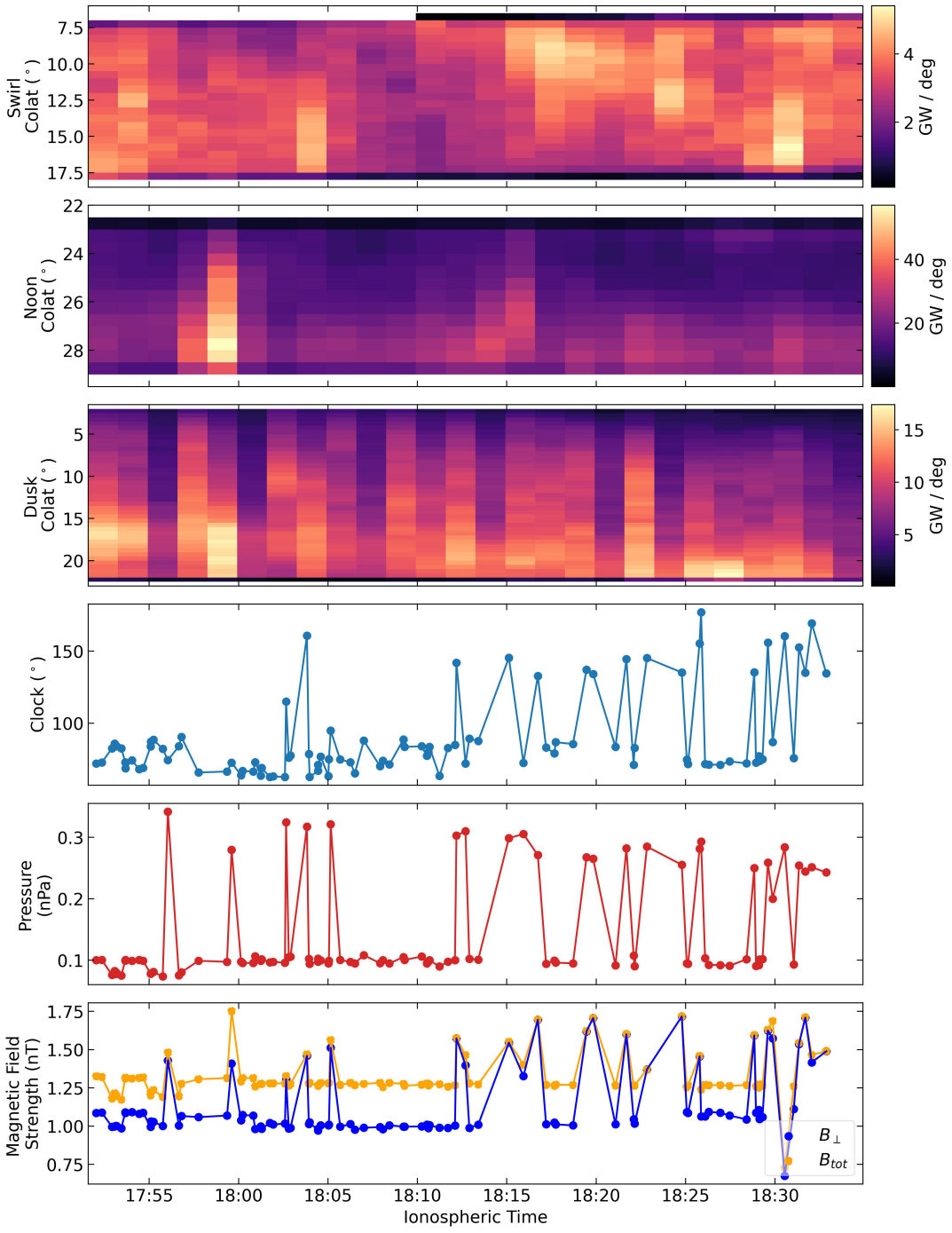

Figure 4.8: Comparison of auroral power distribution and solar wind conditions during Visit 18. The top three panels display keograms for the Swirl, Noon, and Dusk regions as a function of colatitude and Ionospheric Time. The bottom three panels show the corresponding IMF clock angle, solar wind dynamic pressure and IMF strength ($B_\perp$ in blue, B_{tot} in orange), respectively.

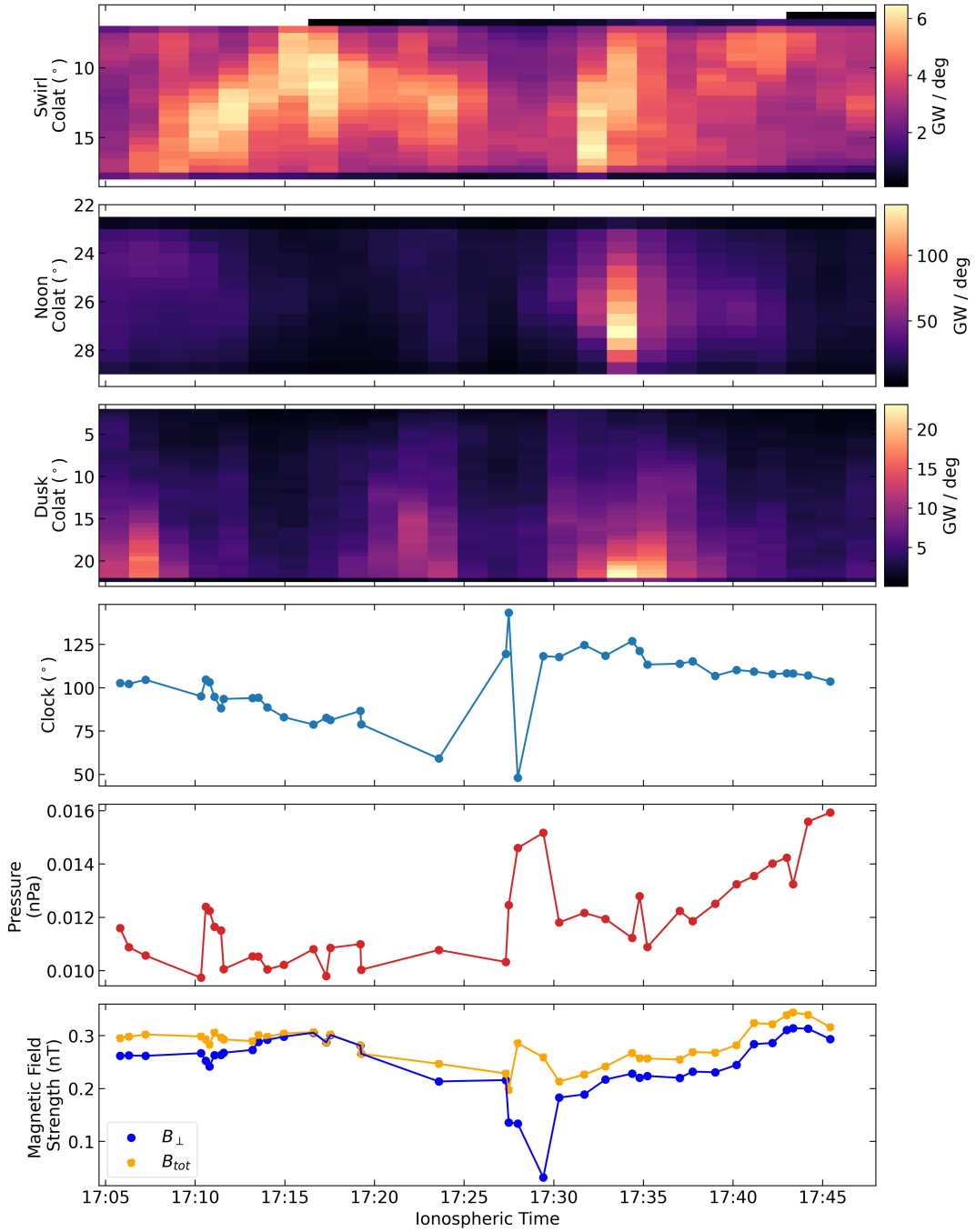

Figure 4.9: Comparison of auroral power distribution and solar wind conditions during Visit 25. The top three panels display keograms for the Swirl, Noon, and Dusk regions as a function of colatitude and Ionospheric Time. The bottom three panels show the corresponding IMF clock angle, solar wind dynamic pressure and IMF strength ($B_\perp$ in blue, B_{tot} in orange), respectively.

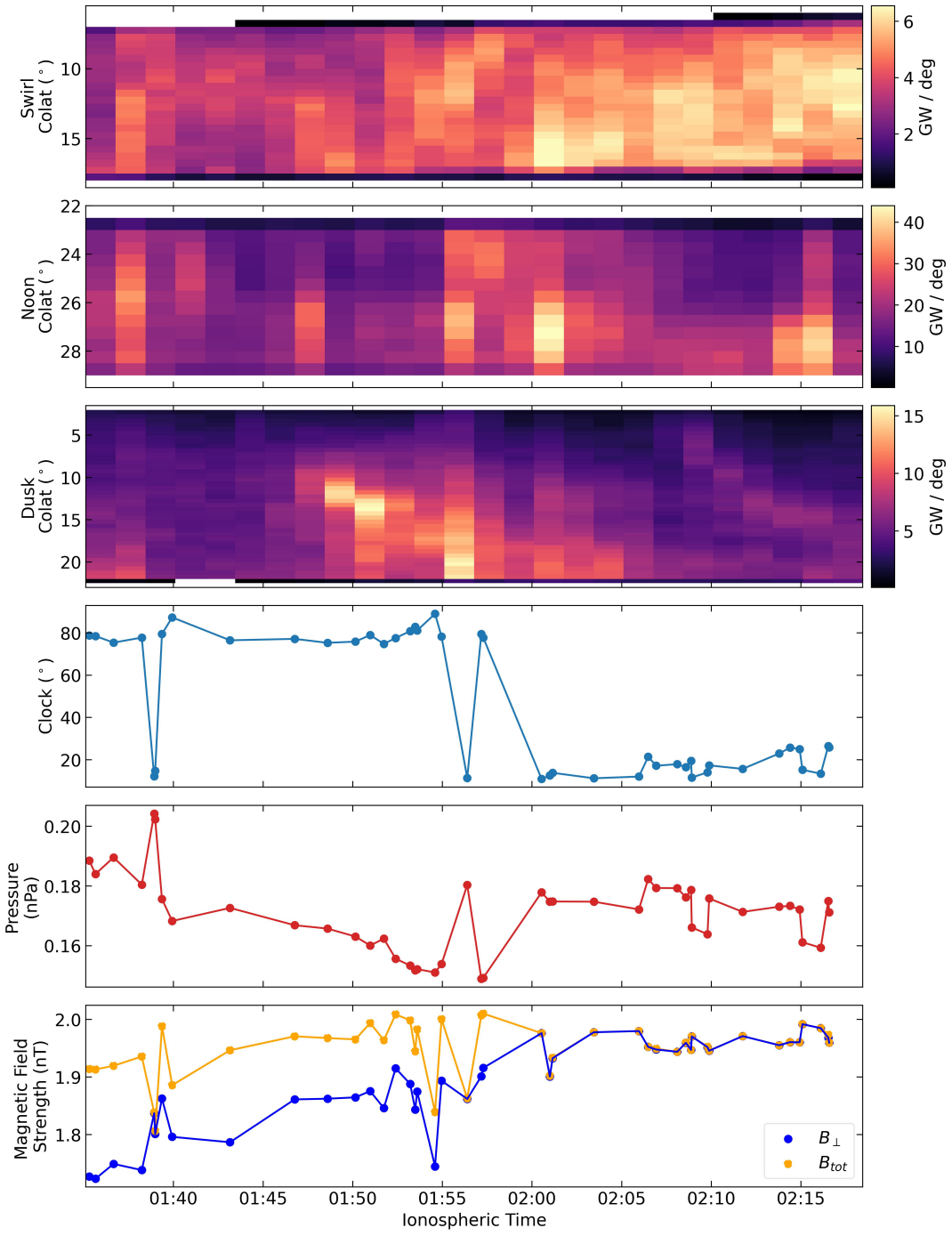

Figure 4.10: Comparison of auroral power distribution and solar wind conditions during Visit 03. The top three panels display keograms for the Swirl, Noon, and Dusk regions as a function of colatitude and Ionospheric Time. The bottom three panels show the corresponding IMF clock angle, solar wind dynamic pressure and IMF strength ($B_\perp$ in blue, B_{tot} in orange), respectively.

in clock angle, suggesting it is likely unrelated. In this case, while the noon auroral feature persists for longer, it still fades despite the clock angle stabilising at a value similar to the initial 'jump' - suggesting that if this is a reconnection signature, it is not sustained.

Although these two visits represent cases where changes in clock angle could potentially be attributed auroral features, the majority of visits do not contain such correlations. Many visits contain prominent auroral features that occur during periods of stable or minimally varying solar wind parameters, while others lack enough solar wind data points to draw any firm conclusions. Additionally, it is often difficult to discern specific features in the swirl region due to the region having consistently low power levels.

The inconsistency of any potential solar wind and the low number of visits showing potential correlations indicate that a frame-by-frame analysis would be scientifically unreliable for this dataset. In addition, the uncertainty in the solar wind propagation times means that brief coincidences cannot be definitively categorised as driver-response relationships. Given that most visits do not show significant variation over the relatively short visit timeframe, the use of median total power provides a more stable characterisation of magnetospheric state for the period. The data for all remaining visits, which further demonstrate this lack of clear correlation, can be found in Appendix B.1.

4.3.2 Clock Angle Dependence on Polar Auroral Power

There is no obvious relationship between clock angle and auroral power in the polar regions, as shown in figure 4.11. The median clock angles shown do not reflect the distribution of all clock angles measured during those visits. Only the $+B_z$ category, which appears as the median for 4 visits, matches the expected distribution. Based on figure 4.2, the expected distribution suggests that approximately 6 visits should

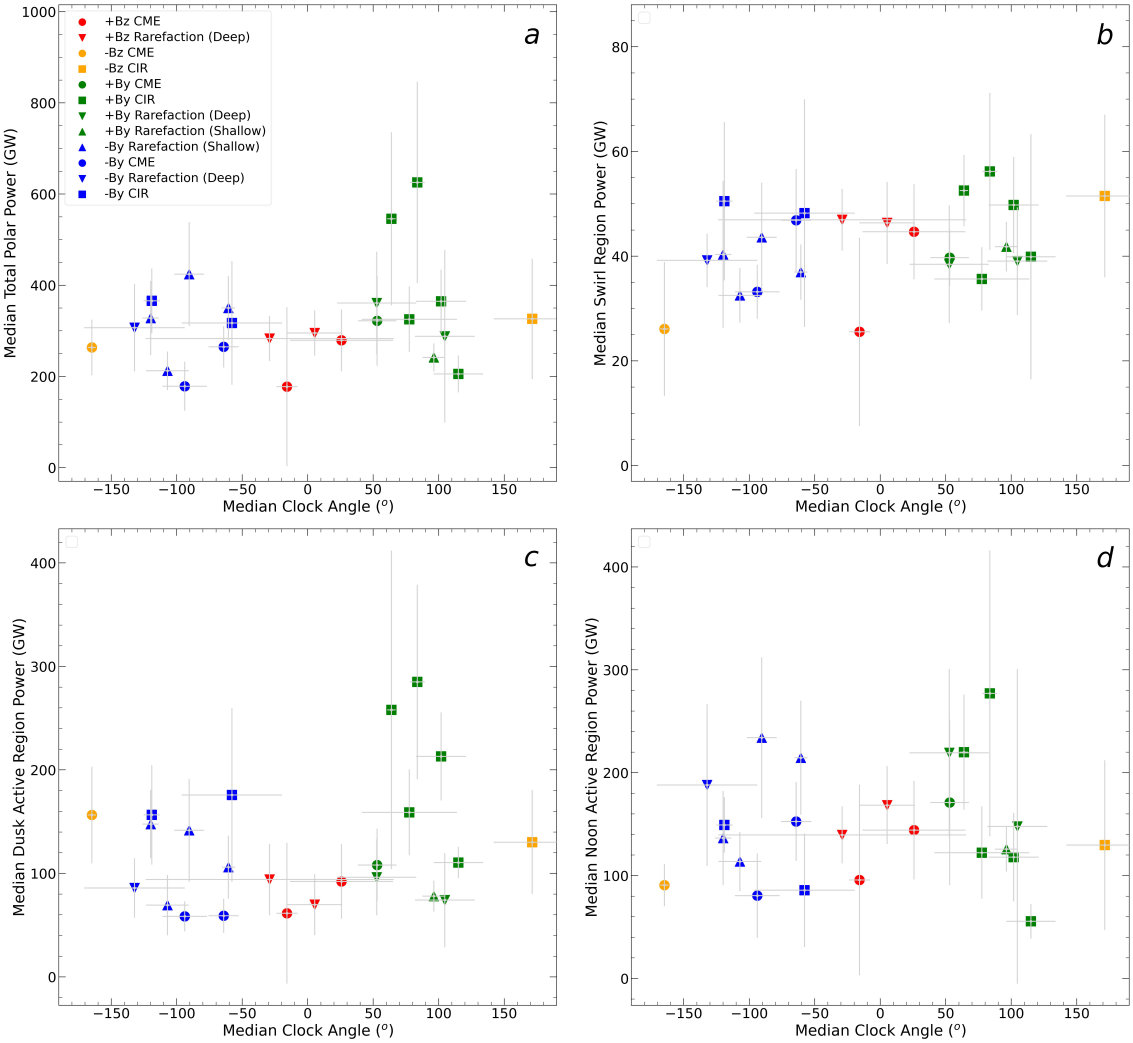

Figure 4.11: The relationship between median averaged clock angle per visit and median a) total polar power, b) swirl region power, c) dusk active region power and d) noon active region power.

have a median in the $+B_y$ sector, 10 in the $-B_y$ sector, and 4 in the $-B_z$ sector. In 4.11, however, these quadrants represent 9, 9 and 2 visits, respectively. This difference does not indicate that the median is an inappropriate measure of clock angle for each visit, but rather reflects the high variability of the clock angle across short timescales - in some cases spanning multiple quadrants within a single visit.

To discern if there is any relationship between the solar wind IMF and Jupiter's polar aurora, predicted auroral powers from each coupling function described in Section 4.2.2.2 are compared with the data presented in figure 4.11. A comparison of the three polar regions with one of the coupling functions will be shown here to describe the process for analysing the results. Any coupling functions that are well correlated with auroral intensity for each region will then be discussed in the context of the Jupiter system and previous literature. The full set of figures for each coupling function can be found in Appendix B.2. The example considers multi-latitude reconnection, utilising equation 4.7, to investigate whether reconnection across multiple latitudes could be responsible for polar auroral driving. Figure 4.12 shows the results of applying this coupling function to each polar region.

To assess whether the coupling function provides a good representation of the data, an adjusted R^2 analysis is performed, following the method outlined in section 4.2.2.3. As it is unlikely that reconnection due changes in the clock angle alone are responsible for polar auroral emissions, high R^2 values (i.e. close to 1) are not expected. For clock angle to be considered a significant trigger for reconnection, a threshold of $R^2 = 0.2$ is adopted, indicating that at least 20% of the variance in the data is explained by the fit.

This threshold is selected to balance the need for statistical significance against the complex internal dynamics of the Jovian system and serves as a necessary filter for the high degree of scatter and the significant error bars associated with taking median averages across each visit (as visible in figure 4.12). Given that auroral power is likely influenced by internal processes acting alongside any solar wind drivers, the

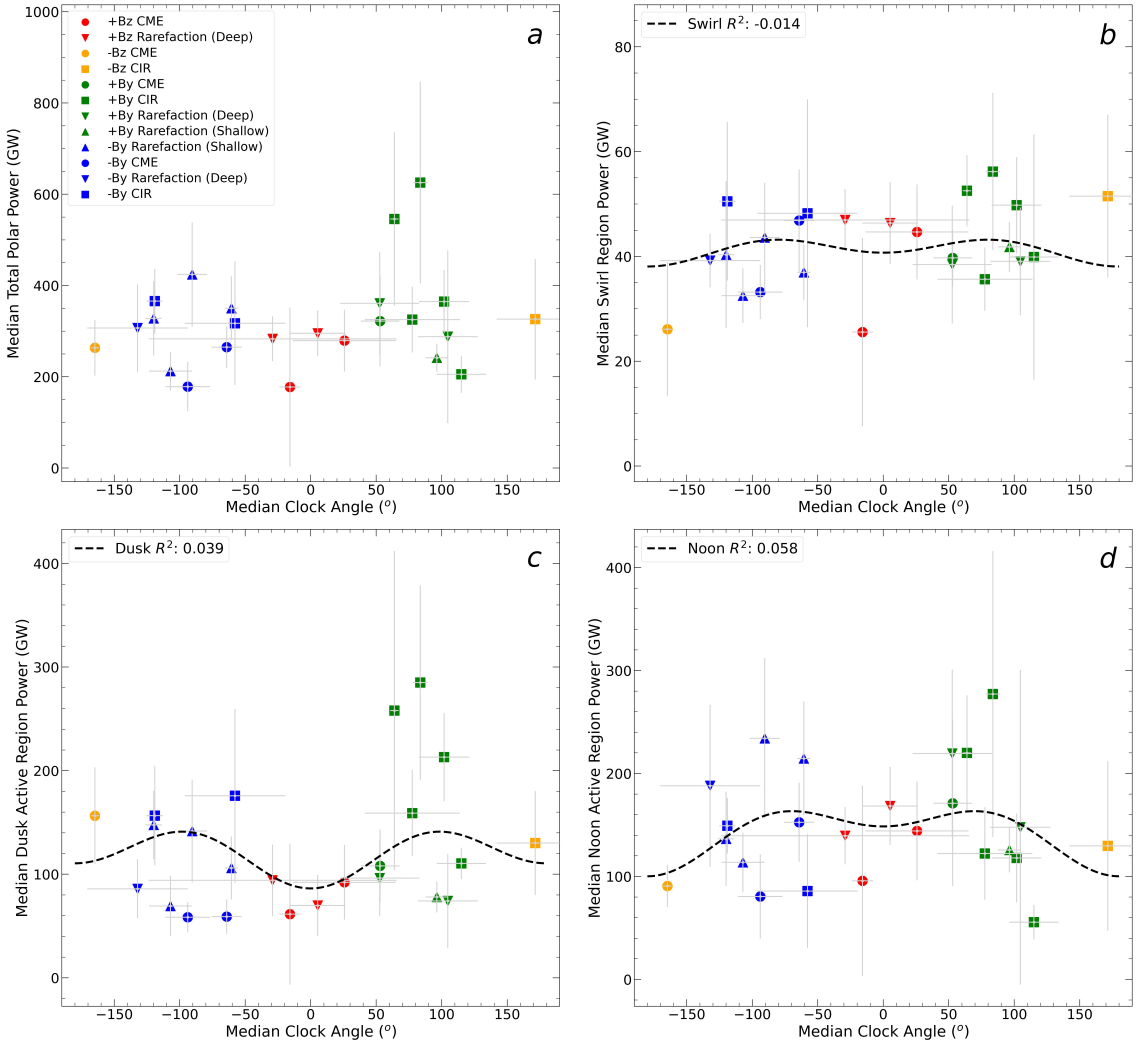

Figure 4.12: The relationship between median averaged clock angle per visit and median a) total polar power, b) swirl region power, c) dusk active region power and d) noon active region power. The relationship is tested using the equation $(A_1 \times \cos^2(\frac{x}{2}) + (A_2 \times \sin^2(x)) + C$, representing multi-latitude reconnection, plotted as the black dashed line.

bulk of the variance in the data is expected to be explained by internal processes. Although the polar regions have not been definitively determined as having a source of internal driving, the persistent lack of quiet intervals suggests an ongoing internal contribution. Additionally, other solar wind parameters, such as dynamic pressure and the perpendicular component of the IMF, have previously been suggested to influence auroral power in the dusk active region (Nichols et al., 2017). It is therefore reasonable to assume that multiple external drivers may contribute to the observed spread of auroral powers, reducing the proportion of the variance that can be attributed to clock angle alone. In this regime, a higher threshold of $R^2 = 0.3$ would likely be over-restrictive, as it would require a single parameter to dominate nearly a third of the observed variance. By adopting $R^2 = 0.2$, the analysis remains sensitive to these secondary but potentially physically meaningful couplings without being obscured by larger contributing drivers or background fluctuations. While an R^2 value of 0.2 is not considered to be a strong indicator of a relationship, it represents a threshold in which the contribution of the clock angle cannot be dismissed; it must be considered further with knowledge of the system and the results of previous studies to determine if the correlation has any physical meaning.

Figure 4.12 shows that the auroral behaviour of none of the three polar regions can be adequately explained by multi-latitude reconnection. This is most evident in the swirl region (panel b), where the R^2 value is -0.0014. The negative value indicates that not only does equation 4.7 fail to explain any of the variability in the data, but that a horizontal line plotted through the mean auroral power would be a better fit of the data. While the dusk active region (panel c) and noon active region (panel d) yield positive R^2 values of 0.039 and 0.058 respectively, they are significantly smaller than the threshold value of $R^2 = 0.2$, and thus cannot be considered to be indicative of an auroral response to clock angle. Although an R^2 value of 0.058 technically implies that 5.8% of the variance in auroral power could be attributed to multi-latitude reconnection, a value this small is more plausibly interpreted to statistical noise or incidental correlation rather than a genuine, albeit weak, physical

relationship suppressed by more dominant sources of auroral driving.

Before this coupling function is dismissed, the ±20% propagation window should be considered. This uncertainty, as discussed in Section 3.2.2 of Chapter 3, accounts for the assumptions used in calculating the timeshift between the Juno solar wind measurements and HST observations. These ±20% bounds serve as 'bookends', representing how the clock angle shifts if the solar wind arrives 20% earlier or later than calculated. If all three produce a similar fit, then the likelihood of any relationship between the IMF clock angle and auroral power is increased.

The purpose of this uncertainty is not only to assess the robustness of the results, but also to evaluate whether the nominal solar wind propagation time is accurate or if one of the 'bookends' is a better representation of the solar wind parameters when they reach Jupiter. As such, the +20% and −20% travel times are also evaluated individually for correlation with auroral power.

If one of the bookend cases shows a stronger relationship between the clock angle and the auroral response, this alone is not sufficient to conclude that a meaningful relationship exists. This is especially true if the nominal case and the opposite bookend have R^2 values below the threshold. Such results should be considered as tentative correlations and interpreted with more caution. This is also the case for correlations with the nominal travel time where the bookends do not meet the threshold.

Where any stronger correlation with a bookend propagation time occurs, it may suggest that this time more accurately represents the true solar wind travel time. However, this interpretation likely depends on whether other solar wind parameters also share a stronger correlation for the same propagation time. For example, this chapter also considers solar wind dynamic pressure and magnetic field strength - both of these solar wind parameters have been suggested to correlate with auroral power (Nichols et al., 2017). An improved correlation with both for the 20% shorter

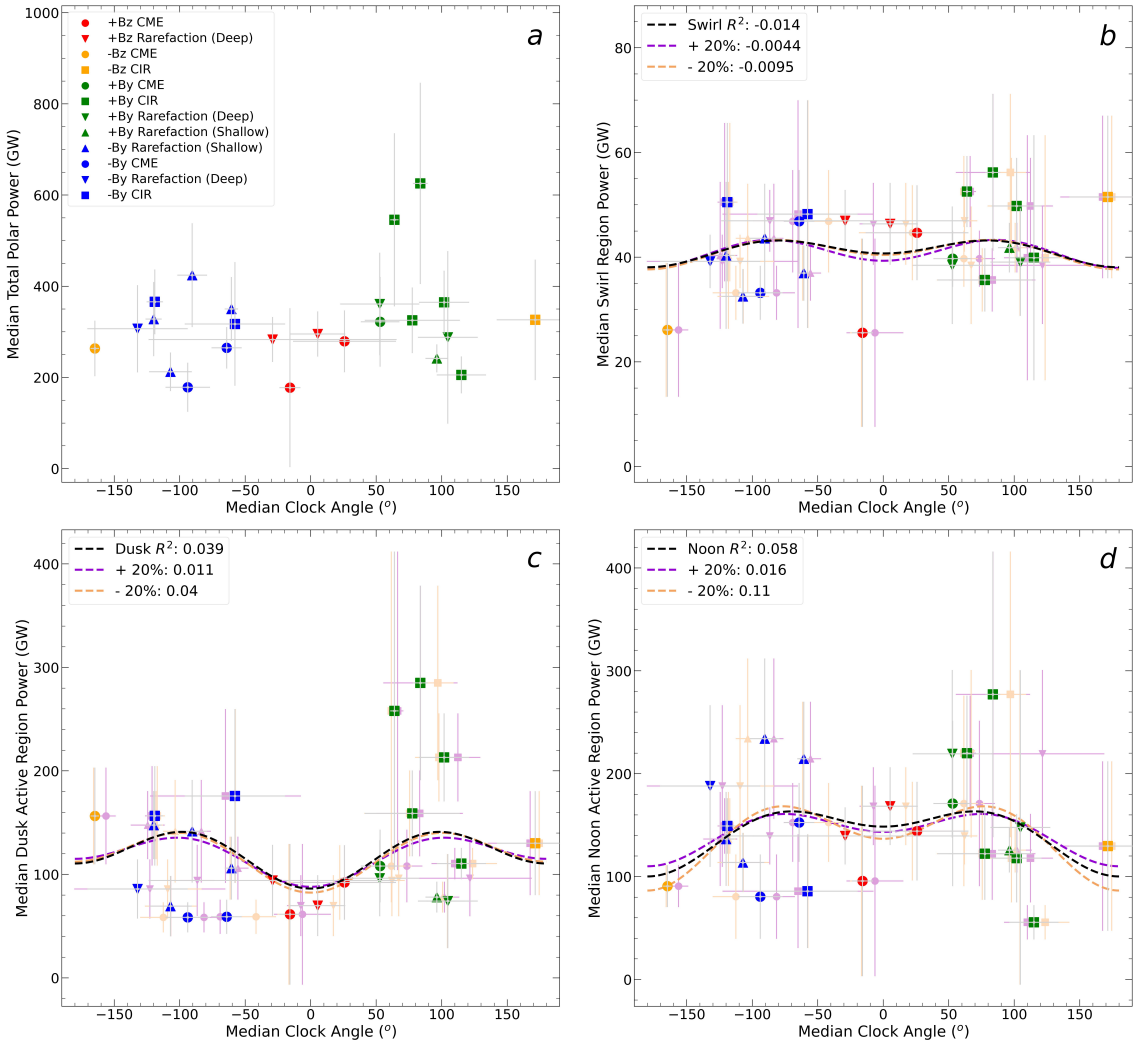

Figure 4.13: The same as figure 4.12 but with the addition of a ±20% propagation time uncertainty window applied to the solar wind travel time calculated from when Juno detected the solar wind to Jupiter's magnetosphere, thus shifting the clock angle data to the new data window for the time of the HST visit.

or longer time would support the case that the actual propagation time of the solar wind is closer to one end of the uncertainty window. However, it is also possible that the time frame for an auroral response is inconsistent for different solar wind parameters due to how the energy transferred into the system is transported through Jupiter's complex magnetosphere. In the situation that one of the bookends appears to be more representative of the auroral response to solar wind factors, then this may account for any lack of a consistency across the full solar wind propagation time window.

Figure 4.13 shows the addition of the ±20% solar wind propagation time uncertainty window, representing a 20% longer or shorter propagation time of the solar wind from Juno to Jupiter's ionosphere, also assessed using the R^2 analysis. Firstly, the difference between the R^2 values is examined. The swirl region (panel b) gives an R^2 value of -0.0044 for the 20% longer travel time and -0.0095 for the 20% shorter travel time, neither of which improve on the nominal fit as they remain negative. The dusk active region (panel c) yields a result of 0.011 for the 20% longer travel time and 0.04 for the 20% shorter travel time, which are worse and comparable, respectively. For the noon active region (panel d) 0.016 is calculated for the 20% longer travel time and 0.11 for the 20% shorter travel time - a stronger correlation for the latter, but weaker for the former. None of these R^2 values are fully consistent across the different solar wind arrival times, but this result is robust in the sense that none of the test times present a good fit, suggesting no driving by multi-latitude reconnection. A visual inspection of the clock angle medians for each visit does indicate that some visits undergo a large shift between these propagation times, and although most do not vary by more than $\sim 15^\circ$ from the nominal value, this is still a significant shift. With a small dataset, the high variability of the solar wind may still be the cause of this inconsistency in clock angle, even when using the adjusted R^2 parameter to compensate.

In terms of analysing the R^2 values for the ±20% propagation times individually,

none reach the threshold value. Although 0.11 for a 20% shorter propagation is a marked improvement in the correlation of auroral power and clock angle for the noon active region, not enough of the variance in auroral power can be explained by multi-latitude reconnection. It is likely also not worth considering the shorter travel time as a better representation of the actual solar wind arrival time.

This logic is followed to determine if any of the coupling functions well describe the relationship between solar wind parameters and auroral power, and thus potentially indicate Jupiter's polar emissions may be driven by the solar wind. This same logic is applied for the results for dynamic pressure and magnetic field strength in sections 4.3.3.1 and 4.3.3.2 later in this Chapter.

4.3.2.1 IMF Clock Angle Driving of the Swirl Region

The swirl region shows no measurable response to IMF clock angle driving, with all coupling functions returning negative R^2 values for all nominal, shorter and longer travel times. These negative values indicate that none of the variability in the auroral power can be explained by any of the coupling functions, with each one performing worse than a horizontal line fit through the mean auroral power. The plots for all coupling functions can been found in Appendix B.2. The lack of correlation suggests that any potential large-scale reconnection processes driven by IMF clock angle do not influence auroral emissions in the swirl region, at least not in a way that can be captured using equations 4.5, 4.6, 4.7 or 4.8.

The absence of solar wind control is particularly notable given that the swirl region is distinct from the rest of Jupiter's auroral emission as exhibiting a significantly higher colour ratio, ranging between 12 and 20 (Greathouse et al., 2021). As colour ratio is a proxy for the characteristic energy of precipitating particles, a higher CR indicates the presence of higher energy electrons in the swirl region that penetrate deeper into the atmosphere. Such a spectral distinction between auroral regions

implies variation in the energies of precipitating particles, which points to either different acceleration mechanisms or distinct electron populations. The lack of relationship with clock angle indicates that the difference in colour ratios between the swirl region and the main emission, which is known to be dominantly driven by internal processes, likely reflects internal factors rather than external solar wind influences. Another theory is photoionisation-induced conductivity, as the swirl region is generally quieter closer to midnight than the rest of the region (Greathouse et al., 2021). While this is a not internal driving, it is not solar wind control either.

Previous studies propose that the swirl region may map to various parts of Jupiter's magnetosphere, including: a mostly closed loop extending into the outer dawn magnetosphere that is occasionally threaded with open flux pulled back into the midnight sector (Zhang et al., 2021), open field lines that resemble a polar cap (Pallier and Prangé, 2001; Stallard et al., 2001; Stallard et al., 2003; Vogt et al., 2011) or a region in the dawn sector that undergoes large-scale, Dungey-like magnetic reconnection with the solar wind (Cowley et al., 2003). Each of these configurations allows for solar wind interaction but results in different auroral generation mechanisms. In all cases, a dependence on IMF orientation is expected - although the specific direction of the dependence varies on the mapping location. However, since auroral emission along open field lines generally requires solar wind driving to energise particles down into the ionosphere (Delamere and Bagenal, 2010), the observed lack of clock angle dependence argues against the swirl region being connected wholly to open field lines. Furthermore, the continuous presence of auroral emission with no observed 'off' periods supports this interpretation, as auroral emission on open field lines tends to be sporadic or absent during intervals of weak solar wind driving. Unless an internal process exists that can drive emission despite open topology, this suggests the swirl region likely maps to mostly closed field lines.

It should be noted, however, that this study cannot rule out the possibility of a

Dungey-like process at Jupiter. Reconnection in the magnetotail, driven by flux opened on the dayside, occurs over longer and less predictable timescales. Due to the size of the Jupiter system, these timescales would likely be on the order of days (McComas and Bagenal, 2007). If the swirl region maps to the dawnside magnetosphere, it might respond to the initial dayside reconnection event. In such a case, a dependence on IMF clock angle would be expected at the onset of the Dungey cycle. However, since no such relationship is observed, it is likely that any dayside reconnection due to a Dungey-like process has no measurable impact on the swirl region.

Transpolar arcs, sometimes known as theta aurora, can occur on open field lines and are present during northward IMF at Earth - in which large-scale reconnection is limited. Associated with both solar wind and ionospheric plasma, transpolar arcs at Earth are suggested to occur due to multiple cases of the Kelvin-Helmholtz (K-H) instability, which occurs due to large shear flows across the magnetopause boundary and internal shear flows in the plasma sheet (Zhang et al., 2020). As the Kelvin-Helmholtz instability has been proposed as a mechanism for energy transfer at Jupiter, (Delamere and Bagenal, 2010; Masters, 2017) this could explain aurora on open field lines with no IMF clock angle dependence for the swirl region. The typical behaviour of swirl region emission, however, is very different to the long extended auroral form of the transpolar arc. It should be noted that features similar to transpolar arcs have been observed in the swirl region of Jupiter, but they have been found to be independent of the solar wind (Nichols et al., 2009a), and they may not represent the same phenomena.

If the swirl region maps to mostly closed field lines on the dawnside, the absence of a response is consistent with previous findings that suggest magnetic reconnection is suppressed on this flank of the magnetosphere. This is due to strong shear flows between the solar wind and Jupiter's rapidly rotating magnetosphere, which introduce turbulence and disrupt the conditions necessary a stable reconnection

region to form (Desroche et al., 2012). In either case, the lack of correlation with clock angle suggests that internal magnetospheric processes are the primary drivers of auroral activity in this region. Why this region exhibits a notably higher colour ratio than the rest of Jupiter's auroral regions remains an open and intriguing question.

4.3.2.2 IMF Clock Angle Driving of the Dusk Active Region

The dusk active region, like the swirl region, shows no response to IMF clock angle driving. For all tested coupling functions, the R^2 values fall below the threshold value, with no notable improvement when the solar wind travel time is adjusted by $\pm 20\%$. Notably, the R^2 values are negative for dayside and post-cusp driving, indicating that the coupling functions are a worse fit to the data than a straight line through the median auroral power. See Appendix B.2 for the full set of plots.

MHD modelling predicts that the dusk active region is coincident with variable regions of open magnetic flux labelled as a 'duskside patch', which trails behind the planet in the midnight sector when open (Zhang et al., 2021). The full dusk active region may not map to this patch, which could potentially explain the highly dynamic and seldom quiet, emission in the region and it seems unlikely that particle precipitation from direct solar wind entry into an open patch of field lines could drive the observed emission without an internal source - particularly if post-cusp reconnection is not significant contributor.

Recent work has suggested the cusp region of Jupiter may be located on the duskside of the planet, in the post-dusk sector, and an area of open flux may arc through the noon active region through to the dark polar region across midnight (Xu et al., 2024). However, the dusk active region is unlikely to magnetically connect to this location as the high brightness of the region is unlikely to be the result of direct solar wind entry via the open flux region. While cusp aurora exist at Earth as a

direct result of particle precipitation (Mende et al., 2016), they are generally much fainter than Earth's main auroral oval. Furthermore, the absence of any measurable response to the IMF clock angle also suggests that any open field lines mapping to the dusk active region do not have a significant input in terms of auroral power in this region. Particles may be accelerated into the ionosphere on these open field lines, but the internal contribution from closed field lines appears to be the main source of emission. As noted for the swirl region, the persistent auroral activity here also supports a majority closed field line interpretation. This conclusion holds unless there is a process capable of generating emission across areas of open field, akin to transpolar arcs at Earth (Frank et al., 1986). Unlike in the swirl region, the dusk active region does contain arcs of emission, making the suggestion of Kelvin-Helmholtz driven aurora (see Chapter 5) that can occur in areas of open field more appropriate for this region.

Magnetic field mapping instead associates the dusk active region with the outer dusk magnetosphere (Vogt et al., 2011). Although shear flows are weaker on the dusk flank, high-latitude reconnection should still be theoretically possible, assuming suppression of reconnection at low latitudes by high $\Delta\beta$ across the magnetopause boundary. Nevertheless, the R^2 value for high-latitude reconnection coupling function is only 0.024, which indicates high-latitude reconnection either does not occur or is not a significant driver of emission. This may be due to Jupiter's complex magnetic structure, including its bent-back magnetic field, which could make reconnection unfavourable at high latitudes. Alternatively, any reconnection-driven aurora may simply be too weak to be distinguished from stronger internally driven processes.

The dusk active region has been observed to brighten in response to magnetopause compressions. Similarly, the main emission has been shown to brighten under enhanced pressure conditions (Giles et al., 2025; Nichols et al., 2009b; Yao et al., 2022). Given that the main emission is dominated by internal dynamics, a pressure-

induced auroral response in the dusk active region may likewise suggest an internal origin for its main driving process. The relationship between solar wind dynamic pressure and the dusk active region is explored further in Section 4.3.3.1.

4.3.2.3 IMF Clock Angle Driving of the Noon Active Region

Similarly to the swirl and dusk active regions, the noon active region shows no statistically significant response to IMF clock angle driving. Across all tested coupling functions, the R^2 values remain below the threshold of 0.2, with the highest value being 0.11 for multi-latitude reconnection at the 20% shorter solar wind travel time. No coupling function is negative for all three travel times, but all include at least one negative R^2 value except for multi-latitude reconnection. This indicates that a horizontal line through the mean may outperform most of the coupling functions. The full set of plots is provided in Appendix B.2. These results show that variations in the auroral power cannot be reliably explained by IMF clock angle-driven reconnection processes, suggesting that it is not a significant driver of emission for the noon active region.

Magnetic field mapping suggests that the noon active region maps to the outer magnetosphere near local noon (Vogt et al., 2011), where dayside reconnection akin to the Dungey cycle at Earth is expected to be suppressed due to high shear flows and high plasma $\Delta\beta$ across the magnetopause boundary (Desroche et al., 2012). The lack of clock angle response is consistent with this interpretation and supports the idea that the noon active region maps to closed field lines, potentially near local noon.

MHD modelling suggests that both the noon active region and the dark polar region may be associated with open magnetic flux that extends across the nightside of the planet, although majority of the noon active region is attributed to closed field lines (Xu et al., 2024; Zhang et al., 2021). The results presented here may also

support this interpretation. Regions of open flux are expected to be quiet in terms of emission (Delamere and Bagenal, 2010), but if the noon active region maps to both open and closed flux, much of the highly dynamic and continuously active emission in this region can be internally driven. The model implies that the closed field lines associated with the noon active region map to the dawn to midnight equatorial magnetosphere and that the auroral activity in the region may potentially be attributed to tail dynamics (Zhang et al., 2021). The dark polar region, which is typically very quiet in terms of auroral emission, does likely map to the open flux described by MHD modelling. In this case, investigating the dark polar region for a correlation with IMF clock angle may be worth pursuing, despite the much lower rate of emission than the other polar regions.

Taken together, these results support the interpretation that internal magnetospheric dynamics dominate auroral emissions in the noon active region, consistent with the dusk and swirl regions.

4.3.3 Other Solar Wind Parameter Relationships with Polar Auroral Power

4.3.3.1 Solar Wind Pressure Driving of the Polar Regions

For the three polar auroral regions studied, only the dusk active region shows a statistically significant response to variations in solar wind dynamic pressure. As shown in figure 4.14, the relationship between median pressure per visit and the median auroral power in the dusk active region yields R^2 values of 0.27 (nominal), 0.29 (longer travel time) and 0.28 (shorter travel time). All three exceed the $R^2 = 0.2$ threshold used throughout this study, indicating a consistent, moderate correlation. In contrast, both the swirl and noon active regions return R^2 values below the threshold for all travel times (see Appendix B.3), suggesting no pressure dependence

in these regions.

As figure 4.14 is a linear fit in semi-log space, this implies a logarithmic relationship between auroral power and solar wind dynamic pressure in the dusk active region. Physically, this suggests that the aurora is more sensitive to pressure fluctuations at lower magnitudes, such as that a small increase in dynamic pressure has a more pronounced effect on auroral power when the pressure is already low rather than when the magnetosphere is already in a compressed state due to a high initial dynamic pressure. This implies that the solar wind's influence on the dusk active region is greater at the onset of a solar wind compression event following a period of rarefaction, with the rate of auroral intensification diminishing as the magnitude of the pressure continues to increase.

Despite this clear physical trend, an R^2 value of 0.27 still represents a weak correlation in absolute terms. This suggests that while pressure may modulate the auroral power in the dusk active region, it is unlikely to be the sole driver of variability. The auroral response may instead be governed primarily by internal processes, with solar wind pressure acting as a secondary, modulating factor - a behaviour also seen in Jupiter's main emission, which brightens during periods of increased solar wind dynamic pressure despite its internal origin (Giles et al., 2025; Nichols et al., 2009b; Yao et al., 2022).

These results are consistent with previous findings, where auroral power was observed to increase during periods of magnetospheric compression (Nichols et al., 2017), and auroral arcs known as 'bridges' are noted to form close to the main emission (Head et al., 2025). The results presented here validate and strengthen this conclusion by applying a more targeted statistical analysis and direct pressure-power comparison not included in previous work. The robustness of the response across the $\pm 20\%$ propagation time uncertainty window further supports the interpretation that the solar wind dynamic pressure has a genuine, though limited, influence on auroral variability in the dusk active region.

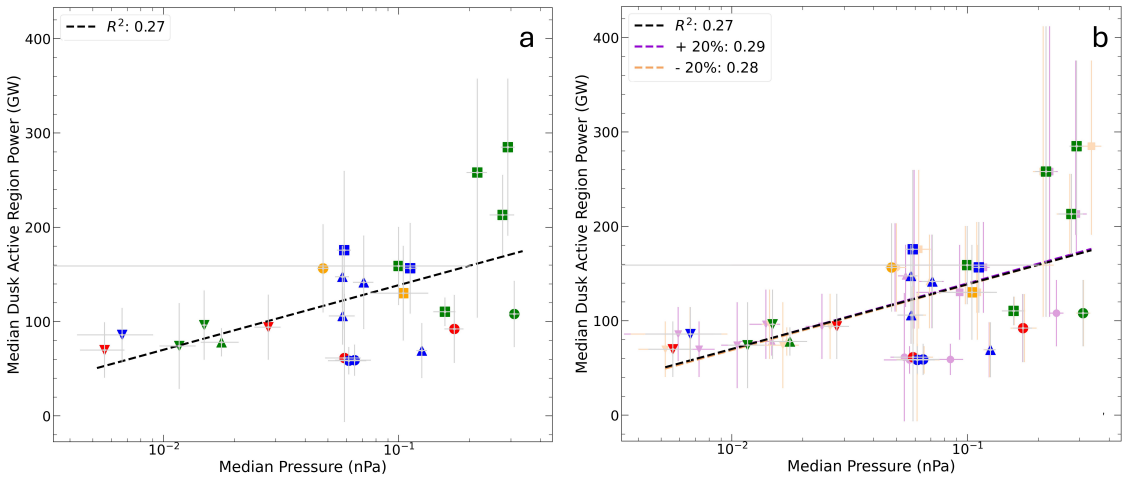

Figure 4.14: The relationship between median averaged solar wind dynamic pressure per visit and the median total power per visit for the dusk active region. Panel a) shows the fit for the nominal solar wind travel time and panel b) includes the fits for the ±20% solar wind travel time shifts. The relationship is plotted on a log_{10} pressure scale. All three fits exceed the $R^2 = 0.2$ threshold, indicating a correlation between pressure and auroral brightness in the dusk active region.

The lack of a pressure response in the swirl and noon active regions indicates that the source of emission in these regions must differ in some way from the dusk active region. Given the absence of any statistically significant clock angle dependence, it remains likely that all three regions are dominated by an internal source of driving. However, if the dusk active region responds to pressure in a similar manner to the main emission while the swirl and noon active regions do not, this may reflect the differences in where the three regions map to in the magnetosphere. These locations may experience varying levels of sensitivity to pressure variations. Notably, the noon active region has been proposed to map to the outer magnetosphere near local noon (Vogt et al., 2011), where strong pressure-driven effects might be expected due to its proximity to the subsolar magnetopause. In this region, variations in dynamic pressure are known to compress or expand the magnetopause boundary, which could in principle modulate auroral processes. The lack of correlation in

this case could imply that the noon active region does not map to this location and may be magnetically connected to the dawn sector of the outer magnetosphere instead, as discussed in Section 4.3.2.3. It is also possible that the pressure-emission relationship is more complex in this region and is not well captured by a simple linear fit.

As previously mentioned, solar wind interaction with Jupiter's magnetosphere has also been proposed to occur through viscous processes, such as the Kelvin-Helmholtz instability - particularly along the dawn and dusk flanks (Delamere and Bagenal, 2010; Masters, 2017; Zhang et al., 2018). The K-H growth rate is influenced by plasma density, which itself is related to dynamic pressure through the relation $\rho = \frac{p}{v^2}$. The observed pressure sensitivity in the dusk active region may therefore point to such flank interactions as a contributing factor to auroral power in this region - either in addition to, or instead of, representing modulation of internal driving. If so, this could explain why the noon active region does not show a pressure response, despite its location near the subsolar magnetopause. The potential contribution of the Kelvin-Helmholtz instability is investigated further in Chapter 5.

4.3.3.2 Solar Wind Magnetic Field Driving of the Polar Regions

The results indicate that only the dusk active region exhibits a potential correlation between auroral power and both the perpendicular component of the solar wind magnetic field ($B_\perp$) and the total field strength (B_{total}) As shown in figure 4.15, the dusk active region yields R^2 values of approximately 0.37 (nominal), 0.076 (20% longer travel time), and 0.37 (20% shorter travel time) for $B_\perp$ and 0.36 (nominal), -0.0019 (20% longer travel time), and -0.0036 (20% shorter travel time) for B_{total}. While the correlation is moderate for the nominal fits, it degrades substantially when accounting for the propagation time uncertainty, especially for longer travel times. This indicates a lack of robustness across the travel time window.

In contrast, the swirl and noon active regions show no statistically significant relationship with either $B_\perp$ or B_{total}, with R^2 values under the threshold value or slightly negative across all travel times (ranging from -0.045 to 0.072). Combined with the absence of any correlation with clock angle, this further indicates that the two regions are likely to be internally driven. At Earth, the IMF clock angle determines whether the orientation of the magnetopause field favours reconnection, while the IMF strength governs the intensity of the reconnection and the subsequent energy transfer into the magnetosphere (Gonzalez and Tsurutani, 1987; Vichare et al., 2005). As such, the lack of auroral response to IMF strength in the swirl and noon active regions reinforces the earlier conclusion that their variability is dominated by internal processes, as also indicated by the absence of clock angle dependence.

The similarity in R^2 values for $B_\perp$ and B_{total} in the dusk active region is expected, as the only difference is the exclusion of the B_x component in $B_\perp$. As B_x lies along the solar wind flow direction and is not considered to contribute significantly magnetospheric driving processes, its inclusion in B_{total} may contribute to the poorer correlation stability across the range of travel times. The better consistency observed in $B_\perp$ across the travel time range may therefore reflect a clearer physical relationship between the solar wind and the dusk active region.

Despite the lack of robustness across all travel times, the nominal result aligns with previous findings. Nichols et al. (2017) report a statistically significant correlation between $B_\perp$ and auroral power in the dusk active region, with a Pearson's correlation coefficient of $r = 0.59$ and a corresponding p-value of 0.023. A Pearson r of 0.59 indicates a moderate positive linear relationship, while the p-value quantifies the probability of obtaining such a correlation by chance. Since a p-value below 0.05 is typically considered statistically significant, the observed correlation is unlikely to be coincidental. For a linear relationship, the Pearson correlation coefficient can be squared to relate it to the R^2 value (e.g. Schober et al. (2018)) presented in

section 4.2.2.3. This gives a value of 0.35 for the Nichols et al. (2017) r value, which is comparable to the $R^2 = 0.37$ found here at nominal travel times. Although a different statistical measure is used, the findings remain consistent and support the interpretation that the dusk active region responds to variations in solar wind magnetic field strength. The present analysis also accounting for propagation time uncertainty, underscores the tentative nature of the observed relationship.

The dusk active region therefore presents a complex case. Despite a moderate correlation with both $B_{\perp}$ and B_{total}, it shows no dependence on clock angle. If reconnection is not the dominant interaction mechanism, the observed sensitivity to magnetic field strength must arise from an alternative process. One possibility, as suggested in both sections 4.3.2.2 and 4.3.3.1, is that the dusk active region is influenced by the Kelvin-Helmholtz instability. While the solar wind magnetic field does not directly control the K-H growth rate, it may play an indirect role by modifying the stability of the boundary layer (Masters, 2017). Whether such effects are sufficient to produce the observed R^2 value is unclear. Other potential mechanisms include wave-particle interactions or magnetospheric current systems driven indirectly by solar wind magnetic field variations, but further investigation is required to clarify if any of these processes contribute to auroral variability.

It is also notable that elevated magnetic field strengths and pressures often co-occur during solar wind compression events, as is the case in this dataset. This shared variability likely contributes to the observed correlation between auroral power and magnetic field strength. However, while the pressure correlation is weaker ($R^2 = 0.27$) compared to the magnetic field strength at nominal travel times (0.38), the correlation for magnetic field strength shows greater variability and lacks robustness across the full propagation time uncertainty window. This variability suggests that the nominal R^2 value for magnetic field strength may be overestimated. Consequently, it remains unclear whether solar wind dynamic pressure or magnetic field strength independently drives auroral variability in the dusk active region,

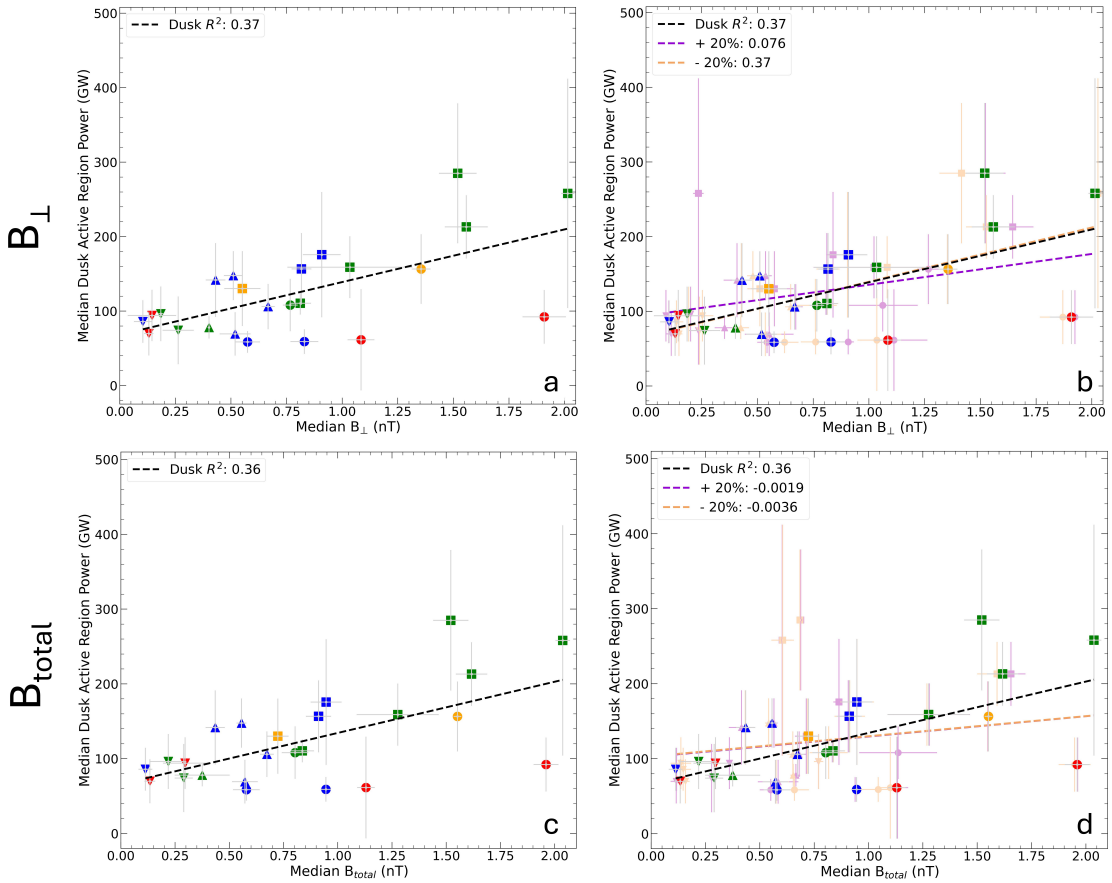

Figure 4.15: Relationship between median solar wind magnetic field magnitude and median auroral power for the dusk active region. Panels a) and b) show the fits for the perpendicular magnetic field magnitude at nominal and ±20% solar wind travel times, respectively. Panels c) and d) show the corresponding fits for the total magnetic field magnitude. While nominal correlations are moderate, the strength of the correlation varies significantly across the travel time uncertainty window, indicating this relationship is not robust.

or whether the observed relationships arise from their mutual correlation or other underlying factors.

Overall, the positive correlation between IMF strength and auroral power in the dusk active region supports the interpretation that this region maps to a magnetospheric location directly influenced by solar wind conditions. This is consistent with previous flux mapping studies that associate the dusk active region with the outer dusk flank of Jupiter's magnetosphere (Vogt et al., 2011).

4.4 Conclusion

Parameter	Swirl Region	Noon Active Region	Dusk Active Region
HL Driving	×	×	×
ML Driving	×	×	×
Dayside Driving	×	×	×
PC Driving	×	×	×
IMF Strength	×	×	Moderate, Tentative ($R^2 = 0.37$)
Pressure	×	×	Moderate ($R^2 = 0.27$)

Table 4.2: Summary of the relationships between polar auroral power and potential solar wind driving parameters. HL = high-latitude; ML = multi-latitude; PC = post cusp. Here, crosses indicate no statistically significant relationship ($R^2 < 0.2$) and "tentative" denotes relationships that are present for nominal propagation times but do not persist across the whole ±20% propagation time window.

This chapter investigates the relationship between auroral power and the solar wind for three auroral regions: the swirl region, dusk active region and noon active region. Solar wind coupling is assessed using the IMF clock angle, dynamic pressure and magnetic field strength. Of the three regions, only the dusk active region shows a

measurable response to solar wind driving, with a moderate correlation with both pressure and magnetic field strength, but no correlation with IMF clock angle.

This suggests the dusk active region may be driven by an internal magnetospheric source, but externally modulated by the solar wind. Jupiter's main emission is known to be dominated by internal driving processes but has been observed to brighten during periods of enhanced dynamic pressure (Giles et al., 2025; Nichols et al., 2009b; Yao et al., 2022), and the dusk active region may exhibit similar behaviour. The response to magnetic field strength is much more tentative, as the correlation is not robust across the travel time uncertainty window, but the combination of pressure and magnetic field strength may be more indicative of other solar wind coupling mechanisms, such as Kelvin-Helmholtz instabilities or wave-particle interactions. However, as high pressure and magnetic field strength typically occur co-currently during the dataset, it is unclear whether one or both parameters independently influence auroral power in this region.

In contrast, the swirl and noon active regions show no significant response to any tested solar wind parameters, suggesting that both these regions are governed entirely by internal sources. While the two regions are very different in terms of auroral behaviours, typical brightness and measured colour ratio (Greathouse et al., 2021), there is no external factor to distinguish between the two regions. Although the noon active region visually has more in common with the dusk active region, the two appear to be clearly separate regions, despite often being described collectively as a single 'active' region.

While the results in this chapter are not definitive, they do provide valuable insights into the relationship between solar wind conditions and auroral emissions in the polar regions of Jupiter. While the results of this study indicate that the auroral emission observed in each region are likely driven by an internal source rather than the solar wind, multiple previously studies imply that the magnetic mapping of the polar regions is complex and does not appear to be as simple as one region

representing open flux and another being closed (Delamere et al., 2024; Xu et al., 2024; Zhang et al., 2021). With no observed relationship with IMF clock angle, no region appears to be composed so that the majority of the connected field lines are open. In the case that some open flux is present within a region, the internal driving may dominate any solar wind contribution, masking any relationship with IMF clock angle, and so these results only indicate that clock angle driving does not represent a measurable contribution to auroral emissions in the polar regions. Further assessment of the solar wind influence is therefore required.

There are some caveats and limitations to this study, however. The first of these is the limited dataset. With only 24 visits, the R^2 analysis is much more sensitive to noise within the data, even when the adjusted R^2 parameter is used. Although more data points would undoubtedly improve this study, there is limited upstream solar wind data concurrent with auroral imagery, and frame-by-frame plasma comparison of HST images with the solar wind plasma data is not feasible due to the some visits having minimal assigned data points after the solar wind is propagated from Juno to Jupiter.

Another caveat is that the calculated travel times for the solar wind rely on the Joy model (Joy et al., 2002). However, a new updated bow shock model by Rutala et al. (2025) indicates that the subsolar standoff distances for the bow shock and magnetopause sit closer to Jupiter than predicted by previous models. As the solar wind travel time is influenced by both the distance to the bow shock from Juno and the time spent in the magnetosheath, the propagation times for the solar wind data from Juno to the ionosphere calculated in Chapter 3 would naturally change to reflect the new boundary locations. As this updated model affects both the 'backwards' distance shift (T_{shift}) and the traversal of the sheath (T_{sheath}), the net impact on the total propagation time depends on the relative change in each component; with Juno approaching Jupiter and both boundaries consistently varying with solar wind conditions, the magnitude of the adjustment to longer or shorter times would vary

throughout the study.

However, the exact magnitude of these changes remains uncertain, and further investigation using the updated model would be needed to assess how the shift in the bow shock's location might influence solar wind propagation times - especially for the dusk active region, where 20% longer propagation times suggest that its correlation with magnetic field strength may no longer hold.

In summary, while solar wind pressure and magnetic field strength show some influence in the dusk active region, the primary driver of auroral emissions in all three regions studied, is likely internal magnetospheric processes. The very different behaviours of the regions, particularly between spectrally distinct swirl region and more dynamic active regions, cannot be explained through solar wind coupling. Why the swirl region has a much higher colour ratio compared to the rest of Jupiter's auroral emissions remains an open question.

Chapter 5

The Relationship between Energy Inputs from Solar Wind-Magnetosphere Coupling and Auroral Power at Jupiter

5.1 Introduction

The aim of this study is to investigate potential energy inputs from the solar wind into Jupiter's magnetosphere and assess whether the power generated by solar wind-magnetospheric coupling shows any correlation with the auroral power in the polar regions. This work builds on the findings of Chapter 4, which suggests that the solar wind may act as an external modulating force for the dusk active region. By evaluating different solar wind coupling processes, this chapter aims to provide further insight into the role of the solar wind in driving auroral emissions at Jupiter.

Reconnection voltages have been historically used to estimate the rate of energy

transferred to a magnetosphere via dayside solar wind coupling. At Jupiter, the low-latitude reconnection voltages have been used as a diagnostic for solar wind energy input (Gershman and DiBraccio, 2024; Nichols et al., 2017, 2006), using the rate of open flux production to assess how much energy within the system can be attributed to large-scale reconnection. While this is estimated to be relatively low (Gershman et al., 2024), it may be able to quantify if energy transferred by this mechanism has any contribution to auroral power in the polar regions. Although no correlation with IMF clock angle has been identified (see Chapter 4), the formulation for reconnection voltage involves additional solar wind factors that may capture any relationship masked by other auroral driving processes.

The other energy transfer process investigated in this chapter is the Kelvin-Helmholtz (K-H) instability. The K–H instability has been proposed as a viable means of transferring solar wind energy into Jupiter's magnetosphere (Delamere and Bagenal, 2010; Gershman and DiBraccio, 2024; Masters, 2017, 2018; Zhang et al., 2018). Though K-H occurs on closed field lines, it has been associated with auroral emission at high-latitudes at Earth, sometimes in regions mapping to open flux (Zhang et al., 2020). As the polar auroral regions are associated with a mixture of open and closed flux (as discussed in Chapter 4), assessing if a relationship exists between the energy transferred into the magnetosphere by the instability and auroral power could address how regions with potentially a significant amount of open flux can have highly dynamic aurora. Although, it may also indicate the region maps to mostly closed field lines as a sufficient transport system would need to exist for K-H transferred energy to drive auroral emission in areas of open flux.

These voltages and powers calculated from upstream solar wind conditions, representing potential energy transfer through these processes, will be compared with auroral power for each of the three polar regions to assess whether any correlation exists. A correlation with one of these estimated reconnection rates may provide insight into the specific processes by which the solar wind transfers energy into the

magnetosphere.

5.2 Reconnection Voltages

5.2.1 Calculation of Reconnection Voltages

5.2.1.1 Calculation of Low-Latitude Reconnection Voltage

Reconnection voltage is a measure of the rate of magnetic flux transfer across the magnetopause due to magnetospheric reconnection. It represents the electric potential generated by solar wind interaction with the planetary magnetic field and serves as a proxy for the strength of solar wind–magnetosphere coupling. Studies at Earth have investigated reconnection voltage as a measure of the reconnection rate (Perreault and Akasofu, 1978), typically expressed as:

$$\phi = V_{sw} B_{\perp} L \tag{5.1}$$

where v_{sw} is the velocity of the solar wind, $B_{\perp}$ is the component of the solar wind IMF perpendicular to the Sun-Jupiter line and L is the width of the channel over which reconnection can occur. This formulation has since been further developed for Saturn (Jackman et al., 2004) and subsequently adapted for Jupiter (Nichols et al., 2006) in the form:

$$\phi_{LL} = V_{sw} B_{\perp} L_o \cos\left(\frac{\theta_c}{2}\right)^4 \tag{5.2}$$

where $L_o = \frac{R_{MP}}{2}$, representing half the subsolar radius of the planet's magnetosphere (Milan et al., 2004), and θ_c is the clock angle (see Chapter 4). The $\cos\left(\frac{\theta_c}{2}\right)^4$ term modulates the reconnection rate based on IMF orientation. When the IMF is unfavourably aligned ($-B_z$ for Jupiter), this factor approaches zero, effectively suppressing reconnection. As seen in Table 5.1, for a $\pm B_y$ IMF orientation this factor equals 0.25 and for $+B_z$ it reaches the maximum value of 1.

Function	$\theta = -90°$ (-B_y)	$\theta = 0°$ (+B_z)	$\theta = 90°$ (+B_y)	$\theta = 180°$ (-B_z)
$\cos^4(\frac{\theta}{2})$	$\frac{1}{4}$	1	$\frac{1}{4}$	0
$\cos^4(\frac{\theta+90}{2})$	1	$\frac{1}{4}$	0	$\frac{1}{4}$
$\sin^4(\frac{\theta+90}{2})$	0	$\frac{1}{4}$	1	$\frac{1}{4}$

Table 5.1: Trigonometric functions and resulting values for each clock angle quadrant, used to determine appropriate functions for modulating the reconnection voltage at different locations along Jupiter's magnetopause.

Equation 5.2 describes the rate of open flux production at Jupiter's dayside magnetopause due to low-latitude reconnection. Variations in auroral power associated with reconnection being favoured at low latitudes are investigated in Chapter 4 using equation 4.5 as a coupling function to examine this dayside process. Although no evidence was found to suggest that reconnection under conditions favouring IMF $+B_z$ significantly drives auroral power in either polar region, the low-latitude reconnection voltage incorporates solar wind velocity and IMF magnitude in addition to the IMF clock angle—factors that may influence the strength of the coupling. As such, auroral power may still correlate with the reconnection voltage, even if no correlation with dayside reconnection itself was observed.

It must be noted that equation 5.2 does not account for the likely suppression of low-latitude reconnection at Jupiter due to high shear flows and high $\Delta\beta$ across the magnetopause boundary. As such, equation 5.2 provides an upper-limit of the reconnection rate, based solely on upstream solar wind conditions and the size of the magnetosphere.

5.2.1.2 Calculation of High-Latitude Reconnection Voltage

Although equation 5.2 has previously been adapted for post-cusp reconnection, prior studies of reconnection voltages at Jupiter (Nichols et al., 2006) have not considered high-latitude reconnection along the dawn and dusk flanks as a mechanism for solar

wind–magnetosphere energy transfer. However, simulations have suggested that such high-latitude reconnection sites may exist at Jupiter (Masters, 2017). In this study, the low-latitude reconnection voltage formulation is adapted for the first time to estimate high-latitude reconnection voltages.

At the high-latitude flanks, Jupiter's magnetic field is primarily orientated along the y-axis. Therefore, IMF $\pm B_y$ is expected to favour reconnection, depending on the local time sector and hemisphere. In the northern hemisphere the dawn flank of the magnetosphere is aligned in the $-y$ direction, favouring reconnection under IMF $+B_y$ conditions and the dusk sector of the magnetosphere is aligned in the $+y$ direction, favouring IMF $-B_y$ conditions. In the southern hemisphere, these orientations are reversed: the dawn flank is aligned in the $+y$ direction and thus favours $-B_y$ IMF, while the the dusk flank is aligned in the $-y$ direction and thus favours IMF $+B_y$. A diagram showing the local time asymmetry of this flank reconnection can be seen in figure 5.1.

Although it may seem intuitive to describe these equations in terms of reconnection occurring on the dawn or dusk flanks, this becomes ambiguous when considering both hemispheres. Although this study focuses only on auroral observations in the northern hemisphere, using IMF polarity ($\pm B_y$) as the basis for distinguishing reconnection conditions avoids confusion and provides a consistent framework for interpreting the results.

To represent this behaviour, two new equations are developed to calculate the reconnection voltage under the two relevant IMF orientations. The choice of sinusoidal dependence in each case is informed by the coupling functions summarised in Table 5.1:

$$\phi_{HL,+B_y} = \frac{1}{2} V_{sw} B_\perp L_o \sin\left(\frac{\theta_c + 90}{2}\right)^4 \tag{5.3}$$

$$\phi_{HL,-B_y} = \frac{1}{2} V_{sw} B_\perp L_o \cos\left(\frac{\theta_c + 90}{2}\right)^4 \tag{5.4}$$

Equation 5.3 corresponds to reconnection driven by $+B_y$ IMF and equation 5.4

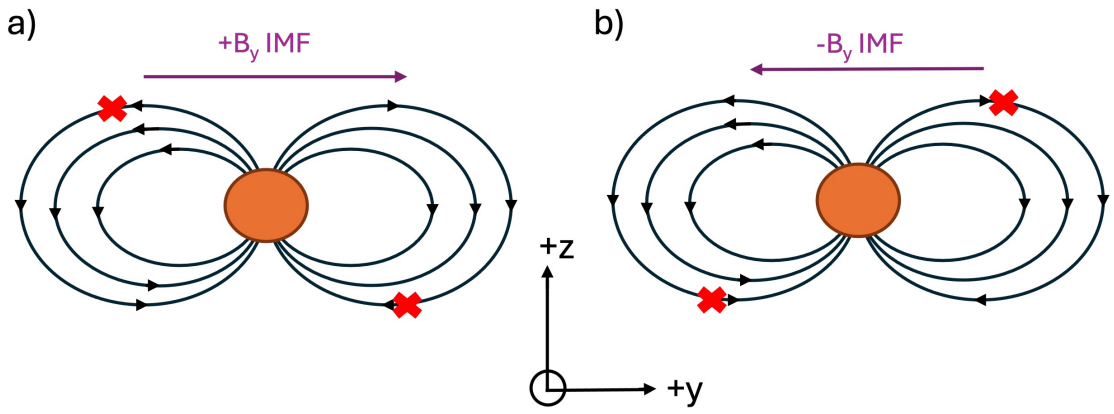

Figure 5.1: The distribution of reconnection sites under (a) $+B_y$ IMF and (b) $-B_y$ IMF conditions. Diagrams are orientated so the sun is out of the page along x, the dawn sector is on the left and the dusk sector is on the right, where the red crosses indicate the reconnection site.

corresponds to reconnection under $-B_y$ IMF.

The factor of $\frac{1}{2}$ in equations 5.3 and 5.4 is included based on models of post-cusp reconnection, (Bunce et al., 2005; Milan, 2004). While this factor is included in previous literature, the reasoning for the value is not explicitly given. As discussed in the literature, it likely reflects the reduced spatial extent of reconnection at higher latitudes and so it is used here under that assumption. The $+90°$ phase shift in the trigonometric terms of both equations modifies the angular dependence such that the maxima and minima of the reconnection voltage now align with a $\pm B_y$ orientated IMF, in contrast to the B_z orientation dependence equation 5.2.

Since reconnection at high latitudes in a closed magnetosphere is expected to occur under both $\pm B_y$ IMF polarities, equations 5.3 and 5.4 will likely only show a correlation between reconnection rate and auroral power if the polar region maps predominantly to open field lines. These equations predict a reconnection voltage of zero for the opposite B_y polarity, implying that reconnection occurs only under one IMF B_y configuration—an unlikely scenario for a closed magnetosphere. Even

if reconnection on the dawnside is suppressed by turbulence from high shear flows disrupting stable reconnection, duskside reconnection should still respond to the opposite B_y orientation in the opposite hemisphere.

However, these equations may still be useful in assessing whether high-latitude reconnection occurs preferentially under one B_y polarity. While this would still represent high-latitude flank reconnection, the coupling function investigated in Chapter 4 was symmetric in B_y. In contrast, equations 5.3 and 5.4 are asymmetric with respect to $+B_y$ and $-B_y$ IMF. Chapter 4 does not test for this asymmetry, but finds no evidence supporting symmetric reconnection under both polarities.

MHD modelling suggests that multiple polar regions may map to open field lines, as shown in figure 2.10 in Chapter 2. For instance, a small portion of the noon active region may connect to open field lines extending from the outer dusk magnetosphere to the midnight sector, while the dusk active region may connect to an area of periodically open flux in the midnight sector (Zhang et al., 2021). Other studies associate the swirl region with open field lines as well (Pallier and Prangé, 2001; Stallard et al., 2001; Stallard et al., 2003; Vogt et al., 2011). However, results presented in Chapter 4 indicate that all polar regions likely map to mostly closed magnetic field lines. No region shows a correlation between IMF clock angle and auroral power or exhibits extended periods of auroral inactivity - which would expected for regions open to the solar wind (Delamere and Bagenal, 2010).

5.2.1.3 Fitting and Error Analysis

To evaluate whether the estimated reconnection voltages correlate with auroral power, equations 5.2, 5.4 and 5.3 are compared with auroral power for each polar region. As in Chapter 4 for solar wind dynamic pressure, these results are presented in semi-log space (linear power vs log voltage) to accommodate the reconnection voltage spanning across multiple orders of magnitude. A linear fit is applied in

each case, which represents a logarithmic relationship; this implies that the auroral response scales with the order of magnitude of the solar wind input rather than its absolute linear value. This is important because a standard linear fit will be disproportionately sensitive to high-voltage extremes, potentially obscuring the relationship across the broader range of solar wind conditions. By using a log scale for the reconnection voltage, the fitting process characterises how the auroral power scales as reconnection voltage increases across its full dynamic range.

The resulting relationship is evaluated using the coefficient of determination (R^2), as described in Section 4.2.2.3 in Chapter 4. A linear relationship is chosen as it provides the simplest form of association without requiring additional assumptions about the data. For R^2, a threshold of 0.2 is set, indicating that at least 20% of the variance in the data must be explained by the fit for the correlation to be considered meaningful.

Section 4.3.2 in Chapter 4 further explains how to interpret results derived from this analysis framework, including the R^2 values and the use of the solar wind propagation time uncertainty window.

5.2.2 Reconnection Voltage and Auroral Power

None of the three reconnection voltage formulations show a significant correlation with auroral power, with all nominal and ±20% travel time R^2 values falling under the threshold value. A significant portion of the R^2 values are negative, including all values for low-latitude reconnection, indicating that a horizontal line through the mean auroral power would be a better representation of the data. The dusk active region shows a consistently positive R^2 value for both high-latitude reconnection voltages, but the highest R^2 value is only 0.081, which is below the 0.2 threshold. Therefore, this value is too low to support any meaningful relationship or asymmetric high-latitude reconnection driving this region. The full results are provided in

Appendix B.4, whereas the results for the dusk active region are shown in figure 5.2 for the purposes of comparing the functions in this analysis.

It is worth noting, however, that there is an absence of high auroral power at low reconnection voltages (upper-left quadrant) for low-latitude reconnection (panels a and b) and high-latitude reconnection favouring $+B_y$ IMF (panels c and d). While the overall lack of correlation suggests that reconnection is not a primary driver of auroral intensity, consistent with a system dominated by internal magnetospheric processes, these 'empty' upper-left quadrants suggest that high power emissions are statistically infrequent when solar wind coupling is weak or unfavourably orientated. Conversely, in the high-latitude $-B_y$ case (panels e and f), the absence of high power emissions is at high reconnection voltages (upper-right quadrant) instead. This suggests that the 'empty' regions across all of these plots are likely a function of IMF-dependent asymmetries rather than a functional relationship between auroral power and the calculated reconnection voltage.

Given that auroral power shows no response to IMF clock angle (see Chapter 4), this result is not unexpected. Since clock angle modulates the reconnection voltage (Nichols et al., 2006), the lack of correlation is consistent with the absence of a clock angle-aurora relationship. For example, low-latitude reconnection voltage is expected to maximise where the IMF lies in the $+B_z$ quadrant, as this is when the IMF is anti-parallel to Jupiter's magnetic field, but $+B_z$ visits do not show enhanced auroral power relative to other clock angle quadrants (see figure 5.1, panels a and b). Although the dusk active region shows a moderate correlation with magnetic field strength (see Chapter 4), it also exhibits the weakest correlation with low-latitude reconnection voltage. Given that magnetic field strength is a key factor in equations 5.2, 5.3 and 5.4, this result suggests that the expected influence of the magnetic field strength is diminished in the reconnection voltage formulations, likely due to the modulating effect of the clock angle.

Although solar wind velocity appears explicitly in the reconnection voltage equa-

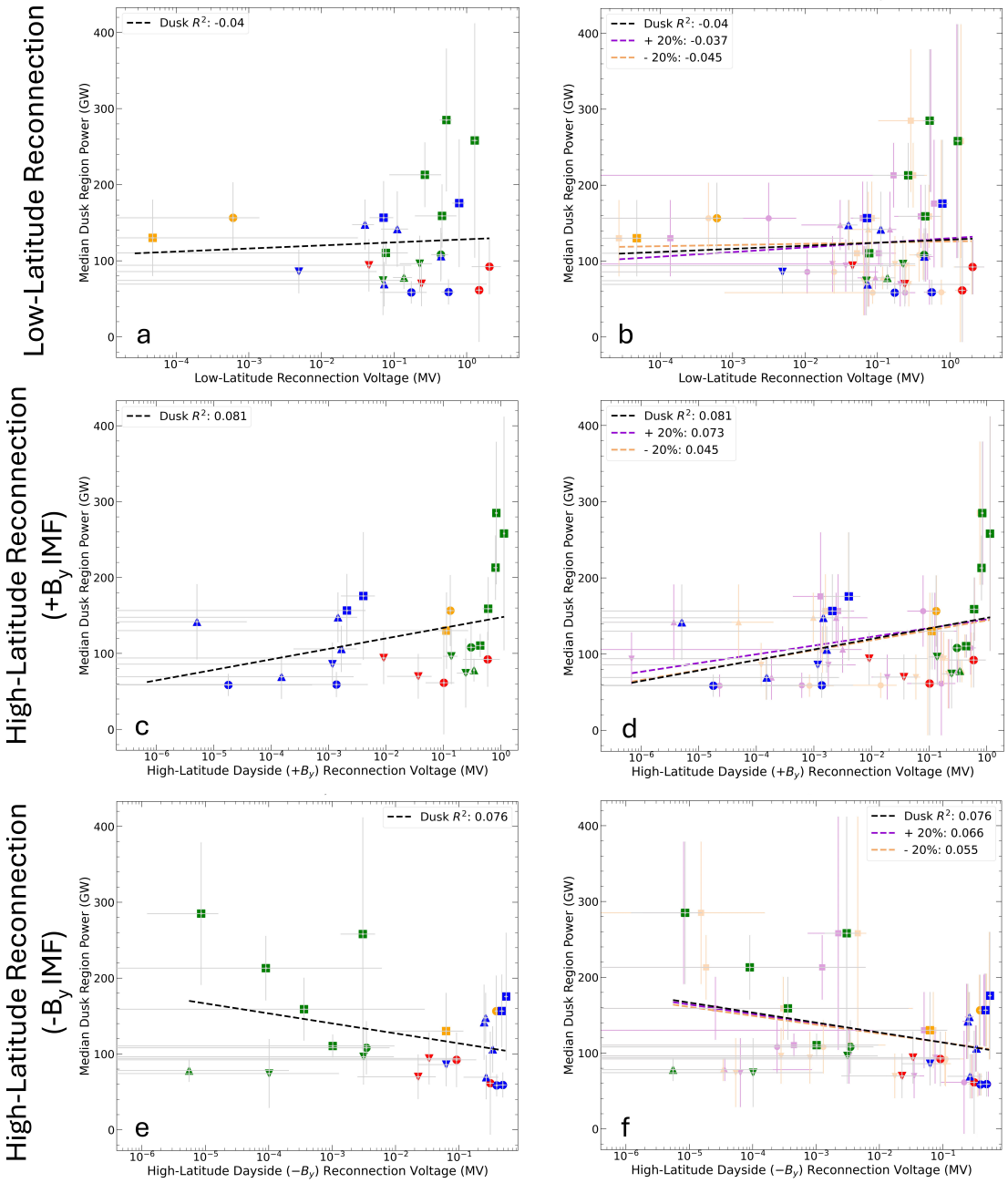

Figure 5.2: The relationship between median auroral power in the dusk active region and median: (a) low-latitude reconnection voltage; (b) the same with the ±20% uncertainty window; c) high-latitude reconnection voltage favouring $+B_y$ IMF; (d) with the ±20% uncertainty window; (c) high-latitude reconnection voltage favouring $-B_y$ IMF; (d) with the ±20% uncertainty window

.

tions, its influence has not been examined directly in this study. Physically, the solar wind drives the convective electric field at the magnetopause, given by $\vec{E} = -\vec{V}_{sw} \times \vec{B}$, which facilitates magnetic reconnection. As such, faster solar wind velocities are expected to produce higher reconnection voltages. However, the solar wind speeds in the dataset examined here mostly fall within the $\sim 400 - 500$ km s^{-1} range, characteristic of slow wind. This may limit the strength of any reconnection-driven coupling and contribute to the lack of observed correlation between the reconnection voltages and auroral power.

In contrast, the very weak correlations seen for the dusk active region for both forms of the high-latitude reconnection voltage are likely due to the elevated auroral power associated with the $+B_y$ clock angle quadrant. Although the clock angle dependence reduces the reconnection voltage under $-B_y$ conditions, auroral power is not lowest in this quadrant, suggesting that the perpendicular magnetic field component ($B_\perp$) continues to influence the voltage even when the clock angle term is small. As shown in figure 5.2, this pattern is consistent for both equations 5.3 and 5.4, where the gradients are reversed: where $+B_y$ IMF is favoured for reconnection (equation 5.3), the gradient is positive; where $-B_y$ is favoured (equation 5.4), the gradient is negative. This suggests that the weak correlations are more likely a result of the shared dependence on IMF strength, rather than a direct indication of reconnection-driven coupling.

Despite the lack of correlation between reconnection voltage and auroral power, this does not necessarily imply that magnetic reconnection is absent of within Jupiter's magnetosphere. While large-scale reconnection is unlikely to be a significant driver of magnetospheric dynamics (Delamere and Bagenal, 2010; Kivelson and Southwood, 2005; Vasyliũnas, 1983), and it does not appear to have any measurable effect on auroral power for any auroral emission at Jupiter over the timescales considered in this study, reconnection may still occur on smaller scales, such as in the tightly wound magnetic field inside the waves generated by the Kelvin-Helmholtz

instability (Masters, 2018; Zhang et al., 2018), which is investigated in section 5.3. Reconnection in general may also be more intermittent or contribute in more complex ways that are not reflected in the auroral output (Delamere and Bagenal, 2010; Masters, 2017).

It is important to note that the reconnection voltage formulations used here originate from formulations developed for Earth's magnetosphere and the equation for low-latitude reconnection voltage (equation 5.2) has recently been reported to likely overestimate the level of solar-wind interaction at Jupiter (Gershman et al., 2024). As equations 5.3 and 5.4 for high-latitude reconnection are adapted from the low-latitude reconnection formulation to incorporate the effects of $\pm B_y$ IMF, they may potentially overestimate the interaction also. These overestimates likely arise due to fundamental differences in magnetospheric scale, magnetic field geometry, and reconnection dynamics between the two planets. As such, the apparent lack of correlation between reconnection voltage and auroral power may reflect the limitations of applying terrestrial models to Jovian conditions, rather than the absence of reconnection-related processes altogether. Consequently, the results presented here should be treated with caution. Future work may explore a more appropriate formulation for reconnection voltage at Jupiter.

5.3 The Kelvin-Helmholtz Instability

5.3.1 Calculation of the Kelvin-Helmholtz Power

The Kelvin-Helmholtz (K-H) instability is unique among the processes investigated in this chapter, as it does not involve traditional magnetic reconnection. Instead, it is an instability that arises from velocity differences across an interface; high shear flows can result in the development of vortical structures along the magnetopause akin to the wind making waves on water. These structures compress the

magnetopause boundary layer and drive small-scale flux transfer events between the magnetospheric and solar wind plasma due to reconnection occurring within the tightly wound magnetic field inside the 'waves'. Although individual events are short-lived, their frequent occurrence across a substantial length of the boundary layer can result in a significant transfer of mass and momentum across the magnetopause boundary (e.g. Hasegawa et al., 2004, Desroche et al., 2012 and references therein).

At Jupiter, the velocity shear is not expected to be uniform along both flanks of the magnetopause. This asymmetry arises due to Jupiter's internal plasma co-rotating with the rapidly rotating magnetosphere, as the plasma is effectively 'frozen-in' to the magnetic field. On the dawnside, internal plasma flows sunward, opposite to the flow of the solar wind, resulting in a large velocity shear. On the duskside, the internal plasma flows in the same direction as the solar wind, which reduces the velocity shear. Consequently, this study considers K-H driven power on the dawn and dusk flanks separately.

The power generated by the Kelvin-Helmholtz instability is estimated using the formulation from Gershman and DiBraccio (2024):

$$P_{K-H} \approx 0.022 \rho \Delta V^3 L_z L_x \tag{5.5}$$

where P_{K-H} is the power, ΔV is the velocity shear across the magnetopause boundary, ρ is the plasma density, L_z is the boundary layer thickness and L_x is the length along the magnetopause where K-H vortices can develop. Although these are given as L_x and L_y in by Gershman and DiBraccio (2024), the coordinate system is changed here to be consistent with the coordinate system used throughout this study. ρ is taken as $\frac{3}{2}\rho_u$, based on upstream density ρ_u, following gasdynamic modelling results (Slavin et al., 1985; Stahara et al., 1989).

The velocity shear is calculated as:

$$\Delta V = v_{int} - \left(-\frac{1}{2} v_u\right) \tag{5.6}$$

where v_{int} is the internal plasma velocity, taken as 350 km s^{-1} on the dawnside and -350 km s^{-1} the duskside to represent flow direction (Zhang et al., 2018). This formulation differs from that in Gershman and DiBraccio (2024) but is adapted here to better reflect Jupiter's rapidly rotating magnetosphere. Unlike Earth, where the solar wind-bases shear dominates, Jupiter's strong internal plasma flow necessitates this adjustment. The factor of $\frac{1}{2}$ also approximated from 3D gasdynamic modelling, representing the effective reduction of the solar wind velocity as it is compressed by the bow shock and deflected around the magnetosphere (Slavin et al., 1985; Stahara et al., 1989).

For L_x, a value of $2R_{MP}$ is used, rather than the $4R_{MP}$ suggested (Gershman and DiBraccio, 2024), to account for the separate treatment of the dawn and dusk flanks in this study. The boundary layer thickness, L_z is estimated from the plasma scale height using the empirical fit from Bagenal and Delamere (2011):

$$\begin{aligned} h = & -0.116 + \left(2.14 \times \log_{10}\left(\frac{RJ_{MP}}{6}\right)\right) - \left(2.05 \times \log_{10}\left(\frac{RJ_{MP}}{6}\right)\right)^2 \\ & + \left(0.491 \times \log_{10}\left(\frac{RJ_{MP}}{6}\right)\right)^3 + \left(0.126 \times \log_{10}\left(\frac{RJ_{MP}}{6}\right)\right)^4 \end{aligned} \tag{5.7}$$

where $h = log_{10}H$, and H is the plasma scale height. The thickness of the plasma sheet is then calculated as:

$$L_z = 2 \times 10^h \mathrm{R_J} \tag{5.8}$$

where $\mathrm{R_J}$ is Jupiter's radius. The factor of two accounts for the vertical extent of the plasma sheet in both hemispheres.

As with the reconnection voltage in section 5.2.1.3, the power generated by the Kelvin-Helmholtz stability is plotted on a log scale, as the calculated power spans multiple orders of magnitude.

5.3.2 Kelvin-Helmholtz Instability and Auroral Power

The correlation between power generated by the Kelvin-Helmholtz instability and auroral power appears to be significant only for the dusk active region when calculated by imposing shear flows appropriate for the dawnside flank, with an R^2 value of 0.25 for the nominal travel time and 0.26 for both the shorter and longer travel times (see figure 5.3, panels c and d). Although the swirl region calculated using dawnside shear flows and the dusk active region calculated using duskside shear flows both show weak positive correlations with auroral power, both remain below the R^2 threshold across all travel times. The swirl region with duskside shear flows and the noon active region for both flank configurations show a consistently negative correlation, indicating that a horizontal line through the mean auroral power would provide a better fit to the data. A full set of figures comparing energy inputs and auroral conditions under both sets of shear conditions are provided in Appendix B.4.

Figure 5.3 shows the relationship between the Kelvin-Helmholtz energy inputs and the auroral power in the dusk active region, shown separately for the dusk (panels a, b) and dawn (panels c, d) flanks, with panels b and d including ±20% travel time uncertainty. As the statistically significant relationship identified for dawnside shear flows is fitted in semi-log space, the resulting linear trend represents a logarithmic relationship between K-H energy input along the dawn flank and auroral power in the dusk active region. Similar to the trend observed for solar wind dynamic pressure in section 4.3.3.1 in Chapter 4, this suggests a diminishing rate of return, as the dusk active region aurora is most sensitive to energy input from K-H vortices when the pre-existing energy transfer between the solar wind and magnetosphere is low. This implies that the coupling between the solar wind and the dawnside magnetosphere becomes less efficient at high levels of energy transfer, as further increases in K-H power results in progressively smaller enhancements in auroral power.

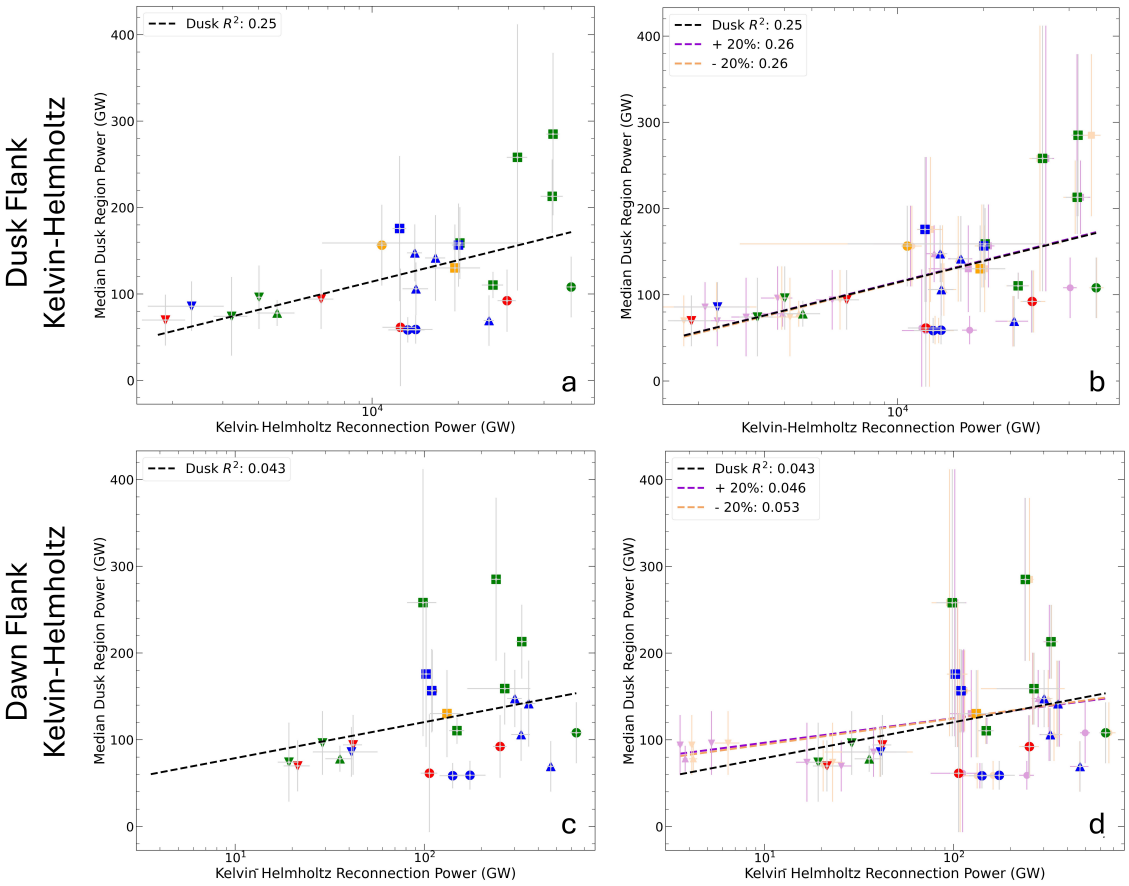

Figure 5.3: The relationship between median power generated by Kelvin-Helmholtz instabilities and median: (a) dusk active region auroral power under dusk flank conditions; (b) the same with the ±20% uncertainty window; (c) dusk active auroral power under dawn flank conditions; (d) with the ±20% uncertainty window

The results for the dawn flank are robust, with the R^2 value for all travel times varying by only 0.01, indicating that the observed correlation is unlikely to be due to noise in the data. Although the gradients of the fitted lines are visually similar, the visits associated with the highest auroral powers are calculated to have the highest level of energy input from K-H vortices formed along the dawn flank. On the dusk flank, the same visits cluster closer with the bulk of the data points, weakening the correlation. The visit associated with the highest energy transferred into the magnetosphere is visit 03, which has a much lower auroral power and does not change position between the dawnside and duskside plots; this visit is associated with a high solar wind mass density. In contrast, the three visits that shift significantly between panels a and c correspond to the highest solar wind velocities, highlighting the importance of high shear velocity in transferring significant amounts of energy into the magnetosphere.

Both high solar wind velocities and mass densities contribute to the energy transferred by the Kelvin-Helmholtz instability, but the much larger variation in mass density across the visits makes it the dominant factor influencing the variability of the energy input, as shown in figure 5.4. While density governs the overall energy input potential, the velocity shear across the magnetopause boundary controls how efficiently this energy can be transferred. This is due to the velocity shear introducing stress at the boundary between the solar wind and magnetosphere, creating surface waves throughout the instability. As the waves grow, they 'roll up' into vortices, which are what facilitate momentum and energy transfer into the magnetosphere. This rolling-up process tightly winds the magnetic field lines within the structures, leading to magnetic reconnection within the waves and allowing for the direct exchange of plasma across the flank magnetopause. Thus stronger shear velocities lead to faster-growing and more vigorous waves and stronger vortex formation - ultimately increasing the rate of energy input.

As the solar wind mass density remains the same for both flanks of the magne-

topause, the only difference between the dawn and dusk flank energy input is the velocity shear across the boundary. On the dawn flank, the internal plasma flow opposes the solar wind flow, producing significantly higher shear velocities and efficient energy transfer. On the dusk flank, the magnetospheric plasma and solar wind flows are generally aligned, resulting in a much slower shear velocity and therefore weaker waves. This leads to an energy input that is multiple orders of magnitude smaller for the dusk flank (see figure 5.3).

A preliminary analysis of shear velocities suggests a non-linear relationship between shear velocity and energy input. When the solar wind velocity is below approximately twice the internal plasma flow speed, lower velocities can actually allow more effective K-H development, as waves are less likely to be convected away before they can grow. Once the solar wind velocity exceeds this point, higher shear becomes more effective again. In the dataset examined, the solar wind velocities remain below double the internal plasma flow speed, and thus the shear is too weak for strong instabilities to develop on the dusk flank. This likely contributes to its limited energy input and weaker correlation with auroral power.

The results of Chapter 4 and previous literature do not indicate that the dusk active region maps to the dawnside of the outer magnetosphere, however. It shows no response to IMF clock angle (see section 4.3.2 in Chapter 4) or any of the reconnection voltages discussed previously. It does show a response to solar wind dynamic pressure and magnetic field strength (see sections 4.3.3.1 and 4.3.3.2 in Chapter 4), however. If K-H vortices on the dawnside drive auroral power for the dusk active region, the dusk active region must therefore either map to the dawnside of the outer magnetosphere or receive the energy transferred into the magnetosphere by K-H via another transport mechanism.

There are several plausible mechanisms that could enable K-H activity on the dawn flank to influence auroral emission in the dusk active region. Firstly, a recent Earth study has shown that Kelvin-Helmholtz vortices can develop on closed

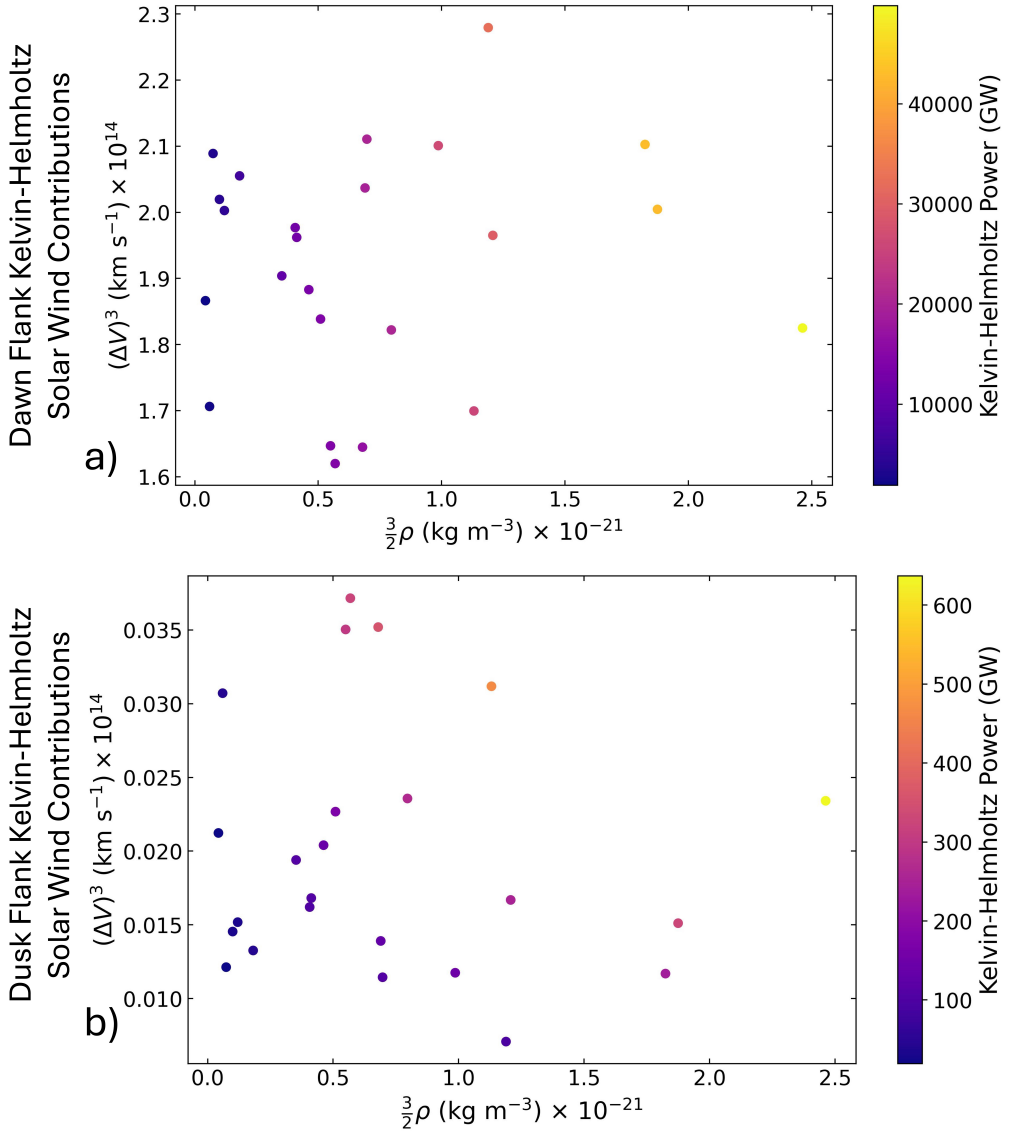

Figure 5.4: Contribution of velocity shear and mass density to the overall Kelvin-Helmholtz power, where panel a) represents the dawn flank and panel b) represents the dusk flank. The contribution of the velocity shear is effectively mirrored between the two flanks due to the oppositely directed internal flow of plasma in Jupiter's magnetosphere, suggesting that unless the solar wind velocity reaches a threshold value of over double the internal flow speed, higher solar wind velocities negatively impact the development of Kelvin-Helmholtz vortices.

magnetic field lines and yet produce auroral emissions in areas mapping to regions of open flux (Zhang et al., 2020). This suggests that auroral responses need not correspond straightforwardly to the magnetic topology where K-H instabilities originate. Applying this insight to Jupiter, it is plausible that K-H activity occurring on the dawnside closed field lines could transfer energy that ultimately drives auroral power in the dusk active region, even if that region periodically maps to open flux (Zhang et al., 2021) or the dusk sector of the outer magnetosphere (Vogt et al., 2011).

This behaviour can be understood by considering the broader role of the Kelvin-Helmholtz instability in magnetospheric energy transport. While it has not been directly linked to auroral emissions at Jupiter, the Kelvin-Helmholtz instability is suggested as the dominant mechanism for transporting mass, momentum and energy between the solar wind and Jupiter's magnetosphere (Delamere and Bagenal, 2010). At Earth, K-H can result in transpolar arcs (Zhang et al., 2020), auroral features driven not only by high shear flows at the magnetopause boundary, but by high shear flows within the magnetosphere as well. At Earth, this occurs between Earthward flows in the distant plasma tail region and tailward flows in the near tail region (Zhang et al., 2020).

Although the K-H energy input in this study only tests for K-H development at the magnetopause, Jupiter's magnetosphere shows a similar internal shear, driven by differential plasma rotation in the middle and outer regions (Bagenal and Delamere, 2011; Kivelson and Southwood, 2005). These similarities suggest that the K-H instability could potentially play a role in Jupiter's high-latitude auroral processes. It should be noted that a similar feature to transpolar arcs has been observed in the swirl region of Jupiter, but their occurrence appears to be independent of solar wind conditions (Nichols et al., 2009a). This does not rule out energy transfer due to the development of K-H instabilities being able to potentially drive auroral emission, however.

Understanding the spatial distribution of K-H instabilities along Jupiter's magnetopause boundary provides important context for a second potential mechanism of energy transport to the dusk active region. Jupiter's low-latitude dawnside magnetopause is thought to be K-H unstable due to strong shear flows. Any resulting vortices are expected to remain mostly stagnant because of the opposing plasma motion on either side (Zhang et al., 2018). The duskside is also suggested to potentially support the growth of K-H instabilities, but typically over a smaller spatial region (Masters, 2017). This is due the rotation of the magnetic field out of the plane of the plasma flow, which minimises the stabilising magnetic tension force (Desroche et al., 2012). The size of the K-H unstable regions are also anti-correlated with the strength of the IMF in simulations; under weak IMF strength the unstable regions become one continuos region along the low-latitude magnetopause but the size of the unstable region on the dawn flank is smaller. B_z orientated IMF is also noted to increase the size of the unstable regions (Masters, 2017), though the dawn flank is unstable regardless of IMF orientation (Desroche et al., 2012).

This opens up another plausible mechanism for energy transfer from the dawn flank to the dusk active region: K-H vortices could form and grow in the pre-noon/noon sector and advect due to magnetospheric flows into the dusk sector, suggesting K-H vortices may be prevalent in the dusk sector (Masters, 2017; Zhang et al., 2018). This offers another possible explanation of why the K-H activity on the dawn flank may influence auroral emission in the dusk active region, distinct from the terrestrial scenario where auroral emissions map indirectly to regions of open flux; if the unstable region becomes continuous across the dayside magnetosphere, this would enable the K-H vortices to develop on the dawnside and move across to the duskside with greater ease. If this is the case, the dusk active region may map to the duskside of the outer magnetosphere instead, as suggested by magnetic flux mapping (Vogt et al., 2011), as the higher shear flows in the pre-dawn sector could trigger the initial growth. However, this would require a continuous unstable region to develop under higher IMF strength than current modelling implies.

These findings raise questions about how IMF strength modulates K-H instability growth at Jupiter. While simulations suggest that a continuous dayside instability is most likely under weak IMF conditions, this appears at odds with the results of this study, which show a positive correlation between auroral power in the dusk active region and both IMF strength and K-H energy input (see Chapter 4). This suggests that stronger IMF conditions do not suppress, and may even enhance, K-H-driven auroral processes at Jupiter. If so, then the size of the unstable region may not significantly limit vortex development under strong IMF, or the relationship between IMF strength and instability growth may be more complex than current models imply.

Although IMF strength shows a stronger correlation with auroral power in the dusk active region than K-H energy input (see Chapter 4), this correlation may also reflect magnetospheric effects unrelated to K-H instability. Since Equation 5.5 does not account for magnetic field strength, it cannot help distinguish whether IMF-driven auroral variations occur independently of K-H activity through other coupling processes or if the auroral variation exists due to their combined influence. Therefore, the exact nature of how IMF strength and K-H instability contribute to auroral power remains unresolved and warrants further investigation.

It is not just the solar wind magnetic field strength that is worth discussing in the context of the K-H power results. The R^2 values for K-H power and solar wind dynamic pressure for the dusk active are very similar (see Chapter 4), at 0.26 and 0.28, respectively. Although an argument can be made for pressure being a modulating factor of emission rather than a driver, considering that Jupiter's main emission is internally driven and appears to be modulated by dynamic pressure (Giles et al., 2025; Nichols et al., 2009b; Yao et al., 2022), it is also possible the correlation found with dynamic pressure exists due to the correlation with K-H. The key components in the calculation of the K-H power are solar wind mass density and velocity, from which dynamic pressure is derived ($p = \rho v^2$). As such, the pressure

correlation may mirror the K-H relation, or vice versa, or both effects may contribute to auroral power variations in the dusk active region.

Furthermore, solar wind dynamic pressure could influence the velocity of the internal magnetospheric plasma through compression of the magnetosphere, altering the plasma flows. Changes in plasma velocity may enhance or suppress the growth of K-H instabilities through modification of the shear velocity between the solar wind and internal plasma or alter the transport of energy within the magnetosphere. As such, this coupling between external pressure and internal plasma dynamics may complicate the interpretation of the correlations between solar wind parameters and auroral power. Future analyses may incorporate variable internal plasma velocities to further clarify the relationship between K-H and auroral power.

On the other hand, the lack of meaningful correlation for both the swirl and noon active regions suggests that neither is significantly influenced by the development of K-H vortices. MHD modelling places the swirl region in the dawn sector of the outer magnetosphere (Zhang et al., 2021), and as the swirl region is the highest latitude polar region, it would be therefore expected to map to the outer magnetosphere. The lack of correlation with K-H power suggests that the swirl region does not map directly to where K-H vortices form, however. As the swirl region is the quietest of the three polar regions investigated in this study, it is unlikely that the main driver of emission can mask any K-H influence. Alternatively, if the swirl region does indeed map to the dawn flank, it suggests that the K-H vortices have a limited influence on auroral activity in the region. As discussed earlier, K-H waves may form on the dawn flank and subsequently advect into the dusk sector, potentially reducing their impact on the dawnside as they are not yet fully developed as vortices. In that context, the slightly positive correlation for the swirl region under dawnside conditions could reflect limited interaction, but it remains well below the R^2 threshold and is not statistically meaningful.

If advection occurs, and the noon active region maps to the noon sector of the outer

magnetosphere as suggested by magnetic flux mapping (Vogt et al., 2011), some response to K-H power might be expected — yet this region shows no meaningful correlation at all. This could indicate either that K-H vortices only become effective at transferring energy once they reach the duskside, or that the noon active region does not interacts with them at all. It remains uncertain whether this is due to a lack of vortex advection across the magnetopause, that the energy transferred into the system is somehow transported away from the region, or because these regions do not map to the outer dayside magnetosphere.

Taken together, the lack of correlation indicates that other processes are likely responsible for driving auroral variability in the swirl and noon active regions, and the absence of any correlation with K-H, reconnection voltage, IMF clock angle, solar wind dynamic pressure or magnetic field strength (see Chapter 4) supports the conclusion that both the swirl and noon active regions are primarily governed by internal driving.

There are some caveats to these results. The solar wind velocities in this dataset range from $\sim$ 400 to just over 500 kms^{-1}, with 400 kms^{-1} considered to be slow wind. Although the shear velocity will always be larger at dawn, high solar wind velocities ($\sim$ 800 kms^{-1}) could produce dusk flank shear velocities comparable to dawnside values under slow conditions. Therefore, the full picture is not seen here in terms of the range in the potential Kelvin-Helmholtz reconnection power. Whether this would further strengthen the trend between K-H and the auroral power is unknown, as corresponding auroral powers for periods of fast solar wind would also be needed to make the comparison.

Additionally, Kelvin-Helmholtz instabilities may not be confined to low-latitudes. At Earth, K-H waves have been have been observed at high-latitudes near the duskward cusp (Hwang et al., 2012), implying that K-H unstable regions may exist at high-latitudes. The multi-fluid Lyon-Fedder-Mobarry model (MFLFM) model suggests high-latitude K-H may also be possible at Jupiter (Zhang et al., 2018). As the

K-H waves will propagate roughly perpendicular to Jupiter's magnetic field at high-latitudes in the dawn and dusk sectors, the threshold for the K-H instability to occur should be reduced (Hwang et al., 2012). Given that boundary layer thickness and the spatial extent of K-H vortices likely differ at high latitudes, additional reconnection power may be generated that is not accounted for by equation 5.5. This could further alter the magnetospheric dynamics and warrants future investigation.

Overall, these results suggest that the development of Kelvin-Helmholtz instabilities contributes to auroral power in the dusk active region, but only when the vortices are formed on the dawn flank, where velocity shear is significantly higher. No meaningful correlation is found for dusk flank conditions, nor for the swirl or noon active regions for either flank configuration. This implies that K-H activity is not a significant driver of auroral variability in the polar regions outside of the dusk active region. Further work is needed to clarify how the dusk active region is influenced by the dawn flank of the magnetosphere, as it seems unlikely that the dusk active region maps to the opposite side of the magnetosphere.

5.4 Conclusions

This chapter evaluates whether solar wind-magnetosphere coupling via large-scale magnetic reconnection and small-scale Kelvin-Helmholtz instabilities can explain the variability in auroral power in Jupiter's polar regions. Table 5.2 shows a summary of the results, which indicate that there is no evidence to support large-scale reconnection as a driving mechanism for the aurora but show that shear-driven Kelvin-Helmholtz instabilities may influence auroral activity in the dusk active region.

None of the three reconnection voltages, which represent low-latitude reconnection, high-latitude reconnection with $+B_y$ orientated IMF and high-latitude reconnection

Parameter	Swirl Region	Noon Active Region	Dusk Active Region
LL Voltage	×	×	×
HL Voltage ($+B_y$)	×	×	×
HL Voltage ($-B_y$)	×	×	×
K-H Power (Dawn Flank)	×	×	Moderate ($R^2 = 0.25$)
K-H Power (Dusk Flank)	×	×	×

Table 5.2: Summary of the relationships between polar auroral power and reconnection rates due to the Kelvin-Helmholtz instability and large-scale reconnection at different magnetospheric latitudes. HL = high-latitude; LL = low-latitude; K-H = Kelvin-Helmholtz. Crosses indicate no statistically significant relationship ($R^2 < 0.2$).

with $-B_y$ orientated IMF, shows a statistically meaningful correlation with auroral power for any polar region. This is consistent with the findings reported in Chapter 4, which exhibits a lack of response to IMF clock angle driving. These results may suggest that the terrestrial models in which the reconnection voltage equations are based may not accurately represent any potential coupling processes occurring at Jupiter. Since these reconnection voltages are modulated by clock angle, the absence of correlation for this parameter may suppress the influence of other parameters, such as the solar wind magnetic field strength, which is shown to have a potential influence on the dusk active region when tested independently (see Chapter 4). Together, these findings imply that either large-scale reconnection does not occur at Jupiter, or that it does not significantly influence auroral power in the polar regions as it is currently calculated.

In contrast, a moderate correlation is found between the Kelvin-Helmholtz power and auroral power in the dusk active region, but only along the dawn flank of the magnetosphere. Several plausible explanations may account for this: the dusk active

region could map to the dawn sector of the outer magnetosphere; K-H vortices may form on the dawn flank and subsequently advect across the magnetopause to the dusk sector (Masters, 2017; Zhang et al., 2018), to which the dusk active region is predicted to be magnetically connected based on magnetic flux mapping (Vogt et al., 2011); or, as suggested by terrestrial studies, K-H activity on closed field lines may transfer energy that ultimately drives auroral emissions in regions mapping to open flux (Zhang et al., 2020), which may explain the suggestion that the dusk active region periodically maps to open flux (Zhang et al., 2021). If this is the case, it remains unlikely that this patch of open flux represents the whole dusk active region, especially as the correlation with the K-H instability cannot explain all of the auroral variability observed between visits, indicating an internal driver is present and thus closed field lines are likely present. Consequently, these results offer no clear indication of where the dusk active region maps to within Jupiter's magnetosphere.

Neither the noon active region nor the swirl region shows any correlation with K-H power. Combined with the absence of correlation with reconnection voltage, this suggests that both regions likely map to areas of the magnetosphere that are largely decoupled from direct solar wind driving. Although MHD modelling predicts that the swirl region maps to the outer dawn sector of the magnetosphere (Zhang et al., 2021), the results presented here may challenge that interpretation - particularly if K-H vortices forming on the dawn flank can influence the dusk active region, but not the swirl region. Alternatively, if auroral variability is influenced more by where the effects of K-H vortices are communicated within the magnetosphere rather than the precise location of instability onset, the absence of correlation in the swirl region may be plausible. In either case, the lack of correlation for all parameters investigated in this chapter supports the conclusion that the swirl and noon active regions are primarily governed by internal magnetospheric dynamics.

In summary, the findings of this chapter reinforce the conclusion that large-

scale interactions with the solar wind do not drive auroral emissions in the polar regions of Jupiter (Delamere and Bagenal, 2010). However, small-scale processes such as Kelvin-Helmholtz instabilities may play a significant role, particularly in contributing to the auroral power observed in the dusk active region. Further work involving an expanded dataset is required to better investigate the impact of Kelvin-Helmholtz instabilities on the polar aurora, alongside the development of reconnection voltage formulations better suited to Jupiter's complex magnetospheric environment.

Chapter 6

Summary and Future Work

The polar regions are the least understood of the auroral regions at Jupiter. Determining the source of emissions in these regions is essential for improving current understanding of solar wind–magnetosphere interactions at Jupiter and for defining the magnetic topology of the high-latitude field lines.

This thesis examines the extent to which solar wind-magnetosphere coupling influences aurora activity in three distinct polar regions: the swirl region, the noon active region and the dusk active region. With a particular focus on whether magnetic reconnection can account for observed variances in auroral power across these regions. Two complementary studies address this aim. Chapter 4 examines statistical correlations between solar wind parameters and auroral power, while Chapter 5 evaluates if energy inputs from reconnection and the Kelvin-Helmholtz (K-H) instability are correlated with auroral power.

The results indicate that only the dusk active region exhibits a measurable response to solar wind drivers, whereas the swirl and noon active regions appear to be primarily governed by internal processes. This chapter summarises the key findings, explores their broader implications for the Jovian auroral system, and outlines recommendations for future research.

6.1 Overview of Results

The results from both studies are summarised in figure 6.1, which presents all adjusted R^2 values indicating the correlation between auroral power and various solar wind parameters derived from Juno measurements taken upstream of Jupiter. These values are shown in heat maps, where colour indicates the relative strength of each correlation within a given propagation time scenario. Here, green indicates a stronger correlation, while red indicates the weakest links.

The dusk active region consistently shows the strongest correlations across all propagation times, while the swirl and noon active regions show consistently poor correlations, with many negative R^2 values. These negative values indicate that simple horizontal line through the median auroral power would be a better fit to the data than the applied functions, highlighting the general lack of response to solar wind variations. To account for uncertainty in the solar wind travel time, three propagation time scenarios are considered. Alongside the nominal value, propagation times that are 20% longer and 20% shorter are considered, capturing the uncertainty introduced by assumptions made in the propagation model.

Chapter 4 investigates the relationship between auroral power and four key upstream parameters: dynamic pressure, total magnetic field strength, perpendicular magnetic field strength, and the IMF clock angle. Linear correlations are tested for pressure and magnetic field strength across the three solar wind propagation times. For the IMF clock angle, four coupling functions are derived to represent different reconnection scenarios along the magnetopause: low-latitude, high-latitude, post-cusp, and a combined multi-latitude case. The analysis finds that none of the three auroral regions exhibit significant correlation with IMF clock angle under any coupling function, with R^2 values below 0.2 and more than half negative. This suggests three possibilities: that the polar regions examined are not magnetically connected to areas of the magnetosphere undergoing large-scale reconnection with

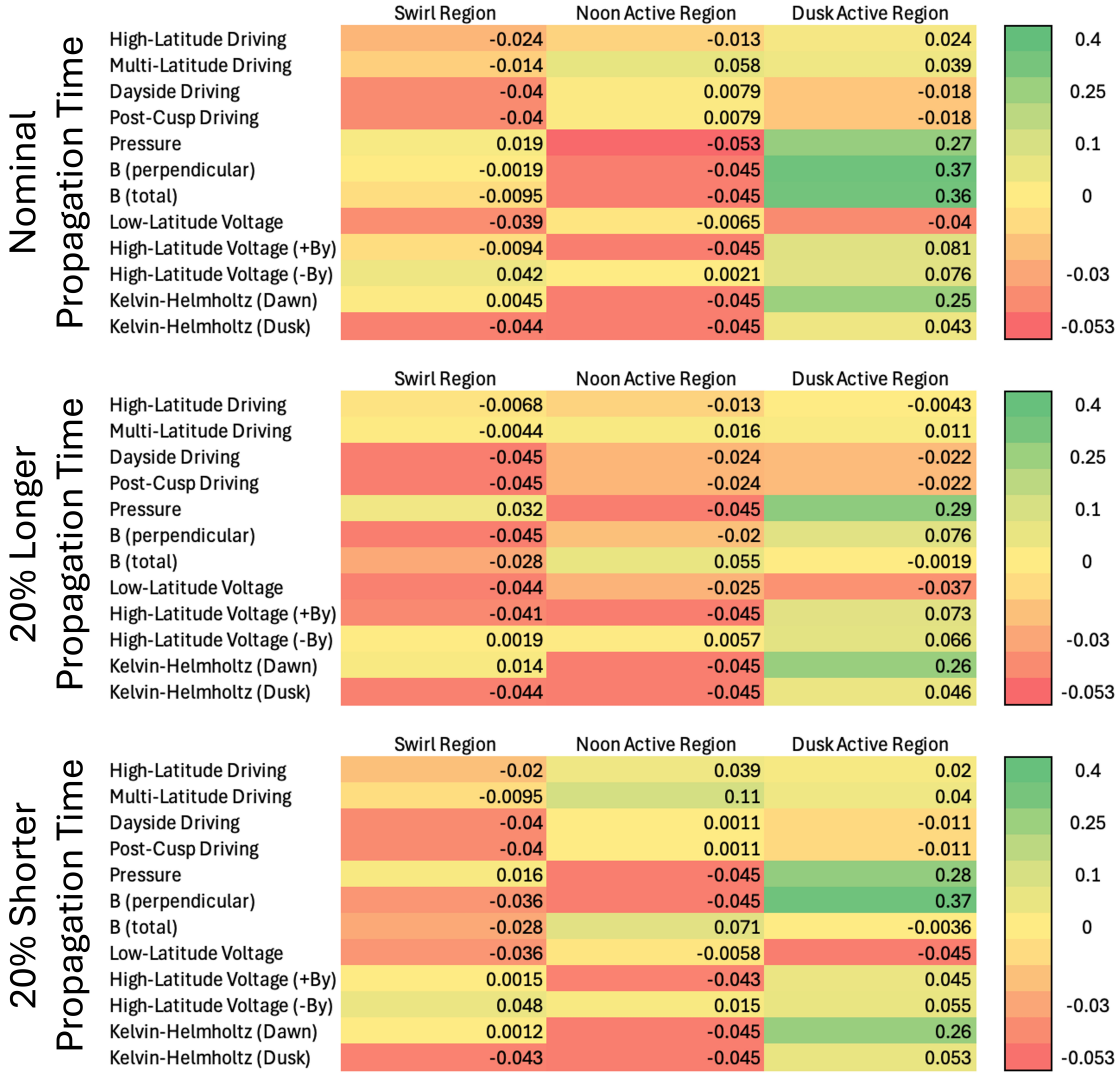

Figure 6.1: Heat maps showing the adjusted R^2 values for correlations between solar wind derived parameters and auroral power, based on three different solar wind propagation time estimates between detection by Juno and the arrival at Jupiter's ionosphere: (top) nominal travel time, (middle) 20% longer travel time and (bottom) 20% shorter travel time. Colours represent the relative strength of the fitted R^2 values across all tested parameters, allowing for comparison of correlation strength under different solar wind arrival times.

the solar wind; that the timescales for such clock angle-related effects to appear in the aurora are not appropriately captured; or that the energy input from such processes is negligible compared to other sources.

Similarly, no significant correlation is found between dynamic pressure or magnetic field strength and auroral power in the swirl or noon active regions. However, the dusk active region shows a moderate correlation with dynamic pressure ($R^2 = 0.27$), and a moderate but tentative correlation ($R^2 = 0.37$) with the magnetic field strength, although this disappears when longer ionospheric propagation times are considered, ie. +20%. These findings suggest that the dynamic pressure and magnetic field strength may act as modulating influences in the dusk active region rather than as primary drivers. Combined with the absence of any IMF clock angle correlation and the presence of continuous auroral activity in all three regions, this supports the conclusion that internal processes are the dominant source of auroral emission across the polar regions. Because high dynamic pressure and strong magnetic field values often occur simultaneously in the dataset, it remains unclear whether the auroral response in the dusk region is driven by one parameter alone or by their combined effect.

Chapter 5 continues the investigation by calculating reconnection voltages for both low-latitude and asymmetric high-latitude reconnection scenarios, in which reconnection only occurs under one $\pm B_y$ orientation. The high-latitude formulation is developed specifically to capture contributions from open field lines that may be overlooked by the post-cusp coupling function. In addition, the role of the Kelvin-Helmholtz (K-H) instability along the magnetopause flanks is evaluated as a potential mechanism for small-scale energy transfer into the magnetosphere. Both reconnection voltage and K-H energy transfer are compared with auroral power in each of the three polar regions, using simple linear relations, where the quality of each fit is again assessed using the adjusted R^2 parameter across all three solar wind propagation time estimates.

No significant correlation is identified between reconnection voltage and auroral power in the swirl, noon active, or dusk active regions. In all cases, the low-latitude reconnection voltage produces negative R^2 values, which suggests there is no relationship between auroral power and the low-latitude reconnection voltage. Together with the previously observed lack of correlation with IMF clock angle, this suggests that large-scale solar wind-driven reconnection plays a minimal role in driving auroral activity at Jupiter - if it plays any role at all. It should be noted, however, that the reconnection voltage equations used in this study were originally developed for Earth's magnetosphere. While these formulations have been adapted for the Jovian context, they may not fully capture the unique configuration and dynamics of Jupiter's magnetosphere, which could limit the accuracy of the voltage estimates.

For the KH instability, energy transfer into the magnetosphere is estimated by calculating the power associated with shear-driven vortices formed along the magnetopause flanks. These vortices arise from velocity differences between the solar wind and the magnetospheric plasma, which vary between the two flanks. On the dawn flank, the solar wind flows largely anti-parallel to the sub-corotating plasma, enhancing velocity shear and creating favourable conditions for vortex growth. On the dusk flank, the flows are more aligned, reducing shear and suppressing K-H instability development. As a result, energy transfer into the magnetosphere via this mechanism is expected to be greater on the dawn flank than on the dusk.

When compared to auroral power, only the dusk active region shows a measurable correlation with this energy transfer, and only for energy inputs associated with dawn flank velocity shear. This implies that the dusk active region either maps to the dawn flank of the outer magnetosphere or receives energy indirectly via transport processes, such as field-aligned currents or advection of dawn vortices into the dusk sector (Masters, 2017; Zhang et al., 2018). No significant correlations are found in the swirl or noon active regions under either flank condition. The moderate

correlation found in the case of the dusk active region for vortices formed on the dawn flank ($R^2 = 0.25$) suggests that K-H driven energy input may contribute to auroral variability in this region, though it is unlikely to represent the primary driver of emission.

6.2 Importance of Results to Research Field

A key result of this study is that neither the swirl nor the noon active regions show a measurable response to solar wind driving. While the possibility of some solar wind influence cannot be fully excluded, the results indicate that it is not a significant driver of auroral emission in either region, which implies that internal magnetospheric processes are the dominant drivers. However, since the swirl and noon active regions exhibit distinct auroral morphologies and colour ratios, distinct internal mechanisms in each region must be responsible for these variations. Identifying the specific internal drivers remains an open question.

In contrast, the dusk active region shows a measurable response to solar wind dynamic pressure, magnetic field strength, and energy transfer via the Kelvin-Helmholtz instability occurring on the dawn flank of the magnetosphere. Whether these parameters represent related or independent influences is not determined here, but none appear to be the dominant driver of auroral emission, given the moderate strength of the correlations observed. While the main source of emission is likely internal, a specific source has not yet been identified. The difference in behaviour between the dusk and noon active regions may be partly explained by the dusk region's sensitivity to solar wind conditions, suggesting that both regions could share a common internal driver.

Another significant finding is that all three polar regions most likely map to mostly closed magnetic field lines. Although some open field lines may be present, the

auroral emission observed is consistent with the majority of the connected field lines being closed. Regions connected to open field lines would typically show reduced or no auroral emission during periods of weak solar wind driving (Delamere and Bagenal, 2010), which is not observed for any of the three regions studied, indicating the presence of closed field lines. In the case of the swirl and noon active regions, internal driving mechanisms likely require closed field lines, supporting the conclusion that both regions map to mostly closed field lines.

The dusk active region is more nuanced. A lack of response to IMF clock angle combined with persistent, dynamic auroral emissions suggested closed field lines. While the dusk active region shows correlations with dynamic pressure and magnetic field strength, these relationships likely reflect modulating influences rather than direct driving forces. The correlation with energy transferred into the magnetosphere by K-H vortices complicates this interpretation, as a response is only seen for vortices on the dawn flank. Since it's unlikely the dusk active region maps to the dawn flank of the magnetosphere, this suggests the energy must be transported or redistributed, potentially via field-aligned currents, after entering the system. This raises the possibility that the dusk active region may contain a significant portion of open field lines, as field-aligned currents have been suggested to be able to transfer flux introduced by K-H to open field lines at Earth (Zhang et al., 2020). Alternatively, if the vortices advect across noon to the dusk sector, as suggested by modelling at Jupiter (Masters, 2017; Zhang et al., 2018), the dusk active region could still predominantly map to closed field lines. This scenario may also explain why the swirl region shows no response to K-H vortices, as significant energy transfer could occur only after the vortices advect toward the dusk sector. Given that the supporting modelling studies are specific to Jupiter, and considering the broader evidence presented in this thesis, it appears to be more likely that the dusk active region maps to closed field lines.

Previous studies have proposed that different polar regions may map to open

magnetic field lines. The swirl region is suggested to be open in several works (Cowley et al., 2003; Pallier and Prangé, 2001; Stallard et al., 2001; Vogt et al., 2011), while Zhang et al. (2021) proposes that the dusk active regions may periodically map to open field lines and the noon active and swirl regions may occasionally contain some open flux. These interpretations should not be dismissed solely on the basis of this analysis alone. Open field lines may exist in all three regions, but closed field lines are likely needed to drive the bulk of auroral power observed. However, all three regions mapping to closed field lines is also supported in literature - MHD modelling suggests that the swirl region maps to a closed loop of flux on the dawnside (Zhang et al., 2021) and magnetic flux mapping suggests the noon and dusk active regions map to the noon and dusk sectors of closed outer magnetosphere, respectively (Vogt et al., 2011). Importantly, a closed field topology does not invalidate previous studies. Jupiter's magnetosphere is a highly dynamic and complex system, and the processes that make the polar regions distinct from one another and the mechanisms that differentiate the polar regions from one another and from the main auroral emissions are likely not yet fully understood. At present, the three regions are defined based on their observed auroral morphology: based on the location, brightness, variability and structure in UV imagery. While they are visually distinct, the underlying magnetic topology may not correspond as straightforwardly, and the boundaries between open and closed field lines may not align cleanly with these morphological divisions.

6.3 Further Questions and Potential Future Work

While this thesis advances the understanding of the polar auroral regions, many questions remain unresolved. The processes driving the swirl and noon active regions are still unclear, and the differences between the regions cannot be explained by solar wind driving. This warrants further investigation, especially considering the

uniquely high colour ratio observed in the swirl region, which is currently only loosely attributed to potential photoionisation effects (Greathouse et al., 2021).

The potential relationship identified between auroral power in the dusk active region and the solar wind also requires additional exploration. Although correlations with solar wind dynamic pressure, magnetic field strength and energy transferred via the Kelvin-Helmholtz instability are found, the interplay of these parameters and whether they contribute to the same driving process remains uncertain. Furthermore, the mechanism by which K-H vortices on the dawn flank influence auroral emission in the dusk active region is still unclear. Uncovering the mechanisms involved will not only further the understanding of Jupiter's internal dynamics but also improve the comprehension of solar wind-magnetospheric coupling at Jupiter.

Several avenues exist for improving and expanding upon the studies conducted here. An initial first step would be to incorporate a more accurate model of the bow shock and magnetopause locations to improve estimates of the solar wind propagation time between Juno and Jupiter's ionosphere, thus increasing the accuracy of aligning solar wind data with HST auroral observations. As detailed in Chapter 4, such a model is now available (see Rutala et al., 2025) and could be potentially implemented into this study. The impact of this updated model on the propagation time, and consequently on the correlations found in this thesis, is currently unknown. Shorter travel times are expected, as the new model predicts the magnetopause boundary to be closer to Jupiter, but this should not be assumed without testing. Therefore, applying this improved model is likely the most crucial next step to verify the robustness and validity of the results presented here.

Investigating the dark polar region should also be considered. Previous work by Swithenbank-Harris et al. (2019) has demonstrated that this region responds to variations in solar wind dynamic pressure, exhibiting changes in both size and shape. Although identifying a relationship between solar wind parameters and auroral power in this region may prove more challenging due to the region being

mostly devoid of auroral emissions, the dark polar region is believed to map to open magnetic field lines. Consequently, the solar wind may still act as a potential driver for the limited auroral emission observed there. While large-scale reconnection is unlikely, since such coupling would be expected to produce more prominent auroral emission, a possible correlation with IMF clock angle should not be entirely dismissed.

Another possible direction for future work is adapting reconnection voltage calculations to better suit Jupiter's magnetosphere. The reconnection voltage equations applied here were originally developed for Earth's magnetosphere, but key differences in magnetospheric size, plasma conditions, and energy conversion scaling at Jupiter likely limit their accuracy. Gershman et al. (2024) have made an attempt at adapting reconnection voltage calculations for other planets by proposing an alternative approach. However, reconnection is most likely to be suppressed as a coupling mechanism at low-latitudes at Jupiter, which is not reflected in their approach. While this is also an issue with the low-latitude reconnection voltage calculated in Chapter 5, it may still be worth developing a version of this formulation for high-latitude reconnection, where the conditions are theoretically more favourable for reconnection. This would test whether the lack of correlation with auroral power seen in Chapter 5 still holds when using a version of the equation more appropriate for Jupiter.

Finally, additional data would greatly benefit this research. Although Juno now orbits Jupiter from mostly within the magnetosphere, it does occasionally leave the magnetosphere during parts of its orbit. JADE and MAG data from these periods could be assessed alongside UVS (Ultraviolet Spectrograph) images or any coincident HST data further investigate possible relationships between the solar wind and auroral power in the polar regions. Future studies could make use of more precise determinations of when Juno crosses the magnetospheric boundaries to improve estimates of solar wind propagation times relative to UV imaging. This would not

only expand the dataset, but may make it possible to examine individual auroral features rather than averaging total auroral power per region over $\sim$ 40 minutes intervals (a visit), enabling more direct comparisons between auroral activity and solar wind behaviour.

Appendix A

Linearisation of Equations

The coupling functions used in Chapter 4 to assess the relationship between IMF clock angle and polar auroral power are sinusoidal in nature and thus are not well represented by traditional error analysis, such as the coefficient of determination (R^2). These equations can, however, be transformed into a linear format in order to conduct this analysis. As an example, using equation 4.7, repeated here to show the full process:

$$A_1 \sin^2 \theta_c + A_2 \cos^2 \left(\frac{\theta_c}{2} \right) + C \tag{A.1}$$

Using the identities

$$\sin^2 \theta = 1 - \cos^2 \theta \tag{A.2}$$

and

$$\cos \frac{\theta}{2} = \sqrt{\frac{1 + \cos \theta}{2}} \tag{A.3}$$

Equation A.1 can be rewritten as:

$$A_1(1 - \cos^2 \theta) + A_2 \left(\frac{1 + \cos \theta}{2} \right) + C \tag{A.4}$$

which becomes

$$A_1 - A_1 \cos^2 \theta + \frac{A_2}{2} + \frac{A_2}{2} \cos \theta + C \tag{A.5}$$

By taking $A_1^{'} = -A_1$, $A_2^{'} = \frac{A_2}{2}$ and $C^{'} = C + \frac{A_2}{2} + A_1$, a polynomial equation can be obtained:

$$A_1^{'} \cos^2\theta + A_2^{'} \cos\theta + C^{'} \tag{A.6}$$

Polynomial equations used for regression models can be considered linear provided they are linear in their coefficients (Montgomery et al., 2012). Although equation A.6 still contains trigonometric terms, this condition is satisfied. By taking $x = \cos\theta$, the equation becomes:

$$A_1^{'} x^2 + A_2^{'} x + C^{'} \tag{A.7}$$

This is now a polynomial expression with linear coefficients and is therefore now an appropriate format to calculate the R^2 value of the fit. Other coupling function equations in chapter 4 can be linearised following the same process of substituting the squared sine and cosine functions with identities to rewrite them as simple sine or cosine functions which can have their sinusoidal component substituted for x.

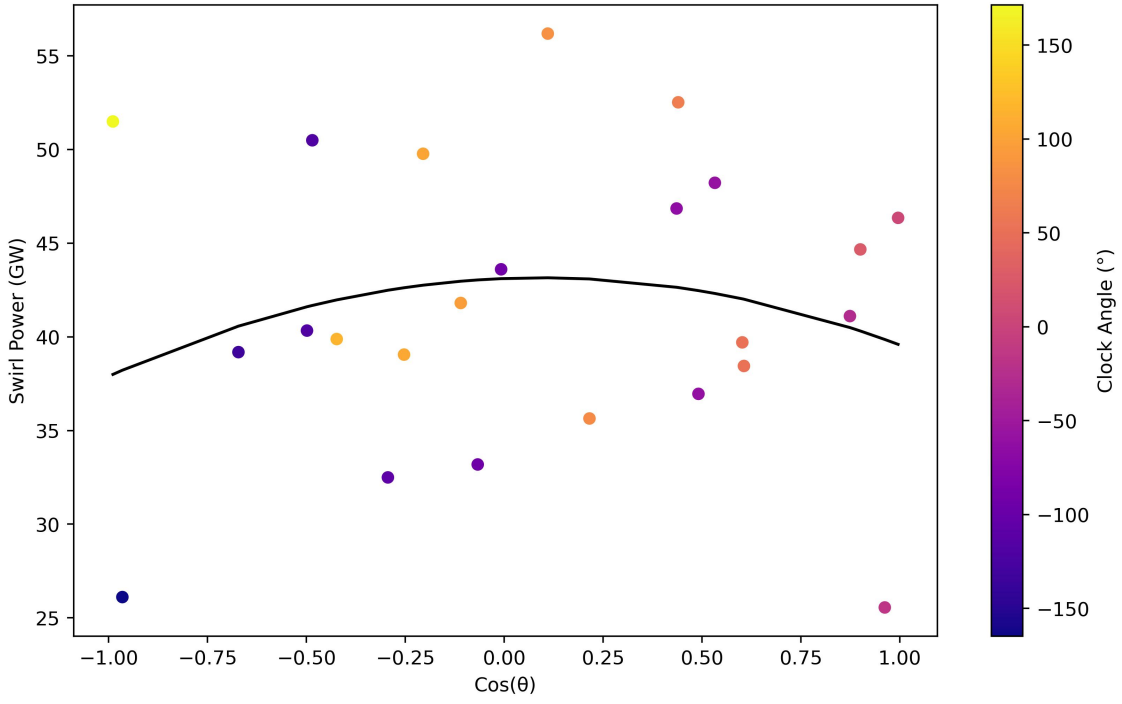

Figure A.0.1: Equation A.7 visualised with $\cos\theta$ representing x.

While figure A.0.1 shows the swirl region auroral power plotted as a function of $\cos\theta$

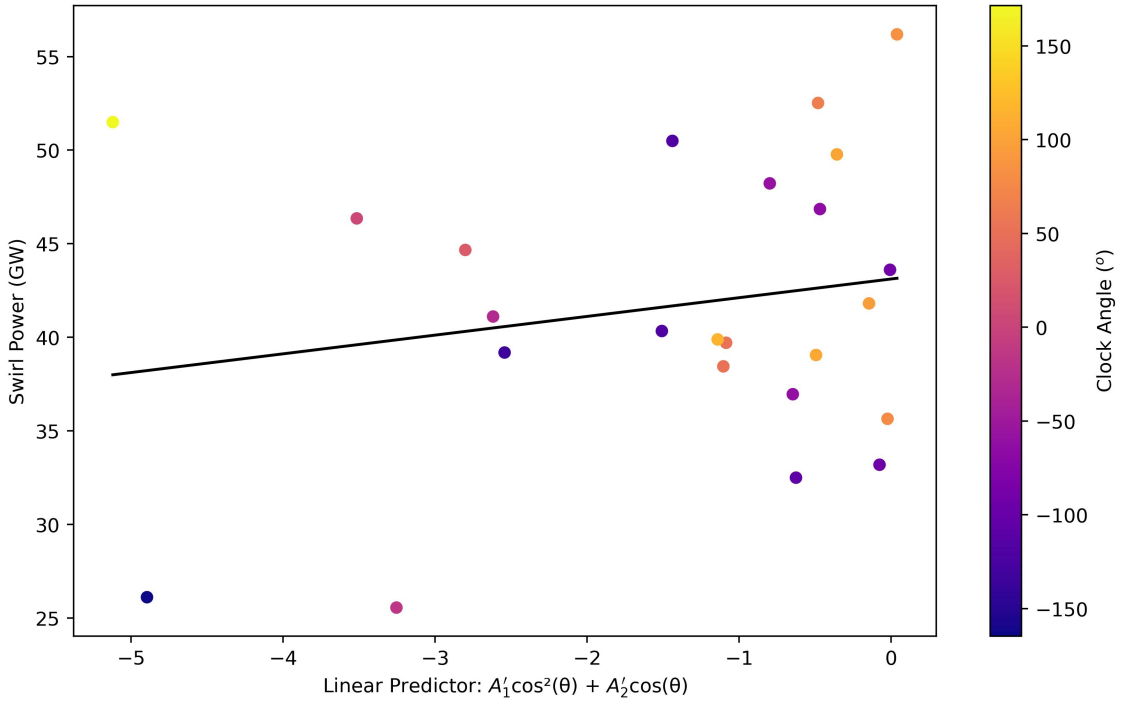

Figure A.0.2: Equation A.7 plotted in linear predictor space with x as the linear predictor, to show equation 4.7 has been successfully linearised. In this form, the quality of the fit is easier visualised.

for interpretability, the regression is linear in the transformed variables $\cos^2\theta$ and $\cos\theta$. This is shown in linear predictor space in figure A.0.2.

Appendix B

Additional Plots

B.1 Auroral Keograms

Auroral keograms for each polar region plotted with corresponding solar wind parameters are provided here to offer a complete overview of the dataset discussed in Chapter 4. These plots illustrate the temporal variation in both the auroral power and solar wind across the 21 visits not shared in the main text and provide the basis for the conclusion that variation in the solar wind cannot consistently explain changes in auroral power. Thus, using the median of the total power is justified when examining the relationship between the solar wind and auroral power.

It should be noted that visit 24 (figure B.1.16) appears to show the clock angle varying drastically across the full $-180°$ to $180°$ range. This is not the case; rather, the change in clock angle for this visit is minimal. The points appearing at opposite ends of the y-axis are a result of the clock angle crossing the $\pm 180°$ boundary. As both extremes of the axis represent the same orientation (the $-B_z$ axis), these jumps represent a visualisation artifact of the coordinate system rather than a physical shift in the IMF clock angle.

In addition, visit 27 (figure B.1.18) shows a bright feature in all three regions at the start of the keograms. This feature is non-physical and represents the first image in the visit having an unusually high background emission which was not successfully removed during the processing phase before this dataset was obtained. The total power in this image is an outlier, and diagnostic checks confirm that its inclusion does not affect the median total power used for this visit in Chapters 4 and 5.

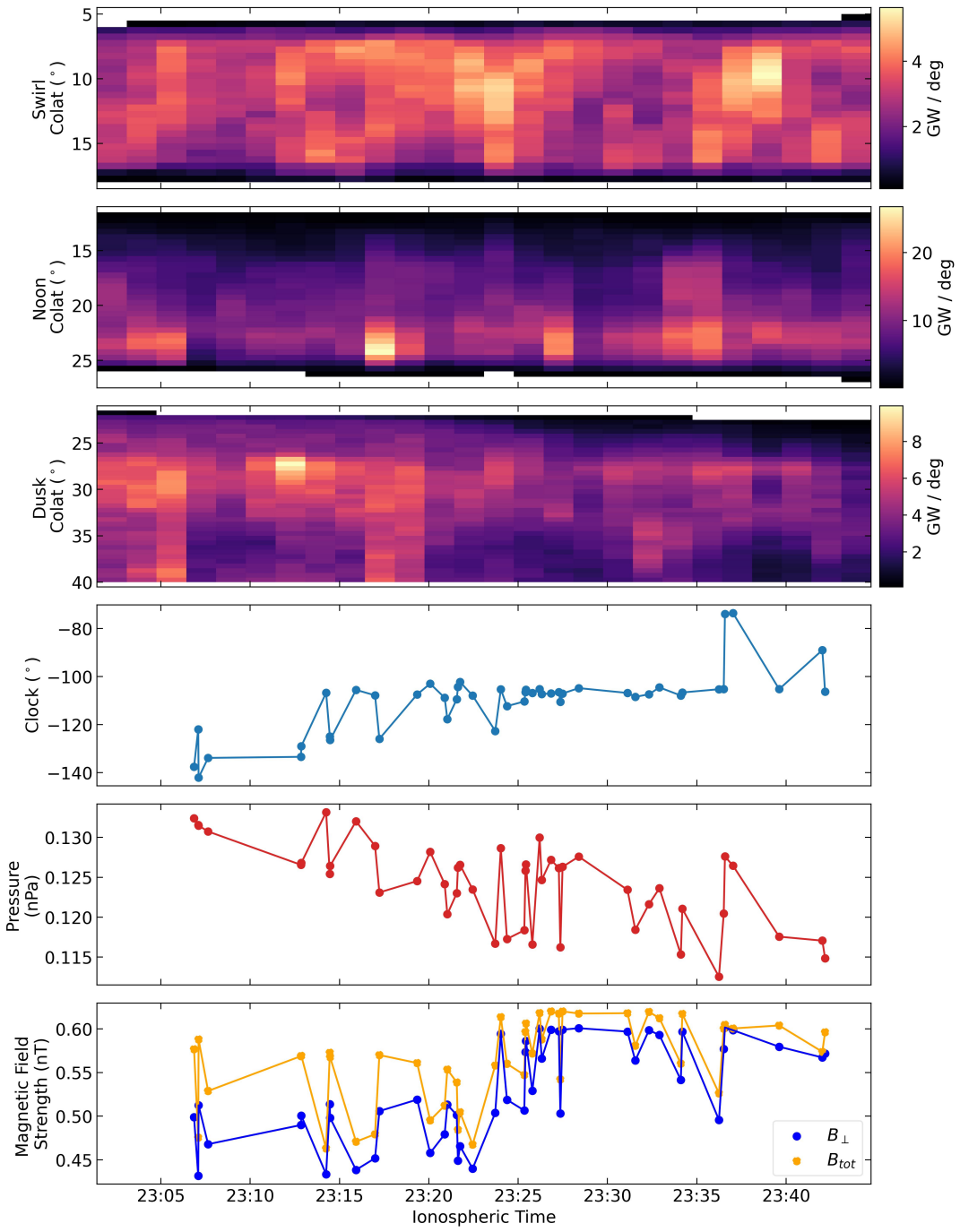

Figure B.1.1: Comparison of auroral power distribution and solar wind conditions during visit 01. The top three panels display keograms for the Swirl, Noon, and Dusk regions as a function of colatitude and Ionospheric Time. The bottom three panels show the corresponding IMF clock angle, solar wind dynamic pressure and IMF strength ($B_\perp$ in blue, B_{tot} in orange), respectively.

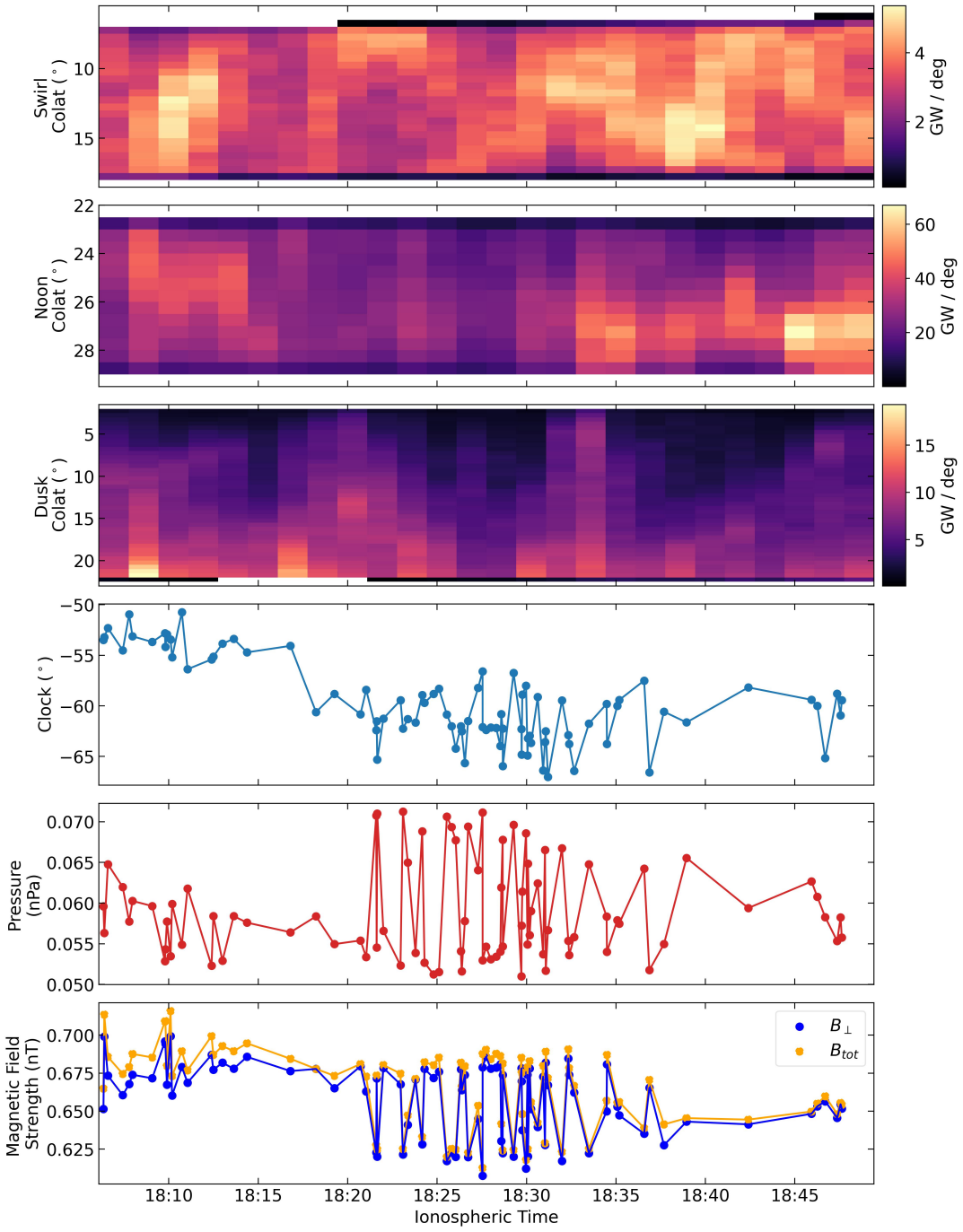

Figure B.1.2: Comparison of auroral power distribution and solar wind conditions during visit 02. The top three panels display keograms for the Swirl, Noon, and Dusk regions as a function of colatitude and Ionospheric Time. The bottom three panels show the corresponding IMF clock angle, solar wind dynamic pressure and IMF strength ($B_\perp$ in blue, B_{tot} in orange), respectively.

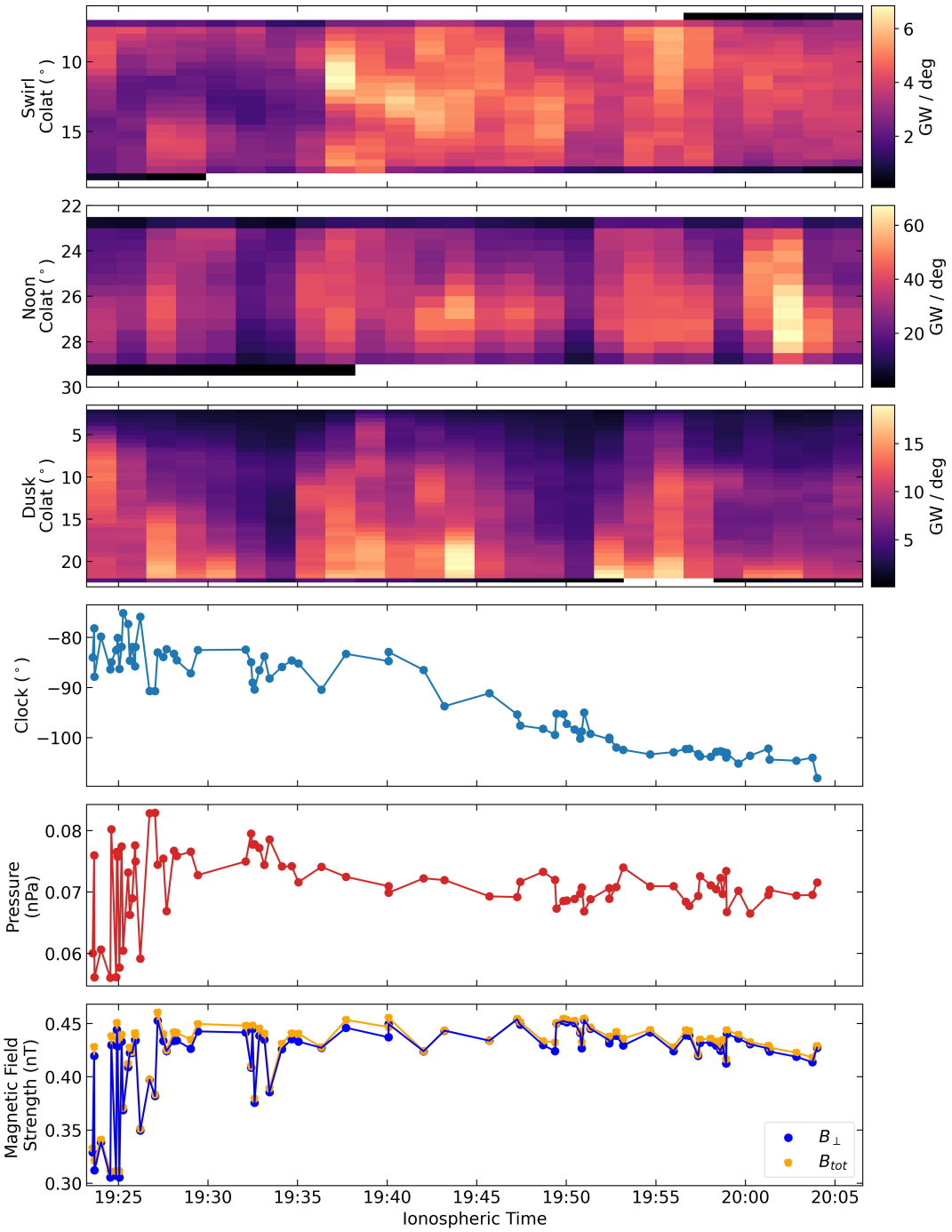

Figure B.1.3: Comparison of auroral power distribution and solar wind conditions during visit 04. The top three panels display keograms for the Swirl, Noon, and Dusk regions as a function of colatitude and Ionospheric Time. The bottom three panels show the corresponding IMF clock angle, solar wind dynamic pressure and IMF strength ($B_\perp$ in blue, B_{tot} in orange), respectively.

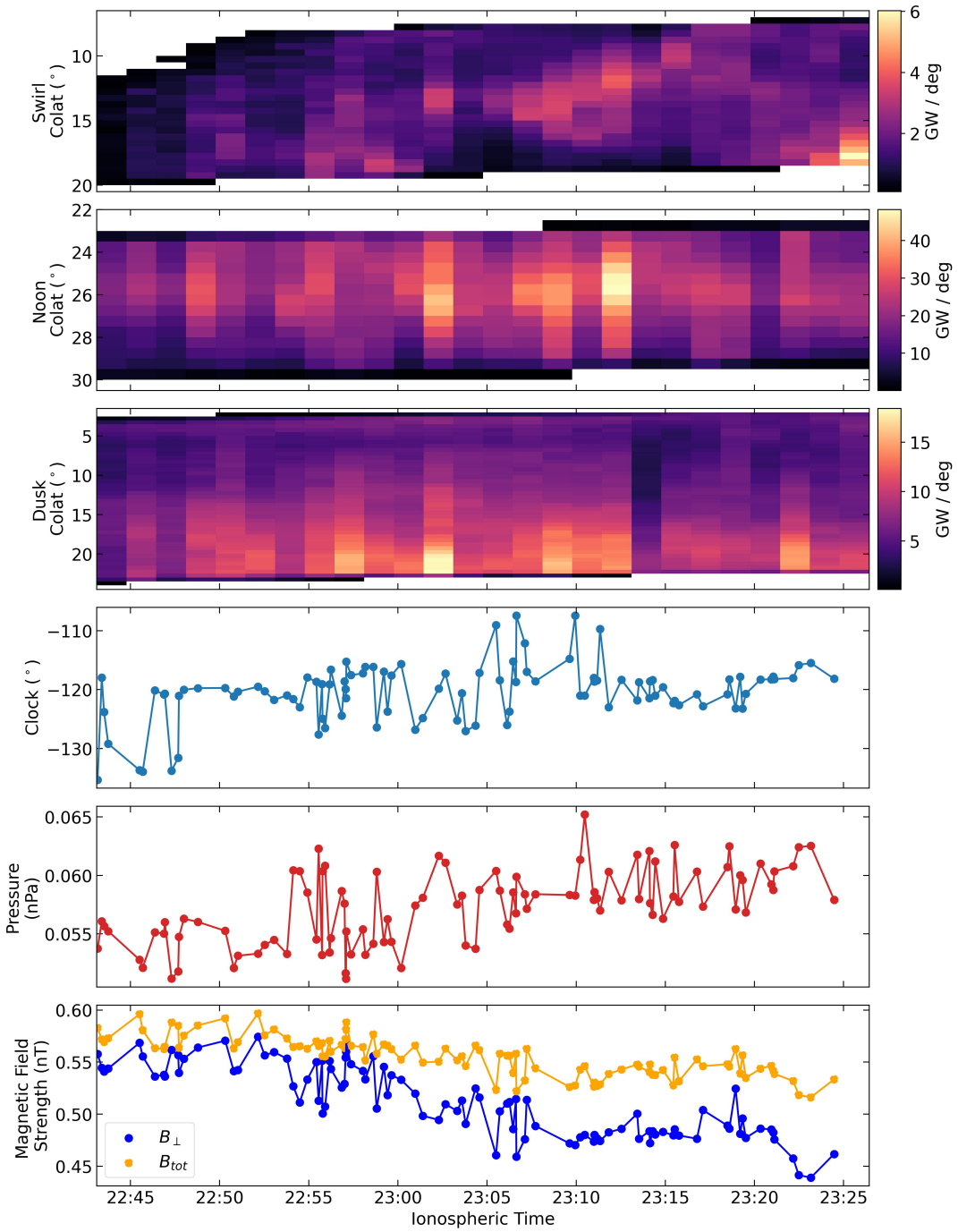

Figure B.1.4: Comparison of auroral power distribution and solar wind conditions during visit 05. The top three panels display keograms for the Swirl, Noon, and Dusk regions as a function of colatitude and Ionospheric Time. The bottom three panels show the corresponding IMF clock angle, solar wind dynamic pressure and IMF strength ($B_\perp$ in blue, B_{tot} in orange), respectively.

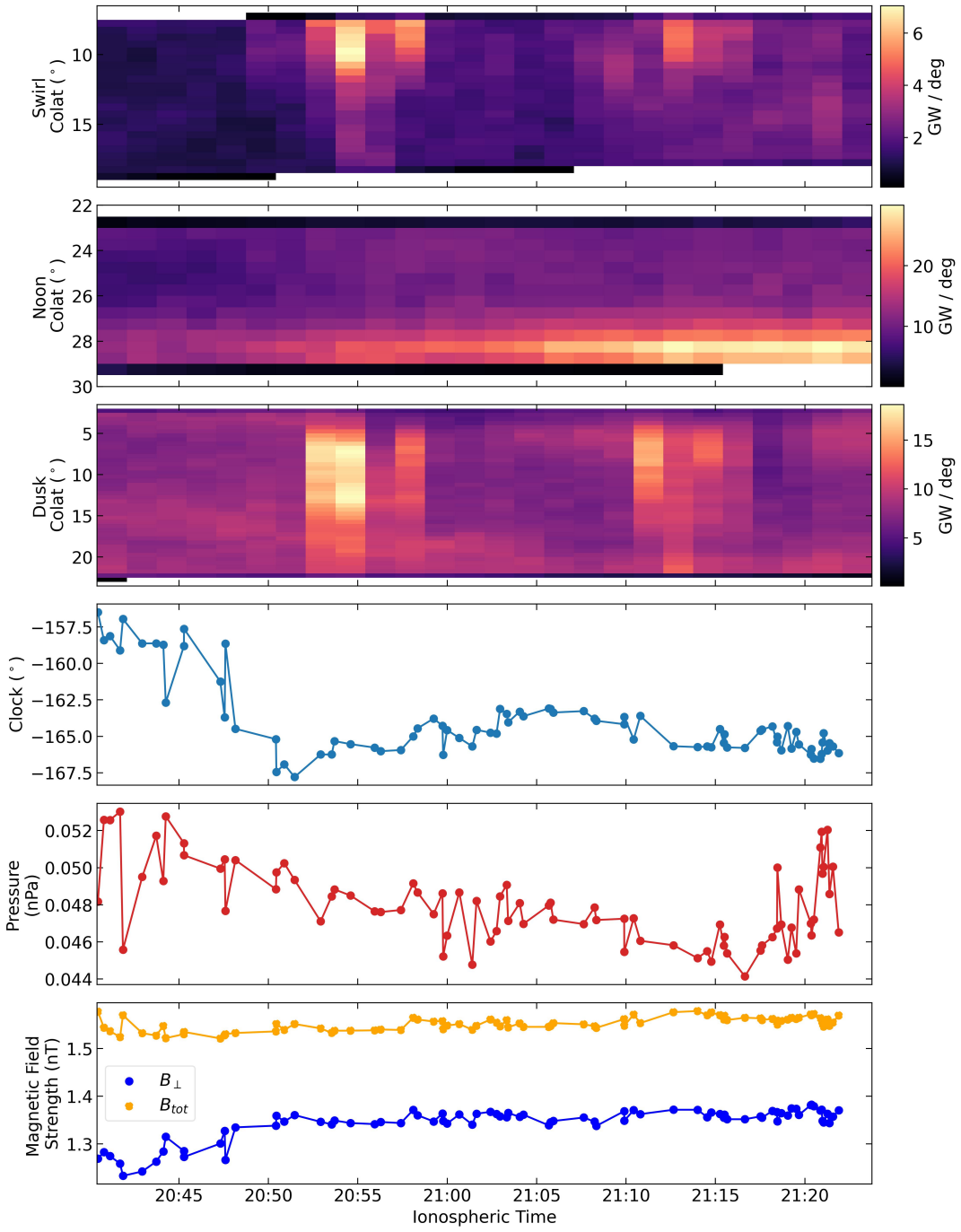

Figure B.1.5: Comparison of auroral power distribution and solar wind conditions during visit 08. The top three panels display keograms for the Swirl, Noon, and Dusk regions as a function of colatitude and Ionospheric Time. The bottom three panels show the corresponding IMF clock angle, solar wind dynamic pressure and IMF strength ($B_\perp$ in blue, B_{tot} in orange), respectively.

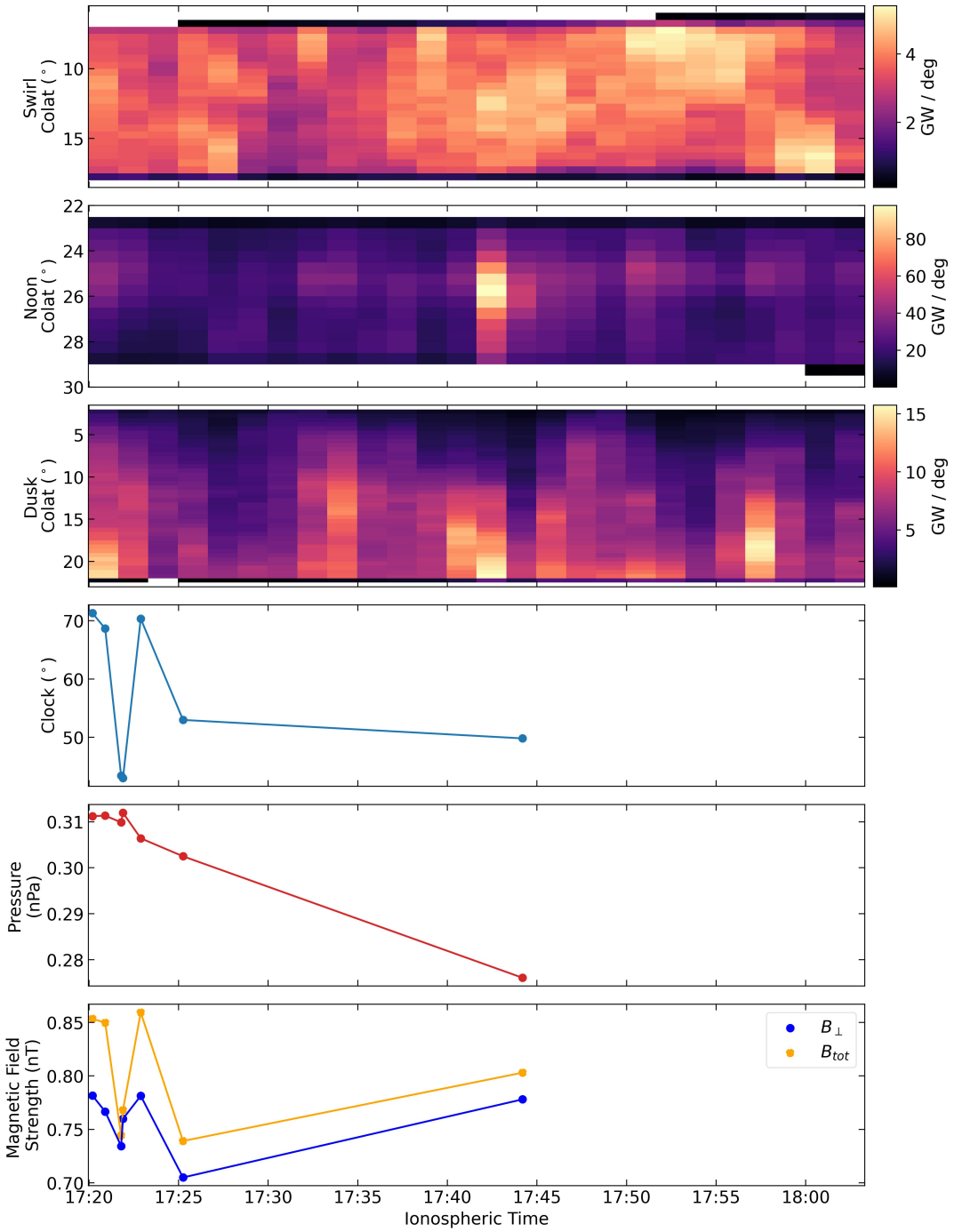

Figure B.1.6: Comparison of auroral power distribution and solar wind conditions during visit 09. The top three panels display keograms for the Swirl, Noon, and Dusk regions as a function of colatitude and Ionospheric Time. The bottom three panels show the corresponding IMF clock angle, solar wind dynamic pressure and IMF strength ($B_\perp$ in blue, B_{tot} in orange), respectively.

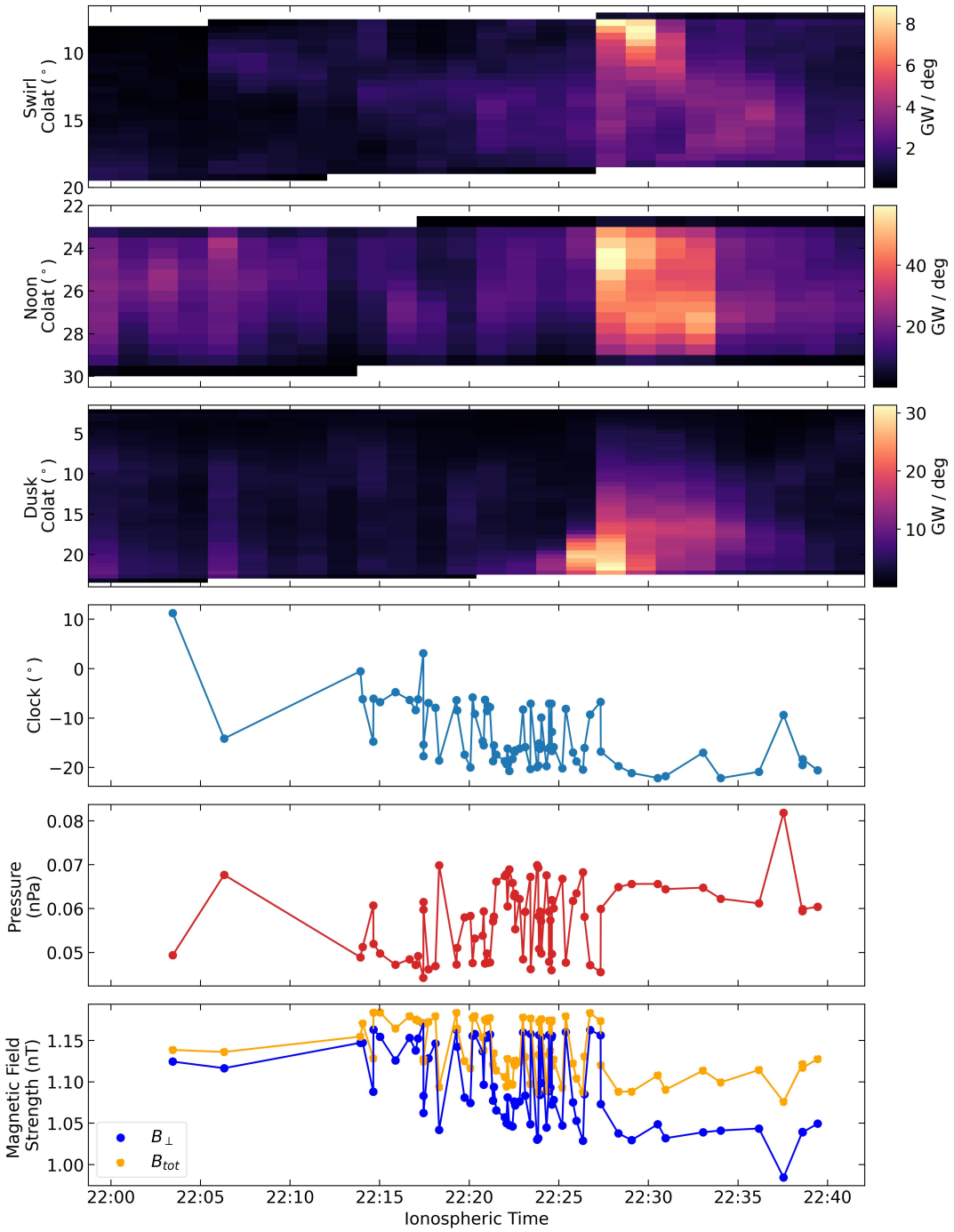

Figure B.1.7: Comparison of auroral power distribution and solar wind conditions during visit 10. The top three panels display keograms for the Swirl, Noon, and Dusk regions as a function of colatitude and Ionospheric Time. The bottom three panels show the corresponding IMF clock angle, solar wind dynamic pressure and IMF strength ($B_\perp$ in blue, B_{tot} in orange), respectively.

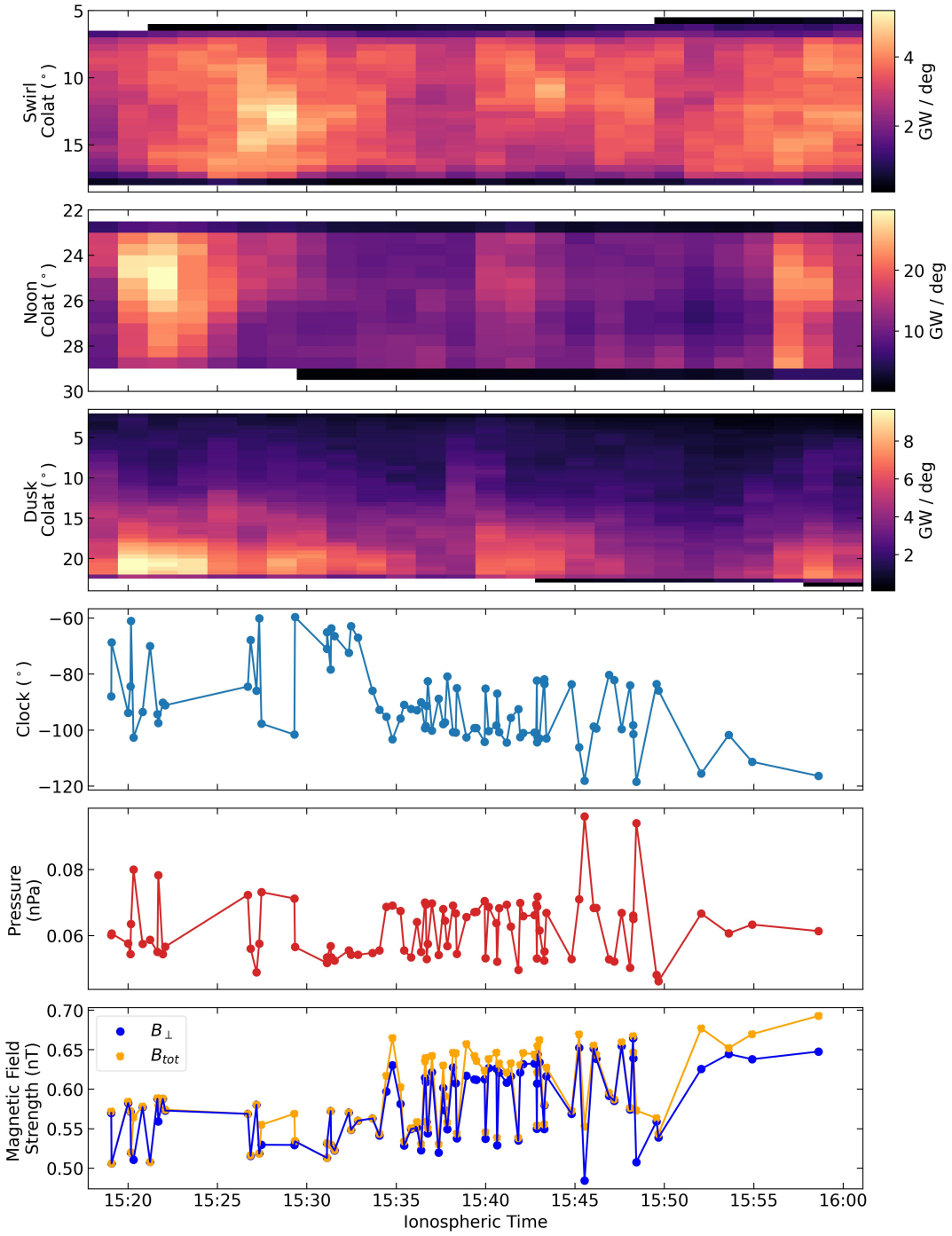

Figure B.1.8: Comparison of auroral power distribution and solar wind conditions during visit 11. The top three panels display keograms for the Swirl, Noon, and Dusk regions as a function of colatitude and Ionospheric Time. The bottom three panels show the corresponding IMF clock angle, solar wind dynamic pressure and IMF strength ($B_\perp$ in blue, B_{tot} in orange), respectively.

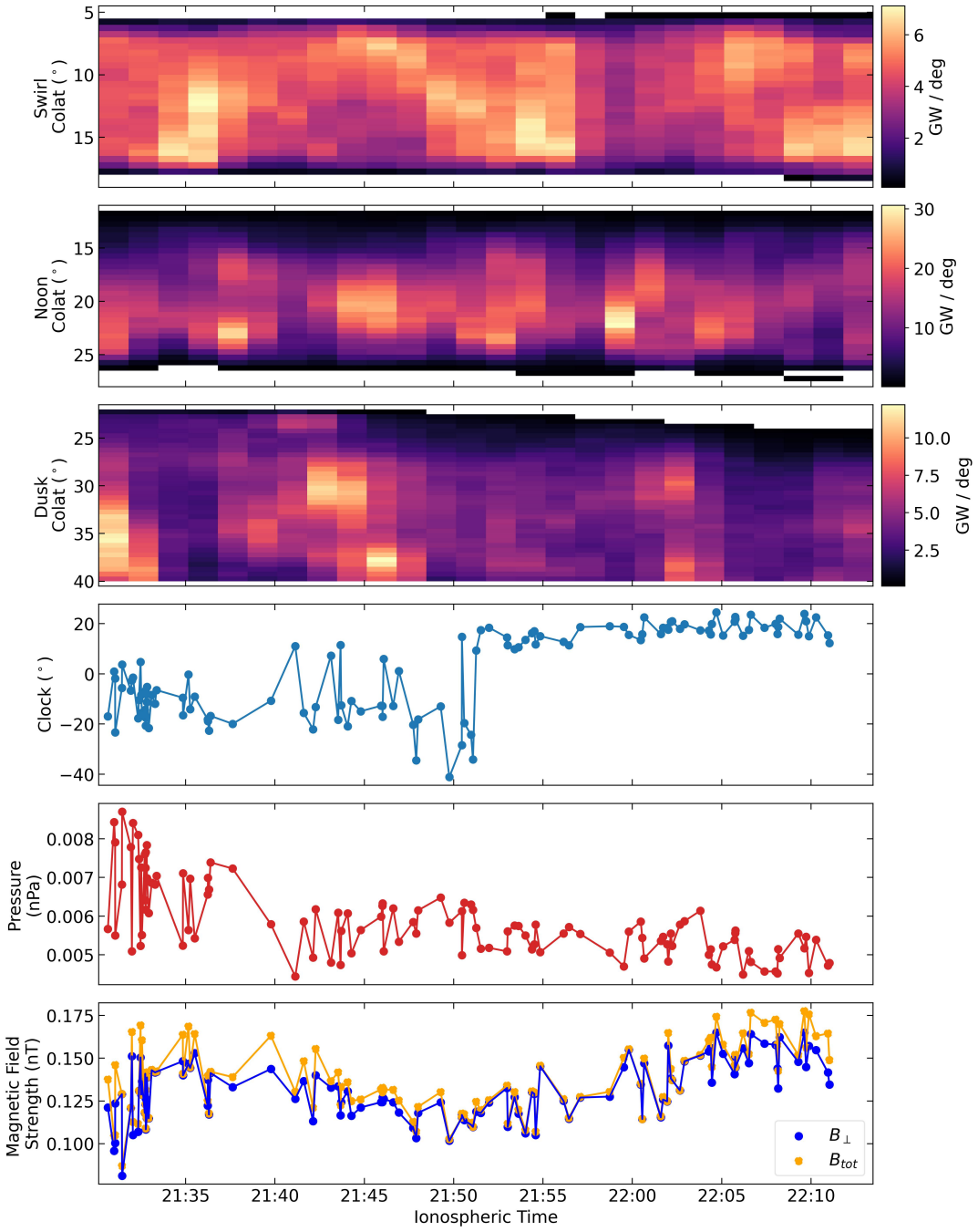

Figure B.1.9: Comparison of auroral power distribution and solar wind conditions during visit 12. The top three panels display keograms for the Swirl, Noon, and Dusk regions as a function of colatitude and Ionospheric Time. The bottom three panels show the corresponding IMF clock angle, solar wind dynamic pressure and IMF strength ($B_\perp$ in blue, B_{tot} in orange), respectively.

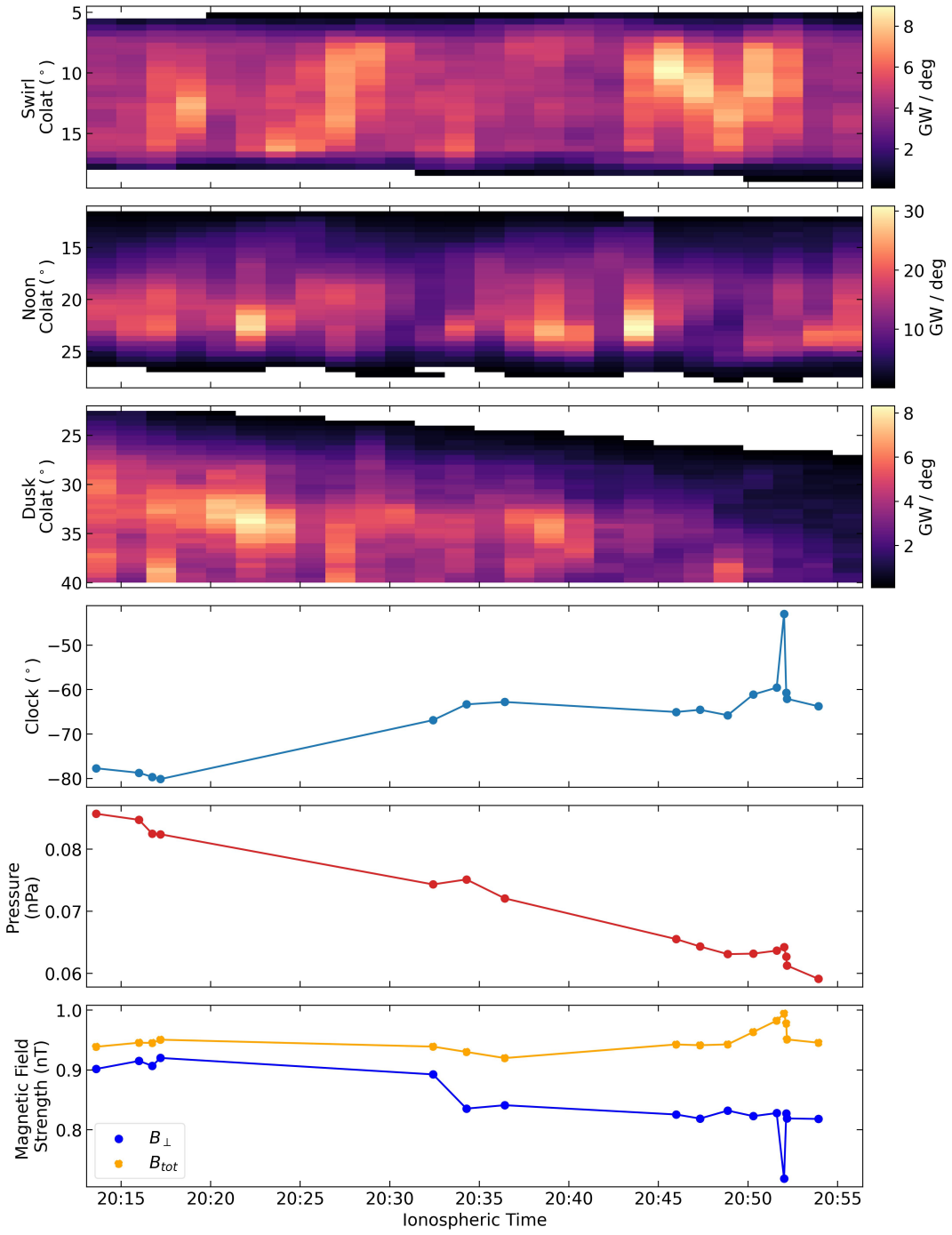

Figure B.1.10: Comparison of auroral power distribution and solar wind conditions during visit 15. The top three panels display keograms for the Swirl, Noon, and Dusk regions as a function of colatitude and Ionospheric Time. The bottom three panels show the corresponding IMF clock angle, solar wind dynamic pressure and IMF strength ($B_\perp$ in blue, B_{tot} in orange), respectively.

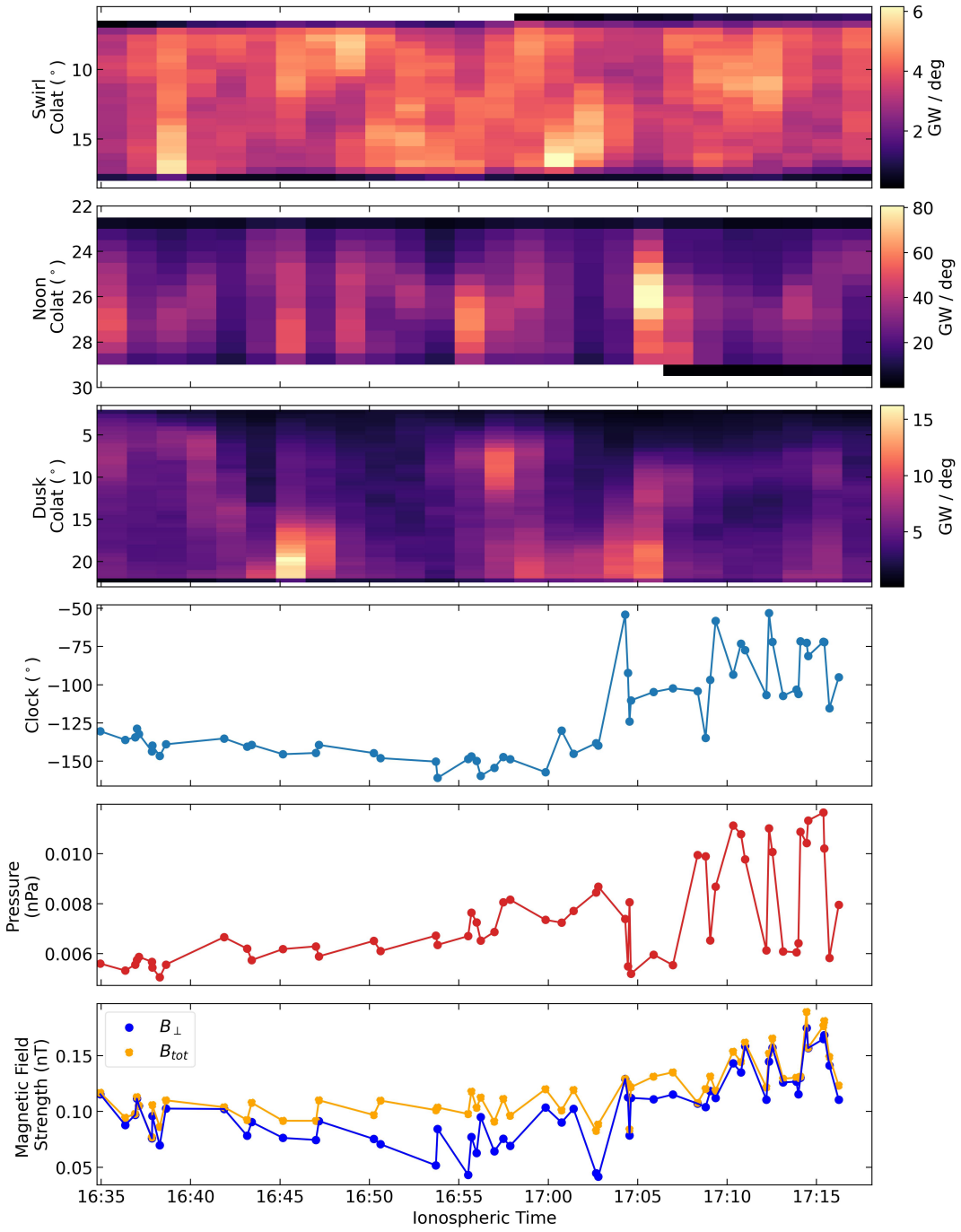

Figure B.1.11: Comparison of auroral power distribution and solar wind conditions during visit 16. The top three panels display keograms for the Swirl, Noon, and Dusk regions as a function of colatitude and Ionospheric Time. The bottom three panels show the corresponding IMF clock angle, solar wind dynamic pressure and IMF strength ($B_\perp$ in blue, B_{tot} in orange), respectively.

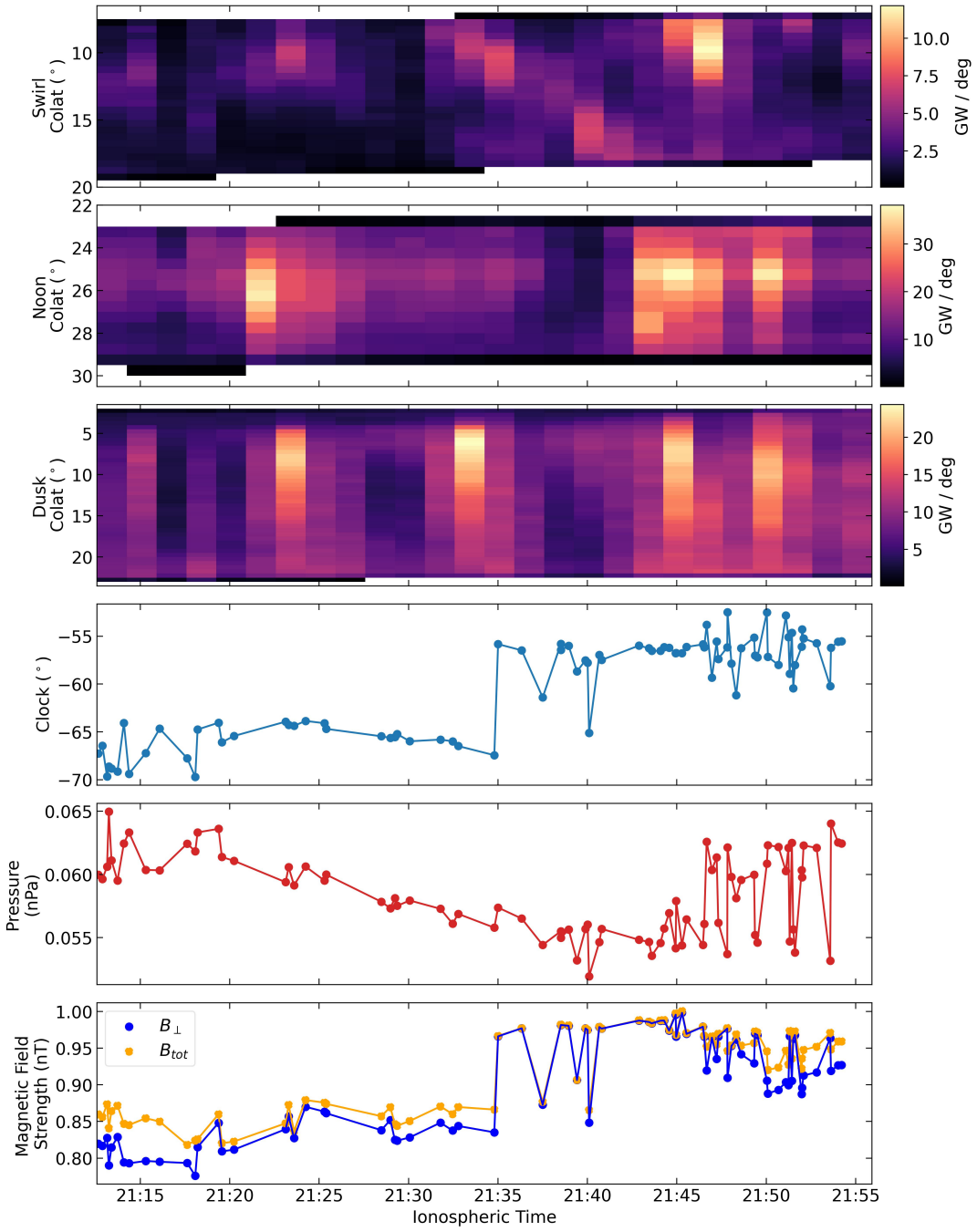

Figure B.1.12: Comparison of auroral power distribution and solar wind conditions during visit 17. The top three panels display keograms for the Swirl, Noon, and Dusk regions as a function of colatitude and Ionospheric Time. The bottom three panels show the corresponding IMF clock angle, solar wind dynamic pressure and IMF strength ($B_\perp$ in blue, B_{tot} in orange), respectively.

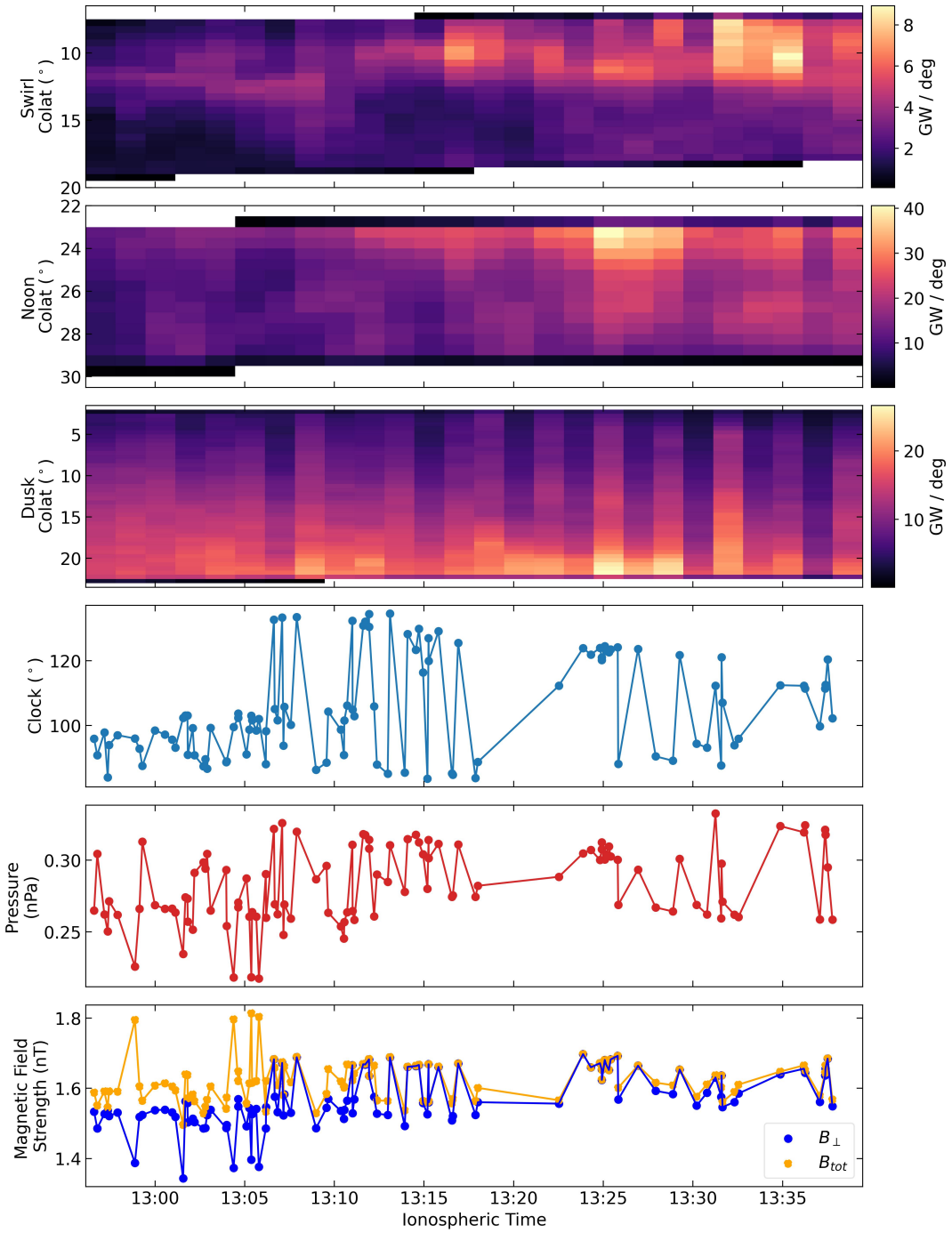

Figure B.1.13: Comparison of auroral power distribution and solar wind conditions during visit 19. The top three panels display keograms for the Swirl, Noon, and Dusk regions as a function of colatitude and Ionospheric Time. The bottom three panels show the corresponding IMF clock angle, solar wind dynamic pressure and IMF strength ($B_\perp$ in blue, B_{tot} in orange), respectively.

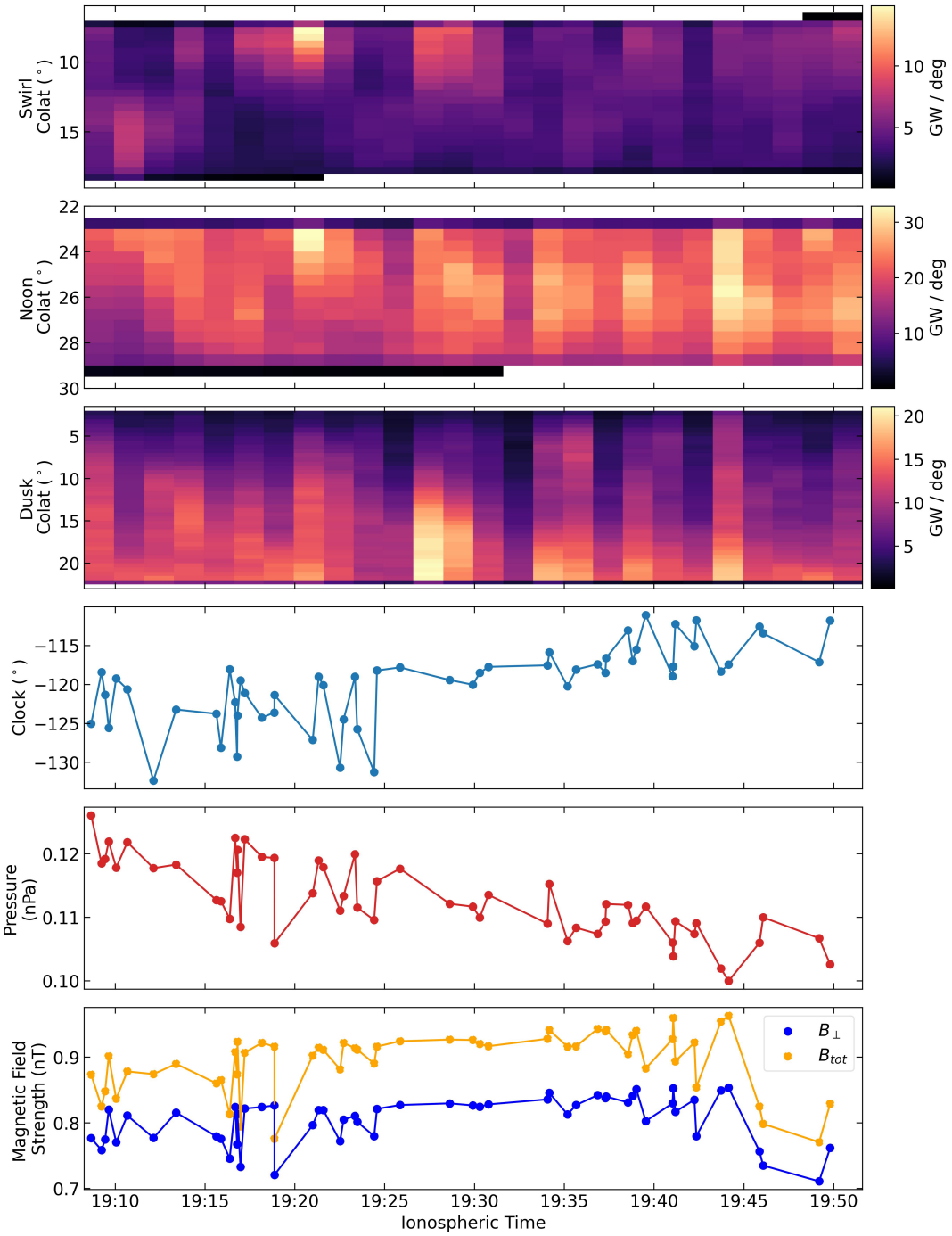

Figure B.1.14: Comparison of auroral power distribution and solar wind conditions during visit 20. The top three panels display keograms for the Swirl, Noon, and Dusk regions as a function of colatitude and Ionospheric Time. The bottom three panels show the corresponding IMF clock angle, solar wind dynamic pressure and IMF strength ($B_\perp$ in blue, B_{tot} in orange), respectively.

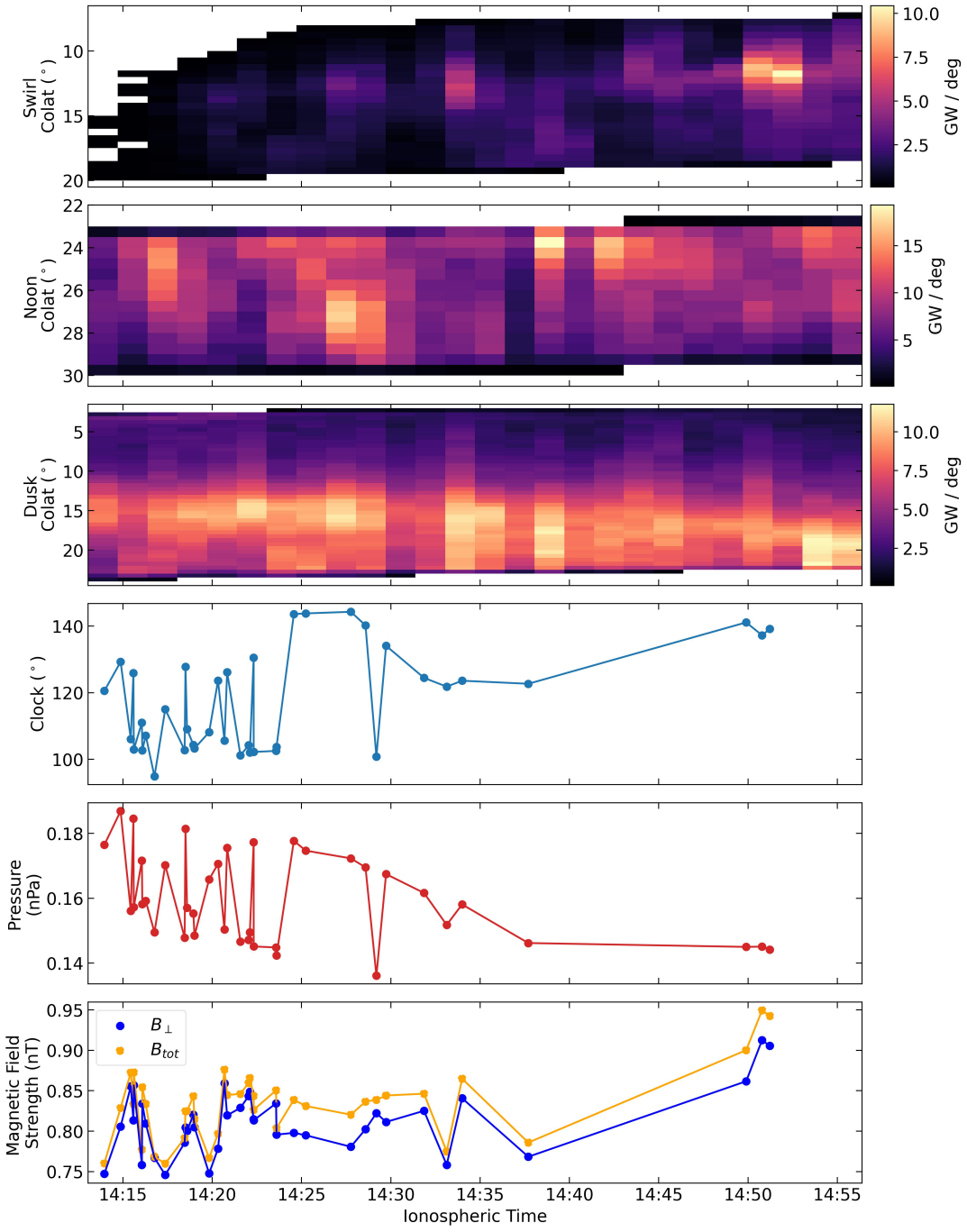

Figure B.1.15: Comparison of auroral power distribution and solar wind conditions during visit 21. The top three panels display keograms for the Swirl, Noon, and Dusk regions as a function of colatitude and Ionospheric Time. The bottom three panels show the corresponding IMF clock angle, solar wind dynamic pressure and IMF strength ($B_\perp$ in blue, B_{tot} in orange), respectively.

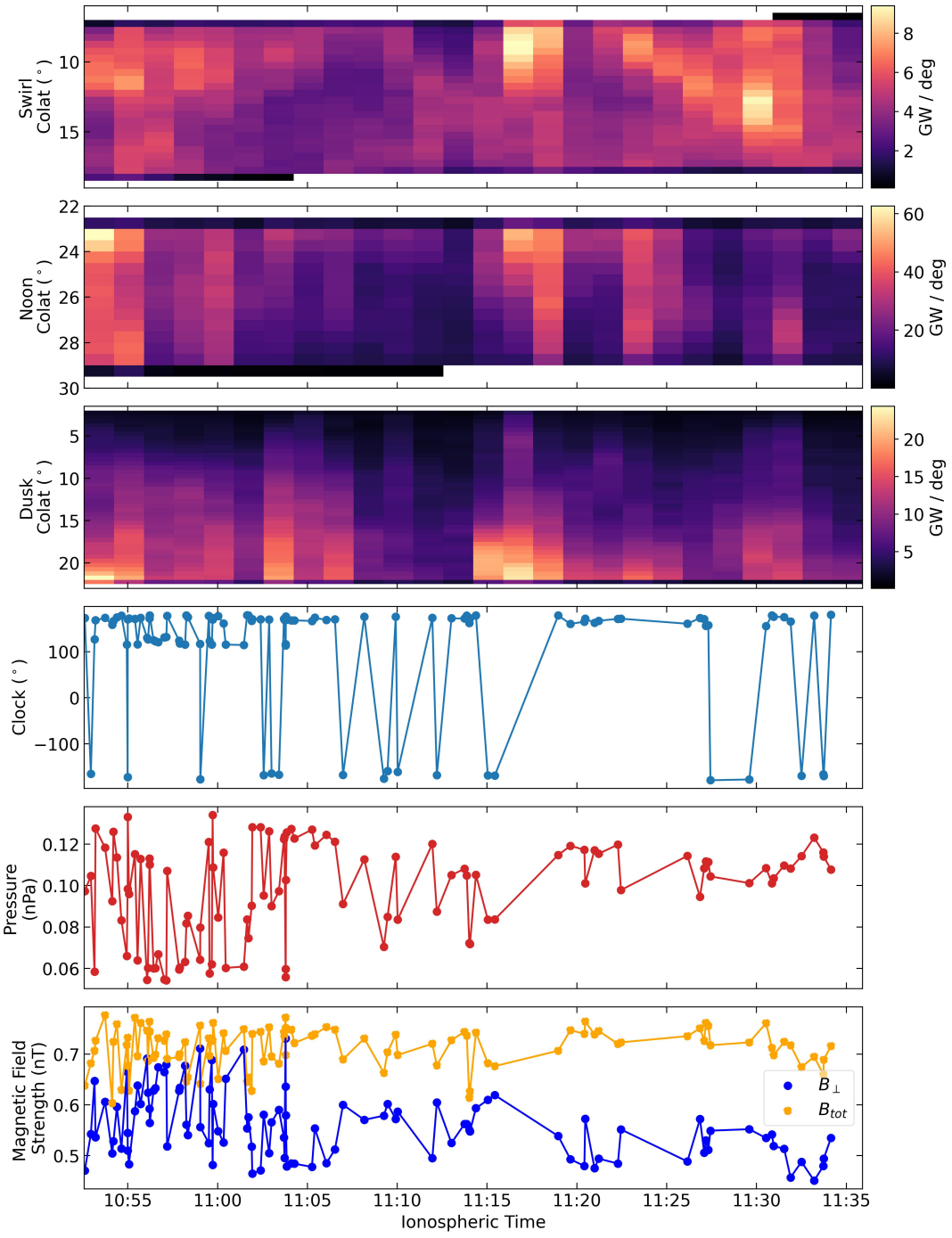

Figure B.1.16: Comparison of auroral power distribution and solar wind conditions during visit 24. The top three panels display keograms for the Swirl, Noon, and Dusk regions as a function of colatitude and Ionospheric Time. The bottom three panels show the corresponding IMF clock angle, solar wind dynamic pressure and IMF strength ($B_\perp$ in blue, B_{tot} in orange), respectively.

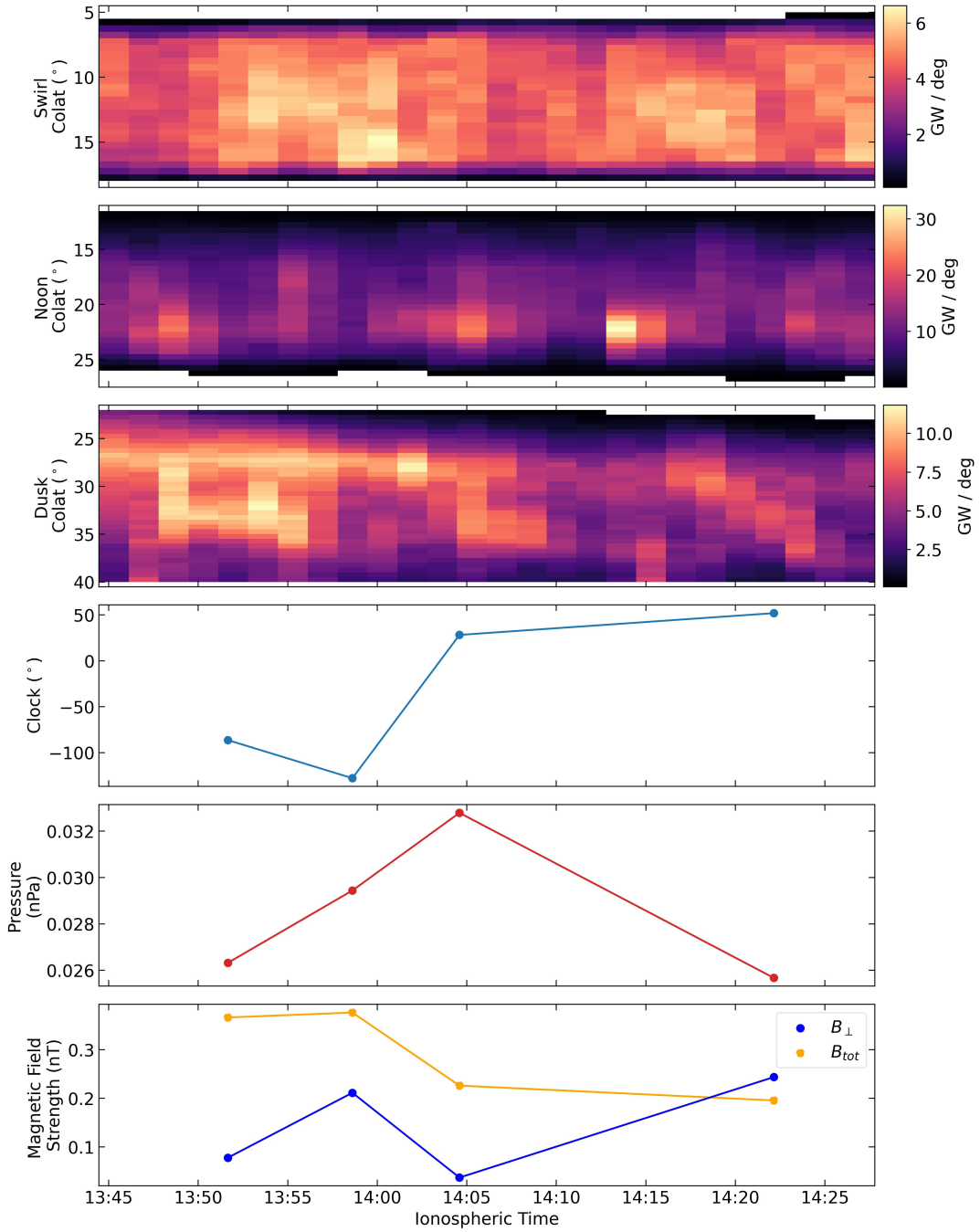

Figure B.1.17: Comparison of auroral power distribution and solar wind conditions during visit 26. The top three panels display keograms for the Swirl, Noon, and Dusk regions as a function of colatitude and Ionospheric Time. The bottom three panels show the corresponding IMF clock angle, solar wind dynamic pressure and IMF strength ($B_\perp$ in blue, B_{tot} in orange), respectively.

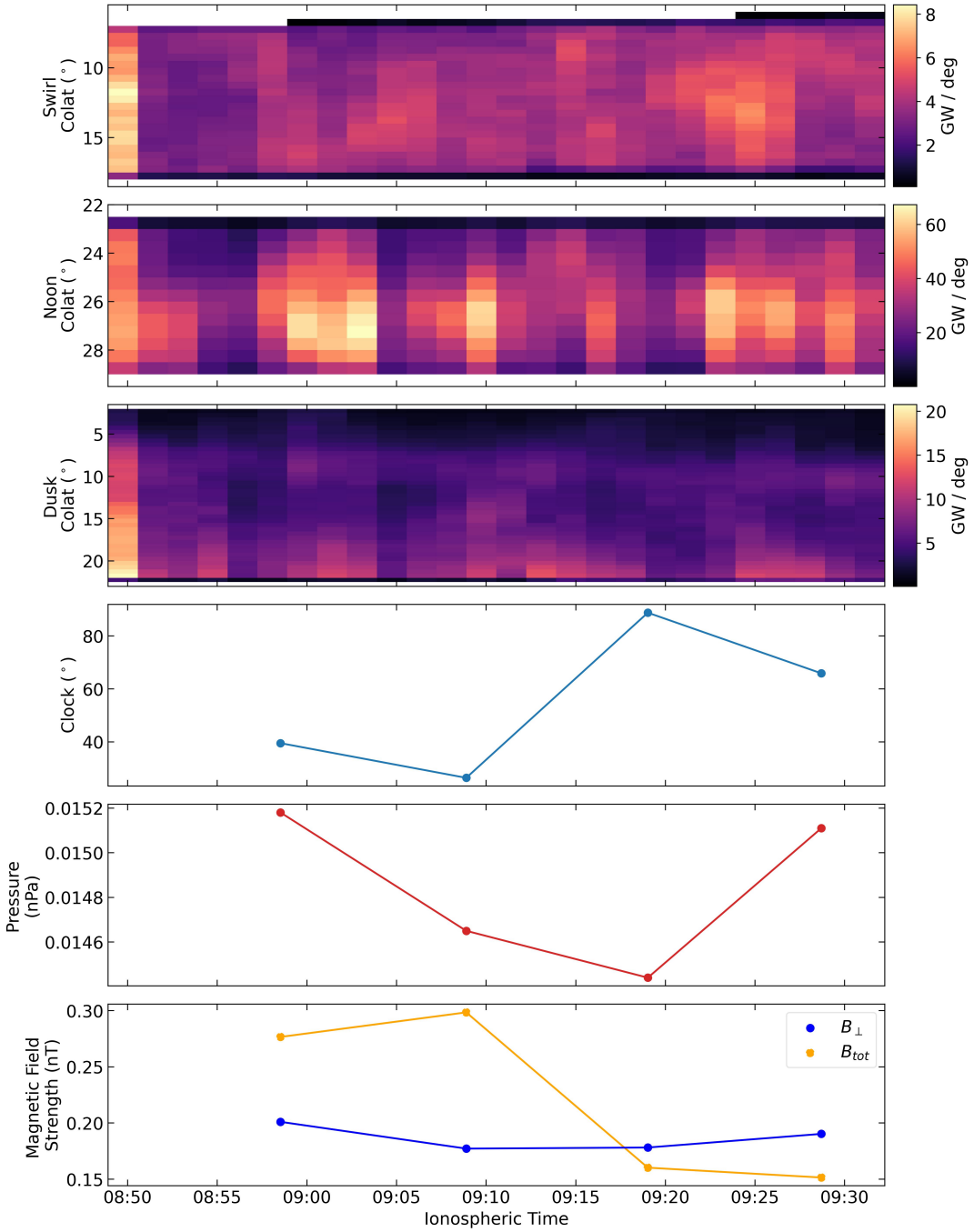

Figure B.1.18: Comparison of auroral power distribution and solar wind conditions during visit 27. The top three panels display keograms for the Swirl, Noon, and Dusk regions as a function of colatitude and Ionospheric Time. The bottom three panels show the corresponding IMF clock angle, solar wind dynamic pressure and IMF strength ($B_\perp$ in blue, B_{tot} in orange), respectively.

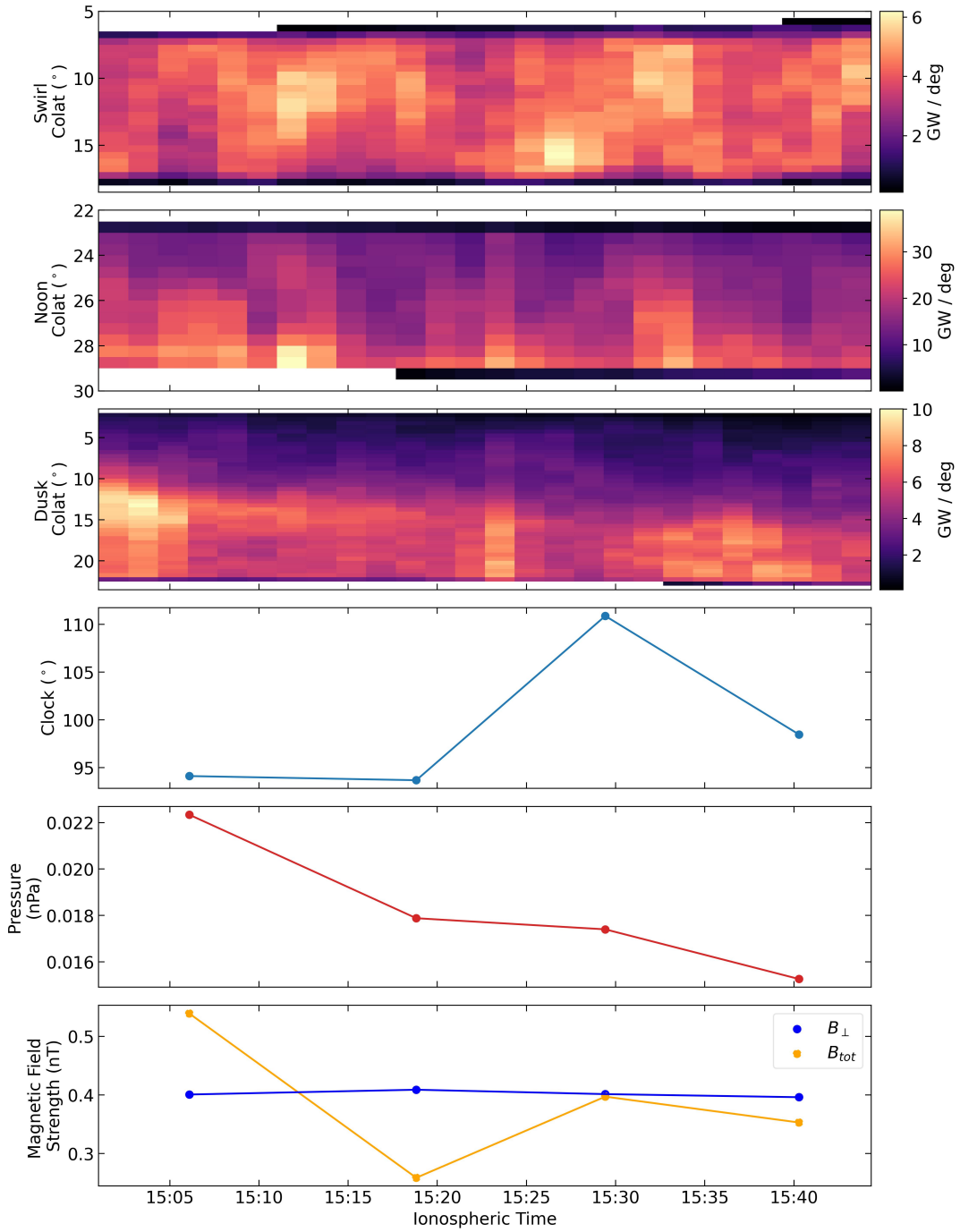

Figure B.1.19: Comparison of auroral power distribution and solar wind conditions during visit 28. The top three panels display keograms for the Swirl, Noon, and Dusk regions as a function of colatitude and Ionospheric Time. The bottom three panels show the corresponding IMF clock angle, solar wind dynamic pressure and IMF strength ($B_\perp$ in blue, B_{tot} in orange), respectively.

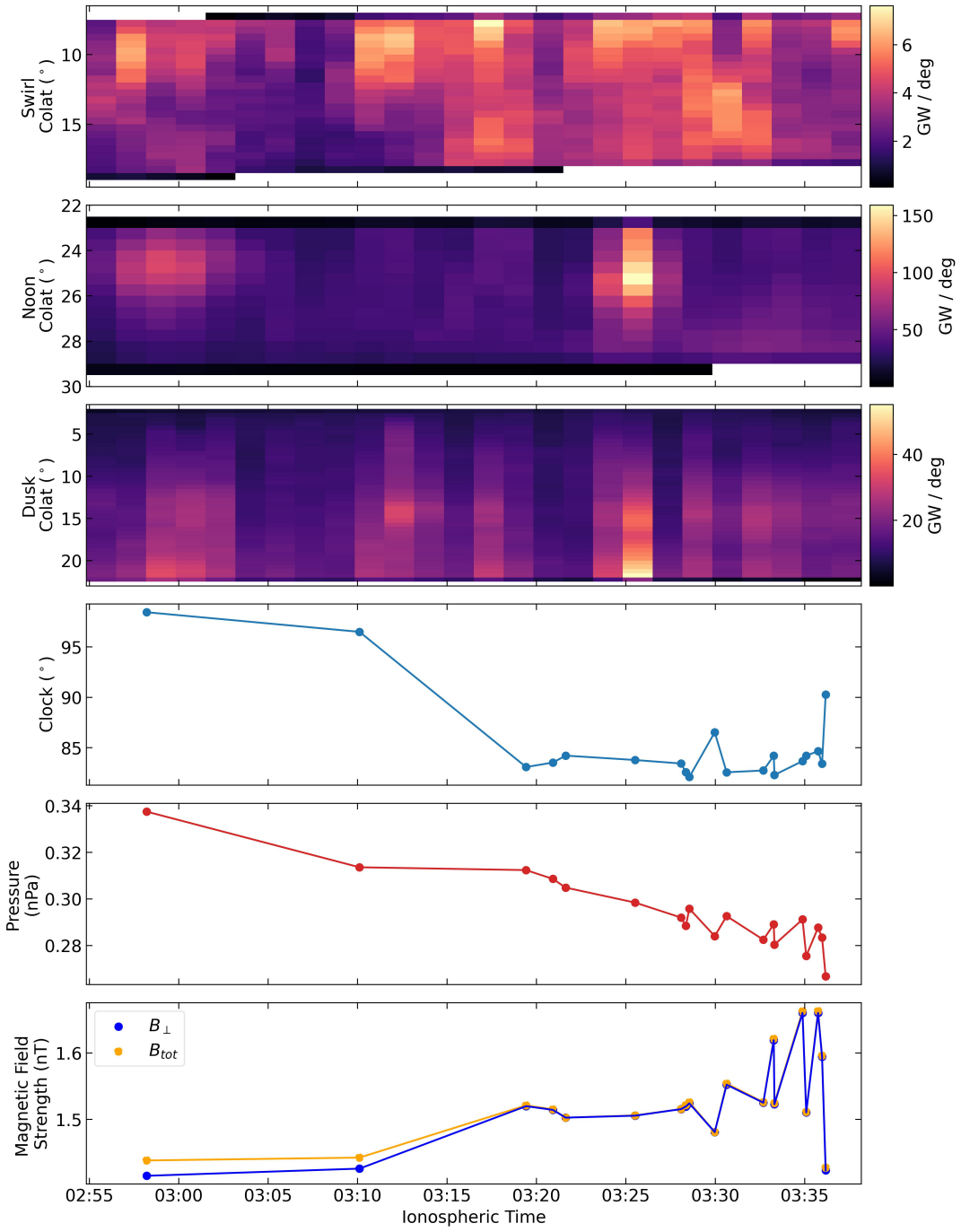

Figure B.1.20: Comparison of auroral power distribution and solar wind conditions during visit 34. The top three panels display keograms for the Swirl, Noon, and Dusk regions as a function of colatitude and Ionospheric Time. The bottom three panels show the corresponding IMF clock angle, solar wind dynamic pressure and IMF strength ($B_\perp$ in blue, B_{tot} in orange), respectively.

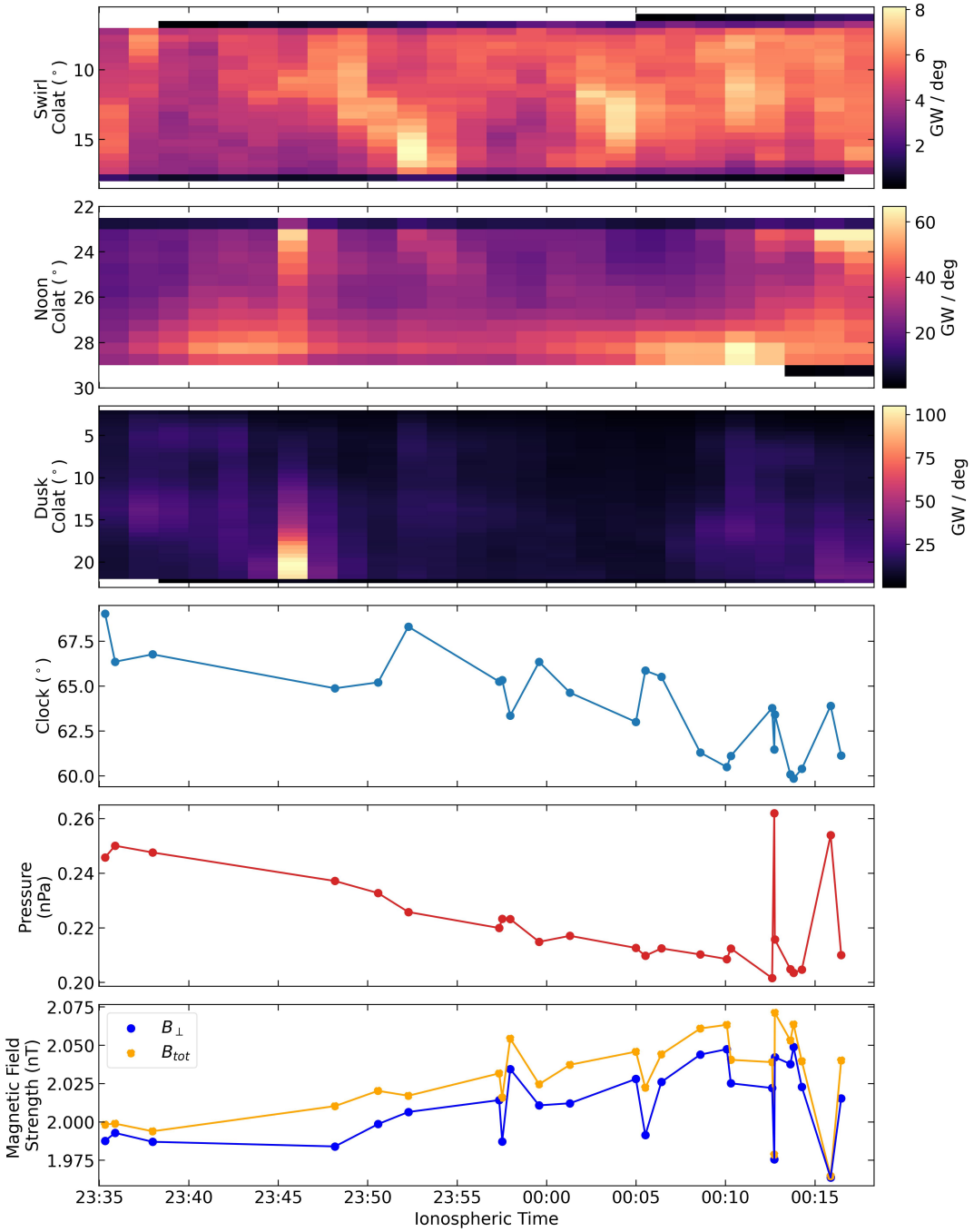

Figure B.1.21: Comparison of auroral power distribution and solar wind conditions during visit 35. The top three panels display keograms for the Swirl, Noon, and Dusk regions as a function of colatitude and Ionospheric Time. The bottom three panels show the corresponding IMF clock angle, solar wind dynamic pressure and IMF strength ($B_\perp$ in blue, B_{tot} in orange), respectively.

B.2 Clock Angle vs Auroral Power

The following figures show the full results from applying the coupling functions in Chapter 4 to the IMF clock angle and auroral power to determine any potential relationship. As no relationships are found and the results of the multi-latitude reconnection coupling function is shared in Chapter 4 for the context of discussing the process of evaluating the fits, the rest are shared here for completeness.

Using equation 4.5, figures B.2.1 and B.2.2 represent dayside reconnection at Jupiter. Figures B.2.3 and B.2.4 show the coupling function 4.6, which represents high-latitude reconnection. Finally, figures B.2.5 and B.2.6 show post-cusp reconnection, the results of fitting equation 4.8. The first figure in each of these sets shows the results for each polar region, whilst the second figure in each pair includes the 20% shorter and longer solar wind propagation times as a measure of uncertainty in the solar wind travel time.

The post-cusp and dayside coupling functions have the same values for R^2 and visually appear identical. As the two coupling functions are opposites, this is as expected. As the dayside coupling function should minimise at $\pm 180°$, the inverted fit in panel c of figures B.2.1 and B.2.2 show that the dusk active region is better fit for post-cusp reconnection than dayside reconnection. The opposite case is shown in figures B.2.5 and B.2.6 for the swirl and noon active regions (panels b and d), where the post-cusp coupling function should maximise at $0°$. Despite each polar region being better fit by the dayside or the post-cusp coupling function than its opposite, neither of these coupling functions represents a good fit to the data.

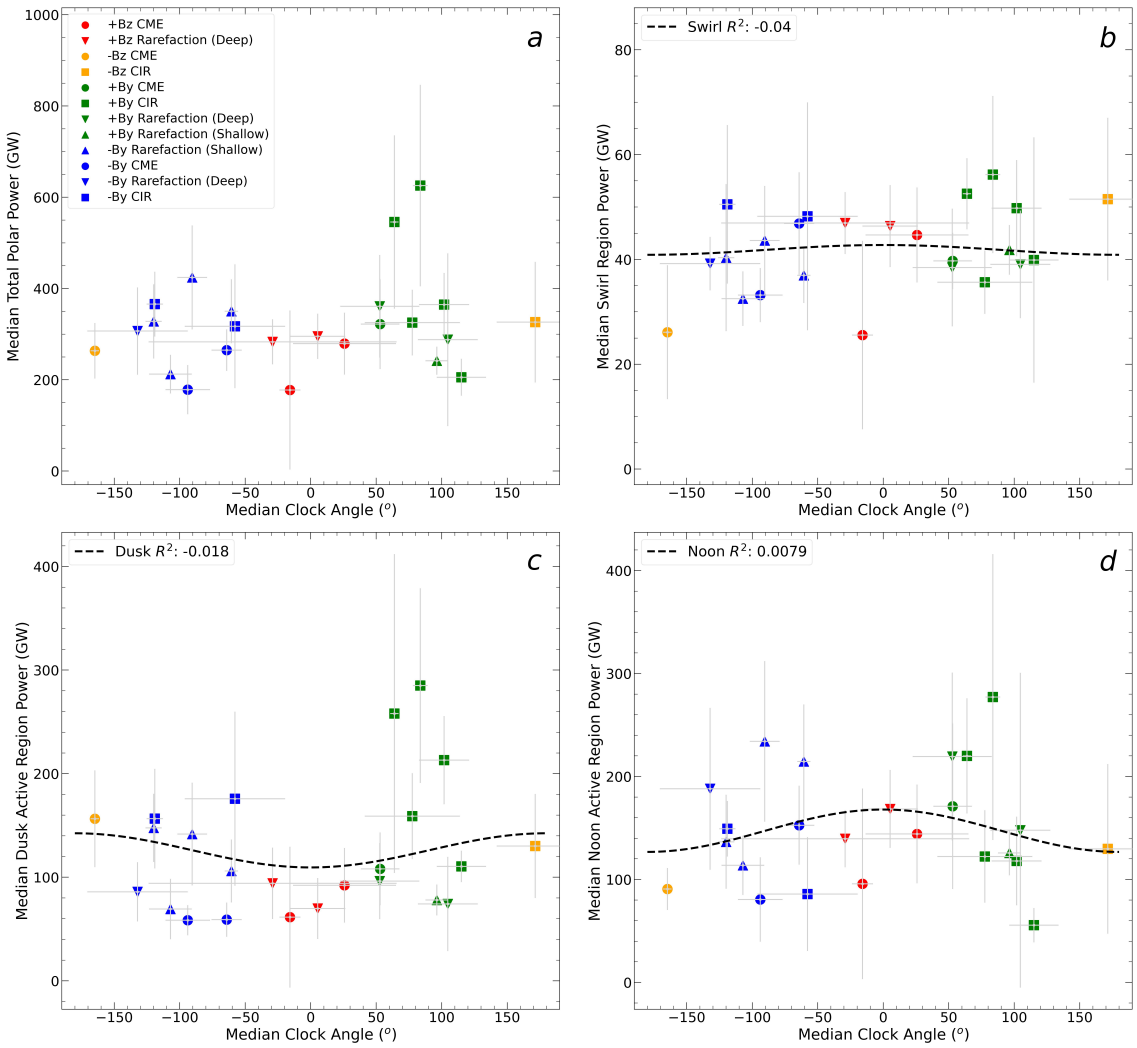

Figure B.2.1: Relationship between median averaged clock angle per visit and the median: (a) total polar power, (b) swirl region power, (c) dusk active region power and (d) noon active region power. The relationship is fitted with the equation $A \times cos^2(\frac{\theta}{2}) + b$, representing large-scale reconnection at low latitudes on the dayside where the use of cosine favours $+B_z$ reconnection due to Jupiter's $-B_z$ field orientation.

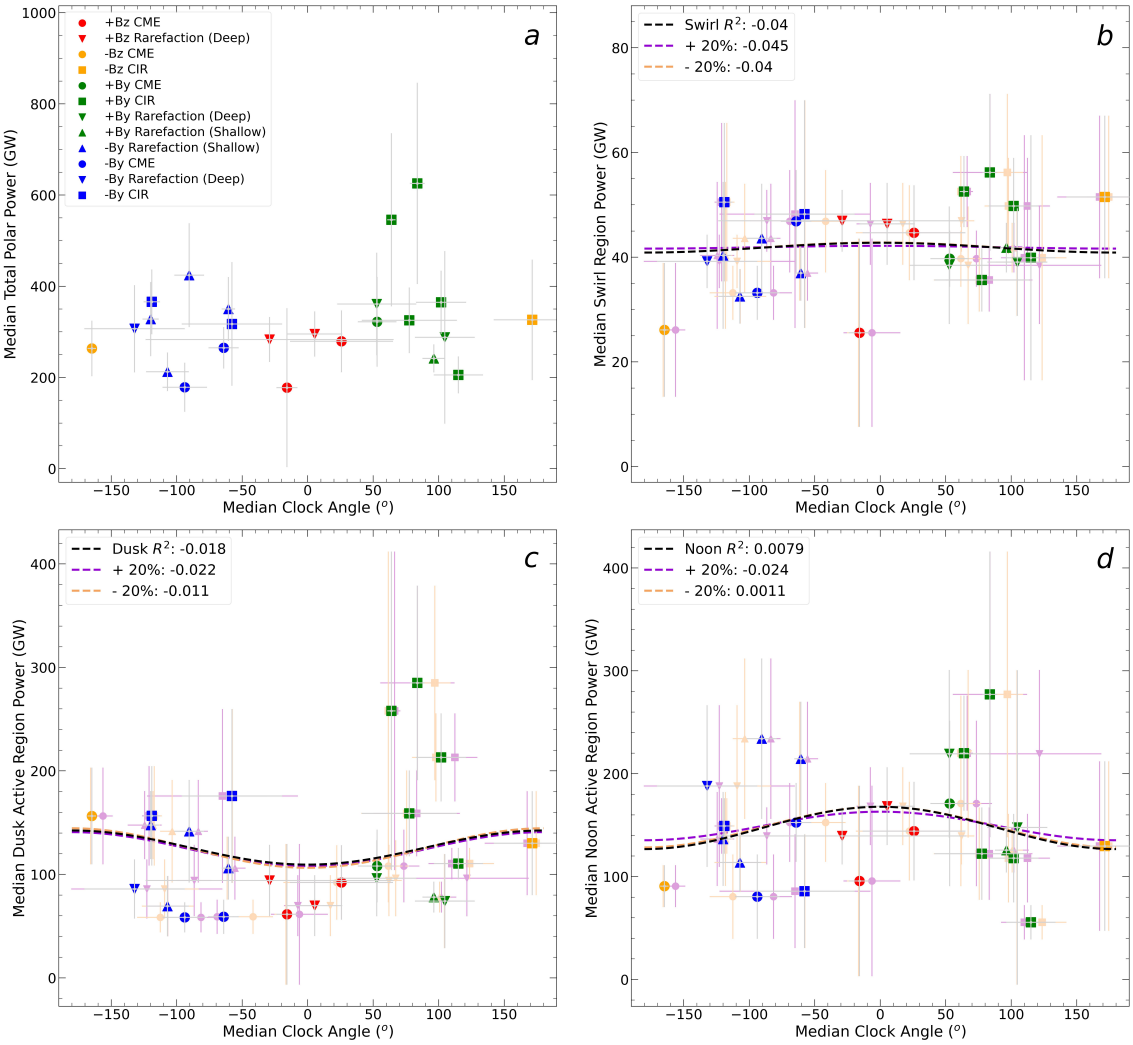

Figure B.2.2: The same as figure B.2.1 but with the addition of a ±20% propagation time uncertainty window applied to the solar wind travel time from Juno to Jupiter's magnetosphere.

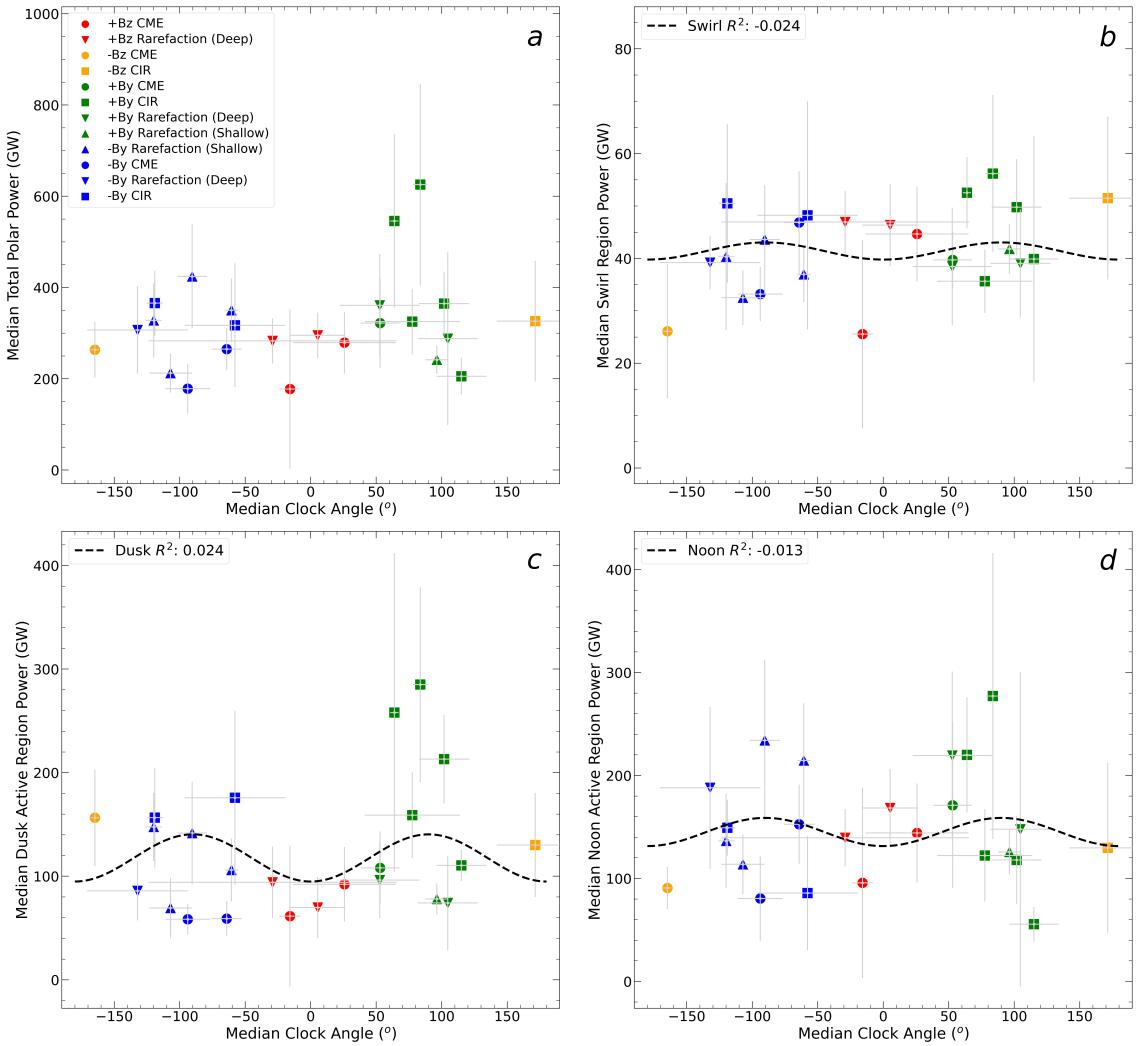

Figure B.2.3: Relationship between median averaged clock angle per visit and the median: (a) total polar power, (b) swirl region power, (c) dusk active region power and (d) noon active region power. The relationship is fitted with the equation $A \times \sin^2(\theta) + B$, representing high latitude reconnection at the dawn and dusk sectors of the dayside magnetic field.

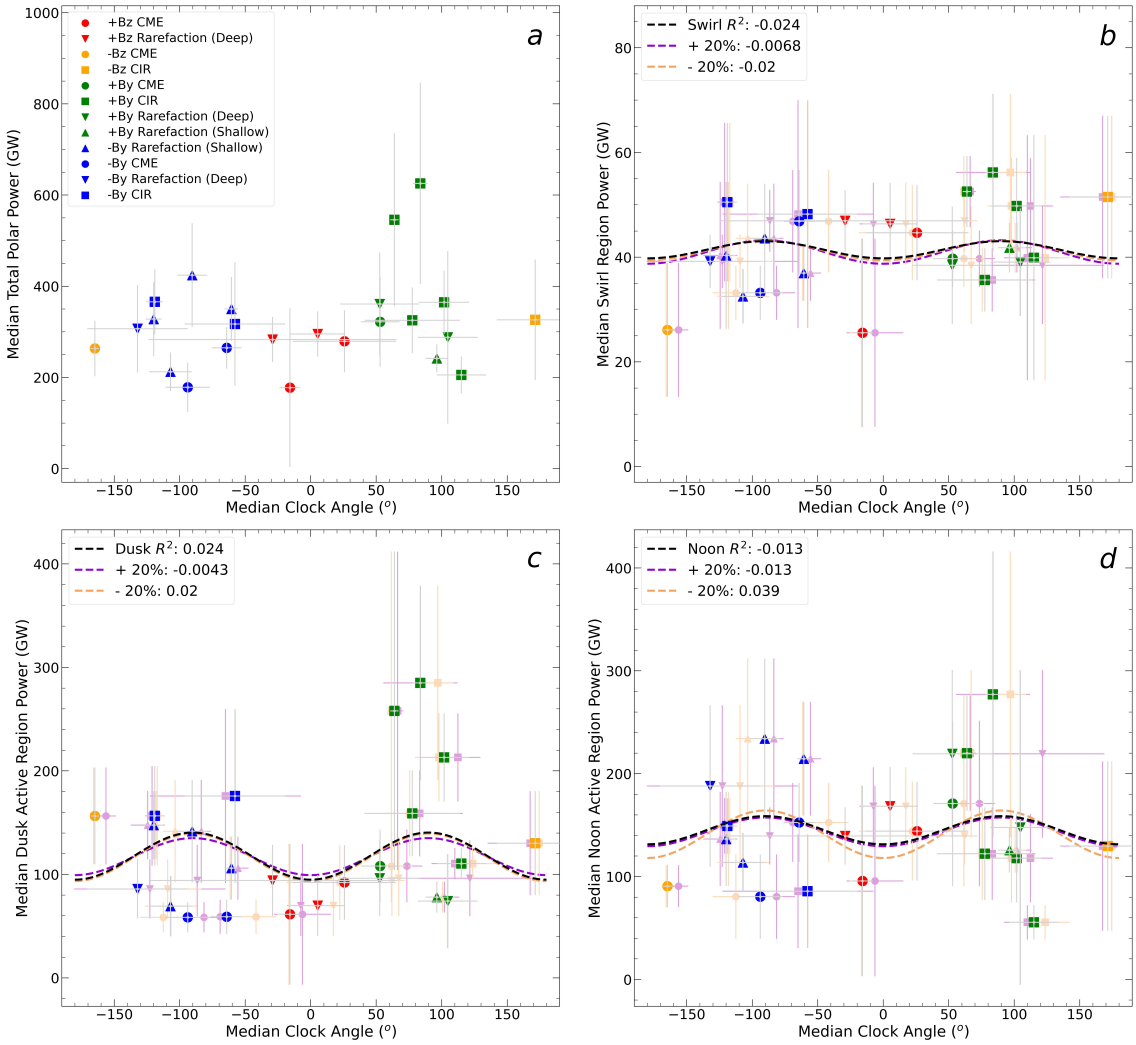

Figure B.2.4: The same as figure B.2.3 but with the addition of a ±20% propagation time uncertainty window applied to the solar wind travel time from Juno to Jupiter's magnetosphere.

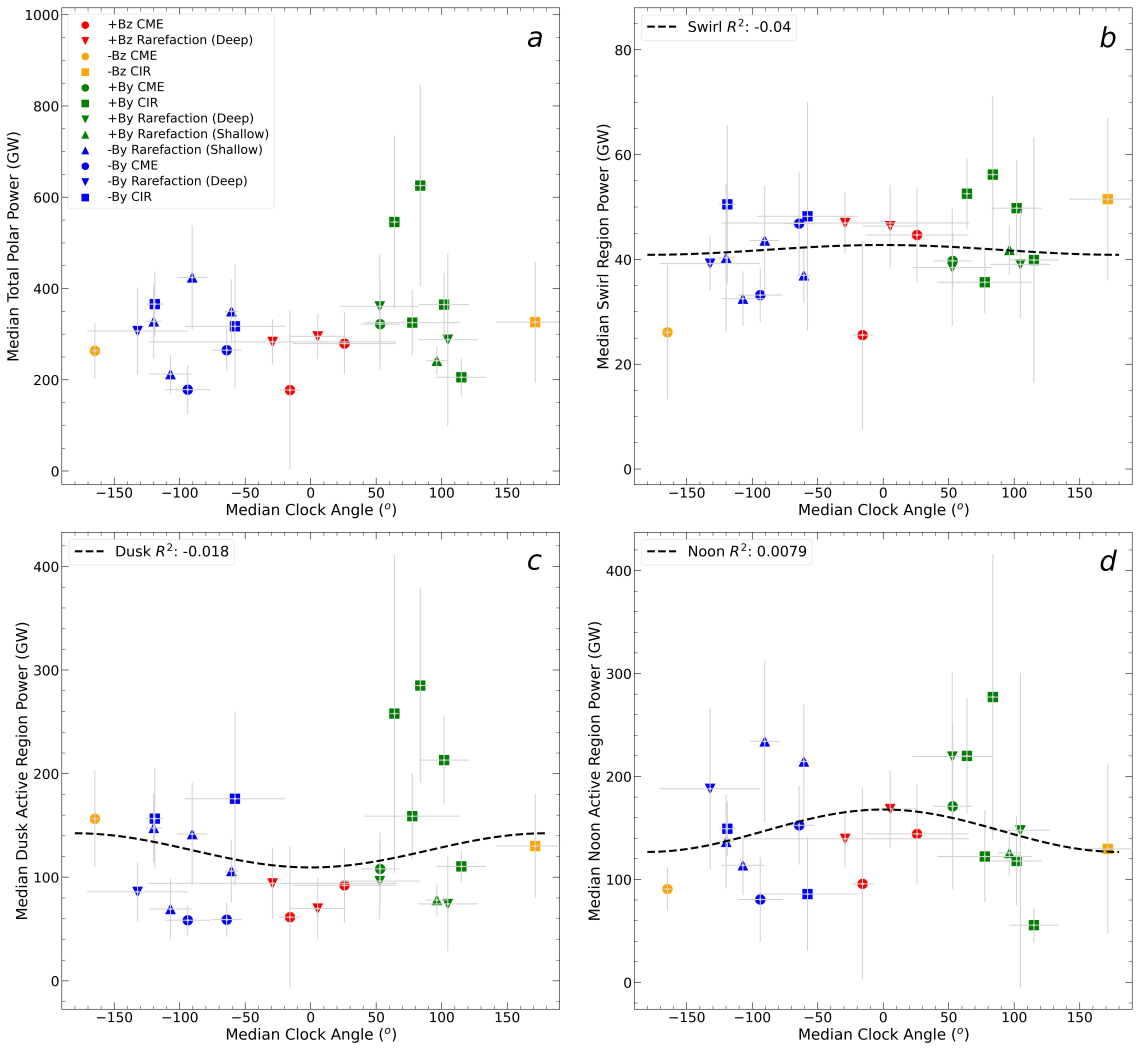

Figure B.2.5: Relationship between median averaged clock angle per visit and the median: (a) total polar power, (b) swirl region power, (c) dusk active region power and (d) noon active region power. The relationship is fitted with the equation $A \times sin^2(\frac{\theta}{2}) + B$, representing reconnection with twisted open field lines emerging from the polar region and trailing behind the planet due to the flow of the solar wind.

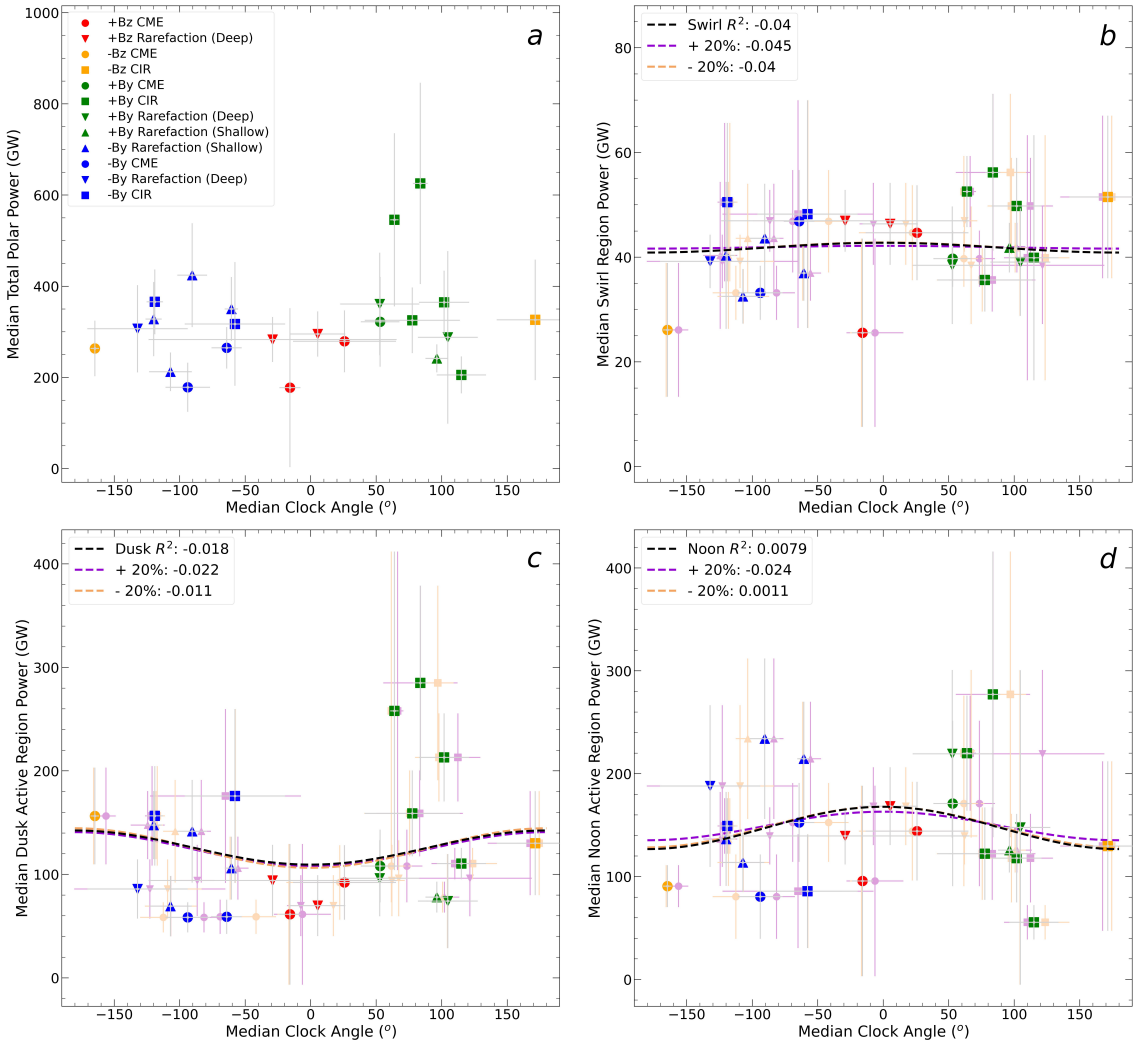

Figure B.2.6: The same as figure B.2.5 but with the addition of a ±20% propagation time error applied to the solar wind travel time from Juno to Jupiter's magnetosphere.

B.3 Other Solar Wind Variables

B.3.1 Pressure

As only the dusk active region is shared in Chapter 4, as it is the only region to show a response in auroral power to solar wind dynamic pressure, the full figures are shown here for completeness. Figure B.3.1 shows the results for all polar regions and figure B.3.2 includes the 20% shorter and longer propagation times as an uncertainty window.

B.3.2 Magnetic Field Strength

In a similar case to pressure, only the dusk active region shows a response to a varying solar wind magnetic field strength, for both the perpendicular and total magnetic field cases. The full comparisons for all regions in both cases can be found in figures B.3.3 and B.3.4 for $B_{\perp}$ and figures B.3.5 and B.3.6 for B_{total}, where the latter of each pair of figures includes the 20% shorter and longer propagation times to represent the uncertainty in the solar wind travel time. The difference between these two sets of plots is the exclusion of the B_x component of the IMF in the calculation of $B_{\perp}$, which results in some differences in the computed R^2 value.

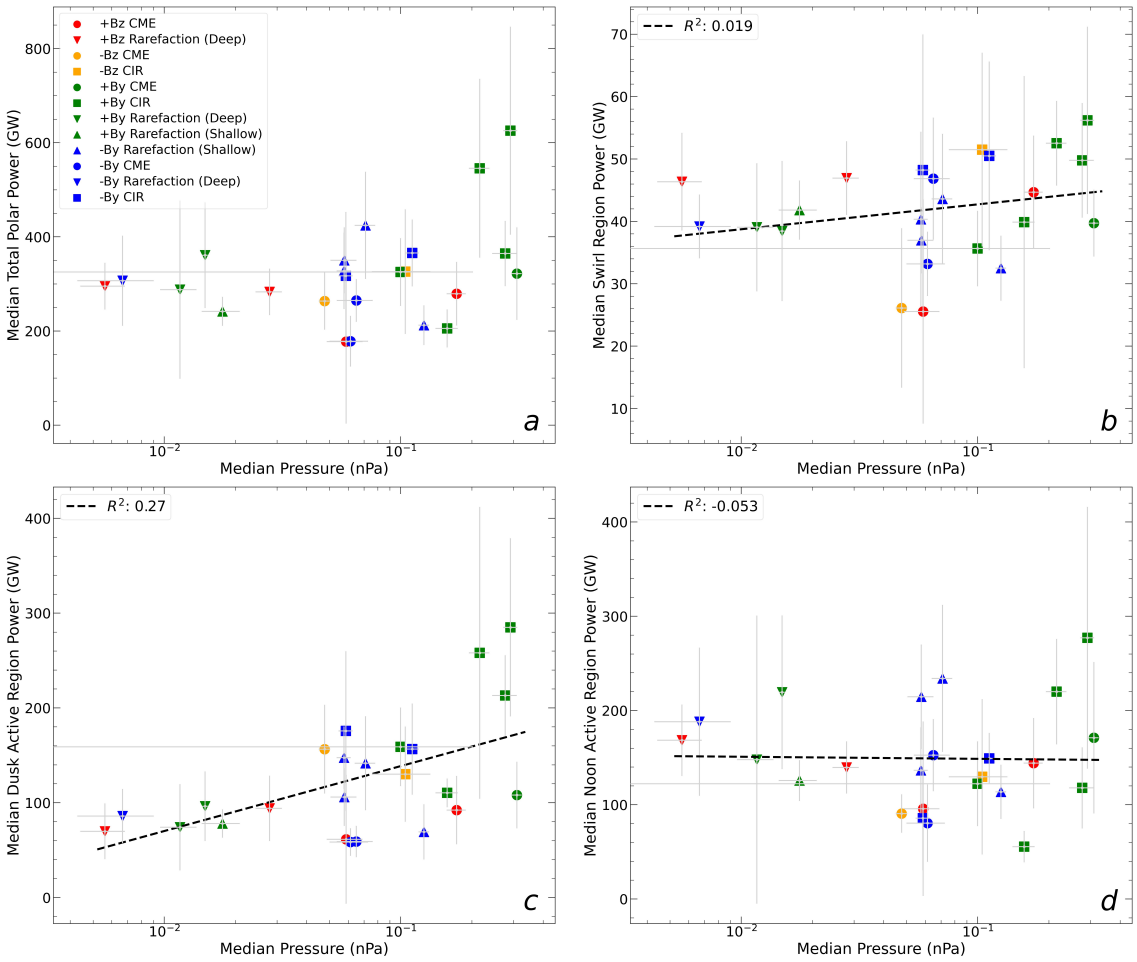

Figure B.3.1: Relationship between median averaged pressure per visit and the median: (a) total polar power, (b) swirl region power, (c) dusk active region power, (d) noon active region power. Pressure is plotted on a log_{10} axis and the relationship is fit by taking a linear fit of $log_{10}(P)$ vs power.

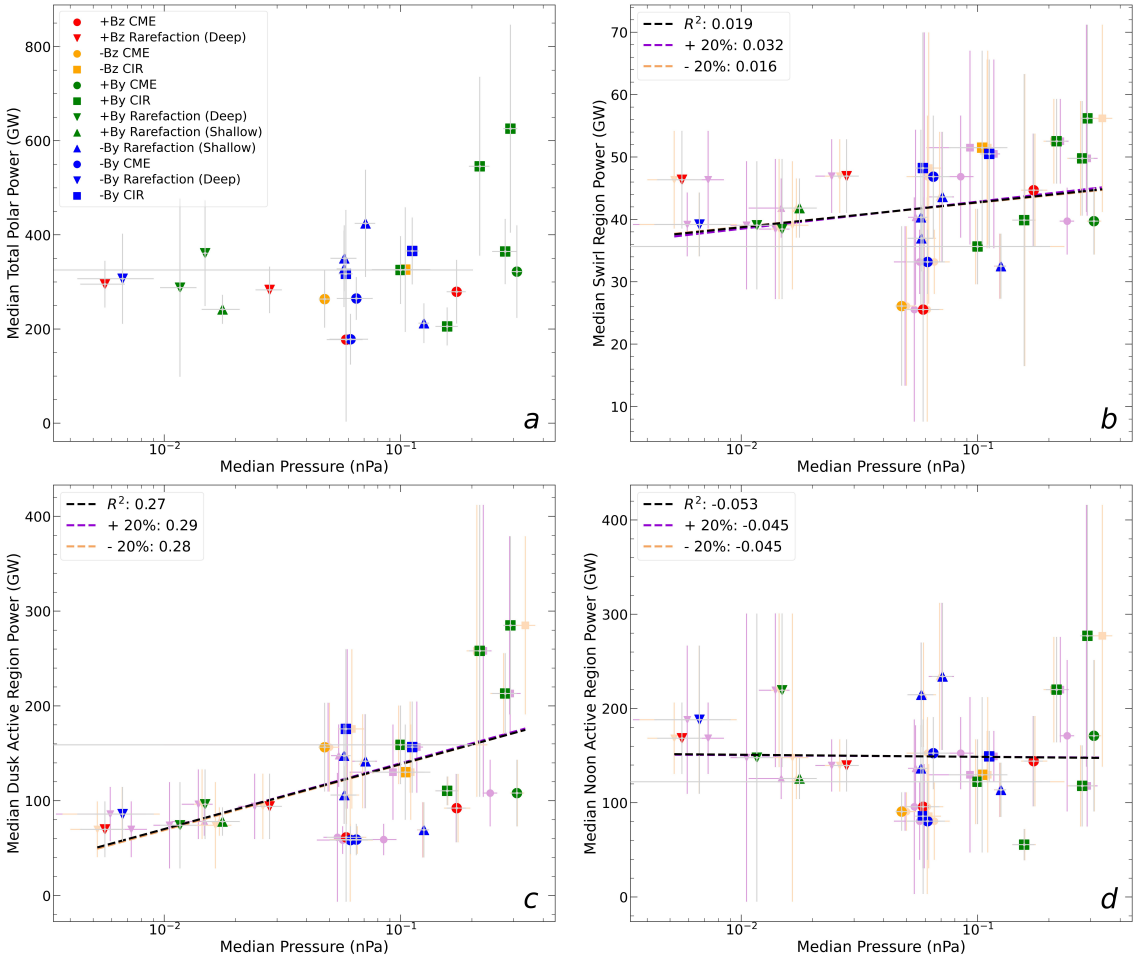

Figure B.3.2: The same as figure B.3.1 but with the addition of a 20% propagation time error applied to the solar wind travel time from Juno to Jupiter's magnetosphere.

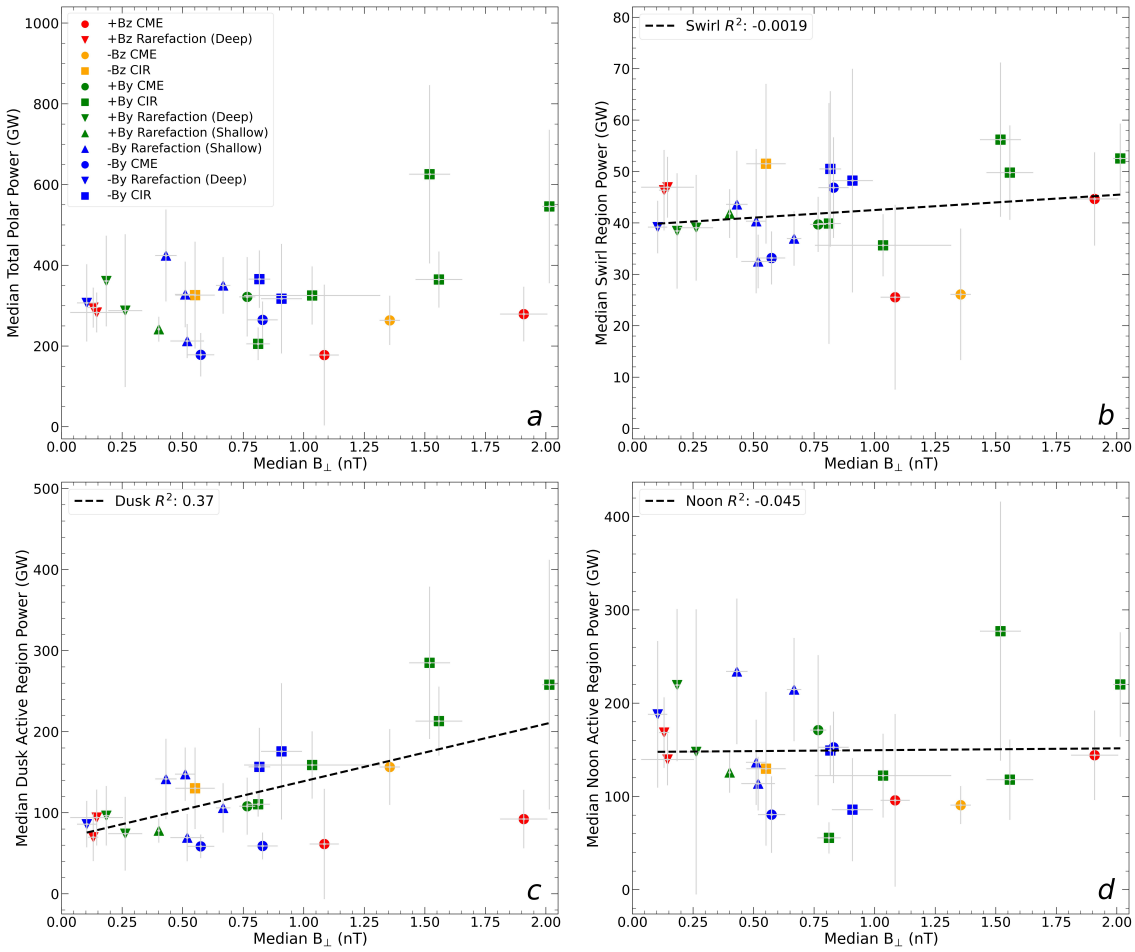

Figure B.3.3: Relationship between median averaged perpendicular magnetic field strength per visit and the median: (b) swirl region power, (c) dusk active region power, (d) noon active region power. Pressure is plotted on a log_{10} axis and the relationship is fit by taking a linear fit of $log_{10}(pressure)$ vs power.

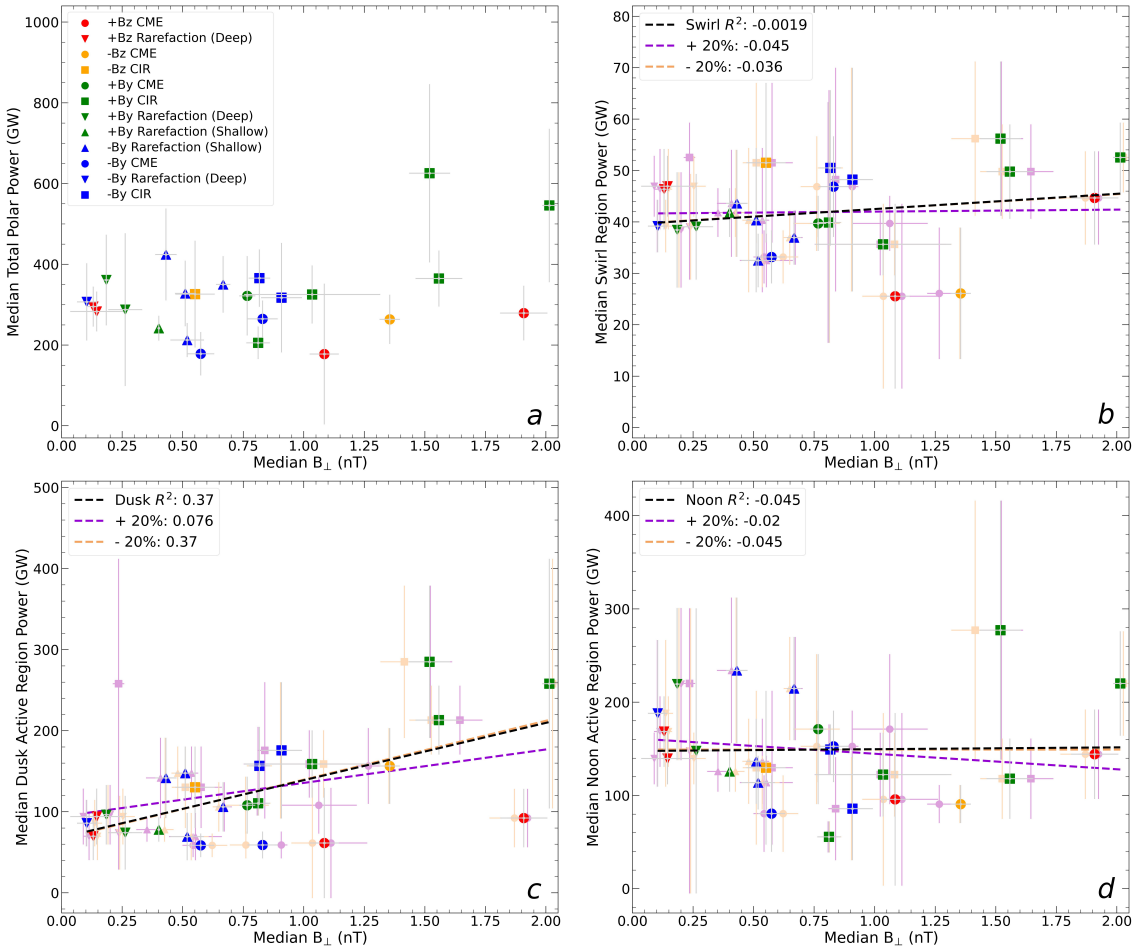

Figure B.3.4: The same as figure B.3.3 but with the addition of a 20% propagation time error applied to the solar wind travel time from Juno to Jupiter's magnetosphere.

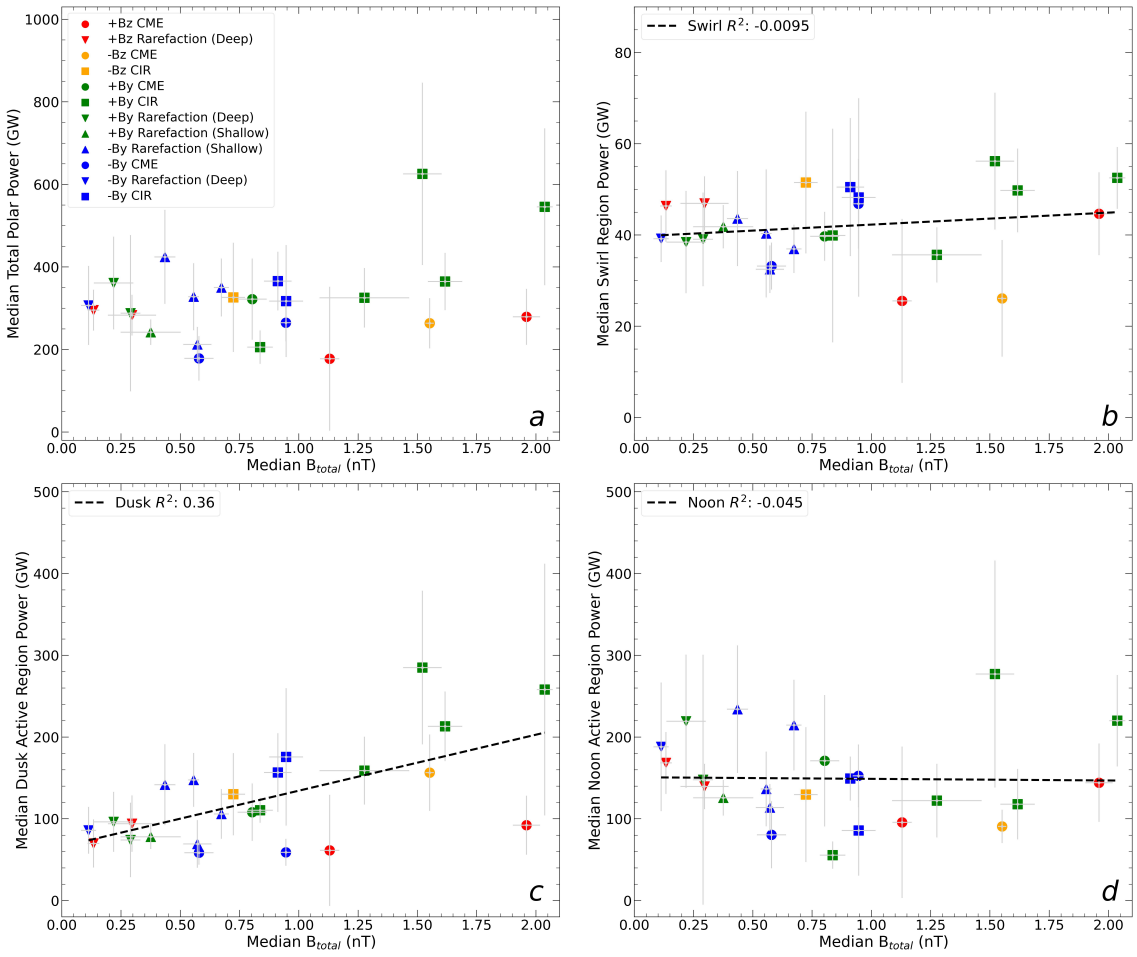

Figure B.3.5: Relationship between median averaged total magnetic field magnitude of the solar wind per visit and the median: (a) total polar power, (b) swirl region power, (c) dusk active region power, (d) noon active region power. The relationship is plotted as a linear line of best fit.

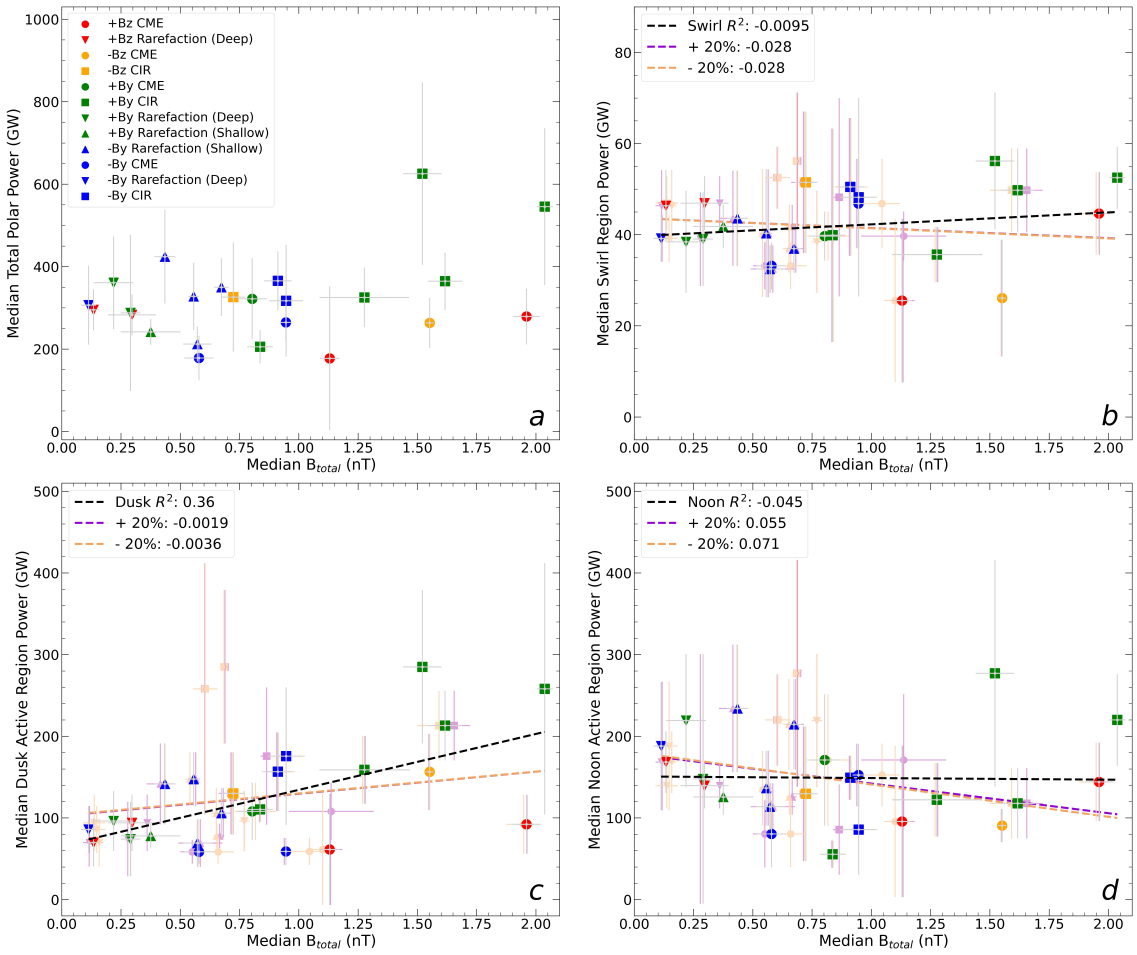

Figure B.3.6: The same as figure B.3.5 but with the addition of a ±20% propagation time error applied to the solar wind travel time from Juno to Jupiter's magnetosphere

B.4 Reconnection Voltages and Powers

B.4.1 Low-Latitude Reconnection Voltage

Calculating the low-latitude reconnection voltage using the solar wind variables at the time of the HST visits yields no relationship with the polar auroral regions. Figure B.4.1 shows the results for each region and B.4.2 includes the 20% shorter and longer solar wind propagation time results as a measure of uncertainty in the travel time calculation.

B.4.2 High-Latitude Reconnection Voltage

Much like the low-latitude reconnection voltage, neither high-latitude voltage shows a significant correlation with the auroral region power. The full results are shown in figures B.4.3 and 5.3 for a $-y$ orientated magnetospheric field line and figures B.4.5 and B.4.6 for a $+y$ orientated magnetospheric field line; the first figure of each pair shows the results for each polar region, whilst the second figure of each also includes the 20% shorter and longer travel times as a measure of uncertainty.

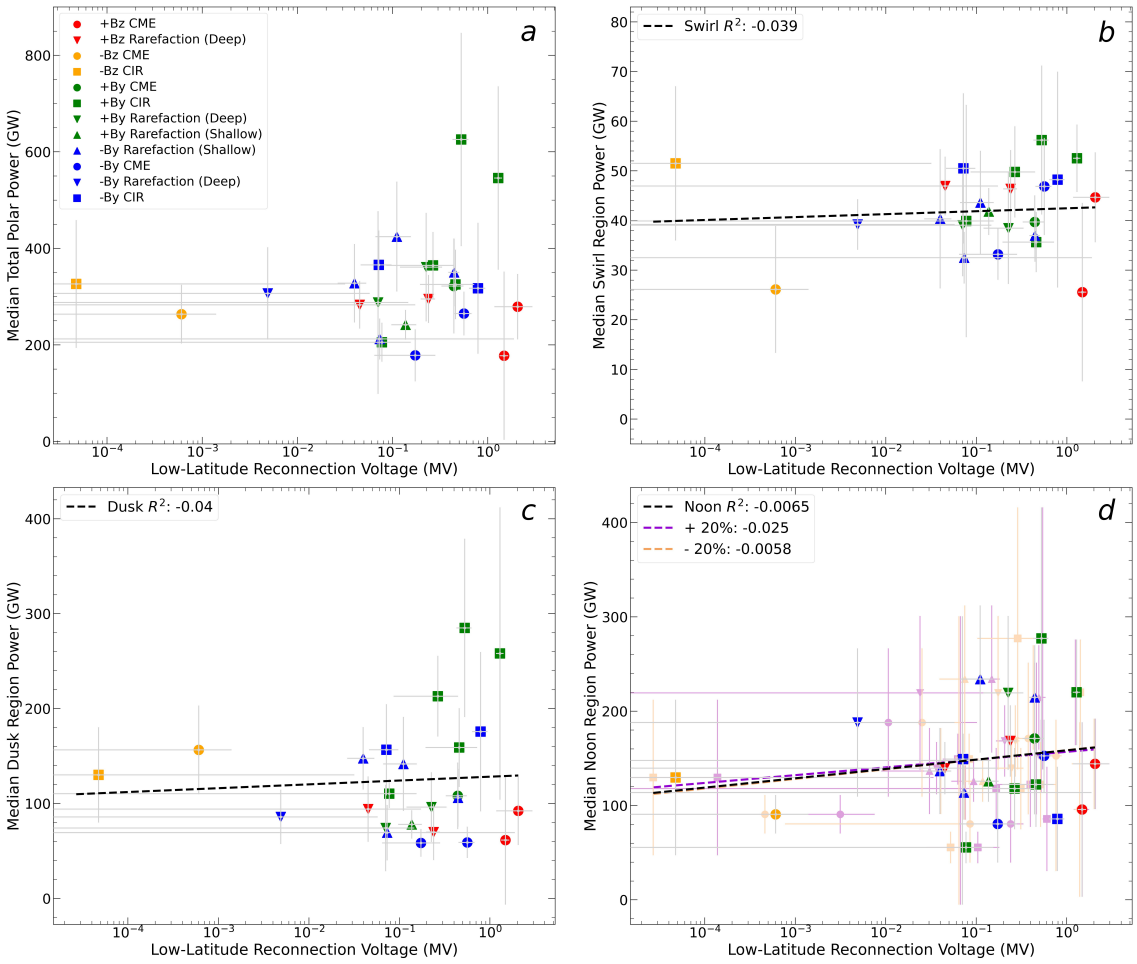

Figure B.4.1: The relationship between low-latitude reconnection voltage per visit, calculated from measured solar wind parameters using equation 5.2, and the median: (a) total polar power, (b) swirl region power, (c) dusk active region power and (d) noon active region power. The reconnection voltage is plotted on a log_{10} axis and the relationship is fit by taking a linear fit of $log_{10}(\phi_{LL})$ vs power.

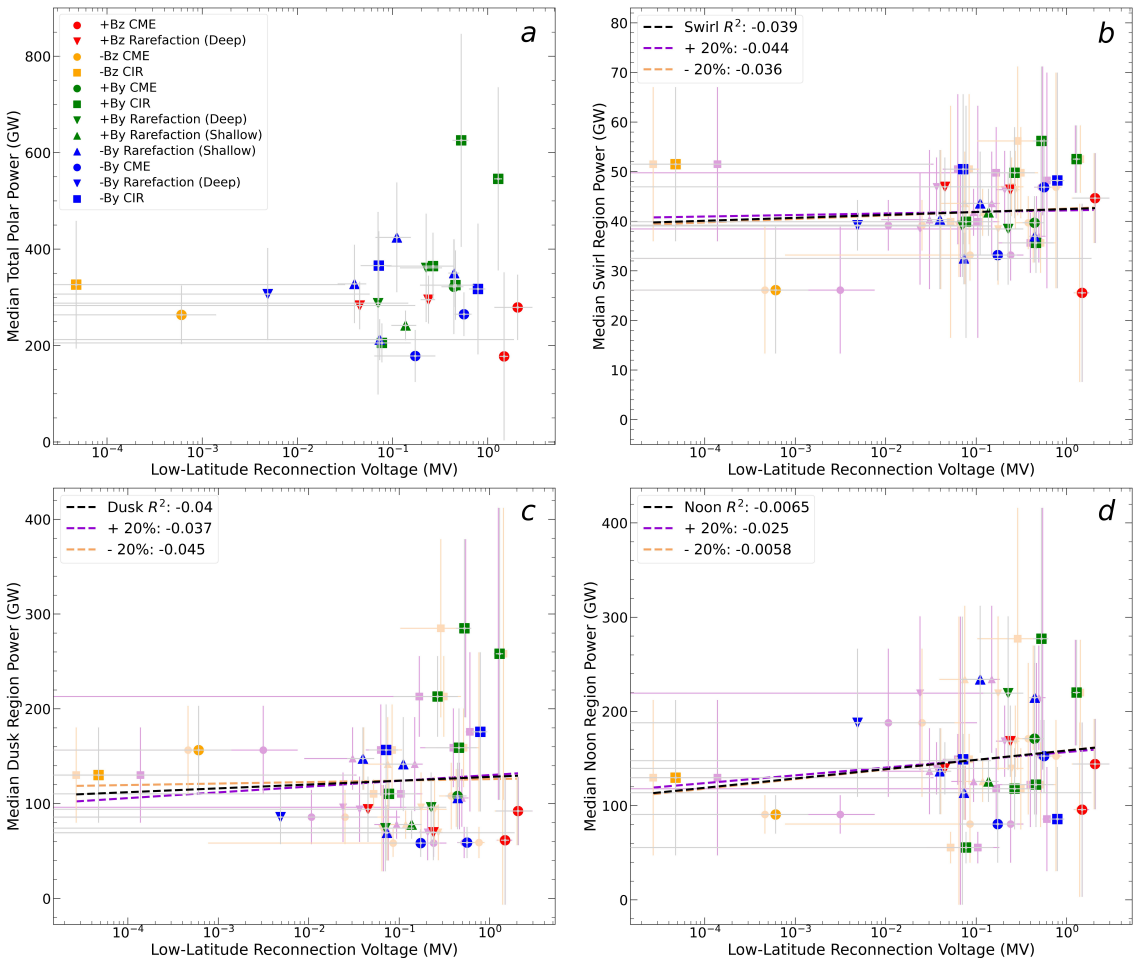

Figure B.4.2: The same as B.4.1 but with the addition of a 20% propagation time error applied to the solar wind travel time from Juno to Jupiter's magnetosphere.

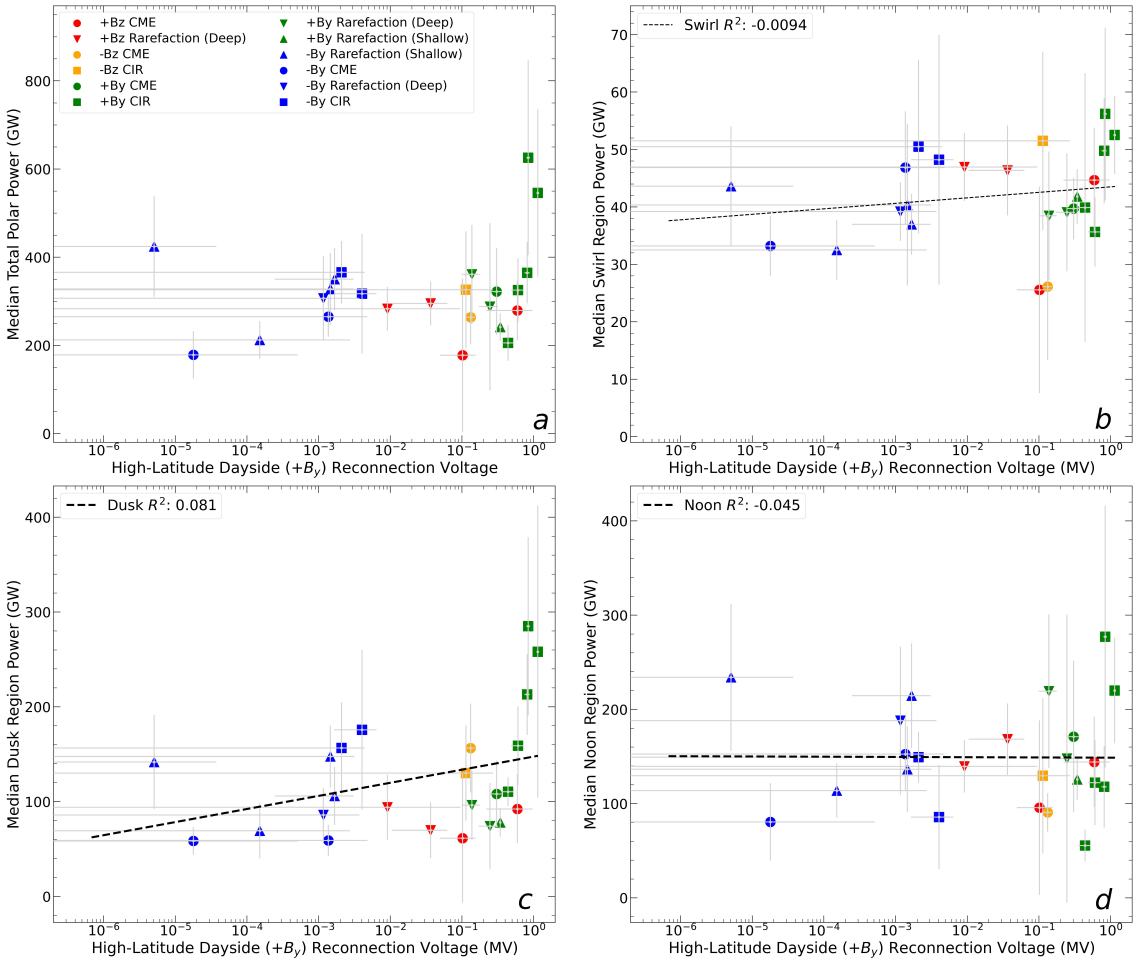

Figure B.4.3: The relationship between high-latitude reconnection voltage per visit, calculated under conditions where reconnection with $+B_y$ orientated field is favoured using equation 5.3 , and the median: (a) total polar power, (b) swirl region power, (c) dusk active region power and (d) noon active region power. The reconnection voltage is plotted on a log_{10} axis and the relationship is fit by taking a linear fit of $log_{10}(\phi_{HL,-y})$ vs power.

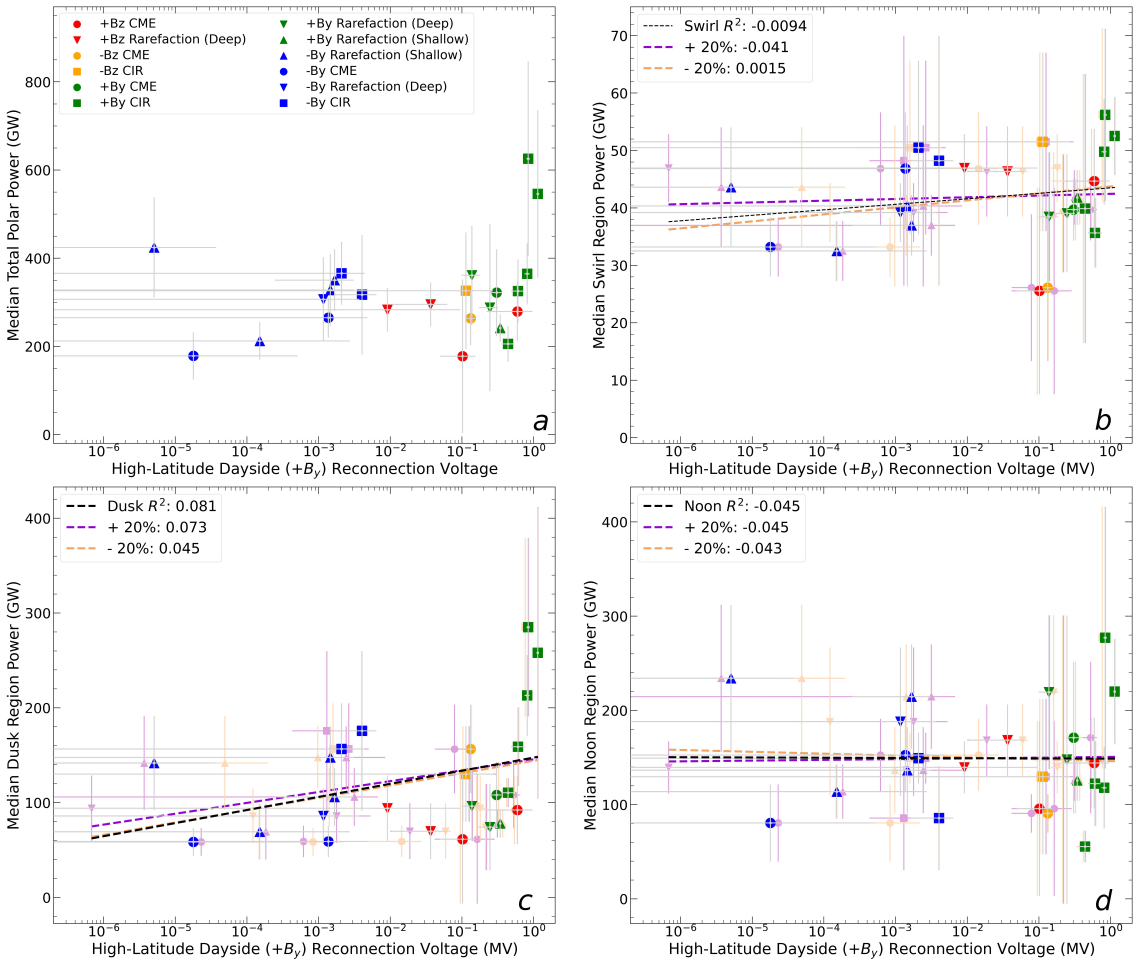

Figure B.4.4: The same as B.4.3 but with the addition of a 20% propagation time error applied to the solar wind travel time from Juno to Jupiter's magnetosphere.

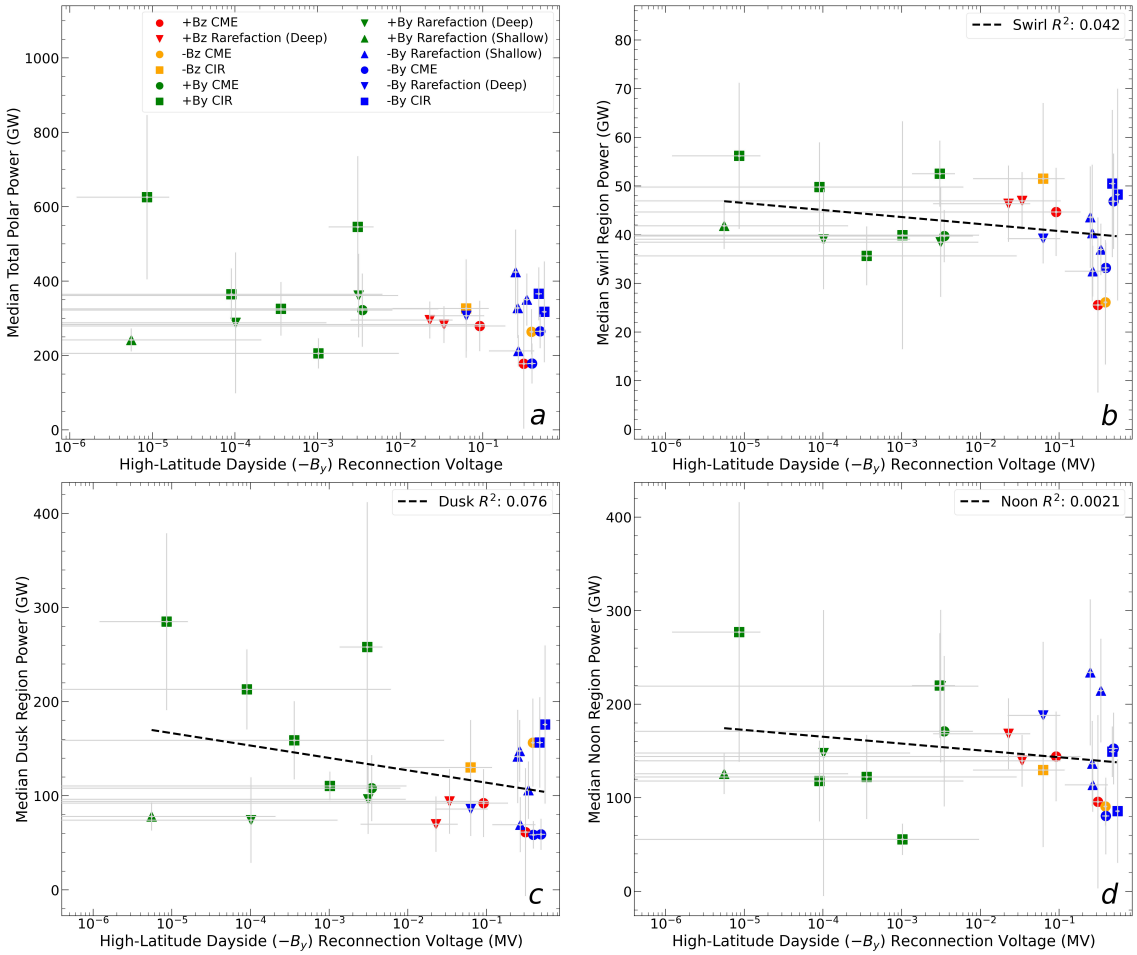

Figure B.4.5: The relationship between high-latitude reconnection voltage per visit, calculated under conditions where reconnection with $-B_y$ orientated field is favoured using equation 5.4 , and the median: (a) total polar power, (b) swirl region power, (c) dusk active region power and (d) noon active region power. The reconnection voltage is plotted on a log_{10} axis and the relationship is fit by taking a linear fit of $log_{10}(\phi_{HL,+y})$ vs power.

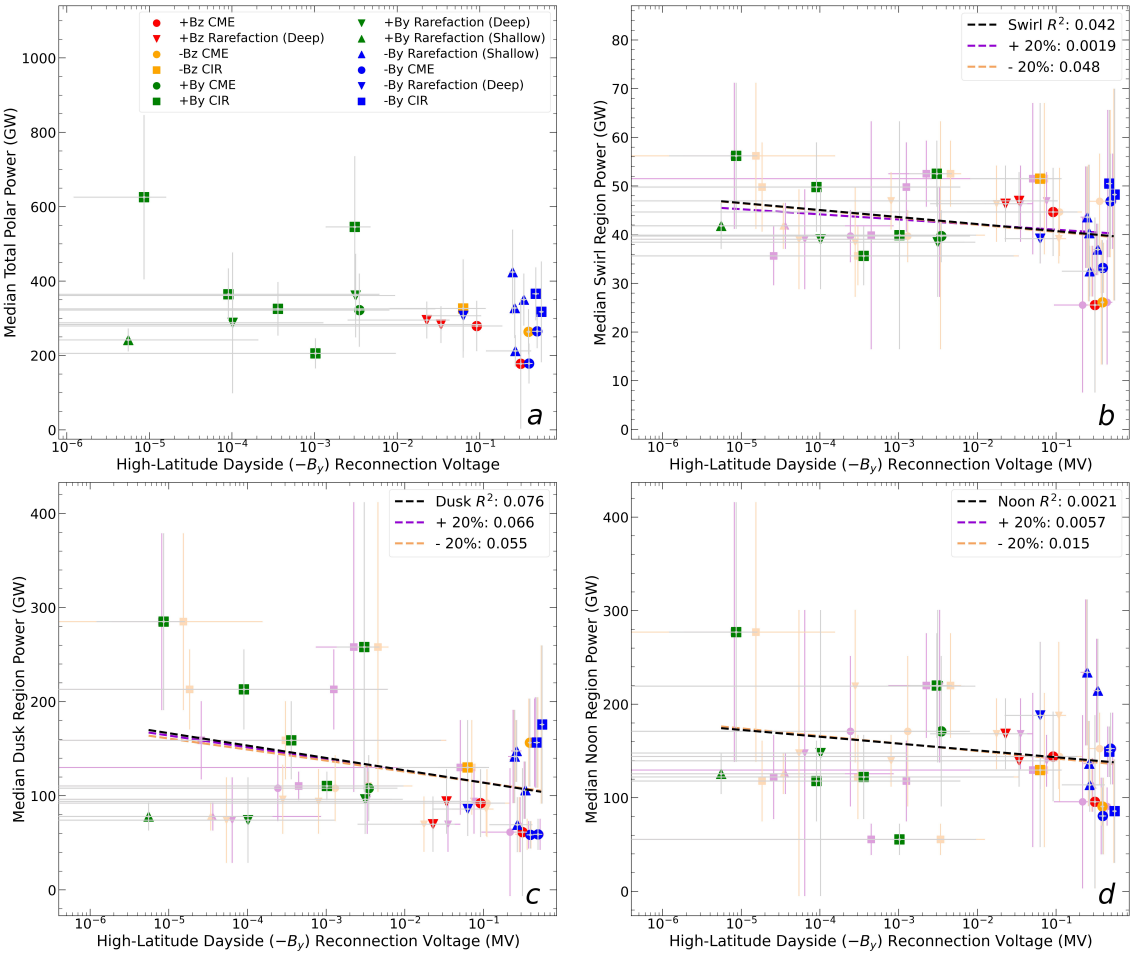

Figure B.4.6: The same as B.4.5 but with the addition of a 20% propagation time error applied to the solar wind travel time from Juno to Jupiter's magnetosphere.

B.4.3 Kelvin-Helmholtz Power

The development of Kelvin-Helmholtz vortices on the dawnside of Jupiter's outer magnetosphere show a positive correlation with the auroral power in the dusk active region, but not for the swirl or noon active regions - and no correlation is found for the duskside. The full set of figures for the power generated by K-H reconnection are shared here for completeness.

For K-H power as the result of vortices along the dawn flank of the outer magnetosphere, figure B.4.7 shows the relationship between generated power and the auroral power, with B.4.8 also showing the 20% same result with shorter and longer solar wind propagation times between Juno and the ionosphere as a measure of the uncertainty for the solar wind travel time. Figures B.4.9 and B.4.10 show the same results for the development of vortices on the dusk flank of the outer magnetosphere, where the difference between the two flanks is the velocity shear between the solar wind and internal flow speed of Jupiter's magnetosphere.

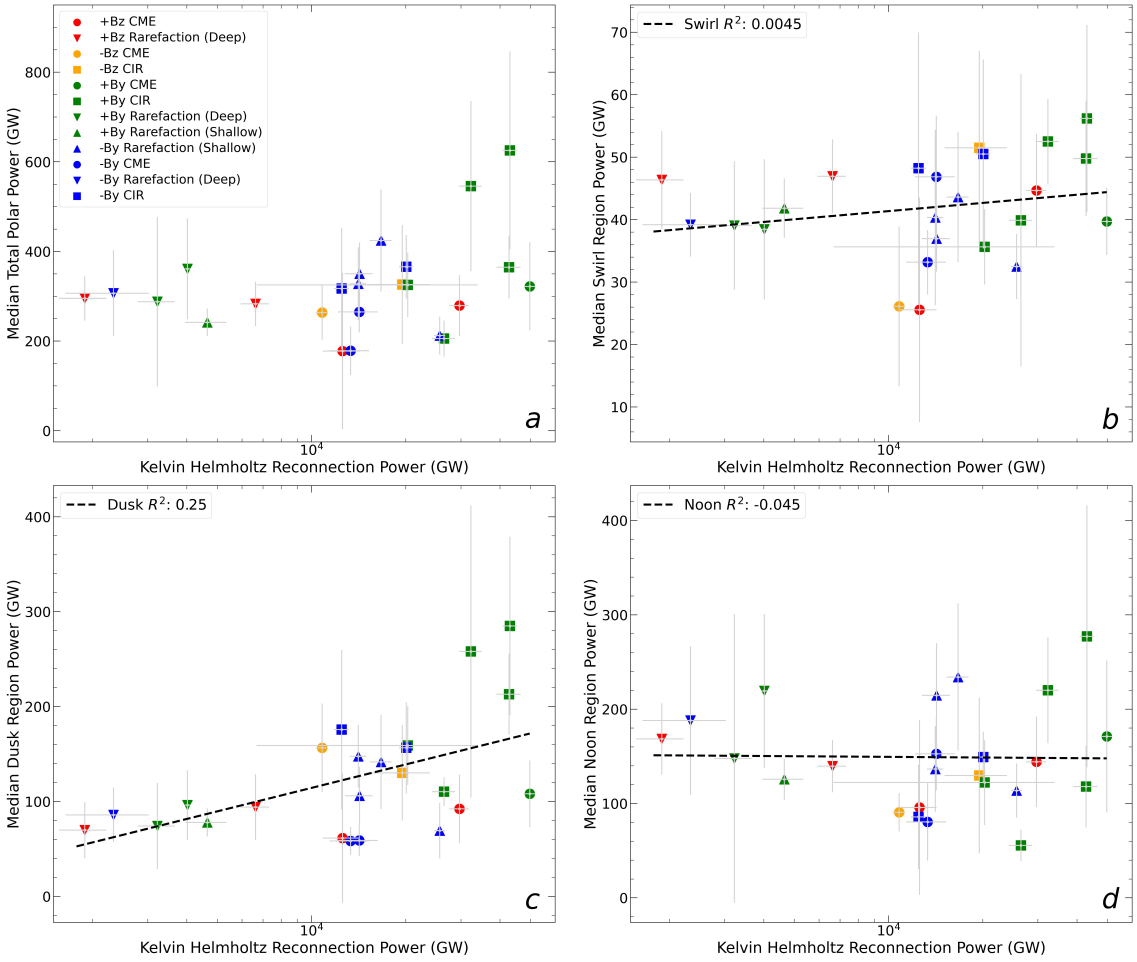

Figure B.4.7: The relationship between Kelvin-Helmholtz generated power, calculated using equation 5.5, for the dawn flank of Jupiter's outer magnetosphere and median: (a) total polar power, (b) swirl region power, (c) dusk active region power and (d) noon active region power. The reconnection power is plotted on a log_{10} axis and the relationship is fit by taking a linear fit of $log_{10}(P_{K-H})$ vs power.

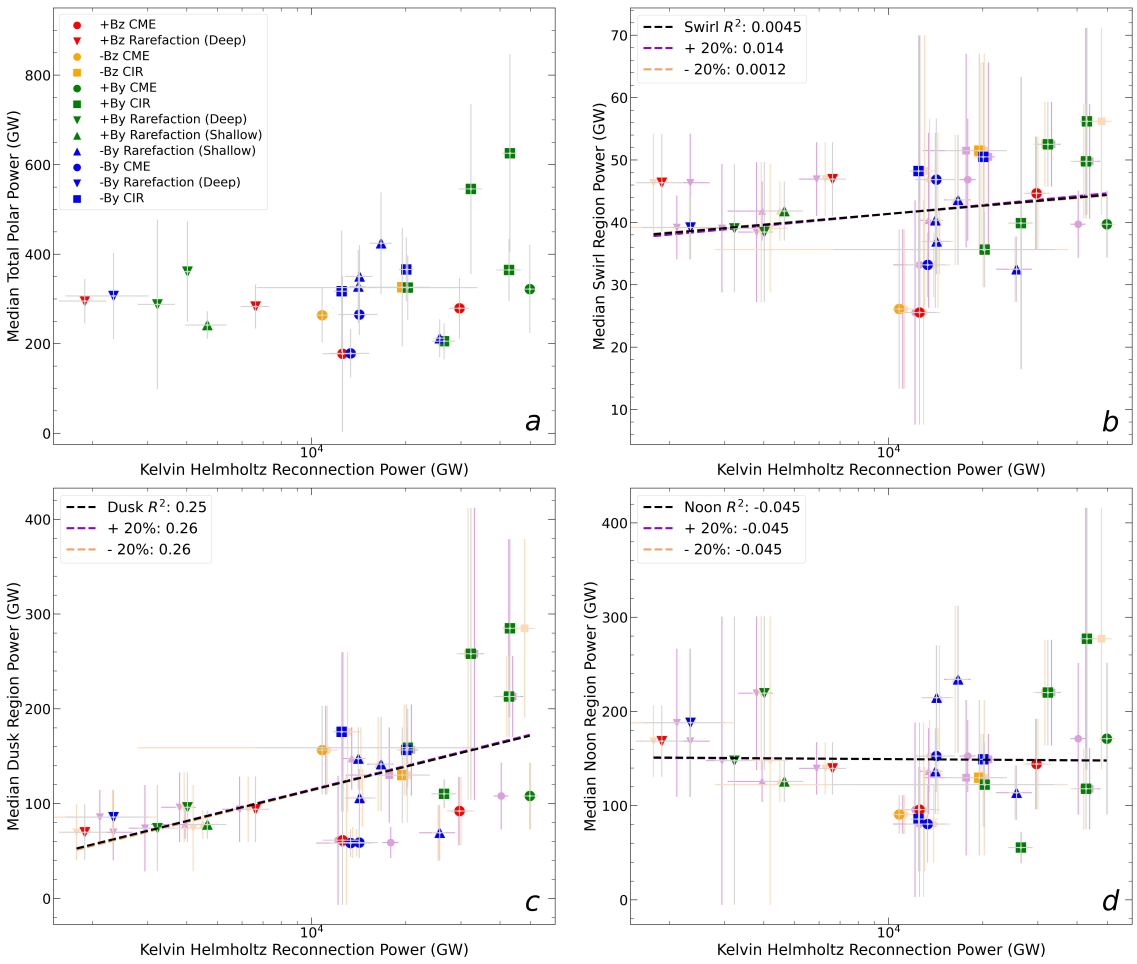

Figure B.4.8: The same as B.4.7 but with the addition of a 20% propagation time error applied to the solar wind travel time from Juno to Jupiter's magnetosphere.

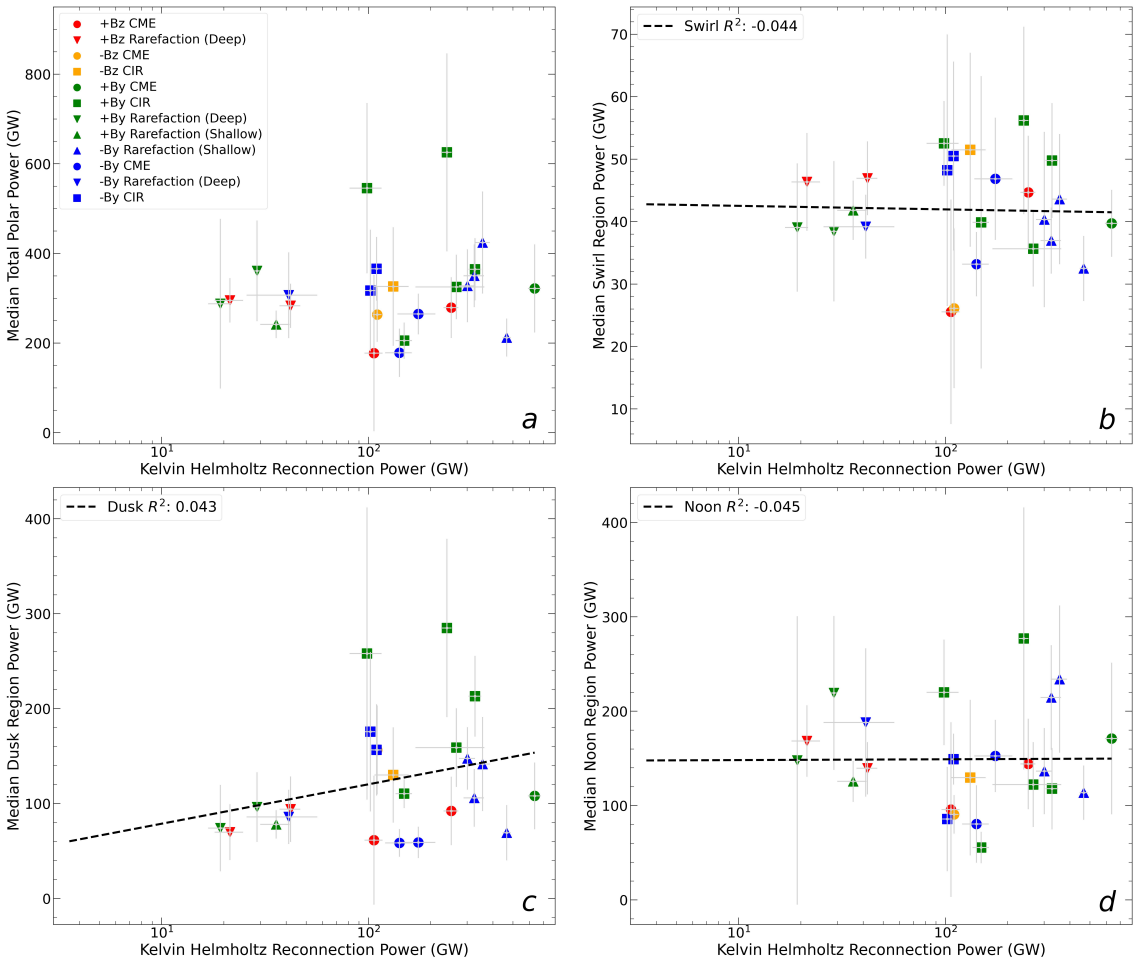

Figure B.4.9: The relationship between Kelvin-Helmholtz generated power, calculated using equation 5.5, for the dusk flank of Jupiter's outer magnetosphere and median: (a) total polar power, (b) swirl region power, (c) dusk active region power and (d) noon active region power. The reconnection power is plotted on a log_{10} axis and the relationship is fit by taking a linear fit of $log_{10}(P_{K-H})$ vs power.

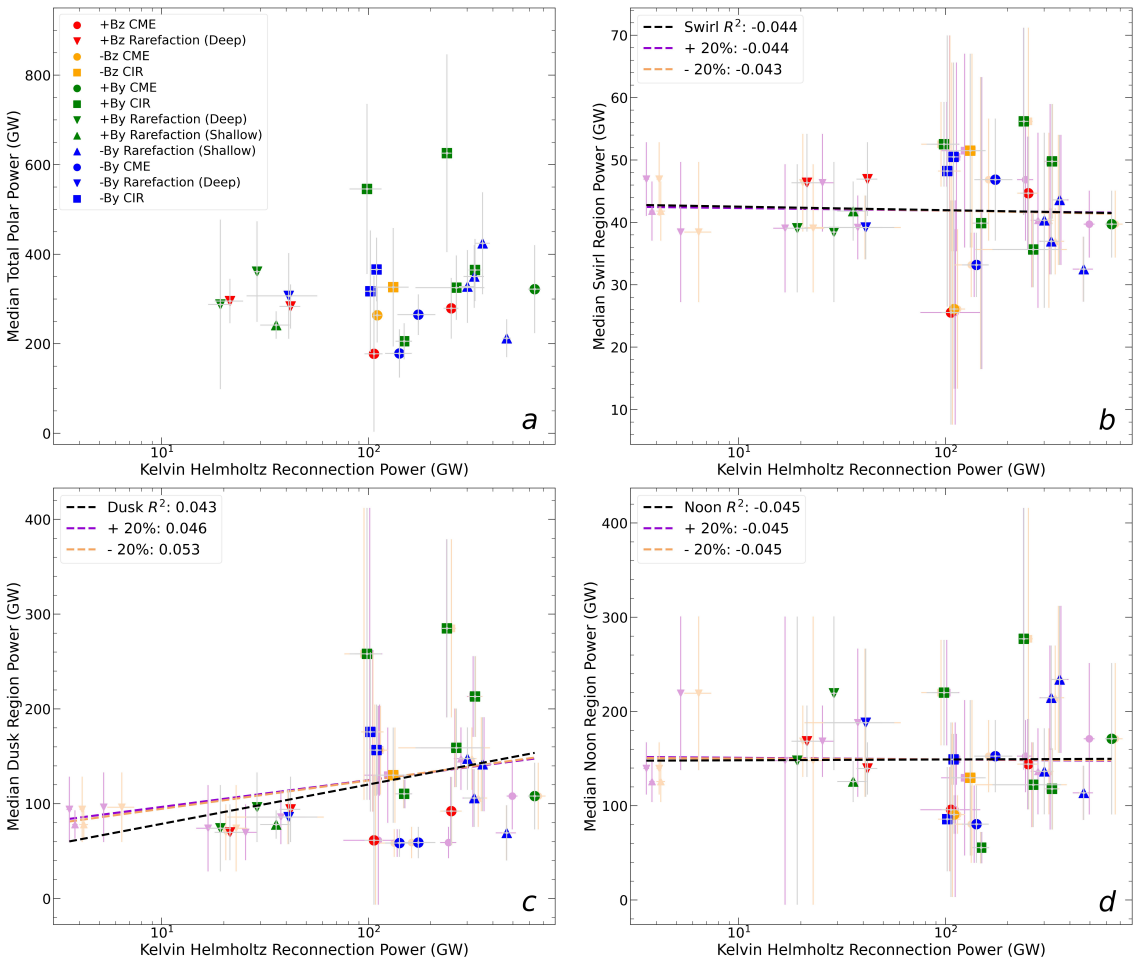

Figure B.4.10: The same as B.4.9 but with the addition of a 20% propagation time error applied to the solar wind travel time from Juno to Jupiter's magnetosphere.

Bibliography

Acton, C. H. (1996). "Ancillary data services of NASA's Navigation and Ancillary Information Facility". In: *Planetary and Space Science* 44.1. Planetary data system, pp. 65–70. ISSN: 0032-0633. DOI: https://doi.org/10.1016/0032-0633(95)00107-7. URL: https://www.sciencedirect.com/science/article/pii/0032063395001077 (cit. on p. 65).

Acton, C. H., N. Bachman, B. Semenov, and E. Wright (2018). "A look towards the future in the handling of space science mission geometry". In: *Planetary and Space Science* 150. Enabling Open and Interoperable Access to Planetary Science and Heliophysics Databases and Tools, pp. 9–12. ISSN: 0032-0633. DOI: https://doi.org/10.1016/j.pss.2017.02.013. URL: https://www.sciencedirect.com/science/article/pii/S0032063316303129 (cit. on p. 65).

Acũna, M. H., K. W. Behannon, and J. E. P Connerney (1983). "Physics of the Jovian Magnetosphere". In: Cambridge University Press. Chap. Jupiter's Magnetic Field and Magnetosphere (cit. on pp. 29, 30, 35).

Allegrini, F., F. Bagenal, S. Bolton, J. Connerney, G. Clark, R. W. Ebert, T. K. Kim, W. S. Kurth, S. Levin, P. Louarn, B. Mauk, D. J. McComas, C. Pollock, D. Ranquist, M. Reno, J. R. Szalay, M. F. Thomsen, P. Valek, S. Weidner, R. J. Wilson, and J. L. Zink (2017). "Electron beams and loss cones in the auroral regions of Jupiter". In: *Geophysical Research Letters* 44.14, pp. 7131–7139. DOI: https://doi.org/10.1002/2017GL073180. eprint: https://agupubs.onlinelibrary.wiley.com/doi/pdf/10.1002/2017GL073180. URL: https:

//agupubs.onlinelibrary.wiley.com/doi/abs/10.1002/2017GL073180 (cit. on p. 52).

Annex, A. M., B. Pearson, B. Seignovert, B. T. Carcich, H. Eichhorn, J. A. Mapel, J. L. Freiherr von Forstner, J. McAuliffe, J. Diaz del Rio, K. L. Berry, K.-M. Aye, M. Stefko, M. de Val-Borro, S. Kulumani, and S. Murakami (2020). "SpiceyPy: a Pythonic Wrapper for the SPICE Toolkit". In: *Journal of Open Source Software* 5.46, p. 2050. DOI: 10.21105/joss.02050. URL: https://doi.org/10.21105/joss.02050%7D (cit. on p. 66).

Bader, A. (2020). "The Dynamics of Saturn's Ultraviolet Aurorae". English. PhD thesis. Lancaster University. DOI: 10.17635/lancaster/thesis/1128 (cit. on p. 78).

Bagenal, F. (2007). "The magnetosphere of Jupiter: Coupling the equator to the poles". In: *Journal of Atmospheric and Solar-Terrestrial Physics* 69.3. Global Aspects of Magnetosphere-Ionosphere Coupling, pp. 387–402. ISSN: 1364-6826. DOI: https://doi.org/10.1016/j.jastp.2006.08.012. URL: https://www.sciencedirect.com/science/article/pii/S1364682606002781 (cit. on pp. 32, 34).

Bagenal, F. and P. A. Delamere (2011). "Flow of mass and energy in the magnetospheres of Jupiter and Saturn". In: *Journal of Geophysical Research: Space Physics* 116.A5. DOI: https://doi.org/10.1029/2010JA016294. eprint: https://agupubs.onlinelibrary.wiley.com/doi/pdf/10.1029/2010JA016294. URL: https://agupubs.onlinelibrary.wiley.com/doi/abs/10.1029/2010JA016294 (cit. on pp. 2, 14, 32–34, 143, 149).

Bagenal, F. and V. Dols (2020). "The Space Environment of Io and Europa". In: *Journal of Geophysical Research: Space Physics* 125.5. e2019JA027485 2019JA027485, e2019JA027485. DOI: https://doi.org/10.1029/2019JA027485. eprint: https://agupubs.onlinelibrary.wiley.com/doi/pdf/10.1029/2019JA027485. URL: https://agupubs.onlinelibrary.wiley.com/doi/abs/10.1029/2019JA027485 (cit. on p. 32).

Bagenel, F. and R.J. Wilson (2016). *Jupiter Coordinate Systems*. LASP, University of Colorado (cit. on p. 60).

Barbosa, D. D., D. A. Gurnett, W. S. Kurth, and F. L. Scarf (1979). "Structure and properties of Jupiter's magnetoplasmadisc". In: *Geophysical Research Letters* 6.10, pp. 785–788. DOI: https://doi.org/10.1029/GL006i010p00785. eprint: https://agupubs.onlinelibrary.wiley.com/doi/pdf/10.1029/GL006i010p00785. URL: https://agupubs.onlinelibrary.wiley.com/doi/abs/10.1029/GL006i010p00785 (cit. on p. 93).

Baumjohann, W. and R. A Treumann (1996). *Basic Space Plasma Physics*. Imperial College Press. DOI: 10.1142/p015. eprint: https://www.worldscientific.com/doi/pdf/10.1142/p015. URL: https://www.worldscientific.com/doi/abs/10.1142/p015 (cit. on pp. xi, 1, 5, 6, 8–10, 22).

Benmahi, B., B. Bonfond, B. Benne, D. Grodent, V. Hue, G. R. Gladstone, G. Gronoff, J. Lilensten, G. Sicorello, L. A. Head, M. Barthélemy, C. Simon Wedlund, R. S. Giles, and T. K. Greathouse (2024). "Energy mapping of Jupiter's auroral electrons from Juno/UVS data using a new H2 UV emission model". In: *Astronomy and Astrophysics* 685, A26. DOI: 10.1051/0004-6361/202348634. URL: https://doi.org/10.1051/0004-6361/202348634 (cit. on p. 43).

Bhattacharyya, D., J. T. Clarke, J. Montgomery, B. Bonfond, J.-C. Gérard, and D. Grodent (2018). "Evidence for Auroral Emissions From Callisto's Footprint in HST UV Images". In: *Journal of Geophysical Research: Space Physics* 123.1, pp. 364–373. DOI: https://doi.org/10.1002/2017JA024791. eprint: https://agupubs.onlinelibrary.wiley.com/doi/pdf/10.1002/2017JA024791. URL: https://agupubs.onlinelibrary.wiley.com/doi/abs/10.1002/2017JA024791 (cit. on p. 46).

Bonfond, B. (2010). "The 3-D extent of the Io UV footprint on Jupiter". In: *Journal of Geophysical Research: Space Physics* 115.A9. DOI: https://doi.org/10.1029/2010JA015475. eprint: https://agupubs.onlinelibrary.wiley.com/

doi/pdf/10.1029/2010JA015475. URL: https://agupubs.onlinelibrary.wiley.com/doi/abs/10.1029/2010JA015475 (cit. on p. 43).

Bonfond, B., J. Gustin, J.-C. Gérard, D. Grodent, A. Radioti, B. Palmaerts, S. V. Badman, K. K. Khurana, and C. Tao (2015). "The far-ultraviolet main auroral emission at Jupiter; Part 1: Dawn–dusk brightness asymmetries". In: *Annales Geophysicae* 33.10, pp. 1203–1209. DOI: 10.5194/angeo-33-1203-2015. URL: https://angeo.copernicus.org/articles/33/1203/2015/ (cit. on pp. 37, 44, 45).

Bonfond, B., J. Saur, D. Grodent, S. V. Badman, D. Bisikalo, V. Shematovich, J.-C. Gérard, and A. Radioti (2017). "The tails of the satellite auroral footprints at Jupiter". In: *Journal of Geophysical Research: Space Physics* 122.8, pp. 7985–7996. DOI: https://doi.org/10.1002/2017JA024370. eprint: https://agupubs.onlinelibrary.wiley.com/doi/pdf/10.1002/2017JA024370. URL: https://agupubs.onlinelibrary.wiley.com/doi/abs/10.1002/2017JA024370 (cit. on p. 46).

Bonfond, B., Z. Yao, and D. Grodent (2020). "Six Pieces of Evidence Against the Corotation Enforcement Theory to Explain the Main Aurora at Jupiter". In: *Journal of Geophysical Research: Space Physics* 125.11. e2020JA028152 10.1029/2020JA028152, e2020JA028152. DOI: https://doi.org/10.1029/2020JA028152. eprint: https://agupubs.onlinelibrary.wiley.com/doi/pdf/10.1029/2020JA028152. URL: https://agupubs.onlinelibrary.wiley.com/doi/abs/10.1029/2020JA028152 (cit. on pp. xii, 36, 37).

Bunce, E. J., S. W. H. Cowley, and S. E. Milan (2005). "Interplanetary magnetic field control of Saturn's polar cusp aurora". In: *Annales Geophysicae* 23.4, pp. 1405–1431. DOI: 10.5194/angeo-23-1405-2005. URL: https://angeo.copernicus.org/articles/23/1405/2005/ (cit. on p. 135).

Bunce, E. J., S. W. H. Cowley, and T. K. Yeoman (2004). "Jovian cusp processes: Implications for the polar aurora". In: *Journal of Geophysical Research: Space Physics* 109.A9. DOI: https://doi.org/10.1029/2003JA010280. eprint:

https://agupubs.onlinelibrary.wiley.com/doi/pdf/10.1029/2003JA010280. URL: https://agupubs.onlinelibrary.wiley.com/doi/abs/10.1029/2003JA010280 (cit. on pp. 43, 55).

Burke, B. F. and K. L. Franklin (1955). "Observations of a variable radio source associated with the planet Jupiter". In: *Journal of Geophysical Research (1896-1977)* 60.2, pp. 213–217. DOI: https://doi.org/10.1029/JZ060i002p00213. eprint: https://agupubs.onlinelibrary.wiley.com/doi/pdf/10.1029/JZ060i002p00213. URL: https://agupubs.onlinelibrary.wiley.com/doi/abs/10.1029/JZ060i002p00213 (cit. on p. 40).

Chandrasekhar, S. (1961). *Hydrodynamic and hydromagnetic stability*. Oxford University Press (cit. on p. 18).

Chané, E., J. Saur, and S. Poedts (2013). "Modeling Jupiter's magnetosphere: Influence of the internal sources". In: *Journal of Geophysical Research: Space Physics* 118.5, pp. 2157–2172. DOI: https://doi.org/10.1002/jgra.50258. eprint: https://agupubs.onlinelibrary.wiley.com/doi/pdf/10.1002/jgra.50258. URL: https://agupubs.onlinelibrary.wiley.com/doi/abs/10.1002/jgra.50258 (cit. on p. 35).

Clarke, J. T., D. Grodent, S. W. H. Cowley, E. J. Bunce, P. Zarka, J. E. P. Connerney, and T. Satoh (2004). "Jupiter: The Planet, Satellites and Magnetosphere". In: Cambridge University Press. Chap. 26: Jupiter's Aurora (cit. on pp. 40, 43–45).

Clarke, J. T., J. Nichols, J.-C. Gérard, D. Grodent, K. C. Hansen, W. Kurth, G. R. Gladstone, J. Duval, S. Wannawichian, E. Bunce, S. W. H. Cowley, F. Crary, M. Dougherty, L. Lamy, D. Mitchell, W. Pryor, K. Retherford, T. Stallard, B. Zieger, P. Zarka, and B. Cecconi (2009). "Response of Jupiter's and Saturn's auroral activity to the solar wind". In: *Journal of Geophysical Research: Space Physics* 114.A5. DOI: https://doi.org/10.1029/2008JA013694. eprint: https://agupubs.onlinelibrary.wiley.com/doi/pdf/10.1029/2008JA013694. URL: https://agupubs.onlinelibrary.wiley.com/doi/abs/10.1029/2008JA013694 (cit. on p. 64).

Connerney, J. E. P. (1981). "The magnetic field of Jupiter: A generalized inverse approach". In: *Journal of Geophysical Research: Space Physics* 86.A9, pp. 7679–7693. DOI: https://doi.org/10.1029/JA086iA09p07679. eprint: https://agupubs.onlinelibrary.wiley.com/doi/pdf/10.1029/JA086iA09p07679. URL: https://agupubs.onlinelibrary.wiley.com/doi/abs/10.1029/JA086iA09p07679 (cit. on p. 30).

Connerney, J. E. P., M. H. Acuña, N. F. Ness, and T. Satoh (1998). "New models of Jupiter's magnetic field constrained by the Io flux tube footprint". In: *Journal of Geophysical Research: Space Physics* 103.A6, pp. 11929–11939. DOI: https://doi.org/10.1029/97JA03726. eprint: https://agupubs.onlinelibrary.wiley.com/doi/pdf/10.1029/97JA03726. URL: https://agupubs.onlinelibrary.wiley.com/doi/abs/10.1029/97JA03726 (cit. on p. 73).

Connerney, J. E. P., M. Benn, J. B. Bjarno, T. Denver, J. Espley, J. L. Jorgensen, P. S. Jorgensen, P. Lawton, A. Malinnikova, J. M. Merayo, S. Murphy, J. Odom, R. Oliversen, R. Schnurr, D. Sheppard, and E. J. Smith (Nov. 2017). "The Juno Magnetic Field Investigation". In: *Space Science Reviews* 213.1, pp. 39–138. ISSN: 1572-9672. DOI: 10.1007/s11214-017-0334-z. URL: https://doi.org/10.1007/s11214-017-0334-z (cit. on pp. xv, 59, 60).

Connerney, J. E. P., S. Timmins, R. J. Oliversen, J. R. Espley, J. L. Joergensen, S. Kotsiaros, P. S. Joergensen, J. M. G. Merayo, M. Herceg, J. Bloxham, K. M. Moore, A. Mura, A. Moirano, S. J. Bolton, and S. M. Levin (2022). "A New Model of Jupiter's Magnetic Field at the Completion of Juno's Prime Mission". In: *Journal of Geophysical Research: Planets* 127.2. e2021JE007055 2021JE007055, e2021JE007055. DOI: https://doi.org/10.1029/2021JE007055. eprint: https://agupubs.onlinelibrary.wiley.com/doi/pdf/10.1029/2021JE007055. URL: https://agupubs.onlinelibrary.wiley.com/doi/abs/10.1029/2021JE007055 (cit. on pp. 27, 71–73).

Cowley, S. W. H. and E. J. Bunce (2001). "Origin of the main auroral oval in Jupiter's coupled magnetosphere–ionosphere system". In: *Planetary and Space Science*

49.10. Magnetosphere of the Outer Planets Part II, pp. 1067–1088. ISSN: 0032-0633. DOI: https://doi.org/10.1016/S0032-0633(00)00167-7. URL: https://www.sciencedirect.com/science/article/pii/S0032063300001677 (cit. on pp. 35, 37).

— (2003). "Modulation of Jupiter's main auroral oval emissions by solar wind induced expansions and compressions of the magnetosphere". In: *Planetary and Space Science* 51.1, pp. 57–79. ISSN: 0032-0633. DOI: https://doi.org/10.1016/S0032-0633(02)00118-6%7D. URL: https://www.sciencedirect.com/science/article/pii/S0032063302001186%7D (cit. on p. 67).

Cowley, S. W. H., E. J. Bunce, T. S. Stallard, and S. Miller (2003). "Jupiter's polar ionospheric flows: Theoretical interpretation". In: *Geophysical Research Letters* 30.5. DOI: https://doi.org/10.1029/2002GL016030. eprint: https://agupubs.onlinelibrary.wiley.com/doi/pdf/10.1029/2002GL016030. URL: https://agupubs.onlinelibrary.wiley.com/doi/abs/10.1029/2002GL016030 (cit. on pp. xiv, 47, 50, 52, 114, 165).

Cranmer, S. R., R. Chhiber, C. R. Gilly, I. H. Cairns, R. C. Colaninno, D. J. McComas, N. E. Raouafi, A. V. Usmanov, S. E. Gibson, and C. E. DeForest (Nov. 2023). "The Sun's Alfvén Surface: Recent Insights and Prospects for the Polarimeter to Unify the Corona and Heliosphere (PUNCH)". In: *Solar Physics* 298.11, p. 126. ISSN: 1573-093X. DOI: 10.1007/s11207-023-02218-2. URL: https://doi.org/10.1007/s11207-023-02218-2 (cit. on p. 23).

Daly, A., W. Li, Q. Ma, X.-C. Shen, L. Capannolo, S. Huang, W. S. Kurth, G. B. Hospodarsky, B. H. Mauk, G. Clark, F. Allegrini, and S. J. Bolton (2024). "Statistical Survey of Interchange Events in the Jovian Magnetosphere Using Juno Observations". In: *Geophysical Research Letters* 51.19. e2024GL110300 2024GL110300, e2024GL110300. DOI: https://doi.org/10.1029/2024GL110300. eprint: https://agupubs.onlinelibrary.wiley.com/doi/pdf/10.1029/2024GL110300. URL: https://agupubs.onlinelibrary.wiley.com/doi/abs/10.1029/2024GL110300 (cit. on p. 34).

Delamere, P. A. and F. Bagenal (2003). "Modeling variability of plasma conditions in the Io torus". In: *Journal of Geophysical Research: Space Physics* 108.A7. DOI: https://doi.org/10.1029/2002JA009706. eprint: https://agupubs.onlinelibrary.wiley.com/doi/pdf/10.1029/2002JA009706. URL: https://agupubs.onlinelibrary.wiley.com/doi/abs/10.1029/2002JA009706 (cit. on p. 32).

— (2010). "Solar wind interaction with Jupiter's magnetosphere". In: *Journal of Geophysical Research: Space Physics* 115.A10. DOI: https://doi.org/10.1029/2010JA015347. eprint: https://agupubs.onlinelibrary.wiley.com/doi/pdf/10.1029/2010JA015347. URL: https://agupubs.onlinelibrary.wiley.com/doi/abs/10.1029/2010JA015347 (cit. on pp. xiii, 19, 27, 30, 35, 36, 39, 47, 114, 115, 119, 122, 131, 136, 140, 141, 149, 157, 164).

Delamere, P. A., F. Bagenal, V. Dols, and L. C. Ray (2007). "Saturn's neutral torus versus Jupiter's plasma torus". In: *Geophysical Research Letters* 34.9. DOI: https://doi.org/10.1029/2007GL029437. eprint: https://agupubs.onlinelibrary.wiley.com/doi/pdf/10.1029/2007GL029437. URL: https://agupubs.onlinelibrary.wiley.com/doi/abs/10.1029/2007GL029437 (cit. on p. 32).

Delamere, P. A., R. J. Wilson, S. Wing, A. R. Smith, B. Mino, C. Spitler, P. Damiano, K. Sorathia, A. Sciola, J. Caggiano, J. R. Johnson, X. Ma, F. Bagenal, B. Zhang, F. Allegrini, R. Ebert, G. Clark, and O. Brambles (2024). "Signatures of Open Magnetic Flux in Jupiter's Dawnside Magnetotail". In: *AGU Advances* 5.2. e2023AV001111 2023AV001111, e2023AV001111. DOI: https://doi.org/10.1029/2023AV001111. eprint: https://agupubs.onlinelibrary.wiley.com/doi/pdf/10.1029/2023AV001111. URL: https://agupubs.onlinelibrary.wiley.com/doi/abs/10.1029/2023AV001111 (cit. on pp. 31, 57, 128).

Desroche, M., F. Bagenal, P. A. Delamere, and N. Erkaev (2012). "Conditions at the expanded Jovian magnetopause and implications for the solar wind interaction".

In: *Journal of Geophysical Research: Space Physics* 117.A7. DOI: https://doi.org/10.1029/2012JA017621. eprint: https://agupubs.onlinelibrary.wiley.com/doi/pdf/10.1029/2012JA017621. URL: https://agupubs.onlinelibrary.wiley.com/doi/abs/10.1029/2012JA017621 (cit. on pp. 19, 26, 27, 55, 93, 116, 118, 142, 150).

Dessler, A. J. (1983). "Coordinate systems". In: *Physics of the Jovian Magnetosphere*. Ed. by A. J. Dessler. Cambridge Planetary Science Old. Cambridge University Press, pp. 498–504 (cit. on p. 28).

Dumont, M., D. Grodent, A. Radioti, B. Bonfond, E. Roussos, and C. Paranicas (2018). "Evolution of the Auroral Signatures of Jupiter's Magnetospheric Injections". In: *Journal of Geophysical Research: Space Physics* 123.10, pp. 8489–8501. DOI: https://doi.org/10.1029/2018JA025708. eprint: https://agupubs.onlinelibrary.wiley.com/doi/pdf/10.1029/2018JA025708. URL: https://agupubs.onlinelibrary.wiley.com/doi/abs/10.1029/2018JA025708 (cit. on p. 46).

Dungey, J. W. (1961). "Interplanetary Magnetic Field and the Auroral Zones". In: *Phys. Rev. Lett.* 6 (2), pp. 47–48. DOI: 10.1103/PhysRevLett.6.47. URL: https://link.aps.org/doi/10.1103/PhysRevLett.6.47 (cit. on p. 15).

Dunn, W. R., G. Branduardi-Raymont, L. C. Ray, C. M. Jackman, R. P. Kraft, R. F. Elsner, I. J. Rae, Z. Yao, M. F. Vogt, G. H. Jones, G. R. Gladstone, G. S. Orton, J. A. Sinclair, P. G. Ford, G. A. Graham, R. Caro-Carretero, and A. J. Coates (Nov. 2017). "The independent pulsations of Jupiter's northern and southern X-ray auroras". In: *Nature Astronomy* 1.11, pp. 758–764. ISSN: 2397-3366. DOI: 10.1038/s41550-017-0262-6. URL: https://doi.org/10.1038/s41550-017-0262-6 (cit. on p. 47).

Ebert, R. W., F. Allegrini, F. Bagenal, S. J. Bolton, J. E. P. Connerney, G. Clark, G. R. Gladstone, V. Hue, W. S. Kurth, S. Levin, P. Louarn, B. H. Mauk, D. J. McComas, C. Paranicas, M. Reno, J. Saur, J. R. Szalay, M. F. Thomsen, P. Valek, S. Weidner, and R. J. Wilson (2017). "Spatial Distribution and Properties

of 0.1–100 keV Electrons in Jupiter's Polar Auroral Region". In: *Geophysical Research Letters* 44.18, pp. 9199–9207. DOI: https://doi.org/10.1002/2017GL075106. eprint: https://agupubs.onlinelibrary.wiley.com/doi/pdf/10.1002/2017GL075106. URL: https://agupubs.onlinelibrary.wiley.com/doi/abs/10.1002/2017GL075106 (cit. on p. 52).

Eriksson, S., B. Lavraud, Victoria Wilder, J. E. Stawarz, B. L. Giles, J. L. Burch, W. Baumjohann, R. E. Ergun, P.-A. Lindqvist, W. Magnes, C. J. Pollock, C. T. Russell, Y. Saito, R. J. Strangeway, R. B. Torbert, D. J. Gershman, Yu. V. Khotyaintsev, J. C. Dorelli, S. J. Schwartz, L. Avanov, E. Grimes, Y. Vernisse, A. P. Sturner, T. D. Phan, G. T. Marklund, T. E. Moore, W. R. Paterson, and K. A. Goodrich (2016). "Magnetospheric Multiscale observations of magnetic reconnection associated with Kelvin-Helmholtz waves". In: *Geophysical Research Letters* 43.11, pp. 5606–5615. DOI: https://doi.org/10.1002/2016GL068783. eprint: https://agupubs.onlinelibrary.wiley.com/doi/pdf/10.1002/2016GL068783. URL: https://agupubs.onlinelibrary.wiley.com/doi/abs/10.1002/2016GL068783 (cit. on p. 19).

Frank, L. A., J. D. Craven, D. A. Gurnett, S. D. Shawhan, D. R. Weimer, J. L. Burch, J. D. Winningham, C. R. Chappell, J. H. Waite, R. A. Heelis, N. C. Maynard, M. Sugiura, W. K. Peterson, and E. G. Shelley (1986). "The theta aurora". In: *Journal of Geophysical Research: Space Physics* 91.A3, pp. 3177–3224. DOI: https://doi.org/10.1029/JA091iA03p03177. eprint: https://agupubs.onlinelibrary.wiley.com/doi/pdf/10.1029/JA091iA03p03177. URL: https://agupubs.onlinelibrary.wiley.com/doi/abs/10.1029/JA091iA03p03177 (cit. on p. 117).

Franklin, K.-L. and B.-F. Burke (May 1956). "Radio observations of Jupiter." In: *The Astronomical Journal* 61, p. 177. DOI: 10.1086/107310 (cit. on p. 40).

Gérard, J.-C., D. Grodent, A. Radioti, B. Bonfond, and J.T. Clarke (2013). "Hubble observations of Jupiter's north–south conjugate ultraviolet aurora". In: *Icarus* 226.2, pp. 1559–1567. ISSN: 0019-1035. DOI: https://doi.org/10.1016/j.

icarus.2013.08.017. URL: https://www.sciencedirect.com/science/article/pii/S0019103513003552 (cit. on p. 63).

Gershman, D. J., J. E. P. Connerney, S. Kotsiaros, G. A. DiBraccio, Y. M. Martos, A. F. Viñas, V. Hue, G. Clark, F. Bagenal, S. Levin, and S. J. Bolton (2019). "Alfvénic Fluctuations Associated With Jupiter's Auroral Emissions". In: *Geophysical Research Letters* 46.13, pp. 7157–7165. DOI: https://doi.org/10.1029/2019GL082951. eprint: https://agupubs.onlinelibrary.wiley.com/doi/pdf/10.1029/2019GL082951. URL: https://agupubs.onlinelibrary.wiley.com/doi/abs/10.1029/2019GL082951 (cit. on p. 46).

Gershman, D. J. and G. A. DiBraccio (2024). "Quantifying External Energy Inputs for Giant Planet Magnetospheres". In: *Geophysical Research Letters* 51.15. e2024GL109660 2024GL109660, e2024GL109660. DOI: https://doi.org/10.1029/2024GL109660. eprint: https://agupubs.onlinelibrary.wiley.com/doi/pdf/10.1029/2024GL109660. URL: https://agupubs.onlinelibrary.wiley.com/doi/abs/10.1029/2024GL109660 (cit. on pp. 131, 142, 143).

Gershman, D. J., G. A. DiBraccio, J. E. P. Connerney, G. Hospodarsky, W. S. Kurth, R. W. Ebert, J. R. Szalay, R. J. Wilson, F. Allegrini, P. Valek, D. J. McComas, F. Bagenal, S. Levin, and S. J. Bolton (2017). "Juno observations of large-scale compressions of Jupiter's dawnside magnetopause". In: *Geophysical Research Letters* 44.15, pp. 7559–7568. DOI: https://doi.org/10.1002/2017GL073132. eprint: https://agupubs.onlinelibrary.wiley.com/doi/pdf/10.1002/2017GL073132. URL: https://agupubs.onlinelibrary.wiley.com/doi/abs/10.1002/2017GL073132 (cit. on p. 14).

Gershman, D. J., S. A. Fuselier, I. J. Cohen, D. L. Turner, Y.-H. Liu, L.-J. Chen, T. D. Phan, J. E. Stawarz, G. A. DiBraccio, A. Masters, R. W. Ebert, W. Sun, Y. Harada, and M. Swisdak (2024). "Magnetic Reconnection at Planetary Bodies and Astrospheres". In: *Space Science Reviews* 220.1, p. 7. ISSN: 1572-9672. DOI: 10.1007/s11214-023-01017-2. URL: https://doi.org/10.1007/s11214-023-01017-2 (cit. on pp. 131, 141, 167).

Giles, R. S., T. K. Greathouse, R. W. Ebert, W. S. Kurth, C. K. Louis, M. F. Vogt, B. Bonfond, D. Grodent, J.-C. Gérard, G. R. Gladstone, J. A. Kammer, V. Hue, R. J. Wilson, S. J. Bolton, and J. E. P. Connerney (2025). "Jupiter's UV Auroral Response to a Magnetospheric Compression Event". In: *Journal of Geophysical Research: Planets* 130.6. e2025JE009012 2025JE009012, e2025JE009012. DOI: https://doi.org/10.1029/2025JE009012. eprint: https://agupubs.onlinelibrary.wiley.com/doi/pdf/10.1029/2025JE009012. URL: https://agupubs.onlinelibrary.wiley.com/doi/abs/10.1029/2025JE009012 (cit. on pp. 26, 38, 41, 45, 117, 120, 127, 151).

Gladstone, G. R., J. H. Waite, D. Grodent, W. S. Lewis, F. J. Crary, R. F. Elsner, M. C. Weisskopf, T. Majeed, J.-M. Jahn, A. Bhardwaj, J. T. Clarke, D. T. Young, M. K. Dougherty, S. A. Espinosa, and T. E. Cravens (2002). "A pulsating auroral X-ray hot spot on Jupiter". In: *Nature* 415.6875, pp. 1000–1003. DOI: 10.1038/4151000a. URL: https://doi.org/10.1038/4151000a (cit. on pp. 43, 55).

Gonzalez, W. D. and B. T. Tsurutani (1987). "Criteria of interplanetary parameters causing intense magnetic storms (Dst ← 100 nT)". In: *Planetary and Space Science* 35.9, pp. 1101–1109. ISSN: 0032-0633. DOI: https://doi.org/10.1016/0032-0633(87)90015-8. URL: https://www.sciencedirect.com/science/article/pii/0032063387900158 (cit. on p. 123).

Gray, R. L., S. V. Badman, E. E. Woodfield, and C. Tao (2017). "Characterization of Jupiter's secondary auroral oval and its response to hot plasma injections". In: *Journal of Geophysical Research: Space Physics* 122.6, pp. 6415–6429. DOI: https://doi.org/10.1002/2017JA024214. eprint: https://agupubs.onlinelibrary.wiley.com/doi/pdf/10.1002/2017JA024214. URL: https://agupubs.onlinelibrary.wiley.com/doi/abs/10.1002/2017JA024214 (cit. on p. 46).

Greathouse, T., R. Gladstone, M. Versteeg, V. Hue, J. Kammer, R. Giles, M. Davis, S. Bolton, S. Levin, J.E.P. Connerney, J.C. Gérard, D. Grodent, B. Bonfond, E. Bunce, and M. F. Vogt (2021). "Local Time Dependence of Jupiter's Polar

Auroral Emissions Observed by Juno UVS". In: *Journal of Geophysical Research: Planets* 126.12. e2021JE006954 2021JE006954, e2021JE006954. DOI: https://doi.org/10.1029/2021JE006954. eprint: https://agupubs.onlinelibrary.wiley.com/doi/pdf/10.1029/2021JE006954. URL: https://agupubs.onlinelibrary.wiley.com/doi/abs/10.1029/2021JE006954 (cit. on pp. xiii, xv, 47–50, 54–56, 74, 79, 83, 113, 114, 127, 166).

Grodent, D. (Apr. 2014). "A Brief Review of Ultraviolet Auroral Emissions on Giant Planets". In: *Space Science Reviews* 187.1, pp. 23–50. ISSN: 1572-9672. DOI: 10.1007/s11214-014-0052-8. URL: https://doi.org/10.1007/s11214-014-0052-8 (cit. on pp. 40, 44).

Grodent, D., B. Bonfond, J.-C. Gérard, A. Radioti, J. Gustin, J. T. Clarke, J. Nichols, and J. E. P. Connerney (2008). "Auroral evidence of a localized magnetic anomaly in Jupiter's northern hemisphere". In: *Journal of Geophysical Research: Space Physics* 113.A9. DOI: https://doi.org/10.1029/2008JA013185. eprint: https://agupubs.onlinelibrary.wiley.com/doi/pdf/10.1029/2008JA013185. URL: https://agupubs.onlinelibrary.wiley.com/doi/abs/10.1029/2008JA013185 (cit. on pp. 45, 75).

Grodent, D., B. Bonfond, Z. Yao, J.-C. Gérard, A. Radioti, M. Dumont, B. Palmaerts, A. Adriani, S. V. Badman, E. J. Bunce, J. T. Clarke, J. E. P. Connerney, G. R. Gladstone, T. Greathouse, T. Kimura, W. S. Kurth, B. H. Mauk, D. J. McComas, J. D. Nichols, G. S. Orton, L. Roth, J. Saur, and P. Valek (2018). "Jupiter's Aurora Observed With HST During Juno Orbits 3 to 7". In: *Journal of Geophysical Research: Space Physics* 123.5, pp. 3299–3319. DOI: https://doi.org/10.1002/2017JA025046. eprint: https://agupubs.onlinelibrary.wiley.com/doi/pdf/10.1002/2017JA025046. URL: https://agupubs.onlinelibrary.wiley.com/doi/abs/10.1002/2017JA025046 (cit. on pp. 41, 63).

Grodent, D., J. T. Clarke, J. Kim, J. H. Waite Jr., and S. W. H. Cowley (2003a). "Jupiter's main auroral oval observed with HST-STIS". In: *Journal*

of Geophysical Research: Space Physics 108.A11. DOI: https://doi.org/10.1029/2003JA009921. eprint: https://agupubs.onlinelibrary.wiley.com/doi/pdf/10.1029/2003JA009921. URL: https://agupubs.onlinelibrary.wiley.com/doi/abs/10.1029/2003JA009921 (cit. on p. 41).

Grodent, D., J. T. Clarke, J. H. Waite Jr., S. W. H. Cowley, J.-C. Gérard, and J. Kim (2003b). "Jupiter's polar auroral emissions". In: *Journal of Geophysical Research: Space Physics* 108.A10. DOI: https://doi.org/10.1029/2003JA010017. eprint: https://agupubs.onlinelibrary.wiley.com/doi/pdf/10.1029/2003JA010017. URL: https://agupubs.onlinelibrary.wiley.com/doi/abs/10.1029/2003JA010017 (cit. on pp. xiii, 42, 47, 48, 54).

Grodent, D., J.-C. Gérard, J. T. Clarke, G. R. Gladstone, and J. H. Waite Jr. (2004). "A possible auroral signature of a magnetotail reconnection process on Jupiter". In: *Journal of Geophysical Research: Space Physics* 109.A5. DOI: https://doi.org/10.1029/2003JA010341. eprint: https://agupubs.onlinelibrary.wiley.com/doi/pdf/10.1029/2003JA010341. URL: https://agupubs.onlinelibrary.wiley.com/doi/abs/10.1029/2003JA010341 (cit. on p. 46).

Gustin, J., B. Bonfond, D. Grodent, and J.-C. Gérard (2012). "Conversion from HST ACS and STIS auroral counts into brightness, precipitated power, and radiated power for H2 giant planets". In: *Journal of Geophysical Research: Space Physics* 117.A7. DOI: https://doi.org/10.1029/2012JA017607. eprint: https://agupubs.onlinelibrary.wiley.com/doi/pdf/10.1029/2012JA017607. URL: https://agupubs.onlinelibrary.wiley.com/doi/abs/10.1029/2012JA017607 (cit. on pp. 43, 78, 79).

Hasegawa, H., M. Fujimoto, T.-D. Phan, H. Rème, A. Balogh, M. W. Dunlop, C. Hashimoto, and R. TanDokoro (Aug. 2004). "Transport of solar wind into Earth's magnetosphere through rolled-up Kelvin-Helmholtz vortices". In: *Nature* 430.7001, pp. 755–758. ISSN: 1476-4687. DOI: 10.1038/nature02799. URL: https://doi.org/10.1038/nature02799 (cit. on pp. 19, 142).

Head, L. A., D. Grodent, B. Bonfond, A. Moirano, B. Benmahi, G. Sicorello, J.-C. Gérard, M. F. Vogt, V. Hue, T. Greathouse, G. R. Gladstone, and Z. Yao (2024). "Effect of magnetospheric conditions on the morphology of Jupiter's ultraviolet main auroral emission as observed by Juno-UVS". In: *Astronomy and Astrophysics* 688, A205. DOI: 10.1051/0004-6361/202450253. URL: https://doi.org/10.1051/0004-6361/202450253 (cit. on p. 45).

Head, L. A., D. Grodent, B. Bonfond, A. Sulaiman, A. Moirano, G. Sicorello, S. Elliott, M. F. Vogt, C. K. Louis, N. Kruegler, J. Vinesse, and T. K. Greathouse (2025). "Ultraviolet auroral bridge of Jupiter - The effect of the solar wind on the morphology of the polar aurora". In: *Astronomy and Astrophysics* 700, A142. DOI: 10.1051/0004-6361/202554759. URL: https://doi.org/10.1051/0004-6361/202554759 (cit. on pp. 41, 47, 56, 120).

Hill, T. W. (1979). "Inertial limit on corotation". In: *Journal of Geophysical Research: Space Physics* 84.A11, pp. 6554–6558. DOI: https://doi.org/10.1029/JA084iA11p06554. eprint: https://agupubs.onlinelibrary.wiley.com/doi/pdf/10.1029/JA084iA11p06554. URL: https://agupubs.onlinelibrary.wiley.com/doi/abs/10.1029/JA084iA11p06554 (cit. on pp. 32, 35).

Hill, T. W., A. J. Dessler, and C. K. Goertz (1983). *Physics of the Jovian Magnetosphere*. Ed. by A.J. Dessler. Cambridge Planetary Science Old. Cambridge University Press (cit. on pp. 28, 29).

Hospodarsky, G. B., W. S. Kurth, S. J. Bolton, F. Allegrini, G. B. Clark, J. E. P. Connerney, R. W. Ebert, D. K. Haggerty, S. Levin, D. J. McComas, C. Paranicas, A. M. Rymer, and P. W. Valek (2017). "Jovian bow shock and magnetopause encounters by the Juno spacecraft". In: *Geophysical Research Letters* 44.10, pp. 4506–4512. DOI: https://doi.org/10.1002/2017GL073177. eprint: https://agupubs.onlinelibrary.wiley.com/doi/pdf/10.1002/2017GL073177. URL: https://agupubs.onlinelibrary.wiley.com/doi/abs/10.1002/2017GL073177 (cit. on p. 30).

Huscher, E., F. Bagenal, R. J. Wilson, F. Allegrini, R. W. Ebert, P. W. Valek, J. R. Szalay, D. J. McComas, J. E. P. Connerney, S. Bolton, and S. M. Levin (2021). "Survey of Juno Observations in Jupiter's Plasma Disk: Density". In: *Journal of Geophysical Research: Space Physics* 126.8. e2021JA029446 2021JA029446, e2021JA029446. DOI: https://doi.org/10.1029/2021JA029446. eprint: https://agupubs.onlinelibrary.wiley.com/doi/pdf/10.1029/2021JA029446. URL: https://agupubs.onlinelibrary.wiley.com/doi/abs/10.1029/2021JA029446 (cit. on p. 30).

Hwang, K.-J., M. L. Goldstein, M. M. Kuznetsova, Y. Wang, A. F. Viñas, and D. G. Sibeck (2012). "The first in situ observation of Kelvin-Helmholtz waves at high-latitude magnetopause during strongly dawnward interplanetary magnetic field conditions". In: *Journal of Geophysical Research: Space Physics* 117.A8. DOI: https://doi.org/10.1029/2011JA017256. eprint: https://agupubs.onlinelibrary.wiley.com/doi/pdf/10.1029/2011JA017256. URL: https://agupubs.onlinelibrary.wiley.com/doi/abs/10.1029/2011JA017256 (cit. on pp. 153, 154).

Ingersoll, P. A., A. R. Vasavada, B. Little, C. D. Anger, S. J. Bolton, C. Alexander, K. P. Klaasen, Tobiska W. K., and Galileo SSI Team (1998). "Imaging Jupiter's Aurora at Visible Wavelengths". In: *Icarus* 135.1, pp. 251–264. ISSN: 0019-1035. DOI: https://doi.org/10.1006/icar.1998.5971. URL: https://www.sciencedirect.com/science/article/pii/S0019103598959711 (cit. on p. 44).

Jackman, C. M., N. Achilleos, E. J. Bunce, S. W. H. Cowley, M. K. Dougherty, G. H. Jones, S. E. Milan, and E. J. Smith (2004). "Interplanetary magnetic field at ∼9 AU during the declining phase of the solar cycle and its implications for Saturn's magnetospheric dynamics". In: *Journal of Geophysical Research: Space Physics* 109.A11. DOI: https://doi.org/10.1029/2004JA010614. eprint: https://agupubs.onlinelibrary.wiley.com/doi/pdf/10.1029/2004JA010614.

URL: https://agupubs.onlinelibrary.wiley.com/doi/abs/10.1029/2004JA010614 (cit. on p. 132).

Jenkins, A., L. C. Ray, T. Fell, S. V. Badman, and C. T. S. Lorch (2024). "Revealing the Local Time Structure of the Alfvén Radius and Travel Times in Jupiter's Magnetosphere". In: *Journal of Geophysical Research: Planets* 129.10. e2024JE008414 2024JE008414, e2024JE008414. DOI: https://doi.org/10.1029/2024JE008414. eprint: https://agupubs.onlinelibrary.wiley.com/doi/pdf/10.1029/2024JE008414. URL: https://agupubs.onlinelibrary.wiley.com/doi/abs/10.1029/2024JE008414 (cit. on pp. 18, 36).

Johnson, R. E., H. Melin, T. S. Stallard, C. Tao, J. D. Nichols, and M. N. Chowdhury (2018). "Mapping H3+ Temperatures in Jupiter's Northern Auroral Ionosphere Using VLT-CRIRES". In: *Journal of Geophysical Research: Space Physics* 123.7, pp. 5990–6008. DOI: https://doi.org/10.1029/2018JA025511. eprint: https://agupubs.onlinelibrary.wiley.com/doi/pdf/10.1029/2018JA025511. URL: https://agupubs.onlinelibrary.wiley.com/doi/abs/10.1029/2018JA025511 (cit. on p. 44).

Jokipii, J. R. (June 2013). "The Heliospheric Termination Shock". In: *Space Science Reviews* 176.1, pp. 115–124. ISSN: 1572-9672. DOI: 10.1007/s11214-012-9914-0. URL: https://doi.org/10.1007/s11214-012-9914-0 (cit. on p. 22).

Joy, S. P., M. G. Kivelson, R. J. Walker, K. K. Khurana, C. T. Russell, and T. Ogino (2002). "Probabilistic models of the Jovian magnetopause and bow shock locations". In: *Journal of Geophysical Research: Space Physics* 107.A10, SMP 17-1-SMP 17–17. DOI: https://doi.org/10.1029/2001JA009146. eprint: https://agupubs.onlinelibrary.wiley.com/doi/pdf/10.1029/2001JA009146. URL: https://agupubs.onlinelibrary.wiley.com/doi/abs/10.1029/2001JA009146 (cit. on pp. 26, 30, 66, 128).

Kavosi, S., J. Raeder, J. R. Johnson, K. Nykyri, and C. J. Farrugia (May 2023). "Seasonal and diurnal variations of Kelvin-Helmholtz Instability at terrestrial magnetopause". In: *Nature Communications* 14.1, p. 2513. ISSN: 2041-1723. DOI:

10.1038/s41467-023-37485-x. URL: https://doi.org/10.1038/s41467-023-37485-x (cit. on p. 19).

Khan, H. and S. W. H. Cowley (1999). "Observations of the response time of high-latitude ionospheric convection to variations in the interplanetary magnetic field using EISCAT and IMP-8 data". In: *Annales Geophysicae* 17.10, pp. 1306–1335. DOI: 10.1007/s00585-999-1306-8. URL: https://angeo.copernicus.org/articles/17/1306/1999/ (cit. on p. 67).

Khurana, K. K. (1992). "A generalized hinged-magnetodisc model of Jupiter's nightside current sheet". In: *Journal of Geophysical Research: Space Physics* 97.A5, pp. 6269–6276. DOI: https://doi.org/10.1029/92JA00169. eprint: https://agupubs.onlinelibrary.wiley.com/doi/pdf/10.1029/92JA00169. URL: https://agupubs.onlinelibrary.wiley.com/doi/abs/10.1029/92JA00169 (cit. on p. 29).

Khurana, K. K., M. G. Kivelson, V. M. Vasyliunas, N. Krupp, J. Woch, A. Lagg, B. H. Mauk, and W. S. Kurth (2004). "Jupiter: The Planet, Satellies and Magnetosphere". In: ed. by F. Bagenal, Dowling, T.E., and W.B. McKinnon. Cambridge University Press. Chap. 24: The Configuration of Jupiter's Magnetosphere, pp. 593–616. ISBN: 0-521-81808-7. URL: https://ui.adsabs.harvard.edu/abs/2004jpsm.book..593K (cit. on pp. 24, 26, 29, 30, 33, 34, 37).

Khurana, K. K. and Hannes K. Schwarzl (2005). "Global structure of Jupiter's magnetospheric current sheet". In: *Journal of Geophysical Research: Space Physics* 110.A7. DOI: https://doi.org/10.1029/2004JA010757. eprint: https://agupubs.onlinelibrary.wiley.com/doi/pdf/10.1029/2004JA010757. URL: https://agupubs.onlinelibrary.wiley.com/doi/abs/10.1029/2004JA010757 (cit. on p. 29).

Kivelson, M. G., K. K. Khurana, C. T. Russell, and R. J. Walker (1997). "Intermittent short-duration magnetic field anomalies in the Io torus: Evidence for plasma interchange?" In: *Geophysical Research Letters* 24.17, pp. 2127–2130. DOI: https://doi.org/10.1029/97GL02202. eprint: https://agupubs.

onlinelibrary.wiley.com/doi/pdf/10.1029/97GL02202. URL: https://agupubs.onlinelibrary.wiley.com/doi/abs/10.1029/97GL02202 (cit. on p. 34).

Kivelson, M. G. and D. J. Southwood (2005). "Dynamical consequences of two modes of centrifugal instability in Jupiter's outer magnetosphere". In: *Journal of Geophysical Research: Space Physics* 110.A12. DOI: https://doi.org/10.1029/2005JA011176. eprint: https://agupubs.onlinelibrary.wiley.com/doi/pdf/10.1029/2005JA011176. URL: https://agupubs.onlinelibrary.wiley.com/doi/abs/10.1029/2005JA011176 (cit. on pp. 30, 37, 140, 149).

Kronberg, E. A., K.-H. Glassmeier, J. Woch, N. Krupp, A. Lagg, and M. K. Dougherty (2007). "A possible intrinsic mechanism for the quasi-periodic dynamics of the Jovian magnetosphere". In: *Journal of Geophysical Research: Space Physics* 112.A5. DOI: https://doi.org/10.1029/2006JA011994. eprint: https://agupubs.onlinelibrary.wiley.com/doi/pdf/10.1029/2006JA011994. URL: https://agupubs.onlinelibrary.wiley.com/doi/abs/10.1029/2006JA011994 (cit. on p. 31).

Kulsrud, R. M. (June 2001). "Magnetic reconnection: Sweet-Parker versus Petschek". In: *Earth, Planets and Space* 53.6, pp. 417–422. ISSN: 1880-5981. DOI: 10.1186/BF03353251. URL: https://doi.org/10.1186/BF03353251 (cit. on p. 15).

Kurth, W. S., J. D. Sullivan, D. A. Gurnett, F. L. Scarf, H. S. Bridge, and E. C. Sittler Jr. (1982). "Observations of Jupiter's distant magnetotail and wake". In: *Journal of Geophysical Research: Space Physics* 87.A12, pp. 10373–10383. DOI: https://doi.org/10.1029/JA087iA12p10373. eprint: https://agupubs.onlinelibrary.wiley.com/doi/pdf/10.1029/JA087iA12p10373. URL: https://agupubs.onlinelibrary.wiley.com/doi/abs/10.1029/JA087iA12p10373 (cit. on p. 30).

Lee, L. C. and K. H. Lee (Aug. 2020). "Fluid and kinetic aspects of magnetic reconnection and some related magnetospheric phenomena". In: *Reviews of Modern Plasma Physics* 4.1, p. 9. ISSN: 2367-3192. DOI: 10.1007/s41614-

020-00045-7. URL: https://doi.org/10.1007/s41614-020-00045-7 (cit. on pp. xi, 16).

Lorch, C. T. S., L. C. Ray, C. S. Arridge, K. K. Khurana, C. J. Martin, and A. Bader (2020). "Local Time Asymmetries in Jupiter's Magnetodisc Currents". In: *Journal of Geophysical Research: Space Physics* 125.2. e2019JA027455 10.1029/2019JA027455, e2019JA027455. DOI: https://doi.org/10.1029/2019JA027455. eprint: https://agupubs.onlinelibrary.wiley.com/doi/pdf/10.1029/2019JA027455. URL: https://agupubs.onlinelibrary.wiley.com/doi/abs/10.1029/2019JA027455 (cit. on pp. 35, 45).

Lorch, C. T. S., L. C. Ray, R. J. Wilson, F. Bagenal, F. Crary, P. A. Delamere, P. A. Damiano, C. E. J. Watt, and F. Allegrini (2022). "Evidence of Alfvénic Activity in Jupiter's Mid-To-High Latitude Magnetosphere". In: *Journal of Geophysical Research: Space Physics* 127.6. e2021JA029853 2021JA029853, e2021JA029853. DOI: https://doi.org/10.1029/2021JA029853. eprint: https://agupubs.onlinelibrary.wiley.com/doi/pdf/10.1029/2021JA029853. URL: https://agupubs.onlinelibrary.wiley.com/doi/abs/10.1029/2021JA029853 (cit. on p. 17).

Masters, A. (2017). "Model-Based Assessments of Magnetic Reconnection and Kelvin-Helmholtz Instability at Jupiter's Magnetopause". In: *Journal of Geophysical Research: Space Physics* 122.11, pp. 11, 154–11, 174. DOI: https://doi.org/10.1002/2017JA024736. eprint: https://agupubs.onlinelibrary.wiley.com/doi/pdf/10.1002/2017JA024736. URL: https://agupubs.onlinelibrary.wiley.com/doi/abs/10.1002/2017JA024736 (cit. on pp. 19, 27, 93, 115, 122, 124, 131, 134, 141, 150, 156, 162, 164).

— (2018). "A More Viscous-Like Solar Wind Interaction With All the Giant Planets". In: *Geophysical Research Letters* 45.15, pp. 7320–7329. DOI: https://doi.org/10.1029/2018GL078416. eprint: https://agupubs.onlinelibrary.wiley.com/doi/pdf/10.1029/2018GL078416. URL: https://agupubs.

onlinelibrary.wiley.com/doi/abs/10.1029/2018GL078416 (cit. on pp. 131, 141).

Mauk, B. H., J. T. Clarke, D. Grodent, J. H. Waite, C. P. Paranicas, and D. J. Williams (Feb. 2002). "Transient aurora on Jupiter from injections of magnetospheric electrons". In: *Nature* 415.6875, pp. 1003–1005. ISSN: 1476-4687. DOI: 10.1038/4151003a. URL: https://doi.org/10.1038/4151003a (cit. on pp. 34, 46).

Mauk, B. H., D. G. Mitchell, R. W. McEntire, C. P. Paranicas, E. C. Roelof, D. J. Williams, S. M. Krimigis, and A. Lagg (2004). "Energetic ion characteristics and neutral gas interactions in Jupiter's magnetosphere". In: *Journal of Geophysical Research: Space Physics* 109.A9. DOI: https://doi.org/10.1029/2003JA010270. eprint: https://agupubs.onlinelibrary.wiley.com/doi/pdf/10.1029/2003JA010270. URL: https://agupubs.onlinelibrary.wiley.com/doi/abs/10.1029/2003JA010270 (cit. on p. 93).

McComas, D. J., N. Alexander, F. Allegrini, F. Bagenal, C. Beebe, G. Clark, F. Crary, M. I. Desai, A. De Los Santos, D. Demkee, J. Dickinson, D. Everett, T. Finley, A. Gribanova, R. Hill, J. Johnson, C. Kofoed, C. Loeffler, P. Louarn, M. Maple, W. Mills, C. Pollock, M. Reno, B. Rodriguez, J. Rouzaud, D. Santos-Costa, P. Valek, S. Weidner, P. Wilson, R. J. Wilson, and D. White (Nov. 2013). "The Jovian Auroral Distributions Experiment (JADE) on the Juno Mission to Jupiter". In: *Space Science Reviews* 213.1, pp. 547–643. ISSN: 1572-9672. DOI: 10.1007/s11214-013-9990-9. URL: https://doi.org/10.1007/s11214-013-9990-9 (cit. on pp. xvi, 59, 61, 62).

McComas, D. J., F. Allegrini, F. Bagenal, F. Crary, R. W. Ebert, H. Elliott, A. Stern, and P. Valek (2007). "Diverse Plasma Populations and Structures in Jupiter's Magnetotail". In: *Science* 318.5848, pp. 217–220. DOI: 10.1126/science.1147393. eprint: https://www.science.org/doi/pdf/10.1126/science.1147393. URL: https://www.science.org/doi/abs/10.1126/science.1147393 (cit. on p. 31).

McComas, D. J. and F. Bagenal (2007). "Jupiter: A fundamentally different magnetospheric interaction with the solar wind". In: *Geophysical Research Letters* 34.20. DOI: https://doi.org/10.1029/2007GL031078. eprint: https://agupubs.onlinelibrary.wiley.com/doi/pdf/10.1029/2007GL031078. URL: https://agupubs.onlinelibrary.wiley.com/doi/abs/10.1029/2007GL031078 (cit. on p. 115).

McComas, D. J., J. R. Szalay, F. Allegrini, F. Bagenal, J. Connerney, R. W. Ebert, W. S. Kurth, P. Louarn, B. Mauk, M. Reno, M. F. Thomsen, P. Valek, S. Weidner, R. J. Wilson, and S. Bolton (2017). "Plasma environment at the dawn flank of Jupiter's magnetosphere: Juno arrives at Jupiter". In: *Geophysical Research Letters* 44.10, pp. 4432–4438. DOI: https://doi.org/10.1002/2017GL072831. eprint: https://agupubs.onlinelibrary.wiley.com/doi/pdf/10.1002/2017GL072831. URL: https://agupubs.onlinelibrary.wiley.com/doi/abs/10.1002/2017GL072831 (cit. on p. 91).

McNutt, R. L., J. W. Belcher, and H. S. Bridge (1981). "Positive ion observations in the middle magnetosphere of Jupiter". In: *Journal of Geophysical Research: Space Physics* 86.A10, pp. 8319–8342. DOI: https://doi.org/10.1029/JA086iA10p08319. eprint: https://agupubs.onlinelibrary.wiley.com/doi/pdf/10.1029/JA086iA10p08319. URL: https://agupubs.onlinelibrary.wiley.com/doi/abs/10.1029/JA086iA10p08319 (cit. on pp. 29, 30).

Mende, S. B., H. U. Frey, and V. Angelopoulos (2016). "Source of the dayside cusp aurora". In: *Journal of Geophysical Research: Space Physics* 121.8, pp. 7728–7738. DOI: https://doi.org/10.1002/2016JA022657. eprint: https://agupubs.onlinelibrary.wiley.com/doi/pdf/10.1002/2016JA022657. URL: https://agupubs.onlinelibrary.wiley.com/doi/abs/10.1002/2016JA022657 (cit. on p. 117).

Milan, S. E. (2004). "A simple model of the flux content of the distant magnetotail". In: *Journal of Geophysical Research: Space Physics* 109.A7. DOI: https://doi.org/10.1029/2004JA010397. eprint: https://agupubs.onlinelibrary.

wiley.com/doi/pdf/10.1029/2004JA010397. URL: https://agupubs.onlinelibrary.wiley.com/doi/abs/10.1029/2004JA010397 (cit. on p. 135).

Milan, S. E., E. J. Bunce, S. W. H. Cowley, and C. M. Jackman (2005). "Implications of rapid planetary rotation for the Dungey magnetotail of Saturn". In: *Journal of Geophysical Research: Space Physics* 110.A3. DOI: https://doi.org/10.1029/2004JA010716. eprint: https://agupubs.onlinelibrary.wiley.com/doi/pdf/10.1029/2004JA010716. URL: https://agupubs.onlinelibrary.wiley.com/doi/abs/10.1029/2004JA010716 (cit. on p. 94).

Milan, S. E., S. W. H. Cowley, M. Lester, D. M. Wright, J. A. Slavin, M. Fillingim, C. W. Carlson, and H. J. Singer (2004). "Response of the magnetotail to changes in the open flux content of the magnetosphere". In: *Journal of Geophysical Research: Space Physics* 109.A4. DOI: https://doi.org/10.1029/2003JA010350. eprint: https://agupubs.onlinelibrary.wiley.com/doi/pdf/10.1029/2003JA010350. URL: https://agupubs.onlinelibrary.wiley.com/doi/abs/10.1029/2003JA010350 (cit. on p. 132).

Miller, S., N. Achilleos, G. Ballester, T. Geballe, R. Joseph, R. Prangé, D. Rego, T. Stallard, J. Tennyson, L. Trafton, and J. Waite (Sept. 2000). "The role of H+3 in planetary atmospheres". In: *Philosophical Transactions of The Royal Society A: Mathematical, Physical and Engineering Sciences* 358, pp. 2485–2502. DOI: 10.1098/rsta.2000.0662 (cit. on p. 44).

Montgomery, D. C., E. A. Peck, and G. G. Vining (2012). *Introduction to Linear Regression Analysis*. Wiley. ISBN: 978-1-119-57872-7 (cit. on p. 170).

Ness, N. F., M. H. Acuña, R. P. Lepping, L. F. Burlaga, K. W. Behannon, and F. M. Neubauer (1979). "Magnetic Field Studies at Jupiter by Voyager 1: Preliminary Results". In: *Science* 204.4396, pp. 982–987. DOI: 10.1126/science.204.4396.982. eprint: https://www.science.org/doi/pdf/10.1126/science.204.4396.982. URL: https://www.science.org/doi/abs/10.1126/science.204.4396.982 (cit. on p. 14).

Nichols, J. D., S. V. Badman, F. Bagenal, S. J. Bolton, B. Bonfond, E. J. Bunce, J. T. Clarke, J. E. P. Connerney, S. W. H. Cowley, R. W. Ebert, M. Fujimoto, J.-C. Gérard, G. R. Gladstone, D. Grodent, T. Kimura, W. S. Kurth, B. H. Mauk, G. Murakami, D. J. McComas, G. S. Orton, A. Radioti, T. S. Stallard, C. Tao, P. W. Valek, R. J. Wilson, A. Yamazaki, and I. Yoshikawa (2017). "Response of Jupiter's auroras to conditions in the interplanetary medium as measured by the Hubble Space Telescope and Juno". In: *Geophysical Research Letters* 44.15, pp. 7643–7652. DOI: https://doi.org/10.1002/2017GL073029. eprint: https://agupubs.onlinelibrary.wiley.com/doi/pdf/10.1002/2017GL073029. URL: https://agupubs.onlinelibrary.wiley.com/doi/abs/10.1002/2017GL073029 (cit. on pp. 47, 54, 56, 63, 72, 74, 91, 95, 100, 109, 110, 120, 123, 124, 131).

Nichols, J. D., E. J. Bunce, J. T. Clarke, S. W. H. Cowley, J.-C. Gérard, D. Grodent, and W. R. Pryor (2007). "Response of Jupiter's UV auroras to interplanetary conditions as observed by the Hubble Space Telescope during the Cassini flyby campaign". In: *Journal of Geophysical Research: Space Physics* 112.A2. DOI: https://doi.org/10.1029/2006JA012005. eprint: https://agupubs.onlinelibrary.wiley.com/doi/pdf/10.1029/2006JA012005. URL: https://agupubs.onlinelibrary.wiley.com/doi/abs/10.1029/2006JA012005 (cit. on pp. 65, 67).

Nichols, J. D., J. T. Clarke, J. C. Gérard, and D. Grodent (2009a). "Observations of Jovian polar auroral filaments". In: *Geophysical Research Letters* 36.8. DOI: https://doi.org/10.1029/2009GL037578. eprint: https://agupubs.onlinelibrary.wiley.com/doi/pdf/10.1029/2009GL037578. URL: https://agupubs.onlinelibrary.wiley.com/doi/abs/10.1029/2009GL037578 (cit. on pp. 48, 115, 149).

Nichols, J. D., J. T. Clarke, J.-C. Gérard, D. Grodent, and K. C. Hansen (2009b). "Variation of different components of Jupiter's auroral emission". In: *Journal of Geophysical Research: Space Physics* 114.A6. DOI: https://doi.org/10.1029/

2009JA014051. eprint: https://agupubs.onlinelibrary.wiley.com/doi/pdf/10.1029/2009JA014051. URL: https://agupubs.onlinelibrary.wiley.com/doi/abs/10.1029/2009JA014051 (cit. on pp. 26, 38, 41, 45, 47, 48, 64, 117, 120, 127, 151).

Nichols, J. D., S. W. H. Cowley, and D. J. McComas (2006). "Magnetopause reconnection rate estimates for Jupiter's magnetosphere based on interplanetary measurements at -5AU". In: *Annales Geophysicae* 24.1, pp. 393–406. DOI: 10.5194/angeo-24-393-2006. URL: https://angeo.copernicus.org/articles/24/393/2006/ (cit. on pp. 72, 131–133, 138).

Pallier, L. and R. Prangé (2001). "More about the structure of the high latitude Jovian aurorae". In: *Planetary and Space Science* 49.10. Magnetosphere of the Outer Planets Part II, pp. 1159–1173. ISSN: 0032-0633. DOI: https://doi.org/10.1016/S0032-0633(01)00023-X. URL: https://www.sciencedirect.com/science/article/pii/S003206330100023X (cit. on pp. 47, 48, 50, 114, 136, 165).

Parker, E. N. (1957). "Sweet's mechanism for merging magnetic fields in conducting fluids". In: *Journal of Geophysical Research (1896-1977)* 62.4, pp. 509–520. DOI: https://doi.org/10.1029/JZ062i004p00509. eprint: https://agupubs.onlinelibrary.wiley.com/doi/pdf/10.1029/JZ062i004p00509. URL: https://agupubs.onlinelibrary.wiley.com/doi/abs/10.1029/JZ062i004p00509 (cit. on p. 15).

— (1958). "Dynamics of the Interplanetary Gas and Magnetic Fields." In: *Astrophysical Journal* 128, p. 664. DOI: 10.1086/146579 (cit. on pp. 20, 23).

Perreault, P. and S. I. Akasofu (Sept. 1978). "A study of geomagnetic storms". In: *Geophysical Journal International* 54.3, pp. 547–573. ISSN: 0956-540X. DOI: 10.1111/j.1365-246X.1978.tb05494.x. eprint: https://academic.oup.com/gji/article-pdf/54/3/547/1682075/54-3-547.pdf. URL: https://doi.org/10.1111/j.1365-246X.1978.tb05494.x (cit. on p. 132).

Prölss, G. W. (Jan. 2004). "Physics of the Earth's Space Environment". In: Springer. Chap. Interplanetary Medium, pp. 277–347. ISBN: 978-3-642-05979-7. DOI: 10.1007/978-3-642-97123-5_6 (cit. on pp. xii, 21).

Radioti, A., A. T. Tomàs, D. Grodent, J.-C. Gérard, J. Gustin, B. Bonford, N. Krupp, J. Woch, and J. D. Menietti (2009). "Equatorward diffuse auroral emissions at Jupiter: Simultaneous HST and Galileo observations". In: *Geophysical Research Letters* 36.7. DOI: https://doi.org/10.1029/2009GL037857. eprint: https://agupubs.onlinelibrary.wiley.com/doi/pdf/10.1029/2009GL037857. URL: https://agupubs.onlinelibrary.wiley.com/doi/abs/10.1029/2009GL037857 (cit. on p. 46).

Ranquist, D. A., F. Bagenal, and R. J. Wilson (2020). "Polar Flattening of Jupiter's Magnetosphere". In: *Geophysical Research Letters* 47.16. e2020GL089818 2020GL089818, e2020GL089818. DOI: https://doi.org/10.1029/2020GL089818. eprint: https://agupubs.onlinelibrary.wiley.com/doi/pdf/10.1029/2020GL089818. URL: https://agupubs.onlinelibrary.wiley.com/doi/abs/10.1029/2020GL089818 (cit. on p. 92).

Ranquist, D. A., F. Bagenal, R. J. Wilson, G. Hospodarsky, R. W. Ebert, F. Allegrini, P. Valek, D. J. McComas, J. E. P. Connerney, W. S. Kurth, and S. J. Bolton (2019). "Survey of Jupiter's Dawn Magnetosheath Using Juno". In: *Journal of Geophysical Research: Space Physics* 124.11, pp. 9106–9123. DOI: https://doi.org/10.1029/2019JA027382. eprint: https://agupubs.onlinelibrary.wiley.com/doi/pdf/10.1029/2019JA027382. URL: https://agupubs.onlinelibrary.wiley.com/doi/abs/10.1029/2019JA027382 (cit. on p. 25).

Ray, L. C., N. A. Achilleos, M. F. Vogt, and J. N. Yates (2014). "Local time variations in Jupiter's magnetosphere-ionosphere coupling system". In: *Journal of Geophysical Research: Space Physics* 119.6, pp. 4740–4751. DOI: https://doi.org/10.1002/2014JA019941. eprint: https://agupubs.onlinelibrary.

wiley.com/doi/pdf/10.1002/2014JA019941. URL: https://agupubs.onlinelibrary.wiley.com/doi/abs/10.1002/2014JA019941 (cit. on p. 45).

Ray, L. C., R. E. Ergun, P. A. Delamere, and F. Bagenal (2010). "Magnetosphere-ionosphere coupling at Jupiter: Effect of field-aligned potentials on angular momentum transport". In: *Journal of Geophysical Research: Space Physics* 115.A9. DOI: https://doi.org/10.1029/2010JA015423. eprint: https://agupubs.onlinelibrary.wiley.com/doi/pdf/10.1029/2010JA015423. URL: https://agupubs.onlinelibrary.wiley.com/doi/abs/10.1029/2010JA015423 (cit. on pp. 28, 35).

Ray, L. C., Y.-J. Su, R. E. Ergun, P. A. Delamere, and F. Bagenal (2009). "Current-voltage relation of a centrifugally confined plasma". In: *Journal of Geophysical Research: Space Physics* 114.A4. DOI: https://doi.org/10.1029/2008JA013969. eprint: https://agupubs.onlinelibrary.wiley.com/doi/pdf/10.1029/2008JA013969. URL: https://agupubs.onlinelibrary.wiley.com/doi/abs/10.1029/2008JA013969 (cit. on p. 37).

Rutala, M. J., J. T. Clarke, J. D. Mullins, and J. D. Nichols (2022). "Illuminating the Motions of Jupiter's Auroral Dawn Storms". In: *Journal of Geophysical Research: Space Physics* 127.6. e2022JA030448 2022JA030448, e2022JA030448. DOI: https://doi.org/10.1029/2022JA030448. eprint: https://agupubs.onlinelibrary.wiley.com/doi/pdf/10.1029/2022JA030448. URL: https://agupubs.onlinelibrary.wiley.com/doi/abs/10.1029/2022JA030448 (cit. on p. 37).

Rutala, M. J., C. M. Jackman, C. K. Louis, A. R. Azari, F. Bagenal, S. P. Joy, W. S. Kurth, T. B. Keebler, R. S. Giles, R. W. Ebert, C. F. Bowers, and M. F. Vogt (2025). "New Models of Jupiter's Magnetopause and Bow Shock Through the Juno Prime Mission: Probabilistic Location, Shape, and Internally-Driven Variation". In: *Journal of Geophysical Research: Space Physics* 130.5. e2025JA033842 2025JA033842, e2025JA033842. DOI: https://doi.org/10.1029/2025JA033842. eprint: https://agupubs.onlinelibrary.wiley.com/

doi/pdf/10.1029/2025JA033842. URL: https://agupubs.onlinelibrary.wiley.com/doi/abs/10.1029/2025JA033842 (cit. on pp. 26, 128, 166).

Schober, Patrick, Christa Boer, and Lothar A. Schwarte (2018). "Correlation Coefficients: Appropriate Use and Interpretation". In: *Anesthesia and Analgesia* 126.5. ISSN: 0003-2999. URL: https://journals.lww.com/anesthesia-analgesia/fulltext/2018/05000/correlation_coefficients__appropriate_use_and.50.aspx (cit. on p. 123).

Schunk, R. W. and A. F. Nagy (2000). *Ionospheres: Physics, Plasma Physics and Chemistry*. Cambridge University Press. ISBN: 978-0-521-87706-0 (cit. on pp. 28, 43).

Slavin, J. A., E. J. Smith, J. R. Spreiter, and S. S. Stahara (1985). "Solar wind flow about the outer planets: Gas dynamic modeling of the Jupiter and Saturn bow shocks". In: *Journal of Geophysical Research: Space Physics* 90.A7, pp. 6275–6286. DOI: https://doi.org/10.1029/JA090iA07p06275%7D. eprint: https://agupubs.onlinelibrary.wiley.com/doi/pdf/10.1029/JA090iA07p06275%7D. URL: https://agupubs.onlinelibrary.wiley.com/doi/abs/10.1029/JA090iA07p06275%7D (cit. on pp. 67, 142, 143).

Snodgrass, M., Herschel B., and R. K. Ulrich (Mar. 1990). "Rotation of Doppler Features in the Solar Photosphere". In: *Astrophysical Journal* 351, p. 309. DOI: 10.1086/168467 (cit. on p. 23).

Southwood, D. J. and M. G. Kivelson (1987). "Magnetospheric interchange instability". In: *Journal of Geophysical Research: Space Physics* 92.A1, pp. 109–116. DOI: https://doi.org/10.1029/JA092iA01p00109. eprint: https://agupubs.onlinelibrary.wiley.com/doi/pdf/10.1029/JA092iA01p00109. URL: https://agupubs.onlinelibrary.wiley.com/doi/abs/10.1029/JA092iA01p00109 (cit. on p. 34).

— (1989). "Magnetospheric interchange motions". In: *Journal of Geophysical Research: Space Physics* 94.A1, pp. 299–308. DOI: https://doi.org/10.1029/JA094iA01p00299. eprint: https://agupubs.onlinelibrary.wiley.com/doi/

pdf/10.1029/JA094iA01p00299. URL: https://agupubs.onlinelibrary.wiley.com/doi/abs/10.1029/JA094iA01p00299 (cit. on p. 34).

Stahara, S. S., R. R. Rachiele, J. R. Spreiter, and J. A. Slavin (1989). "A three dimensional gasdynamic model for solar wind flow past nonaxisymmetric magnetospheres: Application to Jupiter and Saturn". In: *Journal of Geophysical Research: Space Physics* 94.A10, pp. 13353–13365. DOI: https://doi.org/10.1029/JA094iA10p13353. eprint: https://agupubs.onlinelibrary.wiley.com/doi/pdf/10.1029/JA094iA10p13353. URL: https://agupubs.onlinelibrary.wiley.com/doi/abs/10.1029/JA094iA10p13353 (cit. on pp. 142, 143).

Stallard, T., S. Miller, G. Millward, and R. D. Joseph (2001). "On the Dynamics of the Jovian Ionosphere and Thermosphere: I. The Measurement of Ion Winds". In: *Icarus* 154.2, pp. 475–491. ISSN: 0019-1035. DOI: https://doi.org/10.1006/icar.2001.6681. URL: https://www.sciencedirect.com/science/article/pii/S0019103501966813 (cit. on pp. 50, 114, 136, 165).

Stallard, T., C. Smith, S. Miller, H. Melin, M. Lystrup, A. Aylward, N. Achilleos, and M. Dougherty (2007). "Saturn's auroral/polar H+3 infrared emission: II. A comparison with plasma flow models". In: *Icarus* 191.2, pp. 678–690. ISSN: 0019-1035. DOI: https://doi.org/10.1016/j.icarus.2007.05.016. URL: https://www.sciencedirect.com/science/article/pii/S0019103507002606 (cit. on p. 94).

Stallard, T. S., J. T. Clarke, H. Melin, S. Miller, J. D. Nichols, J. O'Donoghue, R. E. Johnson, J. E.P. Connerney, T. Satoh, and M. Perry (2016). "Stability within Jupiter's polar auroral 'Swirl region' over moderate timescales". In: *Icarus* 268, pp. 145–155. ISSN: 0019-1035. DOI: https://doi.org/10.1016/j.icarus.2015.12.044. URL: https://www.sciencedirect.com/science/article/pii/S0019103515006107 (cit. on p. 48).

Stallard, T. S., S. Miller, S. W. H. Cowley, and E. J. Bunce (2003). "Jupiter's polar ionospheric flows: Measured intensity and velocity variations poleward of

the main auroral oval". In: *Geophysical Research Letters* 30.5. DOI: https://doi.org/10.1029/2002GL016031. eprint: https://agupubs.onlinelibrary.wiley.com/doi/pdf/10.1029/2002GL016031. URL: https://agupubs.onlinelibrary.wiley.com/doi/abs/10.1029/2002GL016031 (cit. on pp. 48, 50, 51, 114, 136).

Strobel, D. F. and S. K Atreta (1983). "Physics of the Jovian Magnetosphere". In: Cambridge Planetary Science Old. Cambridge University Press. Chap. Ionosphere. ISBN: 9780521520065. DOI: 10.1017/CBO9780511564574 (cit. on pp. 28, 43).

Sweet, P. A. (1958). "14. The neutral point theory of solar flares". In: *Symposium - International Astronomical Union* 6, pp. 123–134. DOI: 10.1017/S0074180900237704 (cit. on p. 15).

Swisdak, M., J. F. Drake, M. A. Shay, and J. G. McIlhargey (2005). "Transition from antiparallel to component magnetic reconnection". In: *Journal of Geophysical Research: Space Physics* 110.A5. DOI: https://doi.org/10.1029/2004JA010748. eprint: https://agupubs.onlinelibrary.wiley.com/doi/pdf/10.1029/2004JA010748. URL: https://agupubs.onlinelibrary.wiley.com/doi/abs/10.1029/2004JA010748 (cit. on p. 16).

Swithenbank-Harris, B. G., J. D. Nichols, and E. J. Bunce (2019). "Jupiter's Dark Polar Region as Observed by the Hubble Space Telescope During the Juno Approach Phase". In: *Journal of Geophysical Research: Space Physics* 124.11, pp. 9094–9105. DOI: https://doi.org/10.1029/2019JA027306. eprint: https://agupubs.onlinelibrary.wiley.com/doi/pdf/10.1029/2019JA027306. URL: https://agupubs.onlinelibrary.wiley.com/doi/abs/10.1029/2019JA027306 (cit. on pp. 47, 48, 166).

Szalay, J. R., B. Bonfond, F. Allegrini, F. Bagenal, S. Bolton, G. Clark, J. E. P. Connerney, R. W. Ebert, R. E. Ergun, G. R. Gladstone, D. Grodent, G. B. Hospodarsky, V. Hue, W. S. Kurth, S. Kotsiaros, S. M. Levin, P. Louarn, B. Mauk, D. J. McComas, J. Saur, P. W. Valek, and R. J. Wilson (2018).

"In Situ Observations Connected to the Io Footprint Tail Aurora". In: *Journal of Geophysical Research: Planets* 123.11, pp. 3061–3077. DOI: https://doi.org/10.1029/2018JE005752. eprint: https://agupubs.onlinelibrary.wiley.com/doi/pdf/10.1029/2018JE005752. URL: https://agupubs.onlinelibrary.wiley.com/doi/abs/10.1029/2018JE005752 (cit. on p. 46).

Thomas, N., F. Bagenal, T. W. Hill, and J. K. Wilson (2004). "The Io neutral clouds and plasma torus". In: *Jupiter: The Planet, Satellites and Magnetosphere*. Ed. by F. Bagenal, Timothy E. Dowling, and William B. McKinnon. Cambridge: Cambridge University Press, pp. 561–591 (cit. on pp. 31, 32).

Vasyliũnas, V. (1983). "Physics of the Jovian Magnetosphere". In: Cambridge University Press. Chap. Plasma Distribution and FLow. ISBN: 9780521520065. DOI: 10.1017/CBO9780511564574 (cit. on pp. 31, 37, 38, 140).

— (2001). "Electric field and plasma flow: What drives what?" In: *Geophysical Research Letters* 28.11, pp. 2177–2180. DOI: https://doi.org/10.1029/2001GL013014. eprint: https://agupubs.onlinelibrary.wiley.com/doi/pdf/10.1029/2001GL013014. URL: https://agupubs.onlinelibrary.wiley.com/doi/abs/10.1029/2001GL013014 (cit. on p. 35).

Vichare, G., S. Alex, and G. S. Lakhina (2005). "Some characteristics of intense geomagnetic storms and their energy budget". In: *Journal of Geophysical Research: Space Physics* 110.A3. DOI: https://doi.org/10.1029/2004JA010418. eprint: https://agupubs.onlinelibrary.wiley.com/doi/pdf/10.1029/2004JA010418. URL: https://agupubs.onlinelibrary.wiley.com/doi/abs/10.1029/2004JA010418 (cit. on p. 123).

Vogt, M. F., J. E.P. Connerney, G. A. DiBraccio, R. J. Wilson, M. F. Thomsen, R. W. Ebert, G. B. Clark, C. Paranicas, W. S. Kurth, F. Allegrini, P. W. Valek, and S. J. Bolton (2020). "Magnetotail Reconnection at Jupiter: A Survey of Juno Magnetic Field Observations". In: *Journal of Geophysical Research: Space Physics* 125.3. e2019JA027486 2019JA027486, e2019JA027486. DOI: https://doi.org/10.1029/2019JA027486. eprint: https://agupubs.onlinelibrary.

wiley.com/doi/pdf/10.1029/2019JA027486. URL: https://agupubs.onlinelibrary.wiley.com/doi/abs/10.1029/2019JA027486 (cit. on p. 31).

Vogt, M. F., M. G. Kivelson, K. K. Khurana, S. P. Joy, and R. J. Walker (2010). "Reconnection and flows in the Jovian magnetotail as inferred from magnetometer observations". In: *Journal of Geophysical Research: Space Physics* 115.A6. DOI: https://doi.org/10.1029/2009JA015098. eprint: https://agupubs.onlinelibrary.wiley.com/doi/pdf/10.1029/2009JA015098. URL: https://agupubs.onlinelibrary.wiley.com/doi/abs/10.1029/2009JA015098 (cit. on p. 37).

Vogt, M. F., M. G. Kivelson, K. K. Khurana, R. J. Walker, B. Bonfond, D. Grodent, and A. Radioti (2011). "Improved mapping of Jupiter's auroral features to magnetospheric sources". In: *Journal of Geophysical Research: Space Physics* 116.A3. DOI: https://doi.org/10.1029/2010JA016148. eprint: https://agupubs.onlinelibrary.wiley.com/doi/pdf/10.1029/2010JA016148. URL: https://agupubs.onlinelibrary.wiley.com/doi/abs/10.1029/2010JA016148 (cit. on pp. 47, 50, 51, 55, 57, 83, 114, 117, 118, 121, 126, 136, 149, 150, 153, 156, 165).

Waite, J.-H., G.-R. Gladstone, W.-S. Lewis, R. Goldstein, D.-J. McComas, P. Riley, R.-J. Walker, P. Robertson, S. Desai, J.-T. Clarke, and D.-T. Young (Apr. 2001). "An auroral flare at Jupiter". In: *Nature* 410.6830, pp. 787–789. DOI: 10.1038/35071018 (cit. on pp. 47, 54).

Went, D. R., M. G. Kivelson, N. Achilleos, C. S. Arridge, and M. K. Dougherty (2011). "Outer magnetospheric structure: Jupiter and Saturn compared". In: *Journal of Geophysical Research: Space Physics* 116.A4. DOI: https://doi.org/10.1029/2010JA016045. eprint: https://agupubs.onlinelibrary.wiley.com/doi/pdf/10.1029/2010JA016045. URL: https://agupubs.onlinelibrary.wiley.com/doi/abs/10.1029/2010JA016045 (cit. on p. 30).

Wilson, R. J., F. Bagenal, P. W. Valek, D. J. McComas, F. Allegrini, R. W. Ebert, T. K. Kim, W. S. Kurth, J. R. Szalay, and M. F. Thomsen (2018). "Solar Wind

Properties During Juno's Approach to Jupiter: Data Analysis and Resulting Plasma Properties Utilizing a 1-D Forward Model". In: *Journal of Geophysical Research: Space Physics* 123.4, pp. 2772–2786. DOI: https://doi.org/10.1002/2017JA024860. eprint: https://agupubs.onlinelibrary.wiley.com/doi/pdf/10.1002/2017JA024860. URL: https://agupubs.onlinelibrary.wiley.com/doi/abs/10.1002/2017JA024860 (cit. on pp. 59, 62).

Xu, Y., C. S. Arridge, Z. H. Yao, B. Zhang, L. C. Ray, S. V. Badman, W. R. Dunn, R. W. Ebert, J. J. Chen, F. Allegrini, W. S. Kurth, T. S. Qin, J. E. P. Connerney, D. J. McComas, S. J. Bolton, and Y. Wei (July 2024). "In situ evidence of the magnetospheric cusp of Jupiter from Juno spacecraft measurements". In: *Nature Communications* 15.1, p. 6062. ISSN: 2041-1723. DOI: 10.1038/s41467-024-50449-z. URL: https://doi.org/10.1038/s41467-024-50449-z (cit. on pp. 48, 55, 116, 118, 128).

Yao, Z., B. Bonfond, D. Grodent, E. Chané, W. R. Dunn, W. S. Kurth, J. E. P. Connerney, J. D. Nichols, B. Palmaerts, R. L. Guo, G. B. Hospodarsky, B. H. Mauk, T. Kimura, and S. J. Bolton (2022). "On the Relation Between Auroral Morphologies and Compression Conditions of Jupiter's Magnetopause: Observations From Juno and the Hubble Space Telescope". In: *Journal of Geophysical Research: Space Physics* 127.10. e2021JA029894 2021JA029894, e2021JA029894. DOI: https://doi.org/10.1029/2021JA029894. eprint: https://agupubs.onlinelibrary.wiley.com/doi/pdf/10.1029/2021JA029894. URL: https://agupubs.onlinelibrary.wiley.com/doi/abs/10.1029/2021JA029894 (cit. on pp. 26, 38, 41, 45, 117, 120, 127, 151).

Yao, Z., W. R. Dunn, E. E. Woodfield, G. Clark, B. H. Mauk, R. W. Ebert, D. Grodent, B. Bonfond, D. Pan, I. J. Rae, B. Ni, R. Guo, G. Branduardi-Raymont, A. D. Wibisono, P. Rodriguez, S. Kotsiaros, J.-U. Ness, F. Allegrini, W. S. Kurth, G. R. Gladstone, R. Kraft, A. H. Sulaiman, H. Manners, R. T. Desai, and S. J. Bolton (2021). "Revealing the source of Jupiter's x-ray auroral flares". In: *Science Advances* 7.28, eabf0851. DOI: 10.1126/sciadv.abf0851. eprint: https://www.

science.org/doi/pdf/10.1126/sciadv.abf0851. URL: https://www.science.org/doi/abs/10.1126/sciadv.abf0851 (cit. on pp. 43, 55).

Yelle, R. V. and S. Miller (2004). "Jupiter: The Planet, Satellites and Magnetosphere". In: Cambridge University Press. Chap. Jupiter's Thermosphere and Ionosphere (cit. on pp. 28, 43).

Zhang, B., P. A. Delamere, X. Ma, B. Burkholder, M. Wiltberger, J. G. Lyon, V. G. Merkin, and K. A. Sorathia (2018). "Asymmetric Kelvin-Helmholtz Instability at Jupiter's Magnetopause Boundary: Implications for Corotation-Dominated Systems". In: *Geophysical Research Letters* 45.1, pp. 56–63. DOI: https://doi.org/10.1002/2017GL076315. eprint: https://agupubs.onlinelibrary.wiley.com/doi/pdf/10.1002/2017GL076315. URL: https://agupubs.onlinelibrary.wiley.com/doi/abs/10.1002/2017GL076315 (cit. on pp. 122, 131, 141, 143, 150, 153, 156, 162, 164).

Zhang, B., P. A. Delamere, Z. Yao, B. Bonfond, D. Lin, K. A. Sorathia, O. J. Brambles, W. Lotko, J. S. Garretson, V. G. Merkin, D. Grodent, W. R. Dunn, and J. G. Lyon (2021). "How Jupiter's unusual magnetospheric topology structures its aurora". In: *Science Advances* 7.15, eabd1204. DOI: 10.1126/sciadv.abd1204. eprint: https://www.science.org/doi/pdf/10.1126/sciadv.abd1204. URL: https://www.science.org/doi/abs/10.1126/sciadv.abd1204 (cit. on pp. xv, 31, 48, 52, 53, 55, 57, 83, 94, 114, 116, 118, 119, 128, 136, 149, 152, 156, 165).

Zhang, Q.-H., Y.-L. Zhang, C. Wang, M. Lockwood, H.-G. Yang, B.-B. Tang, Z.-Y. Xing, K. Oksavik, L. R. Lyons, Y.-Z. Ma, Q.-G. Zong, J. Idar Moen, and L.-D. Xia (2020). "Multiple transpolar auroral arcs reveal insight about coupling processes in the Earth's magnetotail". In: *Proceedings of the National Academy of Sciences* 117.28, pp. 16193–16198. DOI: 10.1073/pnas.2000614117. eprint: https://www.pnas.org/doi/pdf/10.1073/pnas.2000614117. URL: https://www.pnas.org/doi/abs/10.1073/pnas.2000614117 (cit. on pp. 115, 131, 149, 156, 164).